Préparation et piégeage d'atomes de Rydberg circulaires individuels pour la simulation quantique

Brice Ravon

PSL
UNIVERSITÉ PARIS

THÈSE DE DOCTORAT
DE L'UNIVERSITÉ PSL

Préparée à École Normale Supérieure

Preparation and trapping of individual circular Rydberg atoms for quantum simulation

Soutenue par
Brice RAVON
Le 05 décembre 2022

École doctorale n°564
Physique en Île-de-France

Spécialité
Physique quantique

Composition du jury :

Frédéric CHÉVY Professor, École Normale Supérieure	*Président*
Thierry LAHAYE Professor, Institut d'Optique	*Rapporteur*
Jeff THOMPSON Professor, Princeton Univeristy	*Rapporteur*
Laurianne CHOMAZ Professor, Physikalisches Institut Heidelberg	*Examinateur*
Bruno LABURTHE-TOLRA Professor, Université Sorbonne Paris Nord	*Examinateur*
Michel BRUNE Professor, Laboratoire Kastler Brossel	*Directeur de thèse*
Clément SAYRIN Professor, Laboratoire Kastler Brossel	*Invité*

1794
ENS | PSL

... for nature cannot be fooled.

— Richard Feynmann

Avant-propos

Cette thèse fut pour moi difficile. J'ai rejoint en avril 2017 l'équipe de la salle « E20 » du groupe d'Électrodynamique Quantique en Cavité. C'est Jean-Michel Raimond qui m'avait convaincu de contribuer à cette expérience. La route à suivre semblait claire. Après avoir préparé des états de Rydberg circulaires à partir d'un nuage de rubidium froid, il fallait mettre en évidence le piégeage pondéromoteur pour ces états circulaires. Nous pourrions alors nous concentrer sur ce que j'espérais être le cœur de ma thèse : la construction d'un simulateur quantique. L'idée était séduisante, pour simuler une chaine de spin, nous allions piéger une chaine d'atomes de Rydberg circulaires entre deux plaques conductrices afin d'inhiber l'émission spontanée, permettant ainsi de sonder la dynamique sur des échelles de temps jamais atteintes. Bien sûr, rien ne devait se passer comme prévu.

Je finissais alors mes études de physique, jusqu'alors principalement orientées sur la théorie : c'était en effet avec brio que j'avais réussi à éviter autant que possible toute forme de travaux pratiques en physique. J'allais maintenant devoir travailler sur un dispositif expérimental particulièrement complexe. En effet, celui-ci devait allier la préparation d'atomes froids, leur excitation et transfert vers l'état de Rydberg circulaire, le tout en environnement cryogénique.

C'est ainsi que je rencontrai Tigrane et Rodrigo, tous deux doctorants de l'équipe, ainsi que Clément, membre permanent en charge de notre manip', et Michel, qui fut mon directeur de thèse et suivait de près nos expériences. Je n'ai pas eu l'occasion d'interagir énormément avec Tigrane, qui allait commencer à rédiger peu de temps après mon arrivée. J'ai en revanche passé nettement plus de temps aux côtés de Rodrigo, toujours en questionnement — parfois jusqu'à l'égarement. Je garde de lui le souvenir de quelqu'un qui contrairement à moi, ne se laissait jamais abattre, même dans les moments difficiles. On le voyait travailler avec acharnement jusque tard, parfois encore présent à notre arrivée le lendemain matin.

J'ai dans un premier temps passé deux ans et demi à travailler sur ce dispositif, pour rattraper le retard et contribuer aux résultats des doctorants précédents. Les expériences que nous réalisions étaient complexes, de celles qui appellent inexorablement à des imprévus et des retards. Afin de compenser ces retards, une approche très populaire consiste à rendre permanentes les améliorations ou réparations temporaires effectuées pour pouvoir avancer. C'est par cette approche qu'une bonne partie du dispositif avait été construite, par ajouts successifs. Il m'a donc fallu énormément de temps pour me familiariser avec toutes ses composantes, dont certaines étaient un peu anciennes et pour le moins artisanales. Ce fut pour moi l'occasion de découvrir que j'étais perfectionniste, et de pester à chaque fois qu'un problème survenait. Il était difficile pour moi d'accepter que les choses restent telles quelles, et j'ai tout mis en œuvre pour apporter des modifications, au grand dam de certains.

Paul, qui nous a rejoint un an après mon arrivée, a apporté un bon équilibre à mes velléités. C'est avec lui que j'ai passé le plus de temps au laboratoire et ai partagé les bons moments comme les galères. Il a rendu agréables les longues journées passées à acquérir des

données.

Nous avons été rejoints un an plus tard par Maxime en post-doc, et Yohann, futur doctorant. C'était au moment où il apparaissait clair que le plan initial n'allait pas pouvoir être suivi : le simulateur quantique proposé était bien trop complexe à mettre en œuvre. Il fut donc décidé, quelque peu malgré moi, d'assembler une nouvelle manip' sur laquelle j'allais devoir obtenir mes résultats de thèse. Ce dispositif devait opérer à température ambiante et accommoder la préparation de pinces optiques. Maxime a contribué à la conception de la partie mécanique et j'ai pu apprécier son flegme, notamment face aux changements imposés à la dernière minute. Yohann s'est chargé des pinces optiques. Ses qualités expérimentales et son sens pratique hors du commun nous ont permis d'avoir un système dont les performances ont dépassé nos attentes.

Il m'apparait nécessaire de saluer leur contribution à ces résultats, ainsi que celle de Paul à qui je dois une partie des données présentées ici, acquises alors que j'avais déjà bien entamé ma rédaction.

Andrès nous a rejoints lorsque j'entamais ma cinquième année de thèse. Il a apporté à cette manip' une bonne dose d'enthousiasme, et je ne l'ai jamais vu démotivé par les vociférations d'un doctorant aigri par trop d'années passées sur ces expériences. Enfin, Gautier nous a rejoint un an plus tard alors que j'étais en pleine rédaction. J'ai la certitude qu'ils assureront l'avenir de la manip'.

Il faut admettre que l'on n'apprend pas grand chose quand tout fonctionne. J'ai eu ici l'occasion d'apprendre une quantité considérable de choses nouvelles, tant sur le plan expérimental que théorique, en mécanique, optique, électronique et programmation notamment. La décision de changer de dispositif au cours de ma thèse m'a aussi offert la possibilité d'acquérir de nouvelles compétences, cette fois-ci en organisation et gestion. J'ai pu mettre à profit ces connaissances à maintes reprises tout au long de mon doctorat.

La rédaction de ce manuscrit a été pour moi l'occasion de m'affranchir des contraintes extérieures et de produire un travail correspondant à mon niveau d'exigence propre. J'ai essayé tant bien que mal de fournir une description détaillée des phénomènes physiques en jeu tant sur le plan théorique qu'expérimental, bien que celle-ci m'apparaisse encore incomplète. Ceci a nécessité le développement de deux programmes informatiques pour d'une part l'analyse unifiée des données expérimentales, et d'autre part la réalisation des simulations de dynamique atomique. Ils ont été écrits au cours de ma rédaction et représentent à mes yeux une part non négligeable de mon travail de thèse dont il est fait usage dans la majeure partie du manuscrit, et il me semble nécessaire de le mentionner ici. Enfin, ces programmes ont été codés dans le langage Python, et s'appuient sur des bibliothèques telles que NumPy, SciPy et Matplotlib dont je tiens à remercier ici les développeurs et contributeurs.

Je tiens aussi à remercier l'ensemble des services du laboratoire ainsi que ceux du Collège de France. Je salue tout particulièrement la réactivité et la disponibilité du service administratif. Ces qualités sont partagées par les services mécanique et électronique, qui fournissent un travail et une expertise dont nous sommes absolument dépendants. Je salue enfin les services techniques et logistiques du Collège de France, qui nous permettent de travailler au quotidien dans un cadre des plus exceptionnels.

Pour conclure, ma vie pendant la thèse ne s'est pas limitée à mon travail au laboratoire. Je tiens enfin à remercier mes amis et mon entourage, avec qui je partage mes meilleurs moments.

Commençons par mes amis de longue date, rencontrés pour la plupart au lycée. Adrien, Agathe, Alexandre, Caroline, Flore, Georges, Jean, Lucile, Marie, Marie, Maud, Nicolas, Pierre, Samuel, Sonia. Je pourrais m'étendre longuement sur les moments qu'on a passés

ensemble et l'importance qu'ils ont pour moi, mais je pense que vous le savez et qu'il n'est pas nécessaire de le rappeler ici. Il y a aussi le groupe de l'X : Mathieu, et ces soirées passées à discuter des curiosités du monde jusque tard, parfois dans le brouillard. Moments de brouillard partagé aussi avec Jules et Malo. Il y a enfin ces gens rencontrés par l'intermédiaire de Marie : son mari Mathieu, Théodore, Gabriel, Nicolas et les autres avec lesquels je retiens quelques soirées tardives.

Le laboratoire ne fut pas non plus un lieu exclusivement dédié au travail, j'y ai aussi rencontré en plus de ceux mentionnés plus haut des gens hauts en couleurs. Igor, intarissable sur les détails techniques de sa manip'. Valentin, presque toujours en short et chemise, même en hiver. Fred, en quête de sens (comme bien des personnes...). Arthur, jamais trop à gauche. Rémi, intègre, la tête bien faite, qui a choisi de suivre sa voie. Haiteng, travailleur acharné qui a eu à lui seul la charge d'une expérience. Andrea, pour qui chaque jour est un combat à mener. Léa, qui trouve rarement le temps de dormir. Angelo, un peu tête en l'air. Et d'autres encore : Eva et Dorian avant moi, Guillaume, Baptiste et Ankul après moi.

Parmi tous les gens qu'on croise, il y en a avec lesquels on tisse des liens plus forts. Ce fut le cas pour moi au cours de ces presque six années. Arthur, Paul, Yohann, je tiens ici à vous exprimer le plaisir que j'ai eu à passer ces moments avec vous, au labo et en dehors. Pour paraphraser Paul : « Je suis entré avec des collègues, je repars avec des amis. »

Contents

Introduction **1**

1 Elements of atomic physics and introduction to Rydberg atoms **11**
1.1 One valence electron: alkali Rydberg atoms 12
1.1.1 The simple system: hydrogen atom 12
1.1.2 Rydberg states 17
1.1.3 Estimation of the corrective energy terms for circular states 20
1.2 Coupling to external fields 21
1.2.1 Static magnetic field: Zeeman and Paschen-Bach effects 21
1.2.2 Static electric field: Stark shift 23
1.2.3 Dipole-dipole interaction 25
1.2.4 Oscillating electromagnetic field 27
1.3 Light-matter interaction: applications 28
1.3.1 Adiabatic transfer to the circular state 28
1.3.2 Light-shift and dipole trapping 31
1.3.3 Ponderomotive trapping 34

2 Experimental setup **37**
2.1 Overview of the setup 37
2.1.1 The UHV environment 38
2.1.2 The sapphire cube 39
2.1.3 State-selective field ionization setup 41
2.2 Optical tweezers setup 43
2.2.1 Tweezer and imaging setup 44
2.2.2 Preparation of optical tweezers 47
2.2.3 Aberrations correction 49
2.3 Preparation of cold atoms in gaussian optical tweezers 51
2.3.1 Atom source and 2D-MOT 51
2.3.2 3D MOT 52
2.3.3 Optical molasses and imaging 52

3 Ground-state atoms trapped in tweezers **57**
3.1 Detection of trapped ground-state atoms 58
3.1.1 Fluorescence imaging 58
3.1.2 General procedure for data analysis 61
3.2 Characterization of the tweezers 63

3.2.1 Light shift spectroscopy . . . 64
3.2.2 Oscillations in the trap . . . 65
3.2.3 Trap parameters . . . 68
3.3 Atoms in tweezers . . . 70
3.3.1 Lifetime in the trap . . . 70
3.3.2 Atom temperature . . . 72

4 Preparation of circular states 75
4.1 Preparation of 52D . . . 76
4.1.1 Optical pumping . . . 77
4.1.2 Laser excitation . . . 79
4.2 Preparation of circular states . . . 84
4.2.1 Microwave transition . . . 84
4.2.2 Circularization . . . 88
4.3 Purity of the circular states and de-circularization . . . 90
4.3.1 Purity . . . 90
4.3.2 Electric field measurement . . . 92
4.3.3 Circularization and de-circularization efficiency . . . 93

5 Ponderomotive trapping of circular states 97
5.1 Ponderomotive trapping of Rydberg states . . . 98
5.1.1 Trapping of 52D . . . 99
5.1.2 Trapping of circular states . . . 102
5.2 Characterization of the traps . . . 105
5.2.1 Description of the traps . . . 106
5.2.2 Trap frequency measurement . . . 110
5.3 Lifetime measurement and coherent state manipulation . . . 112
5.3.1 Lifetime measurement . . . 112
5.3.2 Rabi oscillations . . . 115
5.3.3 Ramsey interferometry . . . 116

Conclusion and outlook 123

A The Kramers relation 127
A.1 The Kramers recurrence relation . . . 127
A.2 Computation of the average values $\langle r^s \rangle$ . . . 129

B Laser setup and frequencies 131
B.1 Ground-state laser setup . . . 131
B.2 Rydberg lasers setup . . . 135
B.3 Laser locking setup . . . 136

C Electric field control in the experiment 137
C.1 The sapphire cube electrode system . . . 137
C.2 Electric field control in the experiment . . . 139
C.3 Voltage switching electronics . . . 140

D Numerical simulations of atomic dynamics **145**
D.1 Gaussian traps . . . 145
D.1.1 Gaussian trap potential . . . 146
D.1.2 Sampling in phase space . . . 147
D.1.3 Monte-Carlo fitting procedure: temperature measurement . . . 149
D.1.4 Classical dynamics in gaussian tweezers . . . 150
D.2 BoB traps . . . 156
D.2.1 BoB traps anharmonicity . . . 157
D.2.2 Convolution with a charge density . . . 157
D.2.3 Classical dynamics in BoB traps . . . 160

E Supplementary material to chapter 5 **167**
E.1 Trapping of circular states: early demonstration . . . 167
E.1.1 Trapping signal . . . 167
E.1.2 Trap frequency . . . 169
E.2 Power-line-induced magnetic field noise measurement . . . 169

Résumé en français **173**

References **179**

Introduction

"Begin at the beginning," the King said gravely, "and go on till you come to the end: then stop."

— Lewis Carroll, *Alice in Wonderland*

The old quantum theory arose in the early 20^{th} century to account for unexplained observations made a few decades before. It succeeded in explaining the black-body spectrum, the photoelectric effect and most importantly the discrete atomic spectra available at the time [1, 2]. Quantum mechanics took a few decades to mature as its modern formulation, successfully accounting for most of the current experimental data available [3]. It underlies several technological advancements that are among the most important of human history, such as lasers [4] and semiconductor technology [5].

Contrary to *classical* theories, that consider states of the world as a distribution of matter and other fields in space and time, the quantum theory encodes the states of a physical system as vectors of a Hilbert space [6]. This approach brings a conterintuitive representation of the world, associated to the emergence of new features [7]. This has led physicists to consider quantum systems as a computational tool by taking advantage of quantum interference along with states superpositions and entanglement [8]. In this perspective, two main approaches emerge.

The first approach is that of quantum computation, which can be considered analogous to the classical implementation of computers. It relies on the assembly of a large number of interconnected individual two-level systems – qubits. The computation protocol consists in the application of successive unitary transforms in what is called a quantum algorithm and terminates with the readout of the state. Currently, the most efficient platforms, that have achieved the so-called *quantum supremacy* [9], are based either on superconducting circuits [10] or integrated photonics [11, 12]. Many quantum algorithms have been proposed [13] and successfully implemented as a small scale proof of principle [14, 15, 16]. However, the physical constraints imposed on any such device for proper scalability are strong. The control over the system must be preserved as its size increases and decoherence processes, that ultimately limit the computational power, must be contained. This, together with the possibility of increasing the number of qubits at limited cost, imposes strong constraints on any potential quantum computer. Up to now, none of the implementations completely solves the problem [17].

The second approach trades the generality of addressable problems for an improved performance on a particular problem. Quantum simulation was thus proposed by physicists [18, 19] to address complex problems which are intractable numerically. The idea is simple: to solve a set of differential equations, build a physical system whose dynamics is governed by

those equations and record its evolution. To quote Richard Feynman [20]:

"*The same equations have the same solutions.*"

Of course, numerical methods can be applied when the number of equations is small, but the computational resources required get prohibitive as this number gets large. Many-body quantum systems fall in the latter category, since the dimensionality of the Hilbert space scales exponentially with the system size. To illustrate this, consider a set of N spin-1/2 particles. Each particle evolves in the smallest non-trivial Hilbert space, of dimension 2. The ensemble as a whole therefore evolves in a 2^N-dimensional space, and is correspondingly ruled by 2^N equations. When the particles interact, those equations are coupled and the problem quickly becomes out of reach for complete numerical resolution. The current computational power available sets a limit on the system size. This limit is generally admitted to be around $N = 40$ for universal quantum computation [21, 22], with most numerical studies carried with $N \sim 20$ (see for example the results reviewed in [23] and [24]). Let us make clear that this does not prevent the study of large interacting quantum systems since in many cases the problem can be simplified: Bose-Einstein condensation [25] and BCS theory of superconductivity [26] are textbook cases. Other approximate methods exist to find solutions in low-energy sectors, such as density-matrix renormalization group methods [27].

However, current research is pointing towards problems for which the state and dynamics of each subsystem must be tracked down. These problems arise from condensed matter physics (spin-systems, high-T_c superconductivity, etc.), but also from other fields such as high-energy physics (with the simulation of gauge fields on lattices) or atomic physics (with the simulation of the Jaynes-Cummings hamiltonian) [21]. The relaxation and thermalization of quantum systems, quantum chaos [23] and associated phenomena such as many-body localization [24] and quantum scars [28] are the subject of growing interest among researchers.

Considering the variety of problems that could be addressed by quantum simulation, a large number of approaches have been proposed to tackle them [29]. Focusing on spin models such as the Ising model, three main implementations stand out:

- Superconducting circuits, as an implementation of the more general quantum computer, are also suited to the simulation of spin systems. Three archetypal categories of superconducting qubits can be distinguished, based on the quantity that encode the quantum state: charge, flux and phase qubits [30]. This gives significant flexibility in the simulation platforms that can be engineered, which translates into a variety of simulated systems [31], such as Mott insulators in the strongly interacting regime [32] or the dynamics of strongly-coupled light and matter [33].
- Trapped ions platforms [34] offer a high degree of control over the individual ions, along with long coherence times (10 ms-100 s depending on the implementation). The interaction scales with the inter-atomic distance r as $1/r^\alpha$ with a tunable range $0 < \alpha < 3$, hence a rather long-range interaction regime. These platforms are naturally suited to study non-equilibrium dynamics. For instance, in [35], the transport of a spin flip excitation in a chain of 15 ions was studied for various interaction parameters. The correlations were demonstrated to spread faster than the Lieb-Robinson bound when the couplings were beyond nearest-neighbor. Ion trapping was extended to 2D geometries [36] with hundreds of atoms, offering the prospect of large-scale simulations.
- Neutral atoms in optical lattices can emulate very large systems of both fermions and bosons. The loading of the lattice is carried with a gas of atoms in the quantum-degenerate regime (Bose-Einstein condensate for bosons and Fermi-degenerate gas for

fermions). So far, this regime has been achived with a wide variety of atomic species [37]. Ultracold atoms in optical lattices were used in early experiments, for intance to demonstrate the quantum phase transition from a superfluid to a Mott insulator [38]. Single-site resolution is now possible with quantum gas microscopes [39]. These platforms offer a broad range of possibilities for quantum simulation [40, 41]. Among them we can cite the possibility to easily introduce disorder on the lattice potential with an optical speckle. This allowed for the study of the disordered counterpart of the Bose-Hubbard model [42].

The idea of trapping neutral atoms in potentials created by light led to the demonstration of single-atom trapping in optical tweezers [43, 44], using the dipole force. Initially, a single tweezer was prepared by focusing a laser beam tightly, but the approach was fruitful and its developpement lead to the preparation of large arrays of optical tweezers. The team of Mikhail Lukin in Harvard was able to prepare and control a row of 100 tweezers by dynamically multiplexing radio-frequencies in an acousto-optic deflector and focusing the many beams with a microscope objective [45]. The use of spatial light modulation techniques in the team of Antoine Browaeys at Institut d'Optique allowed for the preparation of 2D arrays of $\sim$ 100 tweezers [46]. The loading of optical tweezers being probabilistic, such large arrays would be useless without the possibility to prepare deterministic configurations of atoms. The development of atom rearrangement and transport with moving tweezers was therefore concomitant to the increase of array size, now reaching several hundreds of atoms [47, 48]. More recent developments involved the preparation and assembly of 3D atomic structures [49, 50].

Traditionally, rubidium and cesium atoms, being easier to manipulate thanks to their single valence electron, were used for tweezer trapping [43, 44]. Recent advances, mostly related to laser technology, have opened the way for the trapping of other atomic species. Alkali atoms such as potassium are now being used [51], but also species with more than one valence electron, most notably strontium [52, 53] and ytterbium [54].

The inter-atomic distance of such atom assemblies is usually within the $2.5-15\,\mu$m range [55, 56, 57, 58, 59], too large to yield significant interactions for atoms close to the ground state. However, the interactions become significant when the atoms are excited to a *Rydberg state*, in which a valence electron occupies an orbital of high principal quantum number n. The electron orbit, extending far from the ion core, gives rise to a large electric dipole-dipole interaction V_{dd} between neighboring atoms, which can be tuned through the geometry and external fields [60, 61]. We can distinguish two cases, depending on whether the interaction is first or second-order.

The case of a first-order coupling between a pair of atoms in the dipole-coupled states $|\mathrm{r}\rangle$ and $|\mathrm{r}'\rangle$ is associated to an exchange energy $\langle \mathrm{r},\mathrm{r}'|\, V_{dd}\,|\mathrm{r}',\mathrm{r}\rangle = C_3/d^3$, where d is the inter-atomic distance. For an ensemble of atoms with coherent driving of the transition $|\mathrm{r}\rangle \leftrightarrow |\mathrm{r}'\rangle$ (Rabi frequency Ω and detuning δ), the hamiltonian takes the form [62]

$$H/\hbar = \frac{\Omega}{2}\sum_i \sigma_i^x - \frac{\Delta}{2}\sum_i \sigma_i^z + \sum_{i<j}\frac{C_{3,ij}}{d_{ij}^3}\left[\sigma_i^+\sigma_j^- + \sigma_i^-\sigma_j^+\right]. \tag{1}$$

This XY hamiltonian is well suited to the study of excitation transport, and gives rise to a variety of phenomena [63, 64]. In [56], de Leseleuc *et al.* take advantage of the anisotropic dipolar interaction to achieve topologically-protected edges states on a chain of 14 atoms. The model consists in a chain of spins with alternating weak and strong couplings between nearest neighbors. The authors probe the energy spectrum through microwave spectroscopy in both

the trivial (strong coupling at the edges of the chain) and the topological (weak coupling at the edge). They observe the presence of edge states at zero energy in the topological configuration, characterized by high occupancy on the two edge sites (see figure 1 (a)).

The quantum simulation protocols involving Rydberg atoms rather relie on the second-order dipole-dipole interaction between atoms in the same Rydberg state $|\mathrm{r}\rangle$. The so-called van der Waals interaction scales as $1/d^6$. The spin states are usually embodied by an atomic ground state $|\mathrm{g}\rangle$ which is laser-coupled to a Rydberg state $|\mathrm{r}\rangle$. With the notations introduced above for the Rabi frequency and detuning, the hamiltonian now takes the form [62]

$$H/\hbar = \frac{\Omega}{2}\sum_i \sigma_i^x - \Delta\sum_i n_i^z + \sum_{i<j}\frac{C_{6,ij}}{d_{ij}^6} n_i n_j, \tag{2}$$

where $n_i = (\sigma_i^z + 1)/2$. The strong van der Waals interaction leads to the well known *dipole blockade* mechanism [65], illustrated in figure 1 (b), in which an atom excited to the Rydberg state shifts the transition of nearby atoms out of resonance. This can be understood using the *blockade radius* $R_\mathrm{b} = \left(\frac{C_6}{\hbar\Omega}\right)^{1/6}$: only one Rydberg excitation is allowed in a solid sphere of radius R_b.

The dipole blockade has been used in a variety of contexts. It can be viewed as a way to prevent a Rydberg excitation conditionally to the presence of a neighboring Rydberg atom, and hence serves as the basis for proposals [66] and implementation [67, 68, 69] of C-NOT and other quantum gates. The hamiltonian (2) can be mapped to the Ising model with a transverse field. As such, it exhibits a variety of phases that have been probed in one- and two-dimensional arrays of atoms. In [55], the authors access the Z_n-ordered phases of a chain of 13 atoms through a sweep of the driving laser parameters (see figure 1 (c)). Using the full capability of their simulator, a chain of 51 atoms, they study the domain walls in the Z_2 and show the occurrence of oscillations between two many-body anti-ferromagnetic states after a quench. Using a similar methodology of experimental parameters sweep, the build-up of correlations was shown in three array geometries [57]. More recently, the observation of a quantum spin liquid was reported on an array of 219 atoms arranged on the edges of a Kagome lattice [58, 70], as shown in figure 1 (e). It is interesting to note the steady increase over time of the number of atoms involved in those simulations, that now reach more that 200 [47, 48] (with tweezers arrays at least twice as large).

Quantum simulation with 3D structures has recently been published by the team of Jaewook Ahn at KAIST who investigated the phase diagram of the Ising hamiltonian (2) in Cayley-tree structures [59]. The Cayley graphs can be seen as a succession of shells with an exponentially increasing number of vertices. In this study, the atomic structure has adjacent shells spaced by distance d and in-shell inter-atomic distance $\geq \sqrt{3}d$ (with equality for atoms sharing a vertex). In the regime $d < R_\mathrm{b} < \sqrt{3}d$, the authors observe experimentally the expected ground state, which consist in shells alternating between ground-state atoms and Rydberg atoms (see figure 1 (d)).

However, in all the implementations mentioned above, the simulation time is limited by the Rydberg state lifetime and atomic motion [71]. The lifetime is about 100 µs for laser-accessible states, and must essentially be divided by the system size, leading to effective simulation times of a few µs. In a dual way, ground state atoms exhibit very long lifetimes yet have only short-ranged interactions, which limit the hamiltonians that can be simulated. Rydberg dressing has been proposed to circumvent these problems [72, 73, 74]. It either improves the lifetime at the expense of the strength of interactions [75], or improves the interactions strength at the expense of the lifetime [76]. This approach has been successfully used to induce long-range spin-spin correlations in an optical lattice of ultracold atoms in [76].

The dressing scheme used allowed to tune the interaction potential to yield anisotropic correlations. The tunability of the interactions was further investigated with atoms in optical tweezers in [77], with the engineering of programmable interactions for the very general *XYZ* hamiltonian.

The Rydberg-based quantum simulation platforms mentioned above have been proposed for the implementation of lattice gauge theories [78], and for finding a *maximal independent set* of a graph [79]. Experimental investigations of the latter were carried recently [80]. Recent advances in Rydberg-based quantum simulations have been reviewed in [62].

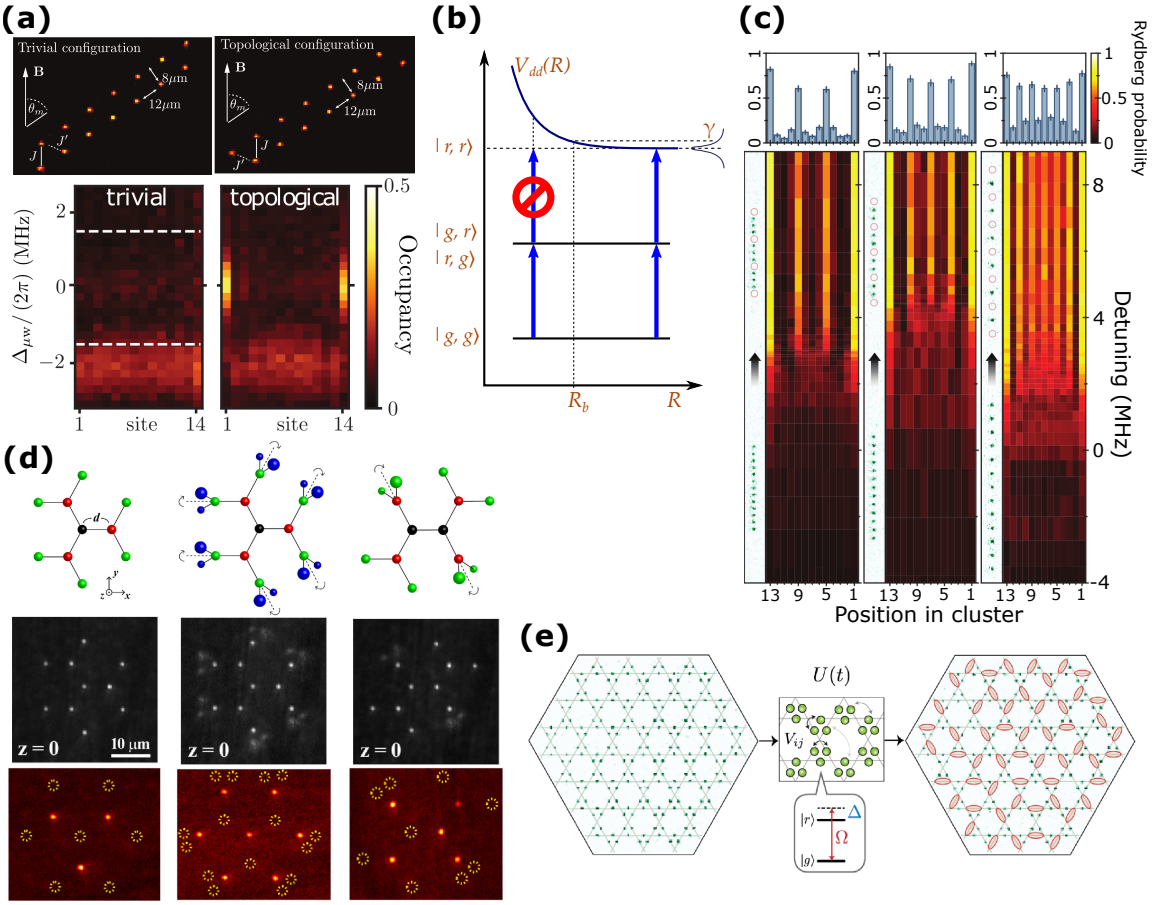

Figure 1: Quantum simulation with Rydberg atoms. (a) Simulation of the SSH model on a chain of 14 atoms. Topologically-protected edge states are characterized by a high occupancy of the edge sites, and are identified by microwave spectroscopy only in the non-trivial configuration. Adapted from [56]. (b) Illustration of the dipole blockade. Realizing multiple Rydberg excitations is forbidden within a volume set by the blockade radius R_b. The width γ of the transition is usually set by the Rabi frequency Ω. Figure taken from [81]. (c) Apparition of Z_n-ordered phases (from left to right: $n = 4, 3, 2$) through adiabatic preparation. Adapted from [55]. (d) Quantum simulation with 3D structures. Top: schemes of the Cayley trees studied in [59]. Center: fluorescence imaging of the structures; the blurred signal corresponds to atoms out of the imaging plane. Bottoms, Averaged images of the ground state in the regime $d < R_\mathrm{b} < \sqrt{3}d$; the dashed circles represent unoccupied sites, where an atom was excited to the Rydberg state. Adapted from [59]. (e) Array of 219 atoms arranged on the edges of a Kagome lattice used for the experimental realization of a spin liquid. Figure taken from [58].

All the above implementations use low-angular-momentum Rydberg states, thus suffering from two main limitations. First, their lifetime limits the simulation duration to a few µs. Second, the often-used red-detuned dipole traps used are repulsive to Rydberg atoms and must be switched off during the actual simulation. The now free atomic ensemble either collapses or explodes due to the van der Waals interaction, further reducing the achievable simulation duration. Schemes for the trapping of Rydberg atoms have been proposed [82], using the repulsive ponderomotive force exerted by the laser light on the almost free Rydberg electron. This led to some experimental demonstrations [83, 69, 84, 85]. However, the interest of low-l states trapping is limited due to their already short lifetime and the possibility of photoionization decay [86, 87].

Maximal angular momentum Rydberg states, called *circular*, avoid some of the bottlenecks mentioned above. These states have few allowed radiative transitions, which lie in the microwave domain. Their lifetime, in the ms-range at 0 K, decreases dramatically as the temperature of the environment increases. For instance, the 29 ms lifetime of $|50\mathrm{C}\rangle$ at 0 K is down to 9 ms at 4 K (typical temperature in a cryogenic environment) and further decreases to 123 µs at 300 K. Moreover, circular states are basically insensitive to photoionization, and the effect of laser light is essentially reduced to the ponderomotive force [88].

These interesting properties led to the recent proposal of new quantum computation [89] and simulation [90] platforms based on circular Rydberg atoms. Focusing on [90], the proposed simulator realizes a 1D chain of N spin-1/2 subject to an XXZ hamiltonian

$$H/h = \frac{\Delta'}{2}(\sigma_1^z + \sigma_N^z) + \frac{\Delta}{2}\sum_{j=2}^{N-1}\sigma_j^z + \frac{\Omega}{2}\sum_{j=1}^{N}\sigma_j^x + \sum_{j=1}^{N-1}\left[J_z\sigma_j^z\sigma_{j+1}^z + J(\sigma_j^x\sigma_{j+1}^x + \sigma_j^y\sigma_{j+1}^y)\right]. \quad (3)$$

The spin particles are embodied by circular Rydberg atoms in the states $|48\mathrm{C}\rangle$ and $|50\mathrm{C}\rangle$. A principal quantum number difference $\Delta n = 2$ was chosen in order to have both van der Waals and exchange interactions of the same order, scaling as $1/d^6$ for an inter-atomic distance d. These two contributions factor into the hamiltonian through the two parameters J and J_z that represent respectively the exchange and van der Waals interaction.

The exchange parameter J sets the global energy scale of the XXZ hamiltonian and is largely independent from the external fields. For the proposed simulator configuration, with $d = 5\,\mu\mathrm{m}$, we have $J = 17\,\mathrm{kHz}$. The Ising coupling parameter J_z is controlled by the applied electric and magnetic field and can be tuned from $-2J$ to $2J$, as shown in figure 2 (b). The parameters Δ and Δ' on the one hand, and Ω on the other hand are related respectively to the detuning and the amplitude of a microwave dressing of the pair of circular states. The high degree of control over the parameters values, which can also be tuned dynamically with high bandwidth, allow for a large range of possible simulation protocols through Floquet engineering [91]. Among the possibilities offered by the simulator, let us mention the exploration of the whole phase diagram of the system, with the study of associated phase transitions, and out-of-equilibrium dynamics such as the relaxation and thermalization after a quench.

However, such a versatility comes at a cost, characterized by the much lower interaction energy scale, $\sim 10\,\mathrm{kHz}$ at the selected inter-atomic distance, as compared to MHz-range interactions for other Rydberg atom-based simulators [55, 56, 57, 58, 59]. To compensate for the reduced interaction, the implementation takes advantage of the long lifetime of circular states. Following the idea [92] and experimental demonstration [93] of Kleppner, our group proposes to further increase this lifetime by inhibiting the spontaneous emission of the circular state. This is achieved by placing the atoms between the plates of a plane-parallel capacitor with a spacing $D < \lambda/2$, where λ stands for the wavelength of the radiated microwave. In this

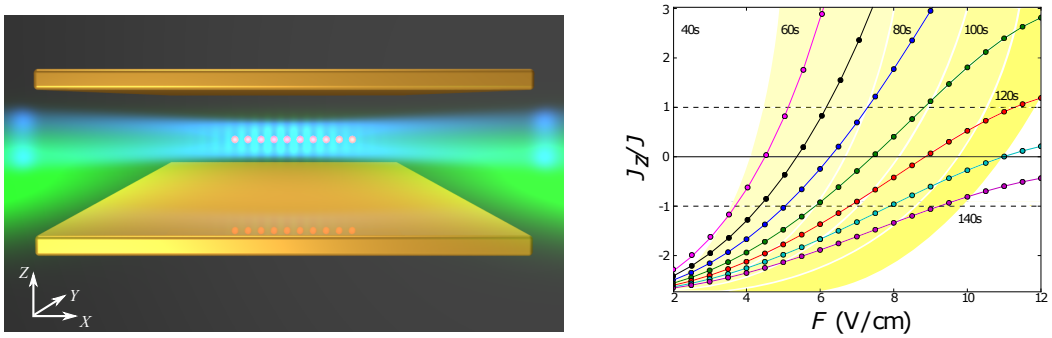

Figure 2: Left: Artist view of the quantum simulation platform proposed in [90], with the two main features highlighted. Atoms are trapped in a hollow Laguerre-Gauss mode of a laser beam superimposed with the axial interference pattern from two contrapropagating gaussian beams. The spontaneous emission is inhibited between the plates of a plane-parallel capacitor. Right: Graph of the coupling ratio J_z/J as a function of the electric field. The accessible range $-2 < J_z/J < 2$ allows to explore the whole phase diagram of the system.

configuration, a single-atom lifetime exceeding 50 s in the presence of interactions is expected for the proposed setup, with the possibility to run simulations over 1 s for a 40-atom chain, corresponding to $\sim 10^5$ interaction cycles. Increasing the strength of interactions through a decrease of d would reduce the lifetime unfavorably, but could be advantageous in regard of other loss processes such as decoherence.

At such long lifetimes, even the free fall of atoms is significant, and their three-dimensional trapping becomes a necessity. This is the second key feature of the proposition, that had no experimental demonstration at the time of publication. The trapping, together with the lifetime enhancement by spontaneous-emission inhibition, is illustrated in the artist view of the simulator presented in figure 2.

However innovative it may be, this proposal is not exempt of difficulties. In order to validate it experimentally and gather technical expertise on the various methods introduced, the components of this complex simulator were identified and set for individual studies:

- A preliminary step was the preparation of circular states out of a cloud of cold ^{87}Rb atoms in a cryogenic environment (4 K), with the recording of their evolution, that goes through a complex population transfer, and the measurement of their coherence [94]. We obtained a lifetime $T_1 = 3.7$ ms, corresponding to an effective temperature of 11 K for the prepared circular state $n = 52$. The corresponding reversible and non-reversible coherence times were measured as $T_2^* = 37\,\mu$s and $T_2 = 270\,\mu$s, respectively. In the course of this work, we identified key elements for the proper operation of the simulator. On the one hand, a tighter control of electric and magnetic fields is necessary to reach high coherence times. On the other hand, we have developed methods to reduce as much as possible the residual microwave black-body and thermalize the environment to 4 K in order to improve the states lifetime.
- The experimental demonstration of bi-dimensional trapping of circular states ensued [85]. Using a hollow Laguerre-Gauss beam, we demonstrated the transverse confinement of the circular Rydberg atoms cloud for 10 ms.
- As mentioned above, the inhibition of spontaneous emission has been demonstrated experimentally [93]. However, this was done on a thermal beam of atoms, while we aim at maintaining them in the capacitor region. In this context, a study of the evolution of

circular states inside a plane-parallel capacitor at room temperature has been carried in a separate experiment by Haiteng Wu [95]. The use of an indium tin oxide-coating, both transparent and conductive, for lifetime enhancement has been investigated. Its use in our proposed simulator architecture would allow for a wider optical access to the trapping region (see figure 2), thus facilitating the design.

I joined the team shortly after the publication describing this new quantum simulation platform. The first two years of my Ph.D were dedicated to the preparation, characterization and trapping of circular states in our cryogenic environment, as briefly summarized in the previous paragraph. This work was done together with Rodrigo Cortiñas, and Paul Méhaignerie who joined us one year later. The description of the experiment, together with the results and their analysis is presented in detail in Rodrigo's thesis [96] and our two publications [94, 85].

For the continuation, it was decided to divert from the original scheme for atom trapping and Rydberg chain preparation. Optical tweezers are increasingly common among research teams to trap ground-state atoms, and offer the ever-growing possibilities mentioned above. Their generation through spatial light modulation techniques was retained as the method of choice to prepare arbitrary arrays of atoms. Its versatility allows one to produce a variety of intensity patterns, such as hollow bottle beams that are well suited to the trapping of individual Rydberg states.

Decision was thus made to build a mock up quantum simulator operating at room temperature, using optical tweezers to trap ground state atoms, that would be catched in superimposed bottle beam traps after Rydberg excitation. Its purpose, as an intermediate stage towards the definitive setup operating at cryogenic temperatures, was the demonstration of the 3D trapping of individual circular Rydberg atoms and measurement of their interactions. It would also allow us to gather technical experience on optical tweezers and spatial light modulation techniques. In return for the increased flexibility offered by optical tweezers, the inhibition of spontaneous emission is not implemented. Its requirements would bring unnecessary complexity to the design, and its usefulness is limited at room temperature where spontaneous decay is dwarfed by black-body-induced transitions.

Two main steps remained towards practical quantum simulation: the demonstration of circular Rydberg states trapping, and the measurement of their dipole-dipole interaction. In this context, the work presented in this manuscript pertains to the first part. We thus describe the numerous stages that are involved in the preparation and trapping of circular states.

There is one notable exception to the topics covered in this manuscript. The physics of the spatial light modulation methods that are used for the preparation of optical tweezers is eluded, as I was not involved in the this part of the experiment. The complete description of the methodology and algorithms used is therefore deferred to a subsequent thesis [97].

The first chapter gives the theoretical framework on which this work is based. We briefly introduce the physics of alkali Rydberg atoms, and especially circular states which have much in common with the hydrogen atom. A general approach to the treatment of the coupling of atoms to external fields is given, with the energy shifts associated to static magnetic and electric fields. The interaction between atoms and radiation is at the core of our experimental work. It is paramount to the dipole trapping of atoms in the ground state, and the subsequent preparation and trapping of circular states. The trapping of atoms is new to our team, and its physics is discussed in some detail.

The results presented here have been obtained with an almost entirely new experimental setup. It was designed mainly by Maxime Favier, a former post-doctoral fellow, Clément

Sayrin and Michel Brune. In the second chapter, we detail the design and how it accommodates for the constraints imposed by the experiment.

The loading of circular Rydberg atoms in ponderomotive traps involves two intermediate steps. The first step, that consists in loading ground-state atoms in an array of gaussian tweezers, is described in the third chapter. We first introducing the optical detection of trapped atoms and the methodology for signal analysis. We then characterize experimentally the gaussian tweezers and introduce the measurement of lifetime and temperature.

The second step, addressed in the fourth chapter, is the Rydberg excitation and transfer to the circular state. Although the procedure is similar to that described in previous works [98, 96], some important changes justify a dedicated chapter. Most notably, the possibility of optical detection of atoms and the spatial resolution offered by the structured array bring significant information that we discuss. This contrasts with the disordered excitation from an atomic cloud in our cryostat setup, with state ionization as the sole detection method. We finally measure the electric and magnetic field in the environment and characterize the circular states thus produced by spectroscopic methods.

We finally demonstrate the ponderomotive trapping of circular states in the fifth and last chapter. The traps produced are characterized both theoretically and experimentally through the measurement of their transverse frequency. We also measure the evolution of circular states in our room temperature environment, following the methodology introduced in [96]. The possibility to trap circular states allows for their optical detection after decircularization to the ground state. We take advantage of the spatial resolution to further characterize the circular states and their environment through Rabi oscillations and Ramsey interferometry.

Chapter 1

Elements of atomic physics and introduction to Rydberg atoms

No, no! The adventures first, explanations take such a dreadful time.
— Lewis Carroll, *Alice in Wonderland*

We begin by introducing elements of the theory that underlie the physical results presented in this thesis. This work is in line with the construction of the quantum simulation platform briefly described in the introduction [90]. However, we focus here only on single-atom physics, with the topic of interactions and many-body physics delayed to a subsequent work.

In this context, we begin by recalling the main characteristics and properties of Rydberg atoms, and in particular of circular Rydberg atoms, which will embody the spin levels of the proposed simulator. These states are characterized by a valence electron occupying an orbit of high principal quantum number n. As such, they benefit from an extended lifetime as compared to the low-lying excited states. Moreover, owing to the large spatial extension of the Rydberg orbit, scaling as n^2, the mutual dipole-dipole interaction between a pair of atoms is exacerbated. This gives rise to the strong inter-atomic interaction that scales as n^{11}. This, together with their long lifetime, makes of Rydberg states a good platform for quantum simulation.

A large part of this work discusses the trapping of individual atoms in both ground and Rydberg states, which is new to our research team and has been introduced in [96]. The theory behind dipole and ponderomotive trapping, in the general context of the coupling of atoms to the electromagnetic field, is thus introduced here.

Other topics, pertaining to well established techniques or already covered in depth, are not discussed here. A first stage of magneto-optic trapping and molasses cooling is necessary for the preparation of individually trapped atoms. Those laser trapping and cooling techniques are described in great detail in [99]. Resonance spectroscopy and coherent population transfer, related to Rydberg excitation and state manipulation, are discussed in [100]. The radiative lifetimes of Rydberg states and the related black body induced transitions are treated in [101].

As announced, the physics of the interactions between Rydberg states is not detailed here. However, the occurrence of interactions is manifest in some of the experiments presented thereafter. We thus briefly introduce interactions in the simple case of circular states, with computations that serve as the basis for order-of-magnitude estimations.

Let us stress that the elements of physical theory given in this chapter are only introductory and by no mean intended to be exhaustive. However, throughout the text, we will point out the reader to references that the author considers to be the most relevant.

1.1 One valence electron: alkali Rydberg atoms

Our experiments use rubidium-87 as the atomic species. As an alkali atom, it can be assimilated to an hydrogenoid system consisting of its valence electron orbiting around the ionic core. For low-lying levels, the corrections to this approximation are important because of the interaction with the core electrons. However, for highly excited Rydberg levels, the electron charge density lies far from the ionic core which thus appears almost point-like. The hydrogen atom, for which analytical computations are possible, is thus a good starting point to alkali Rydberg physics, and allow us to introduce corrections arising from the relativistic nature of the electron motion. The deviation to the hydrogen atom model can be understood from the perspective of quantum defect theory, in which the structure of the ionic core is encompassed in quantities called *quantum defects*. This effect of the charge distribution of the core becomes vanishingly small as the angular momentum of the valence electron increases. This is the case, in particular, of circular states for which the angular momentum is maximal. In this limit, the hydrogen atom provides again an appropriate description.

1.1.1 The simple system: hydrogen atom

In 1926, Erwin Schrödinger published his famous equation [102], describing the wave dynamics for an electron in a Coulomb potential:

$$\left[-\frac{\hbar^2}{2m_e}\Delta - \frac{e^2}{4\pi\varepsilon_0}\frac{1}{r}\right]\psi(\mathbf{r}) = E\psi(\mathbf{r}), \tag{1.1}$$

where $\hbar$ stands for the reduced Planck's constant, ε_0 the vacuum permittivity, m_e the electron rest mass, and e the elementary charge. In this equation, the radial and angular motion can be separated and the solutions $\psi(\mathbf{r})$ can be decomposed in spherical coordinates as a radial and angular component:

$$\psi(r,\theta,\phi) = R_l(r)Y_l^m(\theta,\phi). \tag{1.2}$$

The functions Y_l^m are the well-known spherical harmonics defined for integers $l \geq 0$ and $m = -l, \ldots, l$. It is common practice to introduce the function $y_l(r) = rR_l(r)$, which satisfies the radial equation:

$$\left[\frac{\mathrm{d}^2}{\mathrm{d}r^2} - \frac{l(l+1)}{r^2} + \frac{2m_e e^2}{4\pi\varepsilon_0\hbar^2 r} + \frac{2m_e E}{\hbar^2}\right] y_l(r) = 0. \tag{1.3}$$

Of particular interest are those solutions corresponding to bound states. Their eigenenergies E_n, indexed by an integer $n \geq 1$, can be expressed in terms of the Rydberg unit of energy Ry:

$$E_n = -\frac{\mathrm{Ry}}{n^2}, \quad \mathrm{Ry} = \alpha^2\frac{m_e c^2}{2} = \frac{e^2}{8\pi\varepsilon_0 a_0}, \tag{1.4}$$

where we introduced the fine structure constant α and Bohr's radius a_0:

$$\alpha = \frac{e^2}{4\pi\varepsilon_0\hbar c}, \quad a_0 = \frac{4\pi\varepsilon_0\hbar^2}{m_e e^2}. \tag{1.5}$$

The radial equation (1.3) can be re-expressed, using the above values of E_n as:

$$\left[a_0^2\frac{\mathrm{d}^2}{\mathrm{d}r^2} - l(l+1)\frac{a_0^2}{r^2} + 2\frac{a_0}{r} - \frac{1}{n^2}\right] y_{nl}(r) = 0. \tag{1.6}$$

This equation can be used to derive the very useful Kramers recurrence relation between the average values of powers of r (see appendix A):

$$\frac{s+1}{n^2}\langle r^s\rangle - (2s+1)\,a_0\,\langle r^{s-1}\rangle + \frac{s}{4}\left[(2l+1)^2 - s^2\right] a_0^2\,\langle r^{s-2}\rangle = 0. \tag{1.7}$$

The eigenfunctions themselves write, in spherical coordinates:

$$\psi_{nlm}(r,\theta,\phi) = a_0^{-3/2}\frac{2}{n^2}\sqrt{\frac{(n-l-1)!}{(n+l)!}}F_{nl}\left(\frac{2r}{na_0}\right)Y_l^m(\theta,\phi), \tag{1.8}$$

with $l = 0, \ldots, n-1$. The radial part F_{nl} is

$$F_{nl}(x) = x^l \mathrm{e}^{-\frac{x}{2}} L_{n-l-1}^{2l+1}(x) \tag{1.9}$$

involving the generalized Laguerre polynomials L_p^k defined as:

$$L_p^k(z) = \sum_{i=0}^{p}(-)^i\binom{p+k}{p-i}\frac{z^i}{i!} = \sum_{i=0}^{p}(-)^i\frac{(p+k)!}{(p-i)!(k+i)!}\frac{z^i}{i!}. \tag{1.10}$$

The bound states solutions ψ_{nlm} are indexed by three quantum numbers n, l and m. The principal quantum number n characterizes the energy level of the state. The two angular momentum quantum numbers (l, m) represent the total angular momentum and its projection along the z-axis respectively. Additional energy shifts add-up to the *gross structure* energies E_n, partially lifting their n^2-degeneracy. To account for this observation, made on the atomic transition spectra available at the time, a new quantum number, the electron spin (and its projection) $(s = 1/2, m_s)$ was introduced [103]. It behaves as an intrinsic magnetic moment for the electron and couples as such with the surrounding magnetic field, giving rise to the *spin-orbit* coupling. The latter is one of the corrections to the Schrödinger hamiltonian that are necessary to accurately predict hydrogen transition frequencies. These additional energy terms give rise to the so-called *fine structure* (of which the spin-orbit coupling is a part), *hyperfine structure* and *radiative corrections*.

The fine structure terms, along with the electron spin, arise naturally from the relativistic treatment of the electron motion as given by the Dirac equation [104]:

$$\left[\gamma^\mu(i\partial_\mu - eA_\mu) - m_e\right]\Psi = 0. \tag{1.11}$$

They can be expanded in power series of α^2. To first order, three terms arise:

- The next-to-leading order correction to the relativistic kinetic energy;
- The spin-orbit coupling. It is the most important term as it involves the electron spin;
- The Darwin term.

Taking into account the structure of the nucleus and its dynamics in the treatment of the hydrogen atom also leads to some energy corrections. Of the many contributions that arise, we consider only the two most important. The finite mass M of the nucleus causes corrections of the order of m_e/M, which for rubidium, are of the order of 10^{-5}. The atomic nucleus also

has a magnetic moment $\mathbf{M}$ associated to its spin $\mathbf{I}$. The interaction of the electron with the field produced by this magnetic moment gives rise to the (dipolar) hyperfine splitting.

Finally, the quantum nature of the electromagnetic field gives rises to radiative corrections. This effect was first observed as a splitting of the $^2S_{1/2}$ and $^2P_{1/2}$ levels of hydrogen, known as the Lamb shift [105]. Radiative corrections also contribute to the electron g-factor in what is known as the anomalous magnetic moment.

We now give the expressions for the fine structure terms, the finite nuclear mass corrections, the hyperfine hamiltonian and the radiative corrections.

Relativistic correction to the kinetic energy

The relativistic kinetic energy writes

$$T = \sqrt{p^2c^2 + m_e^2c^4} - m_ec^2 = \frac{p^2}{2m_e} - \frac{p^4}{8m_e^3c^2} + \cdots . \tag{1.12}$$

The first term is the usual non-relativistic kinetic energy, already present in the Schrödinger equation (1.1). The second term gives the correction, which can be evaluated using first-order perturbation theory from the relation

$$p^4 \simeq 4m_e^2(H_0 - V(r))^2, \tag{1.13}$$

where H_0 is the Schrödinger hamiltonian of eq. (1.1). This gives

$$\langle\psi_{nlm}|\, p^4 \,|\psi_{nlm}\rangle = 4m_e^2 \left[E_n^2 - 2E_n \frac{e^2}{4\pi\varepsilon_0}\langle r^{-1}\rangle + \left(\frac{e^2}{4\pi\varepsilon_0}\right)^2 \langle r^{-2}\rangle \right]. \tag{1.14}$$

Substituting $\langle r^{-1}\rangle$ and $\langle r^{-2}\rangle$ for their explicit value (see appendix A), we finally get

$$\langle\psi_{nlm}|\, \frac{p^4}{8m_e^3c^2} \,|\psi_{nlm}\rangle = -\frac{\alpha^4 m_e c^2}{2n^3}\left[\frac{1}{l+1/2} - \frac{3}{4n}\right]. \tag{1.15}$$

Spin-orbit coupling

The spin-orbit hamiltonian writes, in the case of a central potential $V(\mathbf{r}) = V(r)$ [104]:

$$H_{\mathrm{SO}} = \frac{g_S}{4m_e^2c^2}\frac{1}{r}\frac{\mathrm{d}V}{\mathrm{d}r}\,(\mathbf{S}\cdot\mathbf{L})\,. \tag{1.16}$$

We make the electron g-factor appear explicitly to take into account the anomalous moment[1]. This expression is valid for any well-behaved central potential, in particular the effective potential resulting from the partial screening of the nucleus charge by the core electron cloud when considering many-electrons atoms. In the case of a Coulomb potential (hydrogen atom), $V(r) = \frac{e^2}{4\pi\varepsilon_0 r}$, we have

$$\frac{1}{r}\frac{\mathrm{d}V}{\mathrm{d}r} = \frac{e^2}{4\pi\varepsilon_0}\frac{1}{r^3}. \tag{1.17}$$

This gives the expression of the spin-orbit hamiltonian for the hydrogen atom:

$$H_{\mathrm{SO}} = \frac{\hbar\alpha g_S}{2m_e^2c}\frac{(\mathbf{S}\cdot\mathbf{L})}{r^3}. \tag{1.18}$$

[1] The Dirac theory gives $g_S = 2$

To evaluate the $\mathbf{S}\cdot\mathbf{L}$ term, the total angular momentum $\mathbf{J}=\mathbf{L}+\mathbf{S}$ is introduced, and we have

$$\mathbf{S}\cdot\mathbf{L}=\frac{1}{2}\left(\mathbf{J}^2-\mathbf{L}^2-\mathbf{S}^2\right). \tag{1.19}$$

To this new operator $\mathbf{J}$ we associate the quantum numbers (j,m_j), with $j=l\pm 1/2$. Substituting r^{-3} for its average (see appendix A) and using eq. (1.19) in eq. (1.18) yields:

$$\langle H_{\mathrm{SO}}\rangle=\frac{\alpha^4 m_e c^2 g_S}{4n^3}\left[\frac{j(j+1)-l(l+1)-3/4}{l(l+1/2)(l+1)}\right]. \tag{1.20}$$

Darwin term

The Darwin term writes [104]:

$$H_{\mathrm{Darwin}}=\frac{\hbar^2}{8m_e^2c^2}\Delta V=\frac{\hbar^2e^2}{8m_e^2c^2\varepsilon_0}\delta^3(\mathbf{r}). \tag{1.21}$$

This term shifts only the states with zero orbital angular momentum, as the corresponding wavefunctions do not vanish at the origin. Noting that

$$\psi_{n,\,l=0,\,m=0}(0)=\frac{2}{\sqrt{4\pi}}\left(na_0\right)^{-3/2}, \tag{1.22}$$

we get at first order, using the notation $\delta_{l,0}$ for the Kronecker delta,

$$\langle\psi_{nlm}|\,H_{\mathrm{Darwin}}\,|\psi_{nlm}\rangle=\frac{\alpha^4 m_e c^2}{2n^3}\delta_{l,0}. \tag{1.23}$$

Assuming $g_S=2$, the three fine-structure terms sum up to give a simple formula for the total energy shift:

$$\Delta E_{\mathrm{fs}}=\frac{\alpha^4 m_e c^2}{n^3}\left[\frac{3}{8n}-\frac{1}{2j+1}\right]. \tag{1.24}$$

Nuclear motion

The usual procedure to transform a two-particle problem to two one-particle problems is to separate the center-of-mass motion of the system. In doing so, we consider the dynamics of a fictitious particle in the rest frame of the system. For the non-relativistic Schrödinger equation (1.1), this amounts to replace the electron mass with the reduced mass:

$$\mu=\frac{Mm_e}{M+m_e}. \tag{1.25}$$

Such a procedure is, however, only rigorously possible in a non-relativistic context. Nevertheless, it is valid as the electron motion is almost non-relativistic, and gives the correct correction to leading order in m_e/M. The substitution $m_e\to\mu$ in all the above energy terms (Bohr energies and fine-structure terms), that corresponds to the classical separation of center-of-mass motion, is therefore the first (and main) change to account for the finite nuclear mass. Another contribution comes from the apparition of an new term [106]:

$$E_n^{\mathrm{nuc}}=-\frac{\alpha^4 m_e^2 c^2}{8Mn^4}. \tag{1.26}$$

Hyperfine structure

The hyperfine structure arises from the interaction of the electron with the inhomogeneous component of the field generated by the nucleus. We consider here only the magnetic dipole interaction with the nuclear moment $\mathbf{M}$. It consists in two terms: the nuclear spin-electron orbit coupling $H_D^{(a)}$ and the spin-spin coupling $H_D^{(b)}$:

$$H_D^{(a)} = -\frac{2}{4\pi\varepsilon_0 c^2}\frac{\mathbf{M}\cdot\boldsymbol{\mu}_L}{r^3}, \tag{1.27}$$

$$H_D^{(b)} = -\frac{2}{3\varepsilon_0 c^2}\mathbf{M}\cdot\boldsymbol{\mu}_S\,\delta^3(\mathbf{r}) - \frac{1}{4\pi\varepsilon_0 c^2}\frac{1}{r^3}\left[3\left(\mathbf{M}\cdot\frac{\mathbf{r}}{r}\right)\left(\boldsymbol{\mu}_S\cdot\frac{\mathbf{r}}{r}\right) - (\mathbf{M}\cdot\boldsymbol{\mu}_S)\right]. \tag{1.28}$$

Here we have denoted $\boldsymbol{\mu}_L$ and $\boldsymbol{\mu}_S$ for the electron orbital and spin magnetic moment, respectively. Together with $\mathbf{M}$, they can be expressed in a standard form in terms of Bohr's magneton,

$$\mu_\mathrm{B} = \frac{\hbar e}{2m_e} \simeq h \times 1.4\,\mathrm{MHz\,G^{-1}}, \tag{1.29}$$

as:

$$\boldsymbol{\mu}_L = -\frac{\mu_\mathrm{B}}{\hbar}g_L\mathbf{L}, \quad \boldsymbol{\mu}_S = -\frac{\mu_\mathrm{B}}{\hbar}g_S\mathbf{S}, \quad \mathbf{M} = \frac{\mu_\mathrm{B}}{\hbar}g_I\mathbf{I}. \tag{1.30}$$

We introduced the notation g_L, g_S and g_I for the electron orbital, spin and nuclear[2] g-factors respectively [107]. Substituting and taking the average as for the fine-structure, we obtain:

$$\langle H_D^{(a)}\rangle = \frac{\alpha^4 m_e c^2}{2n^3}\frac{g_I g_L}{l(l+1/2)(l+1)}\langle\mathbf{I}\cdot\mathbf{L}\rangle, \tag{1.31}$$

$$\langle H_D^{(b)}\rangle = \delta_{l,0}\frac{8\alpha^4 m_e c^2}{3n^3}\frac{g_I g_S}{\hbar^2}\langle\mathbf{I}\cdot\mathbf{S}\rangle + \frac{\alpha^4 m_e c^2}{4n^3}\frac{g_I g_S}{l(l+1/2)(l+1)}\left\langle 3\left(\mathbf{I}\cdot\frac{\mathbf{r}}{r}\right)\left(\mathbf{S}\cdot\frac{\mathbf{r}}{r}\right) - (\mathbf{I}\cdot\mathbf{S})\right\rangle. \tag{1.32}$$

Further treatment is required to compute the remaining averages, but the above expressions are enough to estimate the order of magnitude of the hyperfine splitting of levels.

Radiative corrections and Lamb shift

Radiative corrections arise from the interaction of the electron with the quantum electromagnetic field. In the language of quantum electrodynamics, these interaction terms add loop diagrams to the electron propagator in the presence of the external field. This brings some finite energy corrections that are state-dependent. For the sake of completeness, we report here the expressions of the Lamb shift to leading order [108]. Two cases must be distinguished, depending on the orbital angular momentum l of the state:

$$\delta E(n, j=1/2, l=0) = -\frac{4\alpha^5 m_e c^2}{3\pi n^3}\left[\ln\left(\frac{m_e c^2}{2\Delta E(n, l=0)}\right) + \frac{19}{30}\right], \tag{1.33}$$

$$\delta E(n,j,l) = -\frac{4\alpha^5 m_e c^2}{3\pi n^3}\ln\left(\frac{2\Delta E(n,j,l)}{\alpha^2 m_e c^2}\right) + \frac{\alpha}{2\pi}\frac{\alpha^4 m_e c^2}{2n^3}\left[\frac{j(j+1) - l(l+1) - 3/4}{l(l+1/2)(l+1)}\right]. \tag{1.34}$$

The second term of the energy shift in the case $l \neq 0$ represents a correction $\frac{\alpha}{2\pi}$ to the electron spin g-factor (compare with eq. 1.18). The quantities $\Delta E(n,j,l)$ must be computed

[2] We define it with respect to μ_B rather than the nuclear magneton $\mu_\mathrm{N} = \frac{\hbar e}{2m_\mathrm{p}}$ to keep the common factor and avoid introducing the proton mass m_p.

numerically and are of the same order as the Rydberg excitation energy Ry. They are roughly constant as n increase, but decrease rather fast with l. From [109], the logarithmic term $\ln\left(\frac{2\Delta E(n,j,l)}{\alpha^2 m_e c^2}\right)$ has a dependency that scales roughly as l^{-2}, which is validated for $l \leq 7$ from the numerical computations carried in [110]. Its value is of the order of unity for $n = 0$, $l = 0$ in the case of hydrogen.

Wrap-up

We have given the corrective terms to the simple Bohr energies of eq. (1.4) for the hydrogen atom. This concludes the description of this simple system to which, as we will see, the circular states are related. We anticipate that these terms, scaling as n^{-3}, will be small for Rydberg states.

The resolution of the Schrödinger and Dirac equations along with the derivation of the fine and hyperfine structure terms of the non-relativistic atomic hamiltonian can be found in [104, 111]. For a more synthetic approach to the resolution of the Dirac equation, with application of quantum electrodymanics to the radiative correction to the energy, see [108].

1.1.2 Rydberg states

We now turn to the more specific description of alkali Rydberg states, for which the principal quantum number n is large (in our experiment, we work with $n \sim 50$). The main complication to the hydrogen atom model is the presence of core electrons that causes additional energy shifts to the levels. In this introduction to the Rydberg states, we return to the situation of a non-relativistic electron in the (spherically symmetric) potential $U(r)$ generated by the nucleus and its procession of core electrons:

$$\left[-\frac{\hbar^2}{2m_e}\Delta + U(r)\right]\psi(\mathbf{r}) = E\psi(\mathbf{r}). \tag{1.35}$$

When the electron is far from the core, that is, as $r \to \infty$, it is exposed to the Coulomb potential resulting from the residual unit charge of the ion. On the other hand, when approaching the nucleus, $r \to 0$, the potential becomes that of the nucleus itself, with its Z charges. In other words, the potential U is subject to the boundary conditions

$$U(r) \underset{r\to 0}{\sim} -\frac{Ze^2}{4\pi\varepsilon_0}\frac{1}{r}, \quad U(r) \underset{r\to\infty}{\sim} -\frac{e^2}{4\pi\varepsilon_0}\frac{1}{r}. \tag{1.36}$$

To get an insight on the influence of the core electrons on the Rydberg levels, we consider the radial extension of the wavefunction in the case of a Coulomb potential. We recall from appendix A that:

$$\langle r\rangle = \frac{a_0}{2}\left[3n^2 - l(l+1)\right], \tag{1.37}$$

$$\langle r^2\rangle = \frac{a_0^2}{2}n^2\left[5n^2 + 1 - 3l(l+1)\right]. \tag{1.38}$$

The expression of $\langle r\rangle$ reveals that the electron orbit is located at a distance $r \sim n^2 a_0$ from the nucleus. This n^2 scaling makes the size of highly excited states huge as compared to the ground state, for instance for $n = 50$, the orbit extends over 200 nm. We can also determine the standard deviation of r:

$$\Delta r = \sqrt{\langle r^2\rangle - \langle r\rangle^2} = \frac{a_0}{2}\sqrt{n^2(n^2+2) - l^2(l+1)^2}. \tag{1.39}$$

This expression can be analyzed in two limit cases. First consider a zero angular momentum state, $l = 0$, for which we have

$$\Delta r \sim n^2 \frac{a_0}{2}, \quad \frac{\Delta r}{\langle r \rangle} \sim \frac{1}{3}.$$

This result is interpreted as the fact that the orbit of the electron always gets close to the nucleus, independently of the energy (characterized by n). Now consider the opposite situation of a maximal angular momentum state $l = n - 1$, which gives

$$\Delta r \sim \sqrt{2} n^{3/2} \frac{a_0}{2}, \quad \frac{\Delta r}{\langle r \rangle} \sim \frac{1}{3}\sqrt{\frac{2}{n}}.$$

Here we see that the relative extension of the orbit vanishes as $n \to \infty$, limit at which the electron is located on a shell of radius $\sim n^2 a_0$. One recovers here the classical limit of circular orbits, in which the electron sees only the potential $U(r)$ in its Coulomb limit.

Low-angular-momentum Rydberg states

The treatment of low-angular-momentum (low-l) Rydberg states is the most difficult since, as we have seen, the Rydberg electron is sensitive to the electronic structure of the ionic core. Starting from eq. (1.35), it is common practice to split the radial and angular components, noting that the latter is not altered by the modified potential $U(r)$. Thus, the effect of the core electrons in encompassed in the radial part of the Rydberg wavefunction. More specifically, the energy deviation with respect to the hydrogen limit comes from the small fraction of the wavefunction that comes in contact with the ionic core. In this region, the potential increases and so does the kinetic energy, which leads to the accumulation of a phase. Quantum Defect Theory [112] (QDT) links this phase to the energy shift to the Rydberg state caused by the core electron cloud.

Set $\rho = r/a_0$ and introduce $y_{nl}(\rho) = \rho R_{nl}(r)$. Within the frame of QDT, the radial equation for the Rydberg wavefunction can be written [113, 101]

$$\left[\frac{\mathrm{d}^2}{\mathrm{d}\rho^2} - \frac{l(l+1)}{\rho^2} + \frac{2}{\rho} - \frac{1}{n^{*2}}\right] y_{nl}(\rho) = 0. \tag{1.40}$$

In this equation, the principal quantum number n is replaced by the non-integer effective value[3] n^* that encompasses the deviation of the potential from the Coulomb potential near the origin. The difference $\delta_{nlj} = (n - n^*)$ is called the quantum defect. It is usually expanded as a power series

$$\delta_{nlj} = \delta_{lj}^{(0)} + \frac{\delta_{lj}^{(2)}}{\left(n - \delta_{lj}^{(0)}\right)^2} + \cdots, \tag{1.41}$$

with the parameters $\delta_{lj}^{(p)}$ independent of n.

The quantum defects are related to the energy shift of Rydberg levels with respect to the hydrogen model:

$$E_{nlj}^* = -\frac{\mathrm{Ry}}{n^{*2}} = -\frac{\mathrm{Ry}}{(n - \delta_{nlj})^2}. \tag{1.42}$$

[3] Another approach (see [114, 115] for instance) consists in also replacing the angular momentum quantum number l by an effective value l^*. This is particularly relevant if we assume that the deviation to the Coulomb potential is $\propto 1/r^2$.

They are determined experimentally by spectroscopic measurements [116]. Their knowledge allows for the resolution of the radial equation (1.40) and determination of corresponding matrix elements. The quantum defects parameters $(\delta_{lj}^{(0)}, \delta_{lj}^{(2)})$ have been measured up to $l = 4$ for ^{85}Rb [117, 118]. They differ little from the corresponding ^{87}Rb values that have been measured [119, 120]. As the angular momentum l increases, the electron interacts less and less with the ionic core. The scaling of the quantum defect goes as l^{-5} for $l \geq 4$ [101].

More precisely, for $l \geq 5$, the energy shift can be written as

$$\delta E_{n,l} \simeq -2\delta_{l\geq 5}^{(0)} \frac{\mathrm{Ry}}{n^3}, \tag{1.43}$$

where we can estimate

$$\delta_{l\geq 5}^{(0)} \simeq \delta_{l=4}^{(0)} \left(\frac{4}{l}\right)^5. \tag{1.44}$$

Circular Rydberg states: hydrogen-like states

We have a special interest in Rydberg states of maximal angular momentum $l = n - 1$ and $|m| = l$, called *circular Rydberg states*. As indicated above, the wavefunction of these states never penetrates the core electron cloud, hence the associated quantum defect vanishes. The hydrogen atom model is fully valid here, and the corresponding wavefunction takes a particularly simple form:

$$\psi_{nC}(r,\theta,\phi) = \frac{1}{\sqrt{\pi a_0^3}} \frac{1}{nn!} \left(-\frac{r}{na_0} e^{i\phi} \sin\theta\right)^{n-1} \exp\left(-\frac{r}{na_0}\right). \tag{1.45}$$

We now introduce another classification of hydrogen states that preserves the axial symmetry at the expense of the spherical symmetry. This is particularly useful when the latter is broken, for instance by the introduction of a directing electric field. As a consequence, the operator $\mathbf{L}^2$ does not commute anymore with the hamiltonian. The total angular momentum l is no longer a good quantum number and the remaining labeling of states with n, m becomes incomplete. To circumvent this, the Schrödinger equation can be solved in parabolic coordinates, which distinguish naturally a particular direction in space [111]. It is also possible to introduce, in spherical coordinates, the Runge-Lenz vector [121]:

$$\mathbf{A}_n = \frac{n}{m_e c\alpha} \left[\frac{1}{2}(\mathbf{p}\times\mathbf{L} - \mathbf{L}\times\mathbf{p}) - \frac{e^2 m_e}{4\pi\varepsilon_0} \frac{\mathbf{r}}{r}\right]. \tag{1.46}$$

This operator commutes with the hamiltonian (provided that the potential is coulombic), albeit not with $\mathbf{L}$. We therefore introduce the two operators:

$$\mathbf{J}_1^{(n)} = \frac{1}{2}(\mathbf{L} + \mathbf{A}_n), \tag{1.47}$$

$$\mathbf{J}_2^{(n)} = \frac{1}{2}(\mathbf{L} - \mathbf{A}_n). \tag{1.48}$$

These operators commute with the hamiltonian, and with each other. Moreover, they both satisfy ($\alpha = 1, 2$):

$$(\mathbf{J}_\alpha^{(n)})^2 = \hbar^2 \frac{n^2 - 1}{4}, \tag{1.49}$$

$$[(J_\alpha^{(n)})_i, (J_\alpha^{(n)})_j] = \epsilon_{ijk}\, i\hbar (J_i^{(n)})_k, \tag{1.50}$$

where ϵ_{ijk} is the completely antisymmetric tensor. The operators $\mathbf{J}_\alpha^{(n)}$ represent two angular momenta $j_\alpha = (n-1)/2$, $m_\alpha = -j_\alpha, -j_\alpha + 1, \ldots, j_\alpha - 1, j_\alpha$. The n^2 states corresponding to a given principal quantum number n can now be labeled[4] as $|n, m_1, m_2\rangle$. For a more intuitive classification of the states, we note that $m = m_1 + m_2$ and define a new quantum number $k = m_1 - m_2$. The levels in the Rydberg manifold for a given n, without fine and hyperfine structure, are presented in figure 1.1. The arrows indicate levels with constant m_1 or m_2. Circular states are indicated which correspond to $m_1 = m_2 = \pm j = \pm\frac{n-1}{2}$ or equivalently, to $m = n - 1$. Nearby levels, with large but not maximal m, are called *elliptical* states. They are also well described by the hydrogen model and are of interest since they are accessible by microwave spectroscopy from circular states.

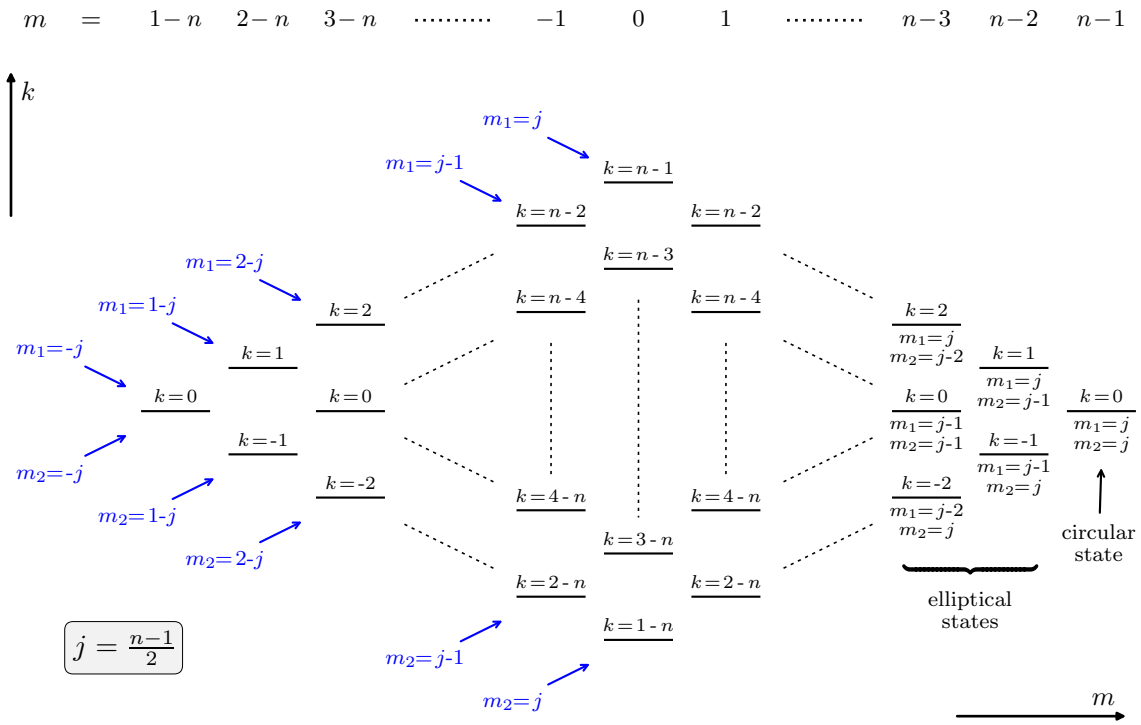

Figure 1.1: Level structure for hydrogen in the Rydberg manifold, without fine and hyperfine structure.

As we will see, the states labeled as $|n, m, k\rangle$ are well suited to express the energy shift in the presence of an external field. Let us note, however, that the Runge-Lenz vector does not commute anymore with the hamiltonian when the potential is not Coulombic. The above classification is therefore rigorously valid only for the hydrogen atom or, in the case of rubidium, for levels with sufficiently high angular momentum (so that the potential becomes effectively Coulombic). We nevertheless retain the given indexation with quantum numbers $|n, m, k\rangle$, keeping in mind that k is not related anymore to an observable for low-l states.

1.1.3 Estimation of the corrective energy terms for circular states

We turn to the estimation of the shifts caused by the corrective terms to the Bohr energy described in section 1.1.1 for circular states. To fix the ideas, we compute the values for the $n = 50$ circular state and consider the differential shift $\Delta E = E_{n=51} - E_{n=50}$.

[4] We recover $n^2 = (2j_1 + 1)(2j_2 + 1)$

- Fine structure (1.24). The fine structure shift is 7.3 kHz, with a corresponding differential shift of 560 Hz.
- Spin-orbit level splitting (1.20). The energy splitting between levels $|nC, m_s = +1/2\rangle$ and $|nC, m_s = -1/2\rangle$ is 573 Hz for $n = 50$ and 519 Hz for $n = 51$, hence a splitting of 54 Hz for the transitions corresponding to the two spin states. The spin-orbit coupling can be significant for low-l states, with splittings usually in the range [101] 1 - 10 MHz. This explained by the increase of the potential from its asymptotic form $\sim 1/r$ to its $\sim Z/r$ behavior at the origin that results in an important gradient.
- Nuclear motion term (1.26). This term is completely negligible, with a shift of 0.05 Hz.
- Hyperfine structure (1.31-1.32). To estimate this quantity, we use the quoted value [107] $g_I \simeq -0.001$. We also have $g_L = 1$ and assume $g_S = 2$ for simplicity. The hyperfine splitting constant is thus -0.01 Hz, again completely negligible for circular states.
- Radiative corrections (1.33). Excluding the anomalous magnetic moment of the electron, the radiative correction prefactor is 8.7 kHz, with a differential value of -500 Hz. However, the "excitation energy" $\Delta E(n, j, l)$ further reduces the effect. With the l^{-2} dependence announced above, the residual effect is approximately 1 Hz, also a negligible contribution.
- Quantum defect (1.43). From [118], we have $\delta^{(0)}_{l=4} = 0.004$. Using the scaling law of eq. (1.44) a shift of 763 Hz and an associated differential of 113 Hz. The effect is of the same order as the fine-structure splitting.

1.2 Coupling to external fields

The general procedure to treat the problem of an atom in an external electromagnetic field consists in introducing the corresponding four-potential $(\varphi/c, \mathbf{A})$ in the wave equation. For instance, including the contribution from the electron spin $\mathbf{S}$, the Schrödinger equation becomes [104]:

$$\left[\frac{1}{2m_e}\left(\mathbf{p} + e\mathbf{A}\right)^2 - e\varphi(\mathbf{r}) - \frac{e^2}{4\pi\varepsilon_0 r} + \frac{\mu_\mathrm{B}}{\hbar} g_S(\mathbf{S}\cdot\mathbf{B})\right]\psi = E\psi, \tag{1.51}$$

where $\mathbf{B} = \nabla \times \mathbf{A}$ is the magnetic field.

1.2.1 Static magnetic field: Zeeman and Paschen-Bach effects

To a constant magnetic field $\mathbf{B}$ we can associate the vector potential $\mathbf{A}(\mathbf{r}) = \frac{1}{2}\mathbf{B}\times\mathbf{r}$, which gives

$$\left(\mathbf{p} + e\mathbf{A}\right)^2 = \mathbf{p}^2 + e\mathbf{B}\cdot(\mathbf{r}\times\mathbf{p}) + \frac{e^2}{4}(\mathbf{B}\times\mathbf{r})^2. \tag{1.52}$$

We drop the quadratic diamagnetic term[5] $\propto \mathbf{B}^2$ and note that $\mathbf{r}\times\mathbf{p} = \mathbf{L}$ to obtain:

$$\left(\mathbf{p} + e\mathbf{A}\right)^2 = \mathbf{p}^2 + e\mathbf{L}\cdot\mathbf{B}. \tag{1.53}$$

[5] To justify this approximation, compare the linear and quadratic terms. The condition is $\frac{e^2}{m_e}B^2r^2 \ll \mu_\mathrm{B}B$. We have $r^2 \sim a_0^2 n^4$, and using the expression of μ_B, the condition becomes $B \ll \frac{\hbar}{a_0^2 e n^4} = 2.35\cdot 10^9$ G. For a field of 10 G, the equality is attained for $n = 123$, well above our typical values $n \simeq 50$.

The effect of the magnetic field is to couple to the angular momentum of the atom. Omitting the contribution from the nuclear spin, the hamiltonian describing the interaction with the magnetic field is thus

$$H_B = \frac{\mu_\mathrm{B}}{\hbar} \left(g_L \mathbf{L} + g_S \mathbf{S}\right) \cdot \mathbf{B}. \tag{1.54}$$

The orbital g-factor in this hamiltonian must take into account a correction from the finite nuclear mass M, and writes, at first order [111]:

$$g_L = 1 - \frac{m_e}{M}. \tag{1.55}$$

The effect of the presence of a magnetic field on the atom depends on the strength of the spin-orbit coupling that we write

$$H_\mathrm{SO} = \frac{\Delta E_\mathrm{SO}}{\hbar^2} \left(\mathbf{S} \cdot \mathbf{L}\right). \tag{1.56}$$

The weak field limit, $H_B \ll H_\mathrm{SO}$, corresponds to the (anomalous) *Zeeman effect*, and the strong field limit is known as the *Paschen-Bach* effect. The general case requires the explicit diagonalization of the hamiltonian in each l subspace [111].

Zeeman effect

We consider H_B as a perturbation to H_SO, which is the case for instance of low-l states with $l \leq 2$. As seen in section 1.1.1, the spin-orbit hamiltonian is diagonal in the basis $|l, j, m_j\rangle$ with

$$\langle l, j, m_j | \, H_\mathrm{SO} \, | l, j, m_j \rangle = \Delta E_\mathrm{SO} \left[j(j+1) - l(l+1) - 3/4\right]. \tag{1.57}$$

We can rewrite H_B using $\mathbf{L} = \mathbf{J} - \mathbf{S}$:

$$H_B = \frac{\mu_\mathrm{B}}{\hbar} \left(g_L \mathbf{J} + (g_L - g_S)\mathbf{S}\right) \cdot \mathbf{B}. \tag{1.58}$$

To compute the average value $\langle l, j, m_j | \, \mathbf{S} \, | l, j, m_j \rangle$, we use the identity

$$\frac{1}{2}\left[\mathbf{J}^2, \left[\mathbf{J}^2, \mathbf{S}\right]\right] = \left(\mathbf{J}^2\mathbf{S} + \mathbf{S}\mathbf{J}^2\right) - 2\mathbf{J}\left(\mathbf{J} \cdot \mathbf{S}\right). \tag{1.59}$$

Evaluating the expectation value of the above expression, the left hand side vanishes, and we get

$$\langle l, j, m_j | \, \mathbf{S} \, | l, j, m_j \rangle = \langle l, j, m_j | \, \mathbf{J} \, | l, j, m_j \rangle \, \frac{j(j+1) - l(l+1) + 3/4}{2j(j+1)}. \tag{1.60}$$

Taking the quantization axis along $\mathbf{B}$, we finally have:

$$\langle l, j, m_j | \, H_B \, | l, j, m_j \rangle = B \mu_\mathrm{B} g_J m_j, \tag{1.61}$$

with g_J the *Landé factor* given by:

$$g_J = g_L + (g_L - g_S) \frac{j(j+1) - l(l+1) + 3/4}{2j(j+1)}. \tag{1.62}$$

The treatment in the presence of the hyperfine coupling is similar.

Paschen-Bach effect

When H_B dominates, the appropriate basis is $|l, m_l, m_s\rangle$, in which we have

$$\langle l, m_l, m_s| H_B |l, m_l, m_s\rangle = B\mu_B (g_L m_l + g_S m_s). \tag{1.63}$$

The spin orbit coupling is a perturbation which diagonal elements are, in the same basis,

$$\langle l, m_l, m_s| H_{SO} |l, m_l, m_s\rangle = \Delta E_{SO}\, m_l m_s. \tag{1.64}$$

1.2.2 Static electric field: Stark shift

To a static electric field $\mathbf{F}$ we can associate the potential $\varphi(\mathbf{r}) = -\mathbf{r}\cdot\mathbf{F}$. The Stark hamiltonian is thus:

$$H_S = -e\varphi(\mathbf{r}) = -\mathbf{d}\cdot\mathbf{F}, \tag{1.65}$$

where $\mathbf{d} = -e\mathbf{r}$ is the dipole operator. Contrary to the magnetic field which couples linearly only to the angular motion of the electron, the electric field also couples with the radial motion. This causes the mixing of states within larger subspaces, and therefore a more complex evaluation of the resulting energy shift. An important remark comes from the fact that the the potential $\varphi(\mathbf{r})$ has no lower bound and therefore the corresponding Schrödinger equation has no square-integrable solution. Nevertheless, the ionization rate is vanishingly small for sufficiently low fields, which allows for the perturbative treatment of H_S.

The operator $\mathbf{r}$ is a vector operator – a rank-1 irreducible tensor – and Wigner-Eckart theorem [104] can be used to decompose the corresponding matrix elements. For this, the operator $\mathbf{r}$ is decomposed in standard components $\mathbf{r}_q$ with $q = 0, \pm 1$. These write

$$\mathbf{r}_{+1} = -\frac{1}{\sqrt{2}}(x + iy), \quad \mathbf{r}_0 = z, \quad \mathbf{r}_{-1} = \frac{1}{\sqrt{2}}(x - iy), \tag{1.66}$$

or, using the definition of spherical harmonics,

$$\mathbf{r}_q = r\sqrt{\frac{4\pi}{3}} Y_1^q. \tag{1.67}$$

Some algebra is required in order to express the matrix elements $\langle \tau, j, m|\, \mathbf{r}_q\, |\tau', j', m'\rangle$, where τ, τ' identify with the remaining quantum numbers defining the basis. In the simple case of a spinless system, $\tau = n$ and $j = l$, relevant when the spin-orbit coupling is negligible, the matrix elements take the form

$$\langle n, l, m\, |\mathbf{r}_q|\, n', l', m'\rangle = (-)^m \langle n, l \| r \| n', l'\rangle \sqrt{(2l+1)(2l'+1)} \begin{pmatrix} l & 1 & l' \\ 0 & 0 & 0 \end{pmatrix} \begin{pmatrix} l & 1 & l' \\ m & -q & -m' \end{pmatrix}. \tag{1.68}$$

In this expression the Wigner 3-j symbols were used. Their symmetries yield the following selection rules:

$$l = l' \pm 1, \tag{1.69}$$

$$m = m' + q. \tag{1.70}$$

A notable property of the Stark shift arises from the symmetries of H_S. To fix the ideas, we assume the field $\mathbf{F}$ to be along the z-direction, the Stark hamiltonian then writes $H_S = ezF$ with $F = ||\mathbf{F}||$. It is invariant by rotation $\mathcal{R}_z(\phi)$ around the z-axis, and also by reflection $\mathcal{S}$ through any plane containing the z-axis. The operators associated to these

transformations are respectively J_z, the z-component of the total angular momentum[6], and S. The invariance of H_S translates into the commutation relations

$$[H_S, J_z] = 0, \quad [H_S, S] = 0. \tag{1.71}$$

From the first relation, we see that the projection m of the angular momentum is a good quantum number. We can therefore consider eigenvectors $|m\rangle$ of both H_S and J_z:

$$H_S |m\rangle = E_m |m\rangle , \quad J_z |m\rangle = m |m\rangle . \tag{1.72}$$

The relation $\mathcal{S}\mathcal{R}_z(\phi)\mathcal{S} = \mathcal{R}_z(-\phi)$ translates into the anti-commutation relation

$$S\, J_z\, S = -J_z. \tag{1.73}$$

Since $[H_S, J_z] = 0$, the projection m of the angular momentum is a good quantum number. We also have

$$J_z(S |m\rangle) = -SJ_z |m\rangle = -m(S |m\rangle), \tag{1.74}$$

hence $S |m\rangle = |-m\rangle$. Since S commutes with H_S, we have

$$H_S |-m\rangle = H_S S |m\rangle = SH_S |m\rangle = SE_m |m\rangle = E_m |-m\rangle .$$

As a consequence, the Stark hamiltonian keeps the states $|m\rangle$ and $|-m\rangle$ degenerate. The shift is only dependent on the absolute value $|m|$ of the angular momentum.

Stark shift for the hydrogen atom

The evaluation of the dipole matrix elements of eq. (1.68) is not trivial, and turns out to be simpler in the parabolic basis introduced in section 1.1.2. Using perturbation theory, the Stark shift is expanded as a power series of the electric field F

$$\Delta E_{\text{Stark}} = \alpha^{(1)}F + \alpha^{(2)}F^2 + \alpha^{(3)}F^3 + \cdots . \tag{1.75}$$

The Stark hamiltonian in the parabolic basis is already diagonal at first perturbation order and the α coefficients write simply as a function of the $\{n, m, k\}$ quantum numbers [111]:

$$\alpha^{(1)} = \frac{3kn}{2} e a_0, \tag{1.76}$$

$$\alpha^{(2)} = -\frac{n^4}{32}(17n^2 - 9m^2 - 3k^2 + 19)\frac{(ea_0)^2}{\text{Ry}}, \tag{1.77}$$

$$\alpha^{(3)} = \frac{3kn^7}{128}(23n^2 + 11m^2 - k^2 + 39)\frac{(ea_0)^3}{\text{Ry}^2}, \tag{1.78}$$

where Ry is the Rydberg energy defined in eq. (1.4). As expected from the symmetry argument of the above section, the coefficients $\alpha^{(i)}$ are dependent only on the absolute value $|m|$ of the angular momentum m. These formulas are valid for alkali Rydberg atoms in the domain where the quantum defect becomes negligible, which corresponds to $m \gtrsim 7$.

Although this approach gives satisfactorily results, the rapid increase of available computational power over time makes it less and less relevant for quantitative estimation of the Stark shift or other perturbations. This is especially true as the precision of experimental measurements tends to increase, which can only be accounted for by including more contributions to the hamiltonian. Recently published Rydberg atoms computation packages [122, 60] are well-suited for this. They proceed essentially by brute-force diagonalization of the hamiltonian in a finite-size Hilbert space. They thus get the perturbations to all orders, only limited by the cutoff imposed on the Hilbert space dimension.

[6] This is actually the *generator* of the group of operators associated to the rotations $\mathcal{R}_z$.

1.2.3 Dipole-dipole interaction

The response of a given Rydberg state to the electric field produced by the dipole moment of another atom in the Rydberg state gives rise to the dipole-dipole interaction. The corresponding hamiltonian is very similar to the spin-spin coupling of the hyperfine hamiltonian (1.32). For a pair of atoms with dipole moment $\mathbf{d}_i$, $i = 1, 2$ and inter-atomic vector $\mathbf{R}_{12} = R_{12}\mathbf{n}_{12}$, the dipole-dipole coupling reads[7] [123]

$$V_{dd} = \frac{1}{4\pi\varepsilon_0 R_{12}^3}\left[\mathbf{d}_1\cdot\mathbf{d}_2 - 3(\mathbf{d}_1\cdot\mathbf{n}_{12})(\mathbf{d}_2\cdot\mathbf{n}_{12})\right]. \tag{1.79}$$

This operator is an irreducible tensor operator of rank 2, and as such can be decomposed as a sum of five standard components:

$$V_{dd} = \frac{1}{4\pi\varepsilon_0 R_{12}^3}\times\sum_{i=1}^{5} A_i(\theta,\varphi) f_i(\mathbf{d}_1,\mathbf{d}_2), \tag{1.80}$$

where the angles θ, φ parametrize the unit vector $\mathbf{n}_{12}$ in spherical coordinates and $f_i(\mathbf{d}_1, \mathbf{d}_2)$ represents the i-th standard component of the operator. The matrix elements associated to this operator are quite complex, especially in the presence of spin-orbit coupling. Their full expression can be found in [123]. The expressions nevertheless simplify in the absence of spin-orbit coupling, such as for circular states.

Let us now consider the dipole operator as a perturbation. For pairs of single-atom eigenstates $|a_1, a_2\rangle$ and $|b_1, b_2\rangle$, the matrix elements

$$\langle a_1; a_2|V_{dd}|b_1; b_2\rangle = \frac{1}{4\pi\varepsilon_0 R_{12}^3}\times\sum_{i=1}^{5} A_i(\theta,\varphi)\,\langle a_1; a_2|f_i(\mathbf{d}_1,\mathbf{d}_2)|b_1; b_2\rangle \tag{1.81}$$

are subject to the dipole selection rules for each atom. In particular the matrix element vanish when both atoms are in the same state, that is, when $a_1 = a_2 = b_1 = b_2$. The dipole coupling can nevertheless become dominant in some cases. For instance, when the coupled states are degenerate pairs $|a; b\rangle$ and $|b; a\rangle$, the term[8] $\langle a; b\,|V_{dd}|\,b; a\rangle = A_3^{ab}/R^3$, called *exchange term*, causes an energy shift

$$\pm\Delta E_{ab}^{(1)} = \pm\frac{A_3^{ab}}{R^3}, \tag{1.82}$$

associated to the new eigenstates

$$|\phi_\pm\rangle = \frac{1}{\sqrt{2}}\left(|a; b\rangle \pm |b; a\rangle\right). \tag{1.83}$$

For a pair of atoms in the same state, we must go to second order perturbation theory to determine the energy shift:

$$\Delta E_{aa}^{(2)} = \sum_{|c;d\rangle}\frac{\langle a; a\,|V_{dd}|\,c; d\rangle\,\langle c; d\,|V_{dd}|\,a; a\rangle}{E_a + E_b - E_c - E_d} = \frac{C_6^{aa}}{R_{12}^6}, \tag{1.84}$$

where E_α is the energy of the single-atom state $|\alpha\rangle$. Exchange is also possible at second order, and leads to a coupling

$$\Delta E_{ab}^{(2)} = \sum_{|c;d\rangle}\frac{\langle a; b\,|V_{dd}|\,c; d\rangle\,\langle c; d\,|V_{dd}|\,b; a\rangle}{2E_a - E_c - E_d} = \frac{A_6^{ab}}{R^6}. \tag{1.85}$$

[7] We do not take retardation effects into account.

[8] We switch to the simpler notation R for the interatomic distance R_{12}

Focusing on circular Rydberg states $|n\mathrm{C}\rangle$, denoted $|n\rangle$ for simplicity, the most important couplings to consider are:

- $A_3^{n,n+1}$, the first-order coupling that gives rises to the flip-flop between circular states with $\Delta n = 1$;
- $C_6^{n,n}$, the second-order shift for a pair of atoms in the same state;
- $C_6^{n,n+2}$, the second-order shift for a pair of atoms in circular states with $\Delta n = 2$;
- $A_6^{n,n+2}$, the second-order exchange for a pair of atoms in circular states with $\Delta n = 2$;

The last three terms are at the heart of the proposal for the new quantum simulation platform published by our group [90]. We show in figure 1.2 some the above quantities in the conditions relevant to our experiments. The electric field $F = 2\,\mathrm{V\,cm^{-1}}$ and magnetic field $B = 7\,\mathrm{G}$ correspond to our experimental conditions. We evaluate the energies as a function of the angle θ between the interatomic axis and the quantization axis, with an interatomic distance $R = 15\,\mu\mathrm{m}$ (see figure 1.2 (a)).

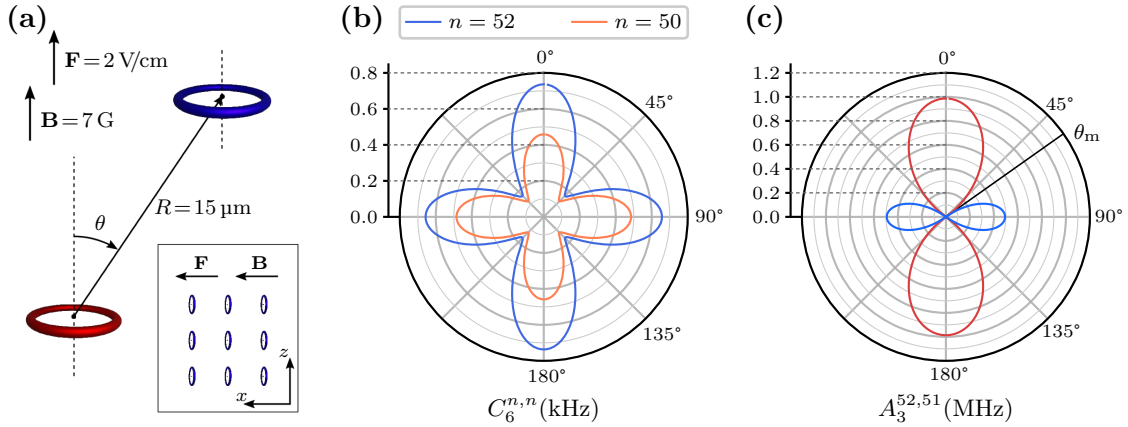

Figure 1.2: Interaction between circular states. (a) Field and geometric configuration for the computation. The inset shows the orientation of the circular states in our experiment. (b) Energy shift $C_6^{n,n}$ for $n = 52$ and $n = 50$. (c) Exchange term $A_3^{n,n+1}$ between 52C and 51C. Note the scale difference: the first-order coupling is three orders of magnitude larger. The computations were carried by exact diagonalization of the hamiltonian in a basis of 8281 pair states.

The energy shift for a pair of atoms in the same circular state is presented in figure 1.2 (b). It lies in the kHz range, and is thus relatively weak. The shift "per atom" on the transition $52\mathrm{C} \leftrightarrow 50\mathrm{C}$ is

$$\Delta\nu_{52,50} = \frac{C_6^{52,52} - C_6^{50,50}}{2}. \tag{1.86}$$

From the graph, we estimate $\Delta\nu_{52,50} \sim 150\,\mathrm{Hz}$ at $\theta = 0°$ and $\sim 75\,\mathrm{Hz}$ at $\theta = 90°$.

The first-order interaction is three orders of magnitudes larger, and lies in the MHz range. Its angular dependence is very close to the classical formula $(1 - 3\cos^2(\theta))$. With a change in sign at the *magic angle* $\theta_\mathrm{m} \simeq 54.7°$.

1.2.4 Oscillating electromagnetic field

The case of a time-dependent external field is more complex. In the absence of currents, the potential vector is subject to Maxwell's equations in vacuum:

$$\left(\nabla^2 - \frac{1}{c^2}\frac{\partial^2}{\partial t^2}\right)\mathbf{A}(\mathbf{r},t) = 0. \tag{1.87}$$

It can be expanded as plane waves

$$\mathbf{A}(\mathbf{r},t) = \int \mathrm{d}\mathbf{k}\mathcal{A}_{\mathbf{k}}e^{i(\mathbf{k}\cdot\mathbf{r}-\omega t)}, \tag{1.88}$$

subject to the dispersion relation $||\mathbf{k}|| = c\omega$. The gauge freedom is conveniently settled by choosing the Coulomb gauge $\nabla\cdot\mathbf{A} = 0$. With this choice, eq. (1.51) can be expanded to give[9]

$$H = H_0 + H_I, \quad H_I = \frac{e}{m_e}\mathbf{A}(\mathbf{r},t)\cdot\mathbf{p} + \frac{e^2}{2m_e}\mathbf{A}^2(\mathbf{r},t) + \frac{\mu_\mathrm{B}}{\hbar}g_S(\mathbf{S}\cdot\mathbf{B}(\mathbf{r},t)), \tag{1.89}$$

with H_0 the atomic hamiltonian in the absence of coupling, and H_I represent the atom-radiation interaction. The expression of H_I is exact in the non-relativistic limit, but inconvenient to work with. The magnetic coupling is usually weak as compared to the other terms, and we drop it for the remainder as it does not intervene in the context of this work. The interaction thus becomes

$$H_I = \frac{e}{m_e}\mathbf{A}(\mathbf{r},t)\cdot\mathbf{p} + \frac{e^2}{2m_e}\mathbf{A}^2(\mathbf{r},t). \tag{1.90}$$

The potential vector in the interaction hamiltonian $\mathbf{A}$ is evaluated at the position $\mathbf{r}$ of the electron. The problem can be simplified when the spatial variation of $\mathbf{A}$ is small over the electron orbit. The *dipole approximation* consists in replacing $\mathbf{A}(\mathbf{r},t)$ with its value at the origin $\mathbf{A}(0,t)$. Taking $\mathbf{A}$ as a plane wave, its spatial variation is characterized by its wavelength $\lambda = \frac{2\pi}{k}$. For usual atomic transitions the atoms are coupled to field modes with $\lambda \gtrsim 100\,\mathrm{nm}$. Denote by R the spatial extension of the atom, the dipole approximation is valid as long as $kR \ll 1$, or equivalently

$$R \ll \frac{\lambda}{2\pi} \tag{1.91}$$

This is justified in most cases as we consider only the interaction with optical, microwave or radio-frequency radiation, with wavelengths much larger than the spatial extension of the atom. A word of caution is nevertheless in order in the case of the excitation to Rydberg states. The laser wavelengths are $\lambda \sim 1\,\mu\mathrm{m}$, to be compared with the extension of the Rydberg state, $R \sim a_0 n^2 = 130\,\mathrm{nm}$ for $n = 50$. The validity of the condition (1.91) is questionable in this case, and even more so for higher values of n.

Under the dipole approximation, the interaction H_I can be re-expressed [124, 125, 126] using the electric field $\mathbf{F} = -\partial_t\mathbf{A}$. We recover the more familiar form of the interaction between the field and an electric dipole:

$$H_I = -\mathbf{d}\cdot\mathbf{F}(0,t). \tag{1.92}$$

This form is often more convenient to work with than the corresponding "momentum interaction" (1.90). In return, unlike the latter, it is bounded to the domain of validity of the dipole approximation. Let us mention that procedures [126] exist to generalize this approach and relax the dipole approximation, giving rise to additional terms that form a multipole expansion.

[9] The potential φ can be set to zero in the absence of external sources.

A quantized field

The radiation field that intervenes in the above equations can be both "classical" or quantized. In what follows we will make use mainly of the quantized form. Working in a quantization volume L^3, the electric field is usually written as a sum of modes decomposed into plane waves of momentum $\mathbf{k}$ and polarization $\boldsymbol{\epsilon}_\sigma$ [104]:

$$\mathbf{F}(\mathbf{r}) = i \sum_{\mathbf{k},\sigma} \sqrt{\frac{\hbar\omega_{\mathbf{k}}}{2\varepsilon_0 L^3}} \left[\boldsymbol{\epsilon}_\sigma \, a_{\mathbf{k},\sigma} e^{i\mathbf{k}\cdot\mathbf{r}} - \boldsymbol{\epsilon}_\sigma^* \, a_{\mathbf{k},\sigma}^\dagger e^{-i\mathbf{k}\cdot\mathbf{r}} \right], \tag{1.93}$$

with $\omega_{\mathbf{k}} = c\|\mathbf{k}\|$ the mode pulsation, and $a_{\mathbf{k},\sigma}^\dagger$, $a_{\mathbf{k},\sigma}$ the corresponding creation and annihilation operators. The hamiltonian associated to the free field is, up to a renormalization constant,

$$H_{\mathrm{Rad}} = \sum_{\mathbf{k},\sigma} \hbar\omega_{\mathbf{k}} \, a_{\mathbf{k},\sigma}^\dagger a_{\mathbf{k},\sigma}. \tag{1.94}$$

When considering the interaction with light (usually a laser source), one often finds a specific mode $(\mathbf{k}, \boldsymbol{\epsilon})$ filled with many photons while the others are empty. A relevant approximation then consists in dropping the contribution from the empty modes. Removing the unnecessary indices, the interaction thus becomes

$$H_I = ie\sqrt{\frac{\hbar\omega}{2\varepsilon_0 L^3}} \left[a(\mathbf{r}\cdot\boldsymbol{\epsilon}) - a^\dagger(\mathbf{r}\cdot\boldsymbol{\epsilon}^*) \right]. \tag{1.95}$$

1.3 Light-matter interaction: applications

Light-matter interaction is at the core of an important part of modern experimental physics, and many of its topics underlie the techniques used in our experiment. In this section, we will focus on topics that bring novelty to the experiment: the dipole and ponderomotive forces, involved in the trapping of individual atoms. We also describe the method used for the preparation of circular states: the adiabatic transfer. This procedure is adapted to the required transfer of dozens of angular momentum quanta to the Rydberg electron.

1.3.1 Adiabatic transfer to the circular state

The difficulty of circular states preparation lies in the transfer of many quanta of angular momentum to the Rydberg electron. We follow the procedure introduced by Hulet and Kleppner in 1983 [127]. It consists in a rapid adiabatic passage through the states $|m, k = m + 1 - n\rangle$, $m = 0, ..., n-1$ in the presence of σ^+-polarized radio-frequency radiation (see figure 1.3).

The course of events can be understood in the dressed-atom formalism [128]. We consider the mode populated by the radio-frequency photons along with the ladder of atomic states indicated above, which we will denote as $|m\rangle$. We further assume that the degeneracy between the atomic states is lifted by an electric field F (that also defines the quantization axis). In the absence of coupling between the atom and the radiation, the eigenstates and eigenenergies write (we only take into account the linear Stark effect):

$$|m; N\rangle\,, \quad E_{m,N} = N\hbar\omega + \frac{3}{2}(m + 1 - n)n\, e a_0 F. \tag{1.96}$$

The atom-field coupling is that of eq. (1.95). For a σ^+ polarization, we have $\mathbf{r}\cdot\boldsymbol{\epsilon} = \mathbf{r}_{+1}$ and $\mathbf{r}\cdot\boldsymbol{\epsilon}^* = \mathbf{r}_{-1}$. The matrix elements are thus

$$\langle m;N|\,H_I\,|m';N'\rangle = ie\sqrt{\frac{\hbar\omega}{2\varepsilon_0 L^3}}\left[\langle m|\,\mathbf{r}_{+1}\,|m'\rangle\,\sqrt{N+1}\delta_{N,N'-1} - \langle m|\,\mathbf{r}_{-1}\,|m'\rangle\,\sqrt{N}\delta_{N,N'+1}\right]. \tag{1.97}$$

They have been computed in [129], and according to the selection rules (1.69), the non-vanishing terms are

$$\langle m|\,\mathbf{r}_{-1}\,|m+1\rangle = \langle m+1|\,\mathbf{r}_{+1}\,|m\rangle = 3a_0 n\sqrt{(n-m-1)(m+1)}. \tag{1.98}$$

Inspection of the matrix elements (1.97) shows that the interaction only couples the states $|m,N\rangle$ and $|m\pm1;N\mp1\rangle$. We can therefore restrict ourselves to the subspace spanned by the vectors $|\tilde{m}\rangle = |m,N_0-m\rangle$, $m=0,...,n-1$. Define $\hbar\omega_0 = \frac{3}{2}nea_0F$ the energy difference between successive atomic states, the eigenenergies write

$$E_{\tilde{m}} = E_{m,N_0-m} = m\hbar(\omega_0-\omega) = m\hbar\Delta, \tag{1.99}$$

where the constant contribution $N_0\hbar\omega + (1-n)\hbar\omega_0$ has been dropped. In the high intensity field limit, $N_0 \gg 1$, the full hamiltonian writes

$$\langle\tilde{m}|\,H\,|\tilde{m}'\rangle = m\hbar\Delta\delta_{m,m'} + i\hbar\Omega\sqrt{(n-m-1)(m+1)}\left[\delta_{m,m'+1} - \delta_{m,m'-1}\right], \tag{1.100}$$

where the pulsation Ω relates to the radio-frequency field amplitude $\mathcal{E}_{\mathrm{RF}}$

$$\Omega = 3ea_0 n\sqrt{\frac{N_0\hbar\omega}{2\varepsilon_0 L^3}} = \frac{3n}{\sqrt{2}}ea_0\mathcal{E}_{\mathrm{RF}}. \tag{1.101}$$

The hamiltonian has the simple matrix form

$$H = \hbar\begin{bmatrix} \ddots & \ddots & \ddots & & 0 \\ \ddots & (m-1)\Delta & -i\Omega\,c_{m-1} & 0 & \\ \ddots & i\Omega\,c_{m-1} & m\Delta & -i\Omega\,c_m & \ddots \\ & 0 & i\Omega\,c_m & (m+1)\Delta & \ddots \\ 0 & & \ddots & \ddots & \ddots \end{bmatrix},$$

where we introduced the shorter notation $c_m = \sqrt{(n-m-1)(m+1)}$. The dressed levels energies are equidistant with spacing $\hbar\sqrt{\Delta^2+4\Omega^2}$, and the eigenenergies are:

$$E_p = \frac{n-1}{2}\hbar\left[\Delta - \sqrt{\Delta^2+4\Omega^2}\right] + p\hbar\sqrt{\Delta^2+4\Omega^2}, \quad p=0,1,...,(n-1). \tag{1.102}$$

The eigenstates can be analyzed in the limit of large detunings $|\Delta/\Omega| \gg 1$. The effect of the coupling on the bare atomic eigenstates $|m\rangle$ can then be neglected (see figure 1.3 (a)). When $\Delta > 0$ the eigenenergies order as $E_{m=0} < E_{m=1} < ... < E_{m=n-1}$, and the lowest energy state is $|m=0\rangle$. This order reverses when $\Delta < 0$, so that the lowest energy stat is now $|m=n-1\rangle$, the circular state.

The adiabatic passage consists in scanning the detuning Δ from a positive to a negative value in the presence of the radio-frequency field. The initial state $|m=0\rangle$ thus evolves adiabatically to the circular state following the lowest energy trajectory (indicated by the

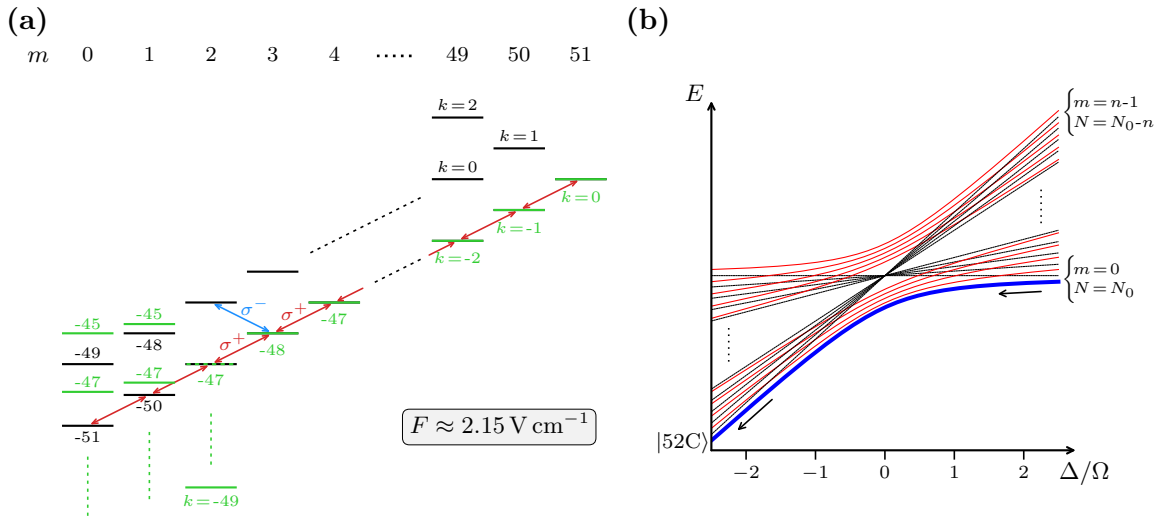

Figure 1.3: Rapid adiabatic passage to the circular state. (a) Depiction of the ladder of levels ($n = 52$) coupled through σ^+-polarized RF; spurious σ^- polarization couples to the interior of the manifold. The Rydberg levels for $m \leq 2$ are shifted due to the quantum defect. They are depicted in green to distinguish them from the pure hydrogen case. At the electric field $F \approx 2.15\,\mathrm{V\,cm^{-1}}$ and RF frequency $\nu_{\mathrm{RF}} \approx 225\,\mathrm{MHz}$ the level $|m = 2, k = -47\rangle$ becomes resonant with the rest of the ladder, allowing to initiate the transfer from this state. (b) Eigenenergies of the ladder levels without (black line) and with (red line) the RF coupling. The atomic state $|m = 0\rangle$ is branched to the circular state $|m = n - 1\rangle$ through a negative sweep of the detuning Δ.

arrow in figure 1.3 (b)). In practice, the detuning Δ is controlled by the electric field through the Stark shift. The adiabatic transfer thus involves three steps: switching on the RF, ramping down the electric field and switching off the RF. We have two adiabatic conditions associated with this process. The dressing of atoms from the gradual application of the RF coupling Ω is adiabatic if:

$$\frac{1}{\Delta^2}\left|\frac{\mathrm{d}\Omega}{\mathrm{d}t}\right| \ll 1. \tag{1.103}$$

The spurious population transfer to non-circular states will remain negligible during the anticrossing provided that [130]:

$$\frac{1}{\Omega^2}\left|\frac{\mathrm{d}\Delta}{\mathrm{d}t}\right| \ll 1. \tag{1.104}$$

A few remarks are in order concerning the practical aspects of the adiabatic transfer. We considered only σ^+-polarized RF which confined the evolution within the subspace indicated on the figure 1.3 (a). However, the σ^--polarization couples to the remaining of the Rydberg manifold as indicated by the arrow on the figure 1.3 (a). This is undesired during the adiabatic passage as it leads to the population of non-circular states. Minimization of the spurious σ^--polarized RF is thus an important step in the optimization process.

Other contributions to the hamiltonian should be taken into account for a more refined analysis or numerical simulation. The quadratic Stark shift contributes to the coupled hamiltonian, and adds up diagonal elements. Its presence does not change significantly the adiabatic transfer dynamics. The presence of a magnetic field parallel to the electric field also adds up diagonal energy terms. The detunings are of opposite sign for the σ^+ and σ^--coupled

subspace. This can be beneficial as it splits the resonance conditions for the two polarizations. The π-polarized component of the RF also gives a diagonal contribution, proportional to m, that simply shifts the resonance condition.

The previous discussion applies to the hydrogen atom, but the situation is more complex in the case of rubidium. For low-l states $m \lesssim 2$, the energy shifts due to the quantum defect put the levels far of resonance with the harmonic ladder. The energy differences between successive levels of the ladder are close enough only for $m \geq 3$, *a priori* preventing us from initiating the adiabatic passage from a level with lower m values. However, for a suitable RF frequency, the state $|m = 2, k = 3 - (n-1)\rangle$ can be made resonant with the harmonic ladder $|m > 2, k = m - (n-1)\rangle$ at a given electric field. This is illustrated in figure 1.3 (a). For the principal quantum number $n = 52$, the corresponding frequency is approximately 225 MHz, with an electric field of $2.15\,\mathrm{V\,cm^{-1}}$. The adiabatic transfer is nevertheless robust with respect to small variations of these values.

1.3.2 Light-shift and dipole trapping

Except in the case of quasi-resonant light fields, such as discussed in the previous section, the coupling of the atom to the radiation field does not results in energy shifts at first perturbation order. However, the so-called *light shift* appears at second perturbation order. The case of an empty field gives rise to the Lamb shift mentioned above. We will focus here on the case of a single field mode occupied with many photons. This corresponds to an atom illuminated by a laser beam, associated to the hamiltonian H_I of eq. (1.95).

We denote by $|\lambda; k\rangle$ the eigenstates of the bare hamiltonian (without the coupling H_I), where λ is the atomic state and k the number of photons. To determine the energy shift to the atomic state $|\alpha; N\rangle$, we compute the second order correction

$$\delta E_\alpha = \sum_{\lambda,k} \frac{|\langle \lambda; k| H_I |\alpha; N\rangle|^2}{E_\alpha - E_\lambda + (N-k)\hbar\omega}. \tag{1.105}$$

The above formula can be rewritten in the more explicit form

$$\delta E_\alpha = \frac{e^2\hbar\omega}{2\varepsilon_0 L^3} \sum_{\lambda,k} \frac{|\langle \lambda| \mathbf{r}\cdot\boldsymbol{\epsilon} |\alpha\rangle \langle k| a |N\rangle - \langle \lambda| \mathbf{r}\cdot\boldsymbol{\epsilon}^* |\alpha\rangle \langle k| a^\dagger |N\rangle|^2}{E_\alpha - E_\lambda + (N-k)\hbar\omega} \tag{1.106}$$

$$= \frac{e^2\hbar\omega}{2\varepsilon_0 L^3} \sum_{\lambda} \left[\frac{(N+1)|\langle \lambda| \mathbf{r}\cdot\boldsymbol{\epsilon} |\alpha\rangle|^2}{E_\alpha - E_\lambda + \hbar\omega} + \frac{N|\langle \lambda| \mathbf{r}\cdot\boldsymbol{\epsilon}^* |\alpha\rangle|^2}{E_\alpha - E_\lambda - \hbar\omega} \right]. \tag{1.107}$$

Let us now focus to the case where $|\alpha\rangle$ is the ground atomic state. The energy difference $E_\lambda - E_\alpha = \hbar\omega_\lambda$ is thus positive. The denominator of the second term of eq. (1.106), proportional to $|\omega_\lambda + \omega| > \omega$. Assuming that the photon energy $\hbar\omega$ is of the same order as the atomic transition energies $\hbar\omega_\lambda$, the second term can safely be neglected. Introducing the detuning $\Delta_\lambda = \omega - \omega_\lambda$, eq. (1.106) becomes

$$\delta E_\alpha = \frac{e^2 I}{2\varepsilon_0 \hbar c} \sum_{\lambda} \frac{|\langle \alpha| \mathbf{r}\cdot\boldsymbol{\epsilon} |\lambda\rangle|^2}{\Delta_\lambda}, \tag{1.108}$$

where we assumed N sufficiently large to substitute the light intensity $I = \frac{N\hbar\omega c}{L^3}$ in the classical limit. The sum of eq. 1.108 is usually dominated by a single term whose detuning determines the sign of the light shift. For a positive detuning (*blue-detuned light*), high-intensity regions are repulsive to the atom, while for a negative detuning (*red-detuned light*), the atom gets attracted to high intensity regions.

The quantitative determination of the light shift δE_α basically amounts to the computation of the dipole matrix elements $\langle\alpha|\, e\mathbf{r}\,|\lambda\rangle$. However, the situation is complex here due to the coupling between the orbital, spin and nuclear angular momenta $\mathbf{L}$, $\mathbf{S}$ and $\mathbf{I}$ respectively. Nevertheless, the dipole operator can be reduced by using the Wigner-Eckart theorem and factoring out the nuclear and electron spin dependence into Wigner 6-j symbols.

We illustrate this with the atomic species relevant to this thesis, ^{87}Rb, for which we have $S = 1/2$ and $I = 3/2$. We write:

$$|\alpha\rangle = |n{=}5, L{=}0, J{=}1/2, F, m_F\rangle \tag{1.109}$$
$$|\lambda\rangle = \left|n', L', J', F', m'_F\right\rangle \tag{1.110}$$

For a π or $\sigma^\pm$ polarization, $\mathbf{r}\cdot\boldsymbol{\epsilon}$ is the standard component $\mathbf{r}_q$, $q = 0, \pm1$. The decomposition of the dipole matrix elements gives

$$\langle\alpha|\, e\mathbf{r}\cdot\boldsymbol{\epsilon}\,|\lambda\rangle = \langle\alpha|\, e\mathbf{r}_q\,|\lambda\rangle = \left\langle n, L, J\middle\|e\mathbf{r}\middle\|n', L', J'\right\rangle c^q_{\alpha,\lambda}, \tag{1.111}$$

where $c^q_{\alpha,\lambda}$ represents the angular contribution (its expression can be found in [107]). The reduced matrix element $\langle n, L, J\,\|e\mathbf{r}\|\, n', L', J'\rangle$ is related to the radiative decay rate Γ_λ of the state $|n', L', J'\rangle$ by the relation[10] [104]:

$$\Gamma_\lambda = \frac{\omega_\lambda^3}{3\pi\varepsilon_0\hbar c^3}\frac{2J+1}{2J'+1}\left|\left\langle n, L, J\middle\|e\mathbf{r}\middle\|n', L', J'\right\rangle\right|^2. \tag{1.112}$$

Combining (1.111) and (1.112) and inserting in (1.108), we finally get

$$\delta E_\alpha = \frac{3\pi I c^2}{2}\sum_\lambda \frac{\Gamma_\lambda}{\omega_\lambda^3\Delta_\lambda}\frac{2J_\lambda+1}{2J_\alpha+1}c^q_{\alpha,\lambda}. \tag{1.113}$$

For ^{87}Rb (and reasonable wavelengths), the main contribution to the sum comes from the 5P states. We then have $\lambda = (J', F', m'_F)$ with $J = 1/2, 3/2$ (the rubidium fine structure) and corresponding F', m'_F. The decay rate Γ_λ is dependent only on J', with the relation

$$\frac{\Gamma_{1/2}}{\omega_{1/2}^3} = \frac{\Gamma_{3/2}}{\omega_{3/2}^3} = \frac{\Gamma}{\omega_0^3}, \tag{1.114}$$

where ω_0 and Γ are respectively the transition frequency and decay rate in the absence of fine structure splitting. When the detuning Δ is large compared with the hyperfine coupling, it can be factored out of the sums corresponding to different fine structure terms. We finally have

$$\delta E_\alpha = \frac{3\pi I c^2}{2}\frac{\Gamma}{\omega_0^3}\left[\frac{1}{\Delta_{\alpha,1/2}}\sum_{F',m'_F} c^q_{\alpha,(1/2,F',m'_F)} + \frac{2}{\Delta_{\alpha,3/2}}\sum_{F',m'_F} c^q_{\alpha,(3/2,F',m'_F)}\right]. \tag{1.115}$$

For a π-polarized light ($q = 0$), the sum rules [107] give

$$\sum_{F',m'_F} c^q_{\alpha,(J',F',m'_F)} = \frac{1}{3}, \tag{1.116}$$

[10] We use here the normalization condition of [107]: $\langle\lambda, J\|\|\lambda', J'\rangle = \delta_{\lambda,\lambda'}\delta_{J,J'}$.

hence the final result

$$\delta E_\alpha = \frac{\pi I c^2}{2}\frac{\Gamma}{\omega_0^3}\left[\frac{1}{\Delta_{\alpha,1/2}} + \frac{2}{\Delta_{\alpha,3/2}}\right]. \tag{1.117}$$

The situation is more complex for σ-polarized light (see [131] for instance). The contribution from other excited states is not negligible and is appropriately accounted for by numerical evaluation.

The excited state also experiences a light shift whose sign is (except by accident) opposite to that of the ground state. The computation in this case is more complex as contributions from both terms of (1.106) must be taken into account.

The light shift is associated with a first-order perturbation of the eigenvector $|\alpha\rangle$, which gets a small contribution from the coupled excited states $|\lambda\rangle$:

$$|\alpha; N\rangle \longrightarrow |\alpha; N\rangle + \sum_\lambda \frac{\langle\lambda; N-1| H_I |\alpha; N\rangle}{\hbar\Delta_\lambda} |\lambda; N-1\rangle . \tag{1.118}$$

The dressed atomic state finds itself in the excited atomic state $|\lambda\rangle$ with a probability[11]

$$p_\lambda = \frac{|\langle\lambda; N-1| H_I |\alpha; N\rangle|^2}{\hbar^2\Delta_\lambda^2}. \tag{1.119}$$

This small excited contribution scatters photons at a rate Γ_λ, hence a total scattering rate

$$\Gamma_{\rm sc} = \sum_\lambda \Gamma_\lambda p_\lambda. \tag{1.120}$$

The computation of the matrix elements is essentially the same as done for the light shift. Actually, the scattering rate can be obtained from eq. 1.113 by multiplying each term of the sum by $\Gamma_\lambda/(\hbar\Delta_\lambda)$ to give

$$\Gamma_{\rm sc} = \frac{3\pi I c^2}{2\hbar}\sum_\lambda \frac{|\langle\alpha|\,\mathbf{r}\cdot\boldsymbol{\epsilon}\,|\lambda\rangle|^2}{\Delta_\lambda^2}\Gamma_\lambda = \frac{3\pi I c^2}{2\hbar}\sum_\lambda \frac{\Gamma_\lambda^2 c_{\alpha,\lambda}^q}{\omega_\lambda^3\Delta_\lambda^2}. \tag{1.121}$$

For a given intensity pattern $I(\mathbf{r})$, the light-shift essentially represents the trapping (or repulsive) potential $V(\mathbf{r})$ exerted on the atom. We can thus write, for a state $|\alpha\rangle$,

$$V(\mathbf{r}) = \beta_\alpha I(\mathbf{r}), \tag{1.122}$$

where the coefficient β_α depends on the polarization and wavelength of the light. In our experimental configuration, the polarization is linear, parallel to the quantization axis. In this case, the shift is independent on the hyperfine level for the ground state $5S_{1/2}$. We computed the corresponding value β_0 using the *ARC-Alkali Rydberg Calculator* package [122], for which the value is

$$\beta_0 = -18.164\ \frac{\rm MHz}{\rm mW\,\mu m^{-2}}. \tag{1.123}$$

In an experiment described thereafter, we determine the peak intensity by measuring the light-shift induced on the transition $\left|5S_{1/2}, F=1\right\rangle \longrightarrow \left|5P_{3/2}, F'=2\right\rangle$. For this purpose, we also computed the coefficient for the excited state $\left|5P_{3/2}, F'=2\right\rangle$, which value, denoted β_1, is independent on the Zeeman sublevel. We have

$$\beta_1 = 5.714\ \frac{\rm MHz}{\rm mW\,\mu m^{-2}}, \tag{1.124}$$

[11] The expression given for the dressed vector is not normalized anymore, but the error is negligible.

giving rise to a light-shift

$$\beta_1 - \beta_0 = 23.877 \ \frac{\text{MHz}}{\text{mW}\,\mu\text{m}^{-2}} \tag{1.125}$$

on the probed transition.

1.3.3 Ponderomotive trapping

The ponderomotive energy is essentially the light-shift resulting from the interaction with laser light in the limit of a large principal quantum number. Contrary to the dipole potential, the derivation of the ponderomotive energy is best carried using the momentum formulation (1.90) of the interaction. Qualitatively, the reason is that in the $\mathbf{d}\cdot\mathbf{F}$ formulation, the dipole matrix elements increase with n, thus partially compensating for the large denominator (see eq. (1.108)). However, the momentum $\mathbf{p}$ of the states decreases with n, so that the $\mathbf{p}\cdot\mathbf{A}$ contribution vanishes. Only the quadratic term $\propto \mathbf{A}^2$ remains. We thus write:

$$V(\mathbf{r},t) = \frac{e^2}{2m_e}\mathbf{A}^2(\mathbf{r},t). \tag{1.126}$$

The instantaneous vector potential is most conveniently written in terms of the electric field $\mathbf{F} = -\partial_t\mathbf{A} = -\omega\mathbf{A}$, where ω is the field pulsation, to yield

$$V(\mathbf{r},t) = \frac{e^2}{2m_e\omega^2}\mathbf{F}^2(\mathbf{r},t). \tag{1.127}$$

Averaging over one period, the instantaneous value $\mathbf{F}^2(\mathbf{r},t)$ is replaced by half the squared amplitude $\frac{1}{2}F^2(\mathbf{r})$. The thus obtained time-averaged potential $V(\mathbf{r})$ can be formulated using the more convenient field intensity:

$$I(\mathbf{r}) = \frac{\varepsilon_0\, c}{2}F^2(\mathbf{r}). \tag{1.128}$$

This leads to the usual expression for the ponderomotive potential experienced by a free electron subject to laser light:

$$V(\mathbf{r}) = \frac{q^2}{2mc\,\varepsilon_0\,\omega^2}I(\mathbf{r}). \tag{1.129}$$

Although it is written as a potential, this energy term is actually a kinetic contribution originating from the fast electron oscillations in the field. The above derivation is kept simple to expose the ideas and highlight the physical origin of the ponderomotive potential. An important point to be made is that we have considered a classical field and thus neglected the coupling to the empty modes of the quantized field. A more complete treatment of the problem, including leading-order relativistic corrections, can be found in [88]. The given approach is completely valid for circular states, but only partially so for low-l Rydberg states. In the latter case, contributions arising from the possibility of photoionization and stimulated de-excitation must be taken into account. These reservations being made, the ponderomotive energy shift is also present in the case of low-l Rydberg states.

To fix the ideas and facilitate subsequent numerical estimations, we specialize to the case of our trapping laser, with a wavelength of 821 nm. This corresponds to a pulsation $\omega = 2\pi \times 365\,\text{THz}$. The ponderomotive potential can be re-expressed as $V(\mathbf{r}) = h\beta_P(\omega)I(\mathbf{r})$, with

$$\beta_P(\omega) = \frac{\alpha}{m_e\omega^2} = 1.52 \ \frac{\text{MHz}}{\text{mW}\,\mu\text{m}^{-2}}. \tag{1.130}$$

Conclusion

We introduced in this chapter some of the theoretical aspects pertaining to the results presented in this thesis. An overview of atomic physics is given through the description of the electron motion in hydrogen as a solution of the Schrödinger equation. The wavefunctions are indexed by three quantum numbers: n, the principal quantum number, l, that represents the total angular momentum and m, its projection along the z-axis. We give various corrections to the energy, of relativistic origin or associated to the structure of the nucleus. This allows us to treat the case of alkali Rydberg atoms whose unique valence electron occupy an orbit of large principal quantum number. Within the frame of quantum defect theory, the interaction of this electron with the ionic core is reduced to one parameter: the quantum defect. Its values are determined from spectroscopic measurements.

Among the Rydberg levels we described in more details the circular states, whose angular momentum is maximal: $|m| = l = n - 1$. As their name suggests, the electron orbit of such states is almost circular and located far from the core, and the quantum defect becomes negligible. For these states, the various corrective terms introduced for the hydrogen atom also turn out to be negligible.

The effect of a static magnetic field, coupled only to the angular motion (and spin) of the electron, is basically the same for low lying and Rydberg levels. The energy shifts correspond to the Zeeman effect in the weak field regime and to the Paschen-Bach effect in the strong field regime. The response to the electric field is, however, different and is at the origin of most of the interesting properties of Rydberg states. The electric field mixes different l-states, giving rise to the Stark shift. A particular case is that of an electric field generated by the dipole of a neighboring Rydberg state. The dipole-dipole interaction can give rise, depending on the pair of states, to a direct interaction scaling as $1/R^3$ for an interatomic distance R, or to a van der Waals interaction that scales as $1/R^6$. These strong interactions are one of the main assets of Rydberg states for quantum simulation.

The manipulation of theses states is usually done by radiative transitions. We introduced the coupling to the electromagnetic field that can take two forms. The general form involves the vector potential and the electron momentum. It is not convenient to work with and can be re-expressed, under the dipole approximation, in a simpler form involving the electric field and the dipole moment of the atom.

This latter form serves as the starting point for the calculations pertaining to the method that we use to prepare circular states. It consists in coupling a series of states with a nearly-resonant radio frequency field. The adiabatic transfer proceeds by scanning the detuning through the resonance. We also introduced the ideas behind the determination of the displacement of (low lying) energy levels caused by a light field in the far-detuned regime. This light-shift is proportional to the light intensity and is used in our experiment to trap ground-state atoms in intensity maxima of optical tweezers. Rydberg states react differently to the light field. The ponderomotive force is always repulsive and is used in our experiments to trap Rydberg states in hollow intensity patterns.

We will now detail how the experimental setup accommodates for the requirements imposed by both the circularization and the preparation of traps.

Chapter 2

Experimental setup

6) Never do something the person standing in front of you can't understand.

— Hunter S. Thompson, *Fear and Loathing in Las Vegas*

The main asset of circular states for the proposed quantum simulation platform lies in their extended lifetime, that allows one to probe the dynamics over long timescales. This requires to work in a cryogenic environment to mitigate the circular states' stimulated emission or absorption of black-body photons. However, working in a cryogenic environment brings some unnecessary complexity for the demonstration of the two important characteristics of the proposed platform: the trapping of circular-state qubits and the measurement of their dipole-dipole interaction.

In this prospect, the main result of this thesis, the characterization of the trapping of circular Rydberg states, was obtained in a new setup operated at room temperature. This setup is designed to allow seamless transfer to the cryostat traditionally used in the team [96], which will host the experiment in the mean term. This chapter is dedicated to its description.

The preparation of circular Rydberg states and their trapping involves a lot of experimental steps: gaussian tweezers must be loaded out of a cold atomic cloud of rubidium-87, followed by the preparation of circular Rydberg states and their trapping in *bottle beam* (BoB) tweezers. Every step requires careful control of the electric and magnetic fields in the region where the experiment takes place, along with proper alignment of the many laser beams involved, thus imposing strong constraints on the design.

Although the experimental techniques involved in the excitation to circular states are well known in the laboratory, the preparation of optical tweezers for their trapping is new.

2.1 Overview of the setup

The complete mechanical assembly of the setup is shown figure 2.1. The experiment takes place in an ultra-high vacuum (UHV) chamber surrounded by a custom made optical table, itself supported on a frame. A U-shaped cut in the optical table accommodates for the future insertion of the cryostat, and a removable optical table extension closes this cut to allow for installation of optics all around. The atom source, a rubidium cell connected to a bi-dimensional magneto-optic trap (2D-MOT), is clamped to the lower side of the optical table

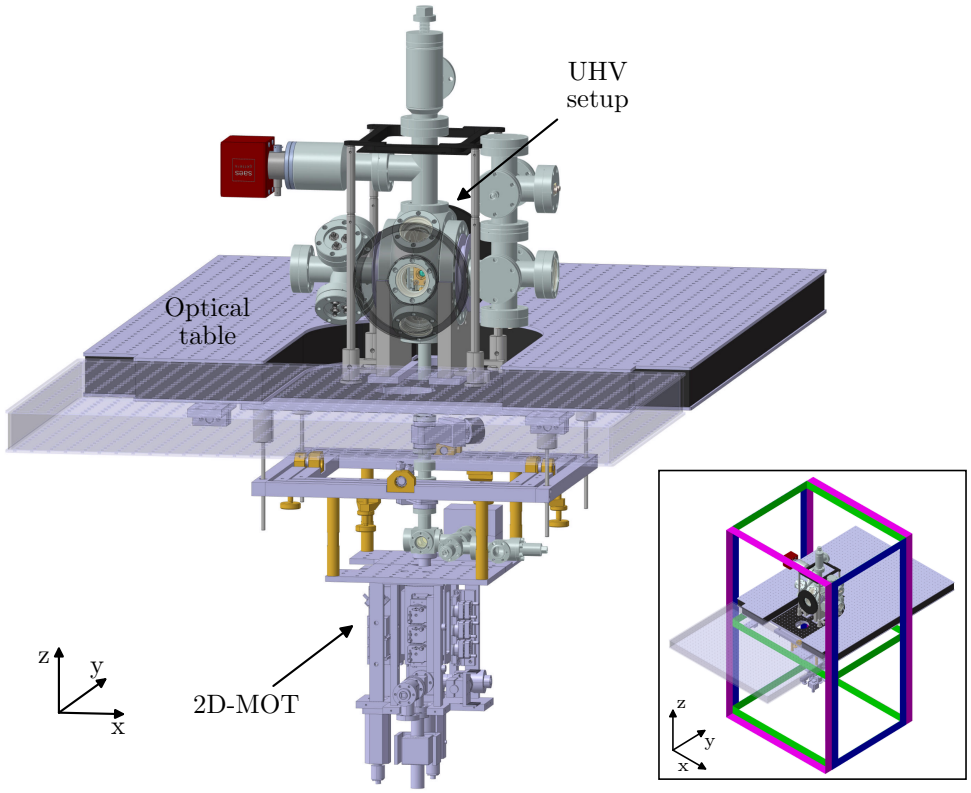

Figure 2.1: Overview of the setup, highlighting the main components. The front circular coil holder and the removable optical table extension are shaded for clarity. The inset shows the large compensation coils indicated as color bands: B_x in blue, B_y in magenta, B_z in green.

and can be connected interchangeably to the UHV setup or to the cryostat. Finally, the top part of the UHV setup, new to this experiment, is installed on an optical breadboard clamped on the optical table. This breadboard assembly can be easily removed to be substituted by the cryostat. Large compensation coils surround the whole setup. They cancel most of the Earth's magnetic field in the region of the experiment.

2.1.1 The UHV environment

We present in figure 2.2 some details of the UHV setup. It is centered on a custom machined piece of sapphire of dimensions $50 \times 50 \times 55$ mm (that will be latter referenced as the sapphire cube). The cube is placed inside a cylindrical UHV chamber having eight openings arranged as an octagon in the yz plane and two additional lateral openings along the x direction. To the $+z$ opening is attached an ion pump (NEXTorr Z100, SAES), that maintains the vacuum of the chamber at a level of 2.5×10^{-10} mbar. The connection with the 2D-MOT is established via the bottom opening. The six remaining octagon openings are viewports through which laser beams pass, one pair lies along the y axis, while the other two pairs form a cross oriented diagonally with respect to the z and y axes. On the left $(-x)$ side opening of the cylindrical chamber is a cross flange holding four sets of electrical feedthroughs along with an additional viewport. On the right $(+x)$ side is installed the ion channeling and detection setup, with another viewport. We therefore have a total of eight optical accesses to the core of the setup (indicated by red beams and arrows on figure 2.2 a)):

- One pair along the x axis,
- One pair along the y axis,
- Two pairs in the yz plane, at a 45° angle with the y, z axes.

Apart from the large compensation coils, the magnetic fields are controlled by three pairs of coils located in the surroundings of the UHV chamber, as depicted in figure 2.2 b). The magnetic gradient required for the magneto-optical trap and the directing magnetic field applied during the experiment are generated along the x-direction. The B_x coils are installed around the lateral flanges of the UHV chamber, as close as possible to the atoms, and their current is switched dynamically between parallel or anti-parallel flow depending on the needs. The B_y and B_z coils, however, serve only to fine tune the magnetic field. They thus produce weaker fields and are located farther from the sapphire cube.

2.1.2 The sapphire cube

The sapphire cube setup, at the center of which the experiment takes place, is shown in detail in figure 2.3. It is attached with positioning brackets to the $-x$ flange of the cylindrical UHV chamber (marked as (2) in figure 2.3 (c)) to center it with respect to the rest of the setup.

The atoms are loaded inside the cube from the bottom through a 26×26 mm square opening, visible in the top view in figure 2.3 (a). Such an opening accommodates for the

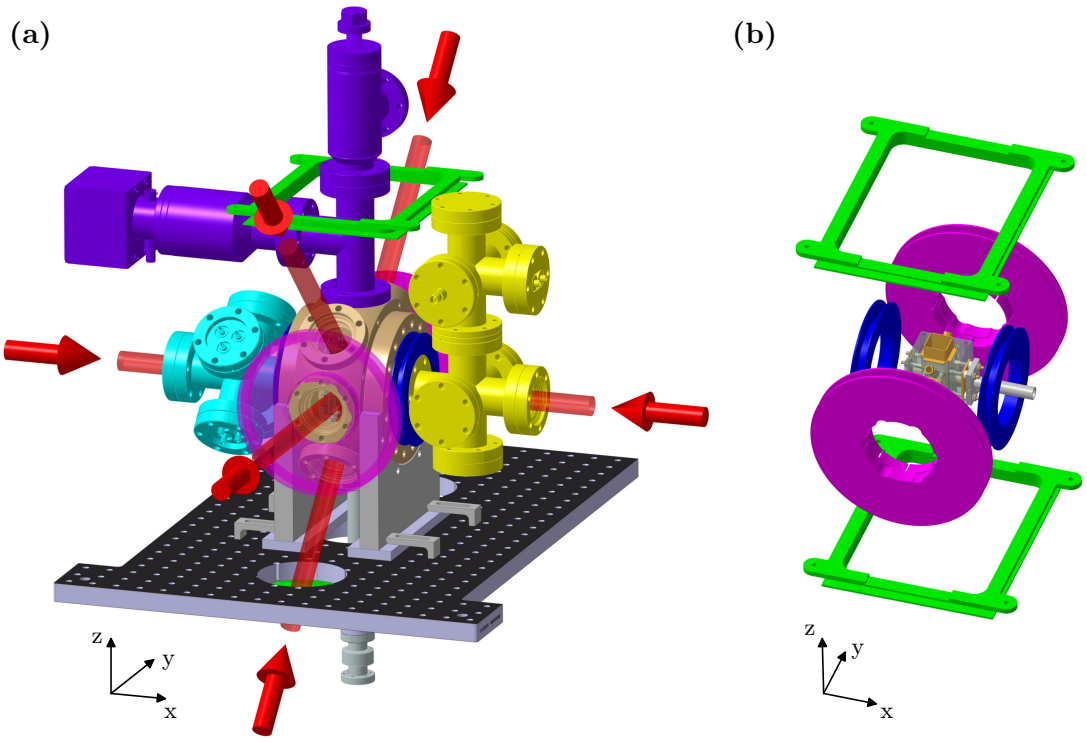

Figure 2.2: Depiction of the UHV setup and its components. (a) The whole setup, with its components highlighted. Beige (center): UHV chamber, where the experiment takes place; purple (top): pumping setup; cyan (left): electrical feedthroughs; yellow (right): ion detection setup. Red beams and arrows indicate the directions of the optical access. (b) the setup without its auxiliary components, revealing the sapphire cube assembly with the surrounding coil holders colored in blue (B_x), magenta (B_y) and green (B_z).

working distance required to focus the optical tweezers and leaves enough space to ensure homogeneous electric and microwave fields over the size of the atomic sample. On the same figure are visible eight holes arranged in four pairs, drilled in the sapphire cube. They are aligned with and are the continuation of the viewports of the UHV setup, pointing to the center of the cube where atoms are located. The lasers involved in the cooling of atoms and the preparation of Rydberg states pass through three pairs of circular holes at right angle. Two pairs, of 8 mm diameter, are located in the yz plane, aligned with the diagonal viewports of the UHV chamber, let MOT/imaging and Raman beams go through. The last pair goes along the x-axis and is larger, with a diameter of 12 mm. It lets the remaining MOT/imaging beams go through, along with the Rydberg excitation and optical pumping lasers. Each of the three pairs of holes is covered with 1 mm-thick electrodes, which effectively reduces the opening diameter by 2 mm. Finally, optical tweezers are focused on the atoms along the y direction by aspheric lenses hosted in lens holders, themselves inserted in specifically designed countersunk holes of the cube.

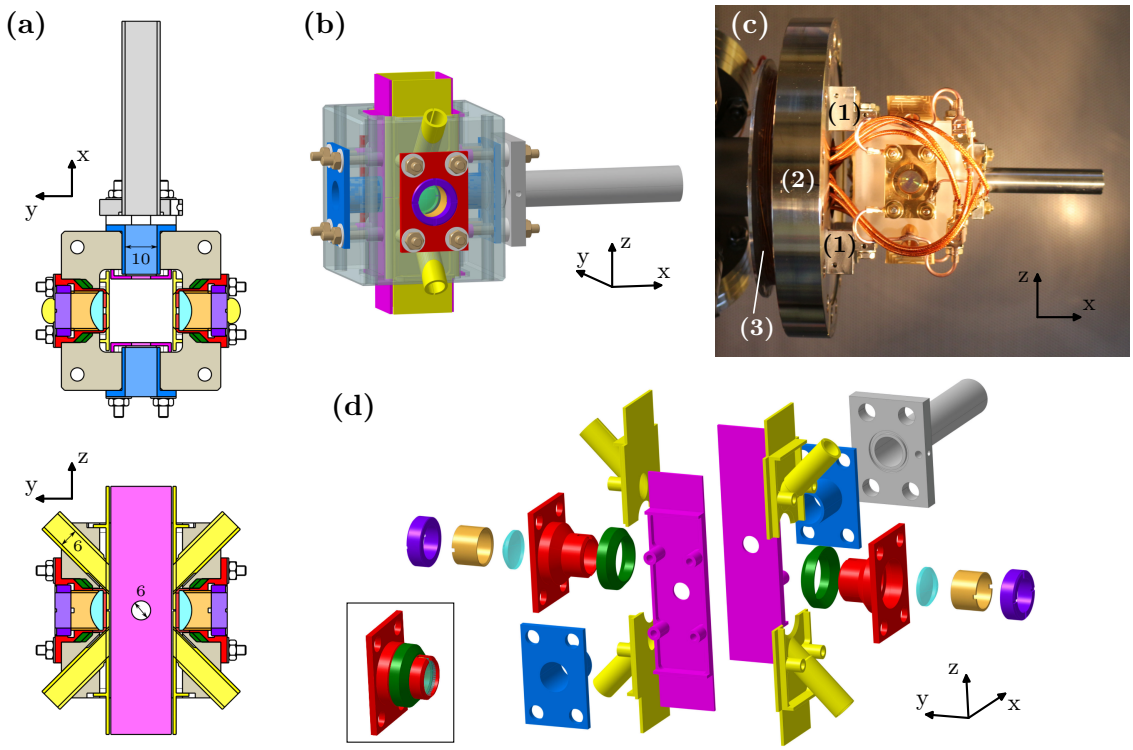

Figure 2.3: View of the sapphire cube and the surrounding electrodes. (a) Cut view of the sapphire cube with electrodes in false colors. (b) 3D view of the cube assembled with its electrodes. The color code is consistent with (a). (c) Photograph of the cube assembly attached via positioning brackets (1) to the flange (2) of the UHV chamber; a B_x coil holder (3) is visible, too. (d) Exploded view of the cube electrodes witch the same color convention as in (a)-(b). Magenta: Stark electrodes; yellow: RF electrodes; blue: Stark electrodes holders; grey: guiding tube electrode. The lens holder assembly (shown assembled in the inset picture) is composed successively of: an adjustment shim (dark green), the lens holder electrode (red), the aspheric lens (light cyan), a spacer (golden yellow), a set screw (purple).

To prevent stray electric fields from perturbating the very sensitive Rydberg atoms during the experiment, all the inner dielectric surfaces of the cube are covered with gold-coated brass electrodes. The potential of each electrode can be controlled individually via a coaxial

connection to the electrical feedthrough, allowing for a precise control of the electric field and its gradients at the position of the atoms. There is a total of ten inner electrodes, as shown in the exploded-view of figure 2.3 (d):

- During the preparation and manipulation of Rydberg states, the quantization axis is maintained along the x axis, but set by an electric field rather than a magnetic field. This electric field is controlled via the potential applied to two electrodes facing each other in the x direction (called Stark electrodes). In addition, the ionization electric field is applied by these same electrodes during ionization detection of the Rydberg states.
- The circularization procedure requires the application of σ^+-polarized radio-frequency field on the atoms. The field direction is orthogonal to the quantization axis defined by the Stark electrodes and generated by four electrodes divided in two pairs facing each other in the y-direction (called RF electrodes). An additional DC potential can be set to fine tune the electric field and its gradients at the atoms' location. These electrodes are connected to tube electrodes that cover the 45° holes of the sapphire cube.
- Two electrodes inserted in the x-direction holes (Stark holder electrodes). Their purpose is mainly to cover the sapphire surface.
- Two lens holder assemblies inserted in the y-direction holes. They are made up of five components. A lens holder electrode ensures mechanical contact with the sapphire cube. It also hosts the aspheric lens and maintains electrical contact with its surface, made conductive by a coating of indium tin oxide (ITO) of 10 nm thickness. The lens is held tight with a spacer and a set screw inside the lens holder. Finally, precise positioning of the lens is ensured by a conic adjustment shim that controls the spacing between the lens holder and the countersunk hole in the sapphire cube.

Attached to the cube is also, on the $+x$ side, a guiding tube electrode. Its role is to channel the ions produced from the ionization of Rydberg states during ion detection. It has no other purpose and is grounded during the rest of the experiment.

2.1.3 State-selective field ionization setup

Circular Rydberg states are impossible to detect optically as they do not have any transition at these wavelengths. The traditional way to detect Rydberg states implemented in the lab takes advantage of their sensitivity to moderately strong electric fields, that leads to their ionization. The detection and discrimination of different Rydberg states is done by collecting and amplifying the charges produced from their ionization. For this purpose, an ion detection setup is installed in the UHV chamber.

Principle

Rydberg states, being close to the ionization threshold, can be ionized with the application of electric fields in the order of $\sim 100\,\mathrm{V\,cm^{-1}}$ [101]. The generated ions can then be detected with a charge amplification device such as a channeltron. The field at which a given Rydberg state ionizes depends on the state, allowing one to distinguish different states from their arrival times when a ramp of electric field is applied. Typical arrival times curves are shown in figure 2.4.

This procedure allows one to detect the different Rydberg states present in the experiment at a given point of the experimental sequence, a necessity to optimize each step of the

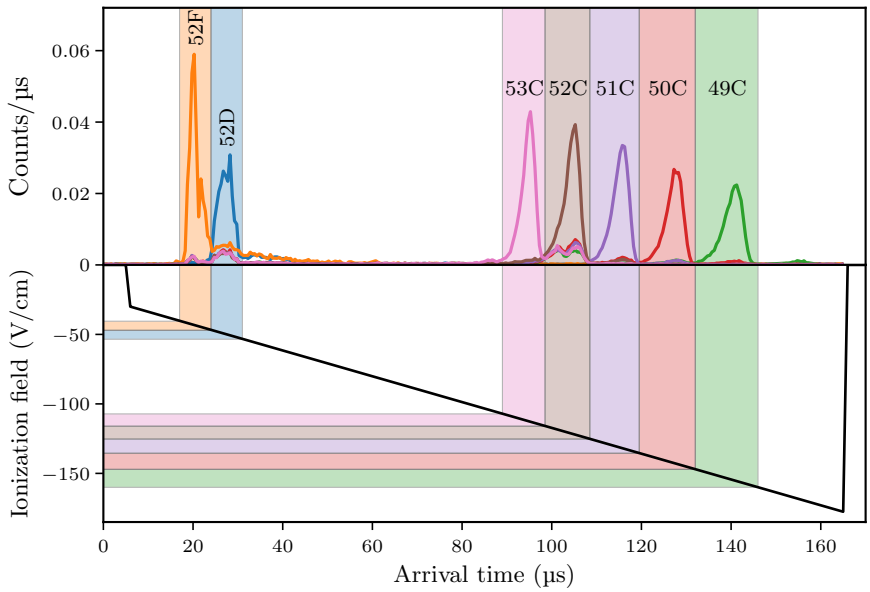

Figure 2.4: Principle of state selective field ionization. A ramp of potential is applied to ionization electrodes, generating a ramp of electric field (bottom panel), successively ionizing different states (top panel). Figure adapted from [94].

preparation of circular states. Table 2.1 presents the ionizing fields of the various Rydberg states involved in the experiment.

Table 2.1: Ionization field for some Rydberg levels involved in the experiment.

Level	Ionization field (V/cm)
52D	50
52F	44
52C	122
50C	142

Setup

We designed the ion detection setup, shown figure 2.5, with the help of the ion optics software Simion. The ions exit the sapphire cube through the x-direction, along which the ionizing field is generated by applying a symmetrical ramp of potential to the Stark electrodes. The positive Rb^+ ions are accelerated in the $+x$-direction. The channeltron (KBL15RS_HMI, Dr. Sjuts Optotechnik GmbH) cannot stand along the same axis, since it would block the optical access in this direction. It is therefore placed along the z axis, pointing downward, and collects the ions deflected upwards by a pair of deflection electrodes. The guiding tube electrode, in which the ions travel from the sapphire cube to the deflection electrodes, is held at a negative voltage of $-380\,\mathrm{V}$. Its role is to accelerate the ions sufficiently for them to have a straight trajectory. The channeltron operates at a potential of $-2500\,\mathrm{V}$, and a voltage of $60\,\mathrm{V}$ on the deflection electrodes is enough to redirect the ions vertically. Produced ions

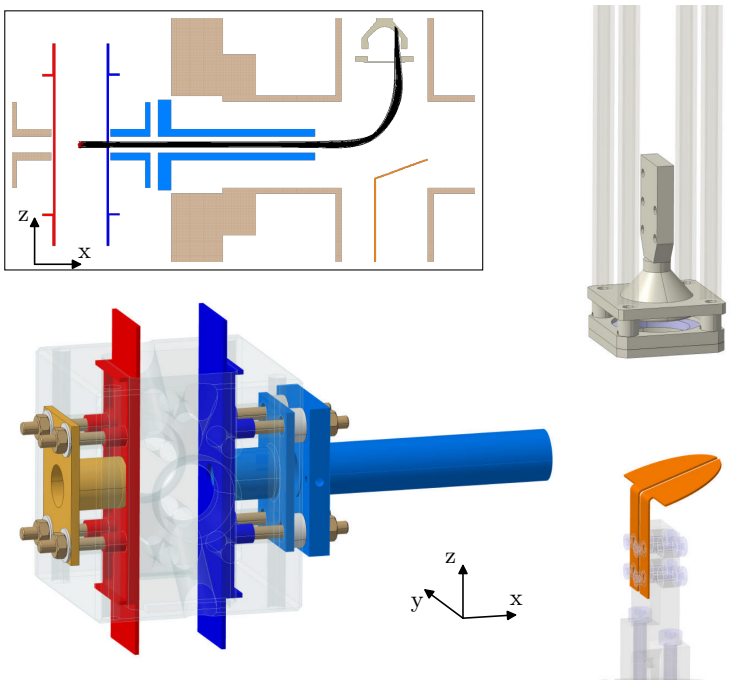

Figure 2.5: The detection setup, designed to detect Rb^+ ions. Ions are produced by applying a symmetric ramp of potential to the Stark electrodes (positive on the red electrode, negative on the blue one). They are accelerated by the guiding tube and Stark holder assembly (light blue) then deflected toward the channeltron (white) by the deflection electrodes (orange). The upper left inset shows (black lines) typical ion trajectories computed with the Simion software suite. It corresponds to a cloud of Rb^+ ions, at the ionization field of $|52C\rangle$ with the electrode voltages given in the text.

travel from the science region to the channeltron in about 7 µs. There is little dispersion of the time of flight of ions produced at different fields, of approximately 1 µs over the whole range of ionizing fields (between 40 and 150 $V\,cm^{-1}$).

The electronic signal produced by the channeltron is amplified and shaped with a pulse discriminator. We can then either timestamp each pulse, allowing to record arrival times of ions, or simply count the number of pulses in predefined time windows that correspond to the arrival of different states. The first case gives a signal similar to the top panel of figure 2.4, which is time-resolved. The second counting method gives only the integral of the peaks, for instance, in the colored rectangles, which is often enough for data analysis.

2.2 Optical tweezers setup

Our experiment necessitates the preparation of both gaussian optical tweezers and BoB tweezers. The retained method to prepare them within the experiment consists in spatially modulating the phase of a collimated laser beam. A lens then focuses the phase-modulated beam to produce the desired intensity profile in the vicinity of its focal plane. Albeit very flexible in generating arbitrary intensity profiles, this approach requires careful control of the imperfections of the system with methods that will be partially described in this section. The exhaustive description of tweezer preparation will be treated in an upcoming thesis by Yohann Machu [97].

The presence of atoms in traps is determined by fluorescence imaging. The design requires single-photon sensitivity to convert the few photons scattered by trapped atoms into a reliable signal, and proper filtering of the parasitic light which potentially dwarfs the signal.

2.2.1 Tweezer and imaging setup

The optical setup is schematized in figure 2.6. A total of five laser beams, involved in the cooling of the atoms and the control of their state (*i.e.* optical pumping and Rydberg excitation), overlap and cross the atoms in the x-direction. Their role will be detailed in dedicated sections.

The actual tweezers preparation and fluorescence collection takes place along the y-axis, where the focusing aspheric lenses lie. Phase modulation is done by spatial light modulators (SLMs). Owing to their slow response time of dozens of milliseconds as compared to a millisecond long sequence with needs of sub-microsecond switching time, two SLMs are necessary to make both varieties of tweezers available during the experimental sequence. The preparation of tweezers begins with two optical paths, one dedicated to the preparation of gaussian tweezers and the other one to the preparation of BoB tweezers. The phase-modulated beams are then gathered on the same path and focused by an aspherical lens. The preparation of the tweezers is combined with fluorescence imaging using the MOT beams to detect trapped ground state atoms.

Laser and optics

The laser light used for the preparation of the tweezers comes from a Toptica TA Pro laser emitting approximately 2 W of power at 821 nm. As shown in the framed scheme of figure 2.6, the output beam is sent to the UHV setup optical table via two optical fibers, one for each variety of tweezers, and power switching is done with acousto-optic modulators (AOMs). Since we do not need to have both types of tweezers in the experiment at the same time, the beam power is shared between the two fibers rather than split. This arrangement allows us to maximize the power available to the BoB traps, which is the limiting factor to the number of such traps that can be prepared in the experiment. The beams at the output of the fibers are collimated to a diameter of 10.4 mm (at $1/e^2$ intensity), a value close to the SLM's effective area of 16×12 mm. The phase modulated reflections on the SLMs are overlapped with a polarizing beamsplitter (PBS) cube. From there on, these two beams act as one beam, producing either gaussian or BoB tweezers, depending on the needs, and will therefore be referenced from now on as the tweezer beam.

The tweezer beam undergoes a first step of spatial filtering at the focus of a $1:1$ telescope (marked (1) on figure 2.6) to dispose of spurious light. The role of this spatial filtering will be detailed later in the text. It is then focused at the center of the sapphire cube, where the atoms are located, by an aspheric lens (AFL12-15-S-U-285, Asphericon) with a working distance of 12.3 mm. It has an effective focal length of 16.3 mm with a numerical aperture (NA) of 0.36 (at the operating wavelength of 821 nm). The outgoing beam is collimated back with a lens of the same model and split with a glass window. The transmitted beam, that contains most of the power, goes to a beam dump, while the reflection is focused on a camera to produce an image of the tweezers in transmission.

A flip-flop mirror is present just before the UHV chamber to deflect the incoming tweezer beam towards a diagnostic camera on which the tweezers can be imaged directly. This imaging of the tweezers allows precise overlap between the arrays of gaussian and BoB tweezers. This

camera is also involved in the correction of the aberrations of the optical path of each SLM as will be described later.

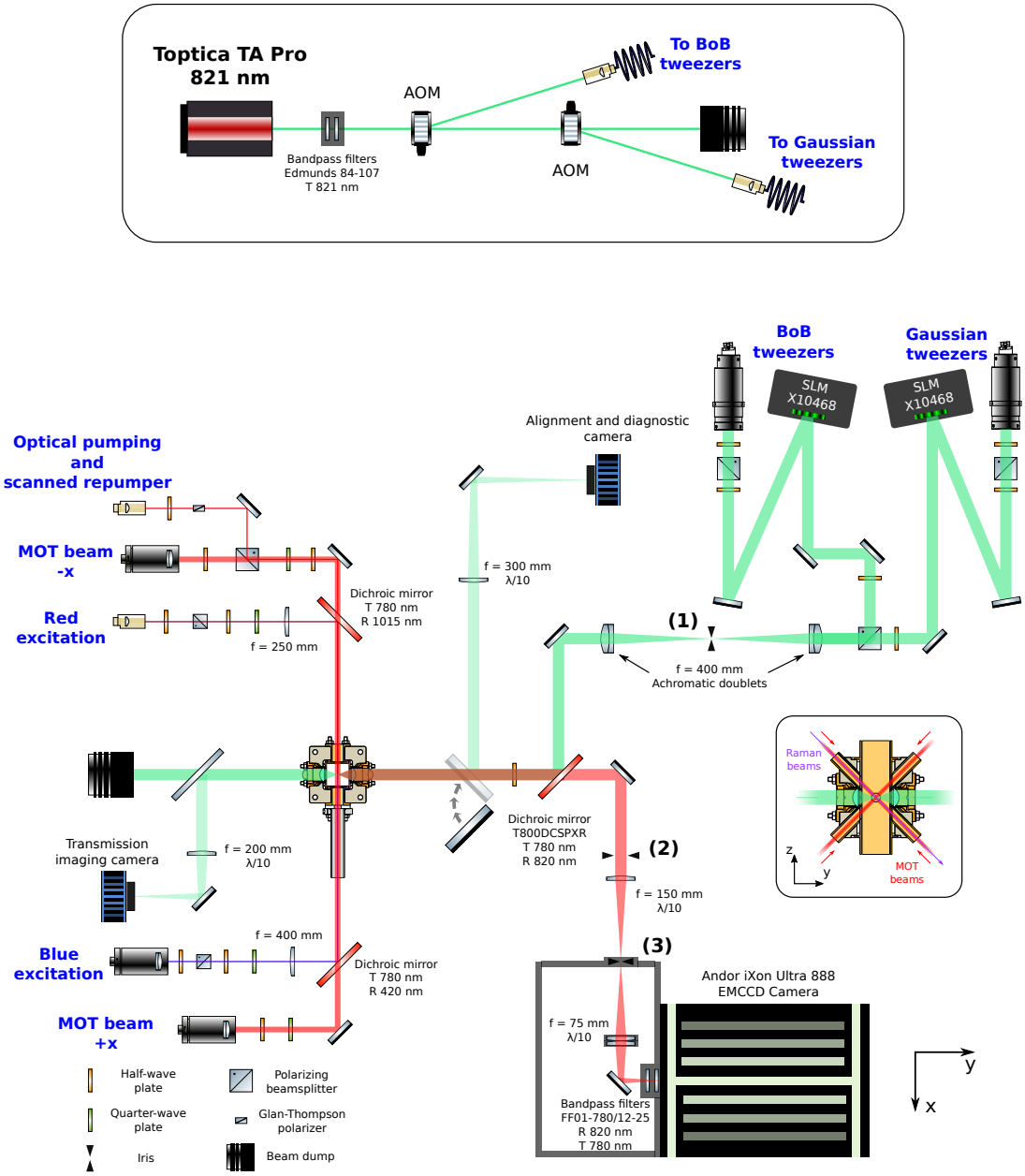

Figure 2.6: Scheme of the optical setup for tweezer preparation and fluorescence imaging. Top: simplified scheme of the laser setup for the preparation and control of the two tweezer beams. Bottom: scheme of the optical setup surrounding the experiment. Two important components are highlighted: the preparation of tweezers and collection of atom fluorescence. For the sake of completeness, laser beams along the x direction are depicted, their role will be described later in the text. The inset shows a yz-cut of the cube along with the laser beams that propagate in this plane.

The spatial light modulators (SLMs)

The devices that we use are Hamamatsu liquid crystal on silicon (LCOS-SLM) model X10468-02. The light modulator consists in a dielectric mirror covered by an array of 792×600 independent phase modulators of dimensions 20×20 µm. Each phase modulator (latter referred as pixel) is controlled by a voltage that changes the refractive index of a layer of liquid crystal, thus changing the phase of a beam going through. The device allows for a phase control from 0 to 2π in about 200 levels[1] that we re-scale to 256 levels (8 bits).

The SLM has some imperfections with respect to an ideal device that must be taken into account when operating it:

- It is not flat, generating an offset of phase shift on each pixel. A factory calibration compensates for most of the departure from flatness, yet some remains.
- The anti-reflection coating of the liquid crystal layer is not perfect.
- The behavior is ill-defined at the boundaries of the pixels, where the electric field is not controlled. For instance, the manufacturer indicates a light utilization efficiency of 97 %.

The imaging setup

The presence of ground state atoms trapped in gaussian tweezers is assessed by fluorescence imaging. A fraction of the 780 nm-wavelength photons scattered by the atoms is collected and collimated by the lens focusing the incoming tweezer beam. This "beam" of photons going in the opposite direction of the tweezer beam is split from the latter and transmitted by a dichroic mirror (T800DCSPXR, Chroma Technology Corp.). A first stage of spatial filtering is done by an iris encircling the collimated beam (marked (2) on figure 2.6), that filters the incoming light emitted outside of the focal plane (which is therefore not collimated).

The camera used for imaging of individual atoms is an Andor iXon ultra 888 EMCCD camera. Its sensor consists in an array of 1024×1024 pixels of size 13 µm. The image of the atoms is magnified so that the fluorescence of an atom in a trap roughly spans the size of a camera pixel. For a pixel size of 13 µm and a trap of about 1 µm, the magnification is a factor[2] ~ 9, performed by a lens of focal length $f = 150$ mm. To prevent any stray light coming from the surrounding environment to saturate the very sensitive imaging camera and also spatially filter fluorescence light emitted out of the tweezers plane, the beam enters a sealed black box through a pinhole at the focus of the magnifying lens (marked (3) on figure 2.6). The image of the atoms is then translated to the sensor of the camera with a lens assembly of focal length $f = 75$ mm in $2f - 2f$ configuration. To remove residual laser light at 820 nm scattered on the various optics, two bandpass filters (FF01-780/12-25, Semrock), having an optical density > 7 at the corresponding wavelength are installed in front of the camera sensor. Let us mention that the laser that serves to prepare the tweezers also emits residual light at 780 nm. We filter it at the output of the laser with another pair of bandpass filter (model 84-107, Edmunds), as shown in the top framed panel of figure 2.6.

We operate the camera with its sensor cooled to a temperature of $-80\,^{\circ}$C and an electron multiplying (EM) gain of 30, recording images with the manufacturer's software.

[1] The manufacturer takes some margin for phase wrapping to ensure that the whole range of phases is accessible.

[2] The magnification is equal to the ratio of the focal lengths of the magnifying lens and the aspheric lens, that is $150/16.3 = 9.2$.

2.2.2 Preparation of optical tweezers

This section introduces the ideas behind the preparation of the tweezers in the experiment. It is by no means intended to be exhaustive and eludes some of the technical aspects.

The first step consists in imprinting the correct phase mask on the SLM. Assuming that the field in the SLM plane (with transverse coordinates u, v) is a gaussian beam of waist w, with wavenumber k, the field $F(x, y, z)$ propagating along the z-direction close to the focal plane $z = 0$ of a lens of focal length f is, within paraxial approximation and up to a phase and a constant amplitude:

$$F(x, y, z) \propto \int e^{i\varphi(u,v) - \frac{u^2+v^2}{w^2}\left(1+i(NAe)^2 kz\right)} e^{-i\frac{k}{f}(ux+vy)} \mathrm{d}u\mathrm{d}v, \tag{2.1}$$

where $NAe = w/f$ is the effective numerical aperture.

The previous equation can be expressed as the Fourier transform (denoted $\mathcal{F}$) of the function

$$f_z(u, v) = \exp\left(i\varphi(u, v) - \frac{u^2 + v^2}{w^2}(1 + i(NAe)^2 kz)\right), \tag{2.2}$$

$$F(x, y, z) \propto \mathcal{F}[f_z]\left(\frac{kx}{f}, \frac{ky}{f}\right). \tag{2.3}$$

Selection of a pupil

The first step for efficient tweezer preparation is to have a controlled illumination pattern to apply phase modulation to, and to get rid of any stray light. The imperfect light utilization efficiency of the SLM causes a fraction of the incoming beam to remain unaffected by the phase modulation. We must get rid of this part of the beam to prevent it from producing uncontrolled interferences with the tweezers. In addition, to preserve the axial symmetry of the system, we discard the light hitting the corners of the rectangle-shaped SLM array, keeping only the light inside a circular pupil at the center of the SLM.

Figure 2.7 shows how the selection of the phase-modulated part of the beam inside a pupil is done. The idea consists in applying the phasemask of a diffraction grating on the SLM to generate a translation at the focus of a lens. This translation permits spatial filtering with a pinhole. In practice, the selected pupil is displaced horizontally by $\sim 1\,\mathrm{mm}$ at the focus of the 400 mm-focal-length lens (at mark (1) on figure 2.6). The light hitting the SLM outside the pupil is translated vertically with a similar grating. The part of the beam that is not phase-modulated appears at order zero of the diffraction pattern.

The two displacements imprinted on the phasemask are orthogonal because of their imperfections: while most of the power is in the order 1 of the diffraction pattern, some residual power goes in order -1. Displacing the light outside the pupil along the same axis as the light inside the pupil would overlap the spurious order -1 of the first with the desired order $+1$ of the latter.

The Gerchberg-Saxton algorithm

The method to produce a given intensity profile in the vicinity of the focal plane is simple in theory: apply the correct phase modulation with the SLM so that the transformation (2.3) matches with the desired profile. Although it is possible to invert the relation (2.3) to recover the field that would produce the desired arbitrary profile, it would not only impose the phase, but also the intensity profile on the SLM. However, we have no control on the latter, hence

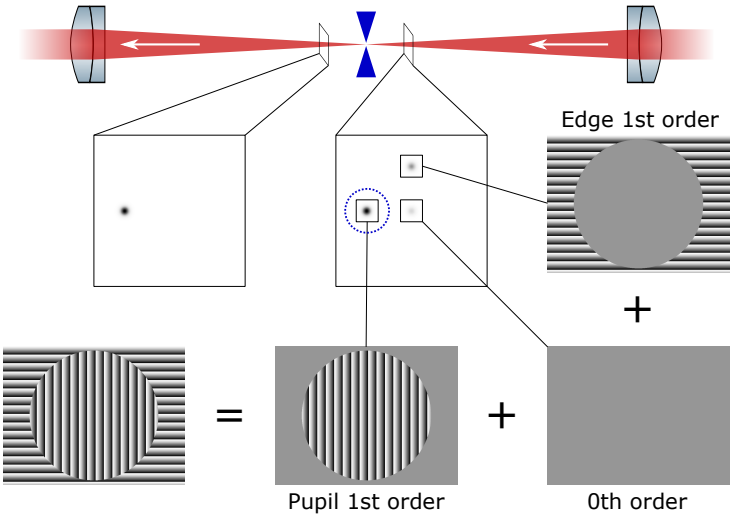

Figure 2.7: Principle of pupil selection. A phasemask is applied to shift different parts of the beam at the focus of a lens. The 0^{th} order corresponds to the part unaffected by phase modulation (equivalent to a flat phasemask). The vertical and horizontal 1^{st} orders correspond to the beam hitting the edges of the SLM and to the desired beam on the pupil, respectively. The iris (represented as a blue dotted circle) selects the beam diffracted at the pupil.

the difficulty of the intensity profile generation at the focus of the lens lies in finding the correct phase mask to apply *with a fixed intensity profile on the SLM*. Iterative methods for phase retrieval exist that in practice converge[3] to a phase mask giving a good approximation of the desired intensity profile.

Let us mention an important algorithm for phase retrieval, introduced in 1972 by Gerchberg and Saxton [132]. It allows one to reconstruct a given intensity profile *in the image plane (the Fourier plane)*, with a fixed intensity profile I_0 in the diffraction plane (the SLM plane).

The principle of the algorithm is depicted in figure 2.8. In essence, it consists in cycling between the SLM plane and the image plane by performing Fourier transform and its inverse, repeatedly substituting the target intensity to the computed intensity. The target phasemask is obtained after a suitable number of iterations. The algorithm goes as follows:

- Initialization
  The field in the SLM plane is set as $\sqrt{I_0}e^{i\phi_0}$, with ϕ_0 a suitable initial phase, usually chosen as an educated guess based on an intuition of the final phasemask or as a mask of random phase in the absence or prior information.
- Iteration
  - Compute the profile in the image plane $A_n e^{i\psi_n} = \mathcal{F}\left[\sqrt{I_0}e^{i\phi_n}\right]$;
  - Replace the module of the amplitude A_n with the target S_{tgt};
  - Compute the image-plane profile obtained previously in the SLM plane: $B_{n+1}e^{i\phi_{n+1}} = \mathcal{F}^{-1}\left[\sqrt{S_{tgt}}e^{i\psi_n}\right]$;
  - Replace the module of the amplitude B_{n+1} with the imposed $\sqrt{I_0}$.
- Termination
  Return the phase ϕ_N obtained after N iterations.

[3] There is however no mathematical proof of the convergence in general.

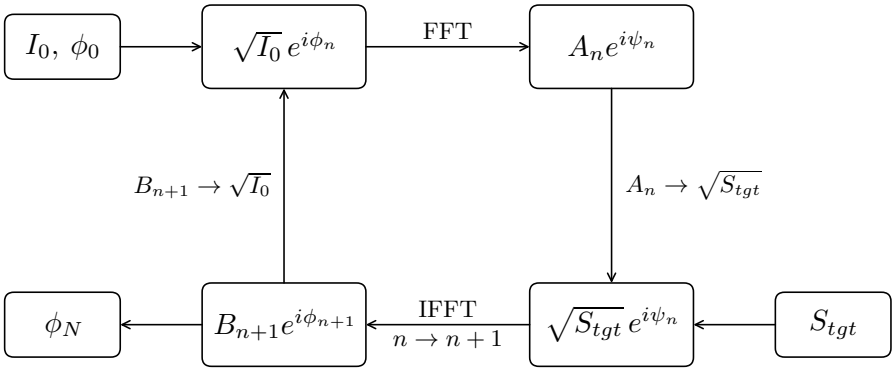

Figure 2.8: Principle of Gerchberg-Saxton algorithm for phase retrieval. The description is given in the text. FFT and IFFT stand for fast Fourier transform and inverse fast Fourier transform respectively.

Nevertheless, this method has limitations that prevents the algorithm to converge in some cases. Let us mention the necessity for a precise knowledge of the intensity profile I_0 on the SLM. Another limitation of the algorithm is that it takes the information of the intensity only in the focal plane, which is not always enough to reconstruct the phase with precision.

2.2.3 Aberrations correction

To produce well defined arrays of tweezers, optical aberrations introduced by the various optical elements on the beam path must be compensated. They contribute to deform the phasemask applied by the SLM, by effectively adding a "phasemask of aberrations" to it. Aberration correction therefore consists in determining this phasemask and applying its opposite on the SLM.

The aberrations introduced by the optics are split in two contributions, each having its own correction procedure. The aberrations introduced by the aspheric lenses and the windows of the UHV chamber are determined in a specific setup before their installation in the UHV environment, as shown in figure 2.9 a). This is necessary as the lenses are assembled as a pair in the UHV chamber, making it impossible to correct the aberrations generated by one lens independently of the other. First, a step of spatial filtering is done at the focus of a telescope (as described section 1.2.2). The aspheric lens then imprints aberrations on the beam, which is collimated back with a 1 mm-focal-length microscope objective (MPLFLN100X, Olympus) that we assume to be perfect. The beam aberrations translate into a deformed intensity pattern measured by a camera at the focus of a lens of good quality surface ($\lambda/10$) and focal length $f = 300\,\text{mm}$, large enough to introduce a negligible amount of aberrations. The assembly of the aspheric lens and the microscope objective make an afocal system that can be replaced by another one, for instance the windows of the UHV chamber.

The second part, shown in figure 2.9 b), concerns the aberrations due to the optics on the beam path (and of the beam itself), which are compensated *in situ*. For this, a flip-flop mirror in front of the UHV chamber deflects the tweezer beam towards a camera located at the focus of a lens. As for the previous case, the additional mirrors and 300 mm-focal-length lens on the beam path are assumed to add negligible deformations to the beam.

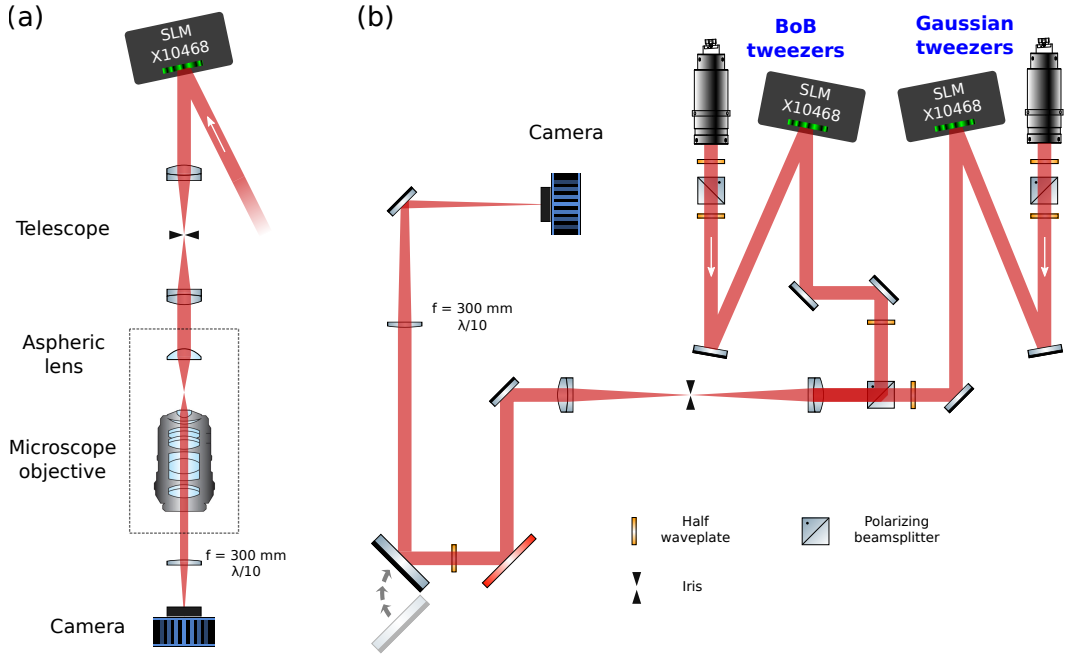

Figure 2.9: (a) Setup for the correction of the aspheric lenses' aberrations. The assembly of the aspheric lens and microscope objective are replaced by UHV chambers windows to correct their aberrations. (b) Deflection of the tweezer beam towards a camera for the correction of aberrations along the beam path outside of the UHV chamber. Compare with figure 2.6.

Principle of aberrations compensation

Let us give briefly the idea behind the aberration compensation procedure that we follow. The mask of aberrations ϕ_{aber} previously mentioned distorts a reference phase mask to yield a distorted intensity profile in the image plane. We can recover the mask ϕ_{aber} by running the GS algorithm with the distorted intensity profile as the target. However, the drawbacks of the GS algorithm mentioned earlier prevent this simple procedure to converge in the case of aberration compensation, and in practice we must take into account information from the distorted intensity profile out of the focal plane.

The procedure that we follow to perform aberration compensation is more involved than the plain GS algorithm introduced section 2.2.2. Indeed, our aspheric lenses exhibit a significant amount of aberrations, and require us to use a correction algorithm that can take into account the additional information.

The algorithm that we use is depicted Figure 2.10. The phasemask on the SLM is initialized to produce a gaussian beam, and the image of the beam at the focus of the lens is recorded by a camera. Rather that displacing the camera in the vicinity of the focal plane, we add phasemasks φ_j corresponding to Fresnel lenses of varying focal length to the SLM to shift the focal plane. Slices S_j of the beam intensity profile are obtained in a region surrounding the focal plane with this procedure, and serve as the target intensity for a modified GS algorithm, that reconstructs the correct phasemask to obtain the intensity profile on the camera.

The modified GS algorithm consists in iterating the single-plane algorithm for each measured slice, a procedure that yields a set of field amplitudes and phases $B_{n,j}e^{i\phi_{n,j}}$. Those fields are, after subtraction of the Fresnel lens mask φ_j, averaged before being used as the starting point of the next iteration.

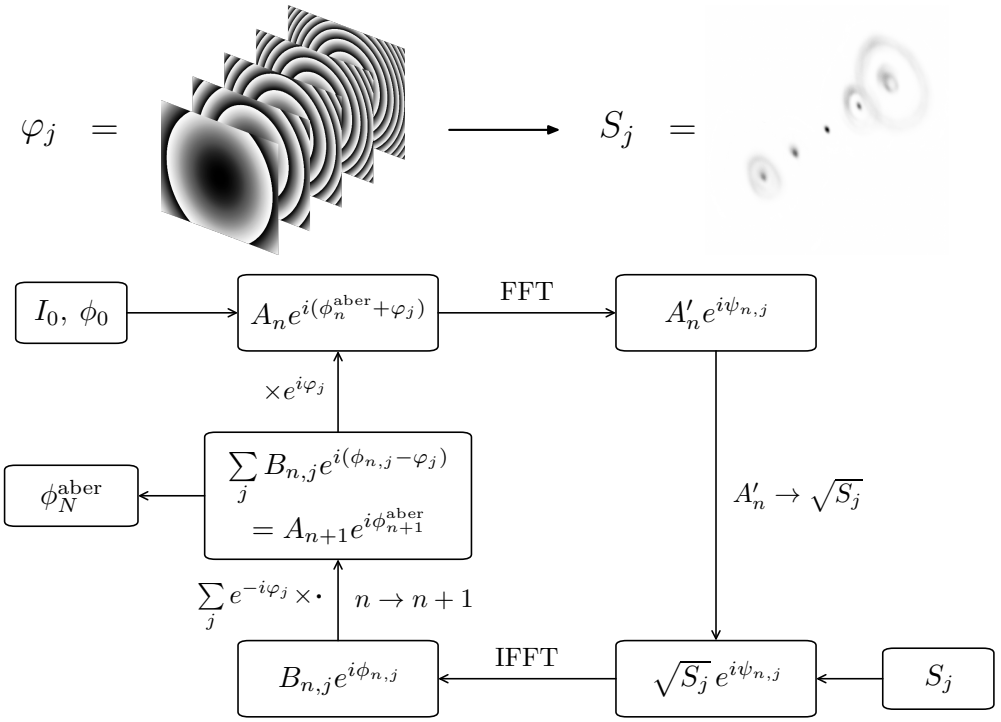

Figure 2.10: Aberration correction procedure. Applying Fresnel lens phasemasks on the SLM yields the gaussian intensity profile deformed by aberrations in the vicinity of the focal plane of the lens. The GS algorithm is run for each slice, retaining the average of the profiles obtained (minus the Fresnel lenses) to initialize of the next iteration.

2.3 Preparation of cold atoms in gaussian optical tweezers

The first step towards the trapping of atoms in the circular state consists in the preparation of a cloud of cold rubidium-87 atoms trapped in gaussian optical tweezers. For this purpose, a vapor of rubidium is first cooled transversely by a 2-dimensional magneto-optic trap (2D-MOT), then travels to a 3-dimensional MOT (3D-MOT) from which tweezers are loaded. The atoms are further cooled by an optical molasses.

2.3.1 Atom source and 2D-MOT

A vapor of rubidium is first obtained from a cell containing the metal in liquid form, heated at 60 °C. The vapor then diffuses to the 2D-MOT to be cooled transversely.

Our 2D-MOT is a commercial device obtained from the SYRTE laboratory. A detailed description is given in [133]. The principle of its operation is schematized in figure 2.11. It consists of an arrangement of three pairs of laser beams and four coils. A current flows in the coils to produce a balanced and centered bi-dimensional magnetic quadrupole in the center of an UHV cell. Each incident laser beam has its polarization adjusted to be σ^- with respect to the quantization axis defined by the magnetic field when deviating from the minimum, and is overlapped with its reflection on a mirror. The polarization of the reflected beam is maintained by passing twice through a quarter waveplate. The three pairs of laser beams intersect at the center of the cell, forming three vertical stages of cooling to produce a rising collimated beam of rubidium. The resulting beam goes out by a 1.5 mm hole and is aimed at the 3D-MOT, located 50 cm higher, by adjusting the orientation of a gimbal holding the

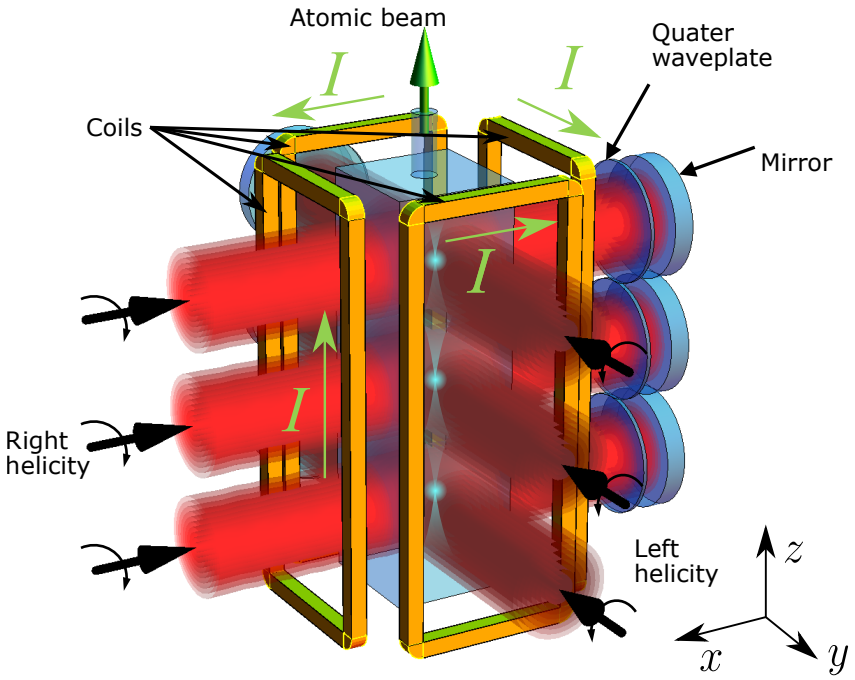

Figure 2.11: Scheme of the 2-dimensional MOT. The collimated atom beam is represented in cyan.

2D-MOT with pressure screws (visible on figure 2.1).

For proper operation, the UHV cell of the 2D-MOT is maintained at a pressure of $\sim 10^{-8}$ mbar with an ion pump located at the top of the cooling stage. The 2D-MOT produces a maximal flux of 10^{10} atoms of ^{87}Rb per second, with a velocity $18 \pm 6.5\,\mathrm{m\,s^{-1}}$.

2.3.2 3D MOT

The rubidium incoming from the 2D-MOT is collected in the tri-dimensional MOT (3D-MOT) depicted figure 2.12. The trapping region is located at the center of the sapphire cube, where the six cooling beams intersect.

The trap operates via the cycling transition $\left|5S_{1/2}, F = 2\right\rangle \longrightarrow \left|5P_{3/2}, F' = 3\right\rangle$, addressed by the cooling laser beams. In order for the cooling to be effective, the frequency of the cooling beams is red-detuned by 14.8 MHz, that is $\sim 2.5\Gamma$ from the resonance (for a natural linewidth $\Gamma = 2\pi \cdot 6.065\,\mathrm{MHz}$ [107]). Owing to its detuning the cooling beam sometimes sends the atom in the state $\left|5P_{3/2}, F' = 2\right\rangle$ that in turn can decay to the dark state $\left|5S_{1/2}, F = 1\right\rangle$. Atoms ending up in this state are pumped back to the level $\left|5P_{3/2}, F' = 2\right\rangle$ with the help of a dedicated laser beam, the "repumper", tuned to this transition.

The magnetic quadrupole is generated by the two B_x coils in which current flows in opposite directions as indicated in figure 2.12 a). The currents in the B_y and B_z coils (shown in figure 2.2) are adjusted to fine tune the center of the quadrupole.

2.3.3 Optical molasses and imaging

A typical cold atom sequence is shown in figure 2.13. It lasts approximately 300 ms in total, including some delays not displayed on the figure. An array of gaussian optical tweezers is first loaded from the MOT for a duration of about 100 ms. However, the atomic temperature

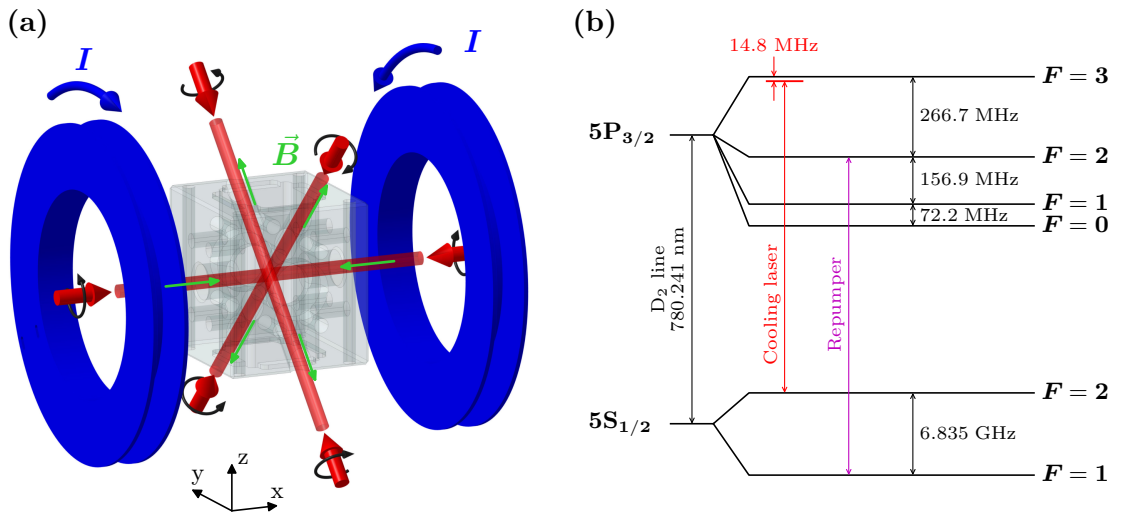

Figure 2.12: (a) Schematic depiction of the 3D-MOT, showing the magnetic coil holders and the orientation of the six cooling beams. (b) Hyperfine structure of ^{87}Rb. The lasers involved in the cooling are indicated.

at this point is too high to proceed. Additional cooling is therefore provided by an optical molasses stage. For that purpose, the magnetic quadrupole applied by the B_x coils is switched off, and the B_y and B_z coils currents are adjusted to cancel the magnetic field at the atoms' location. Moreover, since the B_x coils are also necessary to fine tune the magnetic field to zero during the molasses, their anti-parallel configuration is switched to parallel configuration. This is achieved with the help of a H-bridge that reverses the polarity of the current applied to the $+x$ coil. The optical molasses requires the cooling beams' power to be ramped down and their red detuning to be increased farther from the cycling transition with respect to the MOT configuration [99]. Optimization of these values is done by minimizing the temperature of atoms. The method to measure it will be described in the next chapter. The optimized values are indicated on figure 2.13, relative to the natural transition. It is important to note that the atoms trapped in tweezers experience a lightshift that is, for the $\left|5\mathrm{S}_{1/2}, F = 2\right\rangle \longrightarrow \left|5\mathrm{P}_{3/2}, F' = 3\right\rangle$ transition, of about 30 MHz as compared to the surrounding atoms. Optical tweezers are present for most of the sequence, and therefore the lightshift they induce must be taken into account and added to the indicated detunings during the molasses and imaging.

Before moving to the actual experimental sequence, the fluorescence signal from the trapped atoms is detected using our EMCCD camera. For this, the cooling laser beams are tuned closer to the cycling transition, with a higher intensity (both indicated in figure 2.13), in order to get enough scattered photons from the trapped atoms to distinguish their fluorescence signal from the background. The choice of these values comes from a compromise between the heating of atoms at high intensity / low detuning and a lower signal at low intensity / high detuning. The cooling beams of 5.4 mm diameter (at $1/e^2$) are clipped with irises to a diameter of 4.5 mm to prevent light from scattering from the sapphire cube inner walls, and hence reduce the background signal on the images. Recording fluorescence heats up the atoms, requiring a second stage of optical molasses cooling before initiating the experiment. Finally a second image is taken to detect the atoms that remained trapped at the issue of the experiment. A "repumper" beam is also needed during the molasses and imaging. This role is taken by a frequency scannable beam that is set resonant with the lightshifted $\left|5\mathrm{S}_{1/2}, F = 2\right\rangle \longrightarrow \left|5\mathrm{P}_{3/2}, F' = 2\right\rangle$ transition.

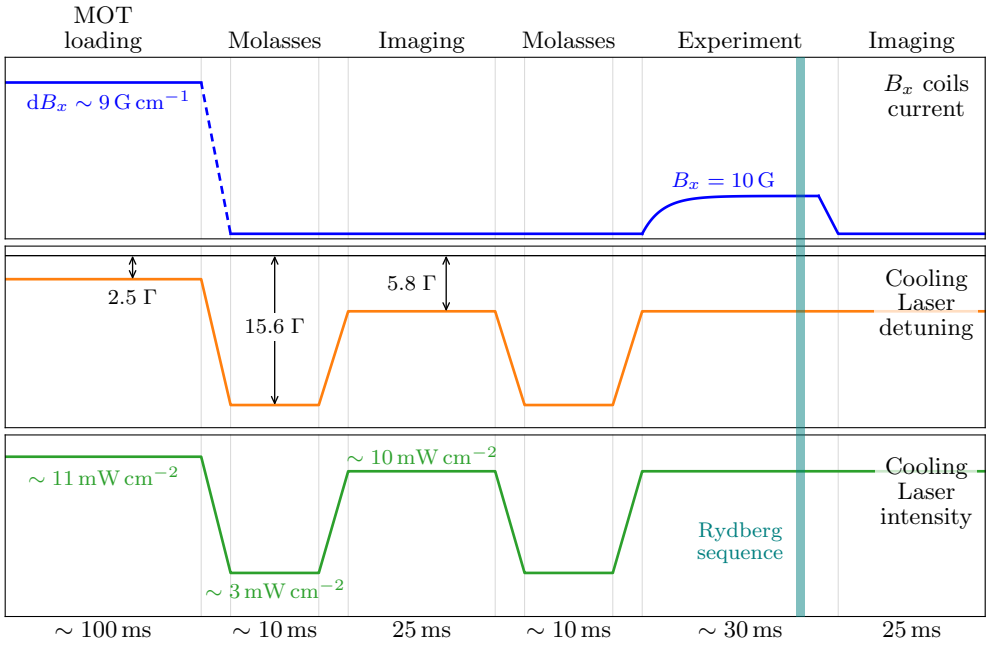

Figure 2.13: Typical cold atom sequence. Each step is described in the text. Transitions between each step take about 10 ms. The settling time of the magnetic field is exaggerated to highlight the necessary delay before the actual Rydberg physics sequence. The duration of the latter is of the order of 1 ms. The horizontal line in the central panel represents the natural frequency of the $\left|5S_{1/2}, F = 2\right\rangle \longrightarrow \left|5P_{3/2}, F' = 3\right\rangle$ transition.

The exact content of an experimental sequence varies, and each one will be detailed in its dedicated section later in the text. Let us mention the case of a Rydberg experiment, which is the most important in the context of this work, and consists in the preparation and manipulation of Rydberg states. A typical Rydberg experiment is carried in the presence of a magnetic field switched on just after the second optical molasses. The experiment, that lasts between 0.5 and 5 ms, is triggered after a 30 ms delay. This delay is necessary for the magnetic fields to settle, owing to the finite response time of the system.

Conclusion

Our results on Rydberg states trapping were obtained in a new experimental setup operating at room temperature. It constitutes an intermediate step before the implementation of the definitive simulation platform in a cryogenic environment. To that end, it is assembled on a custom-made optical table allowing for the seamless transfer to the future setup.

The experimental assembly is centered around a custom-made piece of sapphire located inside an ultra-high vacuum (UHV) chamber. It is connected to four sub-assemblies, each with a dedicated function: an ion pump system, a cross flange equipped with several electrical feedthroughs, an ion detection setup and a bi-dimensional magneto-optic trap (2D-MOT) located at the bottom. Three pairs of coils control the magnetic field in the three spatial dimensions, the directing magnetic field being set along the x-axis. The sapphire piece is empty in its center and pierced with eight holes aligned with the viewports of the UHV chamber, providing optical accesses to the various laser beams involved in the experimental sequence. The sapphire piece holds several electrodes for electric field control, and radio

frequency emission during circular states preparation. Two aspheric lenses facing each other are also mounted. Their role is to focus the optical tweezers used for trapping atoms.

The retained method for optical tweezers preparation is spatial light modulation. It consists in applying an adequate phasemask to an incident laser beam, that is converted to the desired intensity pattern at the focus of a lens. The difficulty is twofold. First, the optical aberrations introduced by the imperfect optics must be compensated. We use an adaptation of the well-known Gerchberg-Saxton algorithm to achieve this. Second, one needs to compute the appropriate phasemask for a target intensity pattern. The methodology is not described in this thesis and delayed to a subsequent work.

An experimental sequence starts from a vapor of ^{87}Rb cooled transversely in the 2D-MOT. It rises to the center of the sapphire piece and atoms are caught in a tri-dimensional MOT. Gaussian optical tweezers are present in the experiment and some atoms get captured. An optical molasses stage ensues that further cools them down. To assess the presence of trapped atoms, we record atomic fluorescence using a very sensitive EMCCD camera (see 2.14). A second molasses stage takes place before the actual experiment, and a second image is recorded after, to see which atoms are still present. The whole sequence – from loading to final detection – is approximately 300 ms-long, with the actual experiment lasting a few ms.

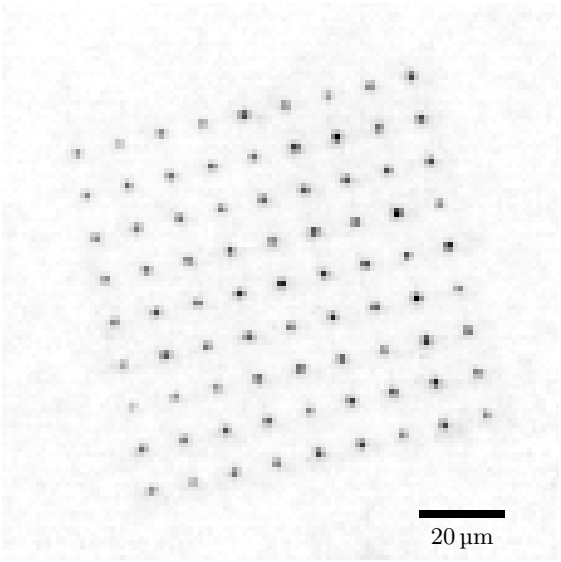

Figure 2.14: Accumulated fluorescence image of atoms trapped in a 9×9 array of gaussian tweezers spaced by 10 µm.

Chapter 3

Ground-state atoms trapped in tweezers

When I was young I played with legos, but now I am older and I play with atoms.

— Anonymous

The loading of gaussian optical tweezers with cold rubidium-87 atoms is the first step towards the preparation of trapped circular states. This chapter focuses on the characterization of the gaussian tweezers, along with some analysis of the atomic dynamics in tweezers. Its main interest lies in the introduction of the various experimental sequences and analysis procedures that are new to our research group.

Trapped atoms are detected by fluorescence imaging, a detection method that is also paramount to the demonstration of circular states trapping as will be shown in chapter 5. We begin with the description and characterization of the atomic fluorescence signal, which is the basis of all subsequent data treatment. In most cases, we take advantage of the possibility to treat individually the signal from each trapping site to get spatially-resolved information. This will prove extremely useful in analyzing some of the results presented in the rest of this manuscript.

Any defect in the array of tweezers, such as an inhomogeneity of power or deformation from aberrations would have an impact on the atomic dynamics. This could impair our ability to transfer the atoms to the BoB traps or lead to excessive losses afterwards. Moreover, the homogeneity of the traps array is a direct assessment of the performance of our tweezer generation algorithm. We thus measure the depth and oscillation frequency of the individual tweezers to recover their power and waist.

We also determine the lifetime of atoms in the tweezers and most importantly their temperature [134]. The latter probes the efficiency of our cooling scheme and is used for its optimization. The temperature is the parameter that has the larger impact on any subsequent experiment. An excessive temperature can lead to significant mechanical losses from the shallow BoB traps. Even if is low enough, it basically sets the residual motion of atoms in BoB traps, which in turn has an incidence on the dipole-dipole interaction between circular states [135].

The number of tweezers that can be prepared in our setup is limited by the laser power at our disposal. Although this allows us to prepare arrays of up to 11×11 gaussian traps,

we are limited to only 18 of the shallower BoB traps. This chapter is concerned only with gaussian tweezers, and the results presented here concern experiments carried on a square array of 9×9 traps with 10 µm inter-atomic spacing. In doing so, we keep some margin to compensate easily for day-to-day fluctuations of power. Moreover, this ensures homogeneous laser intensities over the 80×80 µm extension of our 9×9 array of tweezers.

3.1 Detection of trapped ground-state atoms

The very first step before performing more elaborate experiments on trapped atoms is to detect them properly, with a minimal error rate. The detection is based on a threshold set on the fluorescence signal, we use it to binarize the data by reducing the photon counts to the presence or absence of an atom. This binarization serves as the basis to compute relevant statistics such as the trap loading efficiency, or the recapture probability after performing an experiment.

Before proceeding to the characterization of the gaussian tweezers that we prepare, we briefly describe how this analysis procedure is implemented.

3.1.1 Fluorescence imaging

The simplest experiment that can be done with atoms trapped in tweezers is to image them. This is done by shining the cooling beams, the detuning, power and duration of which are adjusted so as to find the best compromise between the heating of atoms and the collection of enough photons to minimize the error rate of atom detection. The scattered fluorescence photons are therefore collected on the EMCCD camera for a duration of 25 ms, with an intensity per imaging beam $I_0 = 10\,\mathrm{mW\,cm^{-2}}$ (thus a total intensity $I = 6 \cdot I_0$) and a detuning $\Delta \sim 10\,\Gamma$ (taking into account the lightshift induced by the tweezers on the imaging transition). The number of scattered photons is

$$R_{\mathrm{sc}} = \left(\frac{\Gamma}{2}\right) \frac{(I/I_{\mathrm{sat}})}{1 + 4(\Delta/\Gamma)^2 + (I/I_{\mathrm{sat}})}, \tag{3.1}$$

with $\Gamma = 2\pi \cdot 6.065\,\mathrm{MHz}$ the natural linewidth of the D_2 line and $I_{\mathrm{sat}} = 3.58\,\mathrm{mW\,cm^{-2}}$ [107]. We thus get, for our experimental parameters, a scattering rate $R_{\mathrm{sc}} = 7.6 \times 10^5$ photon/s. With a numerical aperture of 0.36, the aspheric lens collects a fraction $(1 - \cos(\arcsin(0.36)) \cdot 2\pi/4\pi = 0.0335$ of the scattered photons. We therefore expect to collect approximately 650 photons during the 25 ms of imaging exposure. However, our optics are not perfect and some photons are lost along the way to the EMCCD camera, as shown in table 3.1 which summarizes their transmission efficiency. The camera software internally converts the electron signal into a number of photons, taking into account the imperfect quantum efficiency at 780 nm. The latter must therefore not be taken into account for the estimation of the measured signal. This should lead to a signal count of approximately 400 fluorescence photons for a total transmission efficiency of 61 %.

Typical images are presented figure 3.1 (a), along with an averaged accumulation of many images showing the whole array of tweezers. The rotation of the array on the camera sensor is caused by the mirrors along the optical path to the camera. The tweezers and the camera sensor are not at the same height, hence the mirrors must displace the incoming beam out-of-plane, which induces this rotation as a side-effect. From an accumulation of the signal from atoms trapped in a given array pattern, we define regions of interest (ROIs) located on the traps. The ROIs are 3×3 pixels in size. The fluorescence signal is analyzed by recording

Table 3.1: Transmission efficiency of optics along the way to the EMCCD camera (see figure 2.6).

Optical element	Transmission
ITO-coated aspheric lens	0.955
UHV chamber window	0.92
Dichroic mirror	0.93
Uncoated singlet lens	0.93
Uncoated lens pair	$0.93^2 = 0.87$
Bandpass filters	$0.96^2 = 0.92$
EMCCD camera quantum efficiency	0.76
Total	0.46 (0.61)[a]

[a] Without the contribution from the EMCCD camera.

many frames, measuring, independently for each ROIs, the total number of photons collected. We thus get, for a imaging acquisition, a list of recorded photon counts for each ROI.

The distribution of the signal in each ROI can be visualized by plotting histograms of the detected counts, as seen in figure 3.1 (b). The histograms show two peaks, corresponding to the background and the fluorescence of a single atom in the trap. The model used to fit the detected signal is a sum of two gaussian peaks:

$$f(n) = \frac{A_1}{\sqrt{2\pi\sigma_1^2}} e^{-\frac{(n-\mu_1)^2}{2\sigma_1^2}} + \frac{A_2}{\sqrt{2\pi\sigma_2^2}} e^{-\frac{(n-\mu_2)^2}{2\sigma_2^2}}, \tag{3.2}$$

where (A_1, μ_1, σ_1) and (A_2, μ_2, σ_2) represent the amplitudes, mean and standard deviation of the background and fluorescence signal, respectively. The background is, of course, always present and uncorrelated to the atomic fluorescence, hence the real fluorescence signal corresponds to $\mu_{\text{sig}} = \mu_2 - \mu_1$, with standard deviation $\sigma_{\text{sig}} = \sqrt{\sigma_2^2 - \sigma_1^2}$. We thus detect in each ROI, a number[1] $\langle \mu_{\text{sig}} \rangle = 289$, $\text{Std}(\mu_{\text{sig}}) = 30$ photons in our imaging conditions, in good agreement with our expectation of 400 detected photons. We note that the signal appears stronger in the center of the array. This can be explained by the deformation of the fluorescence beam caused by aberrations. Indeed, although we do compensate the aspheric lens aberrations for tweezers preparation, the outgoing fluorescence signal is not corrected, which is likely to cause the observed pattern.

The scattering of photons by an atom is a Poisson process, hence the statistics of collected fluorescence photons should correspond to a Poisson distribution of parameter $\lambda = \mu_{\text{sig}}$. All higher order moments are fully determined by λ, in particular the standard deviation which is expected to be $\sqrt{\lambda} = \sqrt{\mu_{\text{sig}}}$. We can therefore compare the previous value to the fitted standard deviation to assess whether our photon count statistics is indeed subject to a poissonian process. From the measured fluorescence signal we infer a theoretical Poisson width $\langle \sqrt{\lambda} \rangle = 17.0$, $\text{Std}(\sqrt{\lambda}) = 0.9$ photon, much lower than the measured width $\langle \sigma_{\text{sig}} \rangle = 31.6$, $\text{Std}(\sigma_{\text{sig}}) = 2.0$ photon. This indicates clearly that our photon count statistics is broadened by other processes.

[1] Here and in the remaining of the manuscript, the notations $\langle X \rangle$ and $\text{Std}(X)$ refer respectively to the mean and standard deviation of the quantity X over all trapping sites.

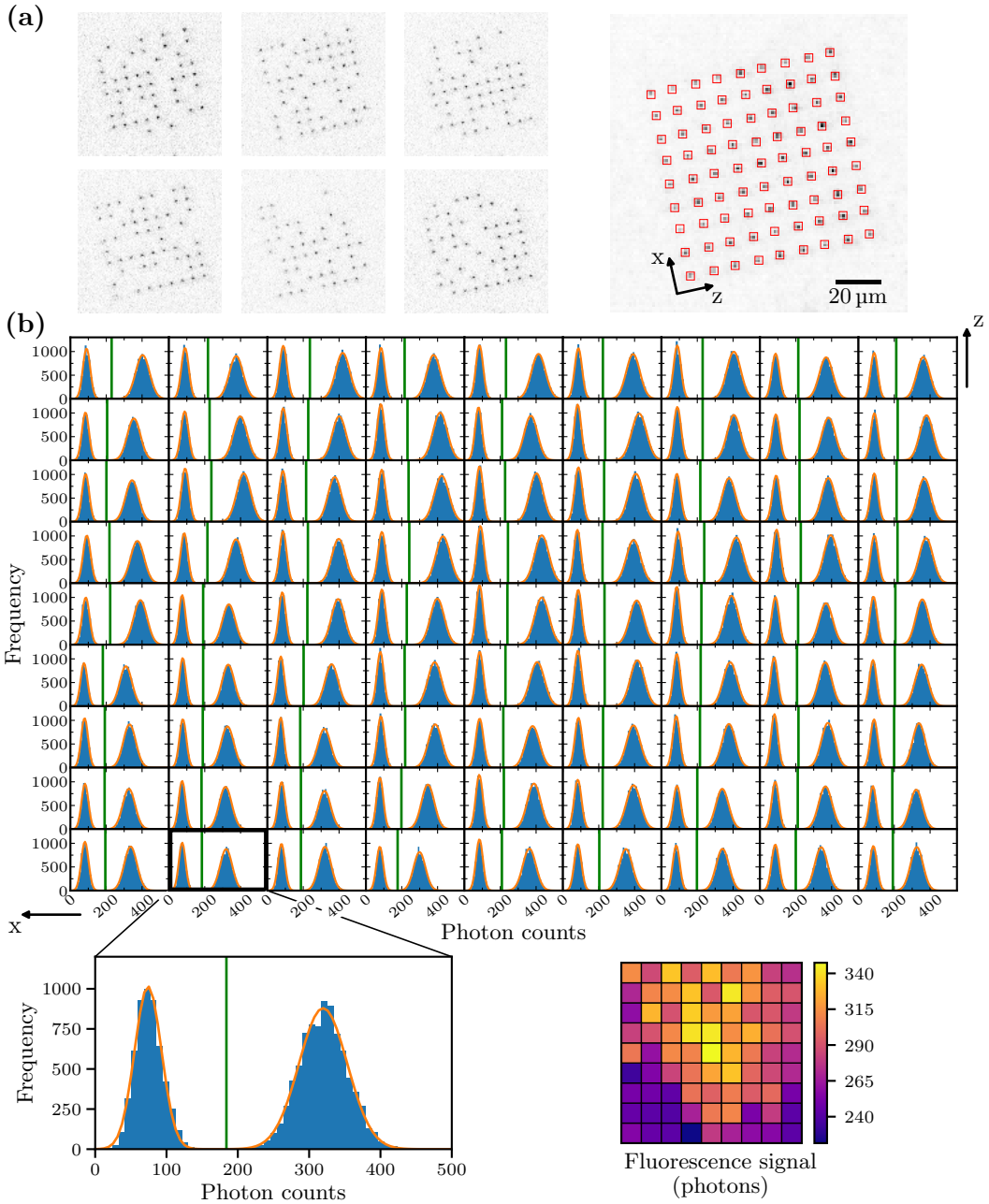

Figure 3.1: (a) Typical images of trapped atoms in a 9×9 array of tweezers spaced by 10 µm. On the right is an accumulation of 100 images from which we position ROIs. The images are oriented as we see them on the camera software. (b) Histograms of the signal measured in each ROI. The lower left histogram is magnified and shows the double gaussian fit of the histogram, along with the threshold as a green vertical line. From this data we infer the loading probability at each trapping site. Note that the orientation is different from that of the camera pictures and corresponds to the physical orientation of the array.

From the parameters of the model 3.2, we can also compute a theoretical loading probability p_{th} as the fraction of the total area that corresponds to the fluorescence peak:

$$p_{\text{th}} = \frac{A_2}{A_1 + A_2}. \tag{3.3}$$

In our experimental conditions, we get a loading probability per site $\langle p_{\text{load}} \rangle = 61.9$ %, $\text{Std}(p_{\text{load}}) = 0.8$ % (from 58 to 63 %). The fluctuations of loading probability are distributed homogeneously among the trapping sites and indicate a good centering of the MOT and the molasses on the tweezers. The signal and loading probability vary from time to time owing to inevitable fluctuations and drift of the experiment, nevertheless we maintain a loading probability > 60 % through all the experiments.

As the background and fluorescence peaks are well separated, the loading probability can also be inferred as the fraction of frames with photon count above a given threshold $\mathcal{T}$:

$$p_{\text{exp}} = \frac{\#(\text{frames with count} > \mathcal{T})}{\#(\text{frames})}. \tag{3.4}$$

We thus compute independent thresholds for each ROI; they are shown as green vertical lines on the histograms of figure 3.1. They serve to discriminate the presence of an atom: a trap is considered loaded with an atom in a given frame if the photon count is above the threshold. The optimal condition for setting the threshold $\mathcal{T}$ is *a priori* to minimize the error rate, that is the sum of false positive and false negative rates, defined respectively as

$$p_{\text{FP}} = \frac{A_1}{\sqrt{2\pi\sigma_1^2}} \int_{\mathcal{T}}^{\infty} e^{-\frac{(n-\mu_1)^2}{2\sigma_1^2}} \mathrm{d}n, \quad p_{\text{FN}} = \frac{A_2}{\sqrt{2\pi\sigma_2^2}} \int_{-\infty}^{\mathcal{T}} e^{-\frac{(n-\mu_2)^2}{2\sigma_2^2}} \mathrm{d}n. \tag{3.5}$$

However, we favor a reduction of false positive rates to decrease the background in the recapture experiments detailed later, thus the threshold is usually shifted towards the fluorescence peak. In practice, we set:

$$\mathcal{T} = 0.55\mu_1 + 0.45\mu_2. \tag{3.6}$$

The loading probability p_{exp} obtained from this threshold is in good agreement with the "theoretical" probability p_{th}, with an absolute difference between the two lower than 0.5 %.

3.1.2 General procedure for data analysis

Apart from simple fluorescence imaging, each run of an experimental sequence involves the recording of two images as shown figure 3.3. A first image comes after loading the atoms, prior to the actual experiment, followed by a second image to assess which atoms are still trapped after the experiment. For each experimental sequence, we compute detection thresholds *a*

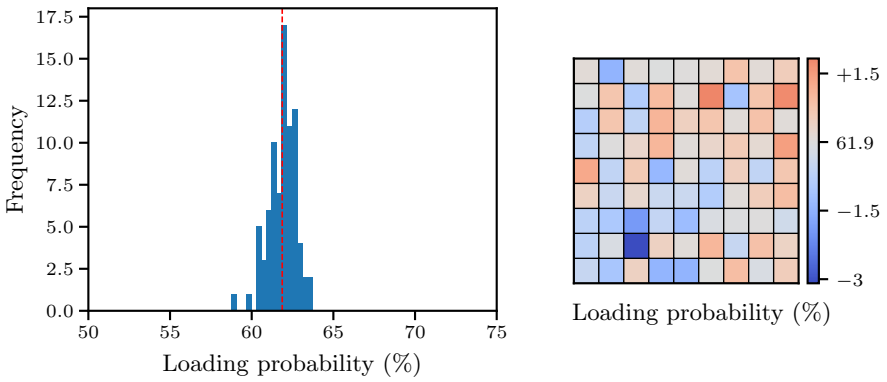

Figure 3.2: Measured loading probabilities according to eq. 3.4. The histogram on the left shows little dispersion, with an outlier having only 58 % loading probability. The mosaic plot on the right reveals the location of this outlier.

posteriori from the histograms built by pooling the fluorescence signal of the first images of each run. Albeit sufficient for the analyses presented in this thesis, it is important to note that detection thresholds could be preset to allow for dynamical detection of atoms, for instance in an atom rearrangement setup.

The recorded signal is converted to an atomic population at each trapping site with the thresholds described previously. The resulting binarized frames, which can be visualized as arrays of booleans, are the basis of all subsequent data treatment. For each experimental run, depending on the presence or absence of atoms in the recorded frames, each trapping site is classified according to the event that occurs:

- A *null* event corresponds to no atom in both frames;
- An *appearance* event corresponds to an atom present in the second frame, albeit absent in the first;
- A *recapture* event occurs when an atom is present in both frames;
- A *loss* event occurs when an atom is present in the first but absent in the second frame.

Such events are determined by simple logical operations on the binarized frames. The recapture/loss events are of most interest to us, and are dependent on the experimental conditions. Except for the lifetime experiment described in the next section, appearance events are not considered during data analysis and occur less than 0.1 % of the time at a given trapping site.

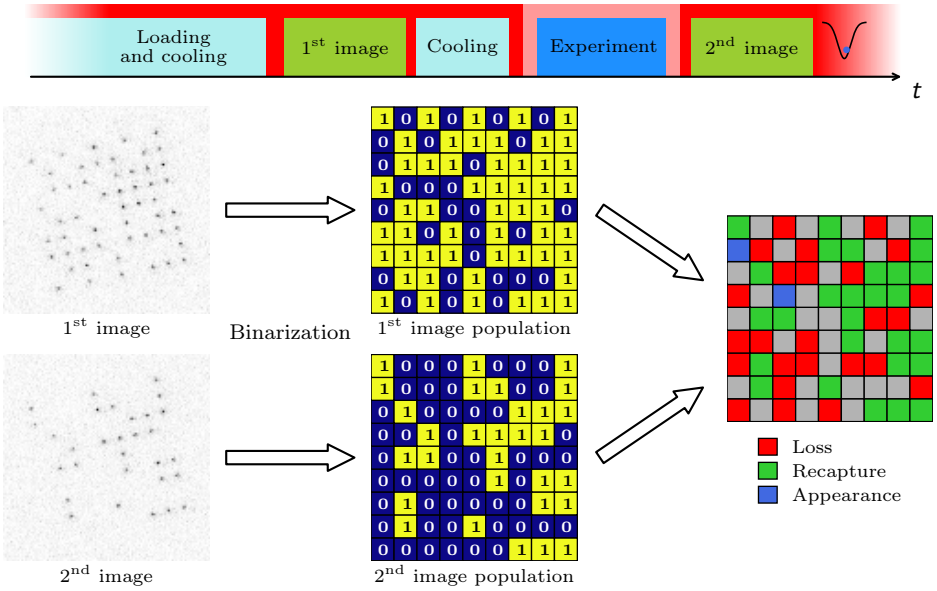

Figure 3.3: General principle of data acquisition by fluorescence imaging. A first image is recorded after loading the tweezers to get prior information of the trap sites that are occupied. A second image is taken after the experiment to determine which sites are occupied. The data treatment process involves the binarization and classification of the trapping sites depending on the event that occurred. The presented data has been selected to show atom appearance events, which are usually exceptional (the probability is about 1 ‰ at each trapping site). In the sequence scheme (and all subsequent ones), the red band represents the optical tweezers. The tweezers are sometimes switched off during an experiment, which we indicate with a lighter color.

Finally, from the data gathered from many repetitions of the experimental run in the same conditions, we estimate the probabilities of the events previously described:

$$p_{\text{appearance}} = P(\text{after} = 1 \,|\, \text{before} = 0) \tag{3.7}$$

$$p_{\text{recapture}} = P(\text{after} = 1 \,|\, \text{before} = 1) \tag{3.8}$$

$$p_{\text{loss}} = P(\text{after} = 0 \,|\, \text{before} = 1) = (1 - p_{\text{recapture}}) \tag{3.9}$$

For each experimental condition, the events are assumed to be samples of independent Bernoulli-distributed variables $X_i \sim \mathcal{B}(p)$. From the N repetitions of the experiment the desired probability p and the standard deviation $\sigma = p(1-p)$ are estimated as:

$$\hat{p} = \sum_i \frac{X_i}{N}, \quad \hat{\sigma} = \hat{p}(1-\hat{p}). \tag{3.10}$$

We therefore obtain recapture (or loss) probabilities in different experimental conditions, usually as a function of a scanned parameter, which can be plotted independently for each trapping site. Further analysis is done by fitting the data and plotting mosaics of the fitted parameters, or by averaging ROI data to improve statistics at the expense of site-resolved information as we will now see.

3.2 Characterization of the tweezers

Proper knowledge of the trapping potential is paramount to the study of the dynamics of trapped atoms. Hence, we first characterize the tweezers effectively generated by the mask imprinted on the SLM. Such a characterization is also a way to assess the efficiency of the tweezer preparation, as improper aberration correction or misalignment would translate into an inhomogeneous array of tweezers.

Assuming gaussian-shaped tweezers, the trapping potential, parameterized by its waist w_0 and depth V_0, is of the form

$$V(r,z) = -V_0 \frac{w_0^2}{w(z)^2} \exp\left(-2\frac{r^2}{w(z)^2}\right), \tag{3.11}$$

where $z_{\text{R}} = \pi w_0^2/\lambda$ is the Rayleigh range, $w(z) = w_0^2\left(1 + (z/z_{\text{R}})^2\right)$ is the waist of the beam at a distance z of the focal plane $z = 0$.

The depth V_0 is proportional to the peak intensity I_0: $V_0 = -\beta_0 I_0$, with β_0 the light shift coefficient of the state $5\text{S}_{1/2}$ introduced in chapter 1. The tweezers also induce different light shift to the $5\text{P}_{3/2}$ states. We get the trap depth from a spectroscopy measurement of the light-shifted transition $\left|5\text{S}_{1/2}, F = 1\right\rangle \longrightarrow \left|5\text{P}_{3/2}, F' = 2\right\rangle$. A measured light shift $\Delta\nu$ is linked to the peak intensity I_0 by

$$\Delta\nu = \frac{(\beta_0' - \beta_0) I_0}{h}, \tag{3.12}$$

with β_0' the light shift induced on the state $\left|5\text{P}_{3/2}, F' = 2\right\rangle$.

The bottom of a gaussian trap can be considered harmonic:

$$V(r,z) \simeq -V_0 + \frac{1}{2}m\omega_r^2 r^2 + \frac{1}{2}m\omega_z^2 z^2, \tag{3.13}$$

with natural frequencies linked to the waist and depth:

$$\omega_r = \sqrt{\frac{4V_0}{m w_0^2}}, \quad \omega_z = \sqrt{\frac{2V_0}{m z_{\text{R}}^2}}. \tag{3.14}$$

3.2.1 Light shift spectroscopy

We determine the trap depth by measuring the light-shift $\Delta\nu$ induced by the tweezers on the transition $\left|5S_{1/2}, F=1\right\rangle \longrightarrow \left|5P_{3/2}, F'=2\right\rangle$ addressed by the "repumper" beam. Figure 3.11 (a) describes the experimental sequence used to probe this transition. We first populate the dark state $\left|5S_{1/2}, F=1\right\rangle$ by shining the detuned cooling beams at the atoms for 20 ms in the absence of repumper. The frequency-tunable repumper beam, switched on for 8 µs with a peak intensity of 1.4 mW cm^{-2}, populates the state $\left|5S_{1/2}, F=2\right\rangle$ when resonant with the probed transition. Finally, a pushing beam resonant with the cycling transition $\left|5S_{1/2}, F=2\right\rangle \longleftrightarrow \left|5P_{3/2}, F'=3\right\rangle$ is applied for 4 µs, with the tweezers switched off. Its peak intensity is much higher than the saturation intensity, and those atoms that have been effectively repumped back to $\left|5S_{1/2}, F=2\right\rangle$ by the repumper pulse are kicked out of the trapping region and are not recaptured. We thus get a dip in the recapture probability that corresponds to the resonance we are looking for.

We first calibrate the zero of light shift by switching the tweezers off during the repumper pulse. This gives us the natural transition to which we compare the light-shifted frequency. The results are presented figure 3.4 (c). We fit the recapture probabilities with a lorentzian

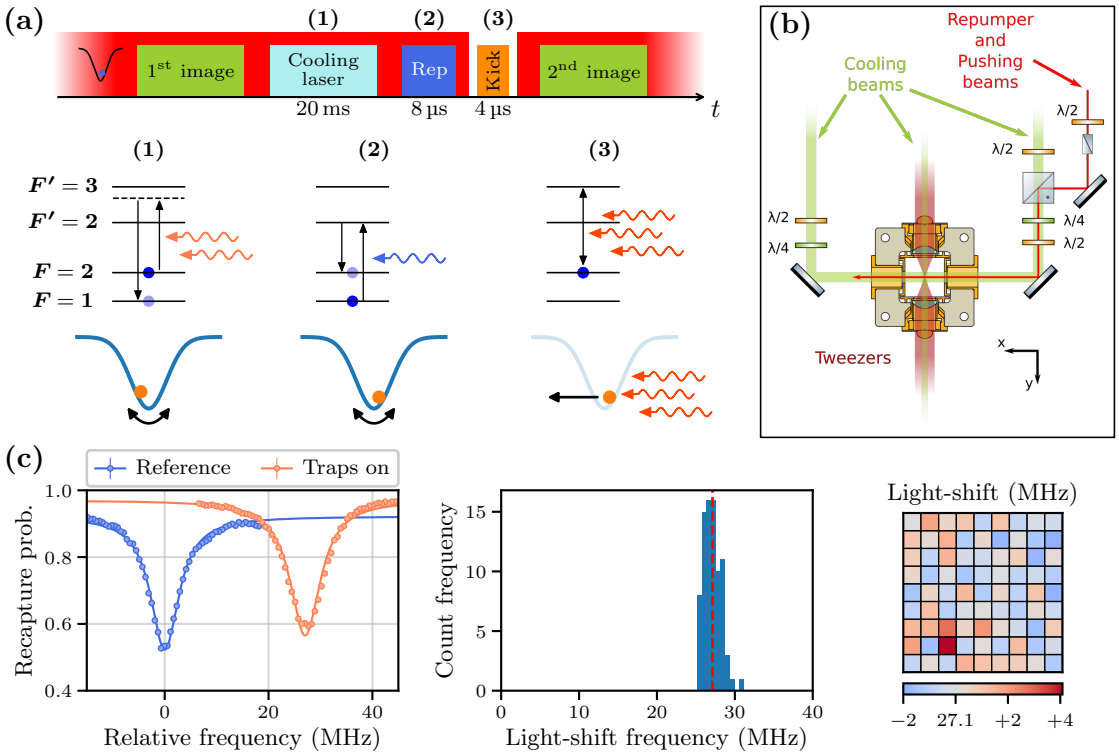

Figure 3.4: Lightshift spectroscopy experiment. (a) Principle of the sequence. (1) The atoms are first de-pumped to $\left|5S_{1/2}, F=1\right\rangle$ with the cooling beams in the absence of the repumper beam; (2) the repumper transfers the population toward $\left|5S_{1/2}, F=2\right\rangle$; (3) a pushing beam resonant with the $\left|5S_{1/2}, F=2\right\rangle \longleftrightarrow \left|5P_{3/2}, F'=3\right\rangle$ transition expels the $\left|5S_{1/2}, F=2\right\rangle$ population from the trapping region. (b) Optical setup for the light-shift spectroscopy experiment. (c) Experimental results. Left: the reference and light-shifted average recapture probability, fitted with a lorentzian peak. Center: histogram of the measured frequencies. Right: site-resolved map. Note that the outlier site of figure 3.2 presents a significantly higher light-shift (+4 MHz)

peak, the theoretical line shape. As expected, all the individual trapping sites give the same peak frequency for the reference spectrum, with inter-site fluctuations of 0.18 MHz, very close to the fit uncertainty, 0.17 MHz. We get a light shift $\langle \Delta\nu \rangle = 27.1\,\mathrm{MHz}$, $\mathrm{Std}(\Delta\nu) = 1.1\,\mathrm{MHz}$, equal to the one deduced from the fit of the pooled data. The width of the peaks is $7.0 \pm 0.6\,\mathrm{MHz}$ for the reference spectrum and $7.2 \pm 0.4\,\mathrm{MHz}$, to be compared with the natural linewidth $\Gamma = 2\pi \cdot 6.065\,\mathrm{MHz}$. This broadening is due to the repumper intensity: we observed that increasing the power of the repumper during this sequence leads to a broader peak.

Figure 3.4 (c) also shows the distribution and spatial map of light-shift frequencies. Apart from two extreme values, the light-shifts are centered on the average value of 27.1 MHz. It is interesting to note that the maximal value corresponds to the site with the lowest loading probability, as seen in figure 3.2.

To conclude, we can convert these frequency measurements into the more intuitive quantities that are the peak intensity I_0 and trap depth V_0. We get:

$$\langle I_0 \rangle = 1.14\,\mathrm{mW\,\mu m^{-2}}, \quad \mathrm{Std}(I_0) = 0.05\,\mathrm{mW\,\mu m^{-2}}, \tag{3.15a}$$

$$\langle V_0 \rangle = k_\mathrm{B} \times 990\,\mu\mathrm{K}, \qquad \mathrm{Std}(V_0) = k_\mathrm{B} \times 42\,\mu\mathrm{K}. \tag{3.15b}$$

3.2.2 Oscillations in the trap

The second trap characterization is the determination of their natural frequencies. Assuming a gaussian trap potential, the axial frequency can be expressed as a function of the radial frequency. We measure the latter by inducing oscillations of the atoms in the trap, looking at the recapture probability after releasing them for a short duration. The detail of the sequence is given figure 3.5 (a). The atoms begin to oscillate after blinking the trap for 6 µs, and do so for a variable duration before being released again for 20 µs. The first release allows the atoms to reach the borders of the trap, increasing the amplitude of oscillations when the trap is switched back on. After the oscillation delay, the second release leads to two scenarios. If the atoms are at the edges of the trap, hence have minimal velocity, they almost don't move and are recaptured with high probability. This situation corresponds to the top panel. However, if they stand at the center of the trap, with maximal velocity, they leave during the release period and are lost, as shown in the bottom panel. This leads to a recapture probability oscillating at twice the trap frequency. It is important to note that the optimal release durations are dependent on the atomic temperature. Anticipating the results of the next section, these parameters were adjusted for a temperature of 14 µK.

The recapture probability averaged over all trapping sites is presented in figure 3.5 (b). It highlights some general characteristics of the oscillation of atoms in the traps. A first observation is that the recapture probability never goes below a level of approximately 20 %. This is due to the fact that the portion of atoms that have a low energy (*i.e.* a low velocity at the bottom of the trap) are insensitive to the releases and stand undisturbed at the center of the trap for the whole sequence. Secondly, the regions of high recapture probability are sharper than the low recapture probability regions. This is explained as follows. The timings giving high recapture rates are those for which the atoms have minimal velocity, therefore are at the edge of the trap. In this situation a small residual velocity is sufficient to allow them to travel outside the trapping region as they have already gone a part of the way, thus causing the sensitivity to the timing of the second release. Finally, the damping at long oscillation times is due to both inhomogeneities in the oscillation frequencies of the various traps and their anharmonicity. The latter effect can be seen in the simulation of figure 3.5 (a). The atoms start the central oscillation period with roughly the same phase and a slightly larger

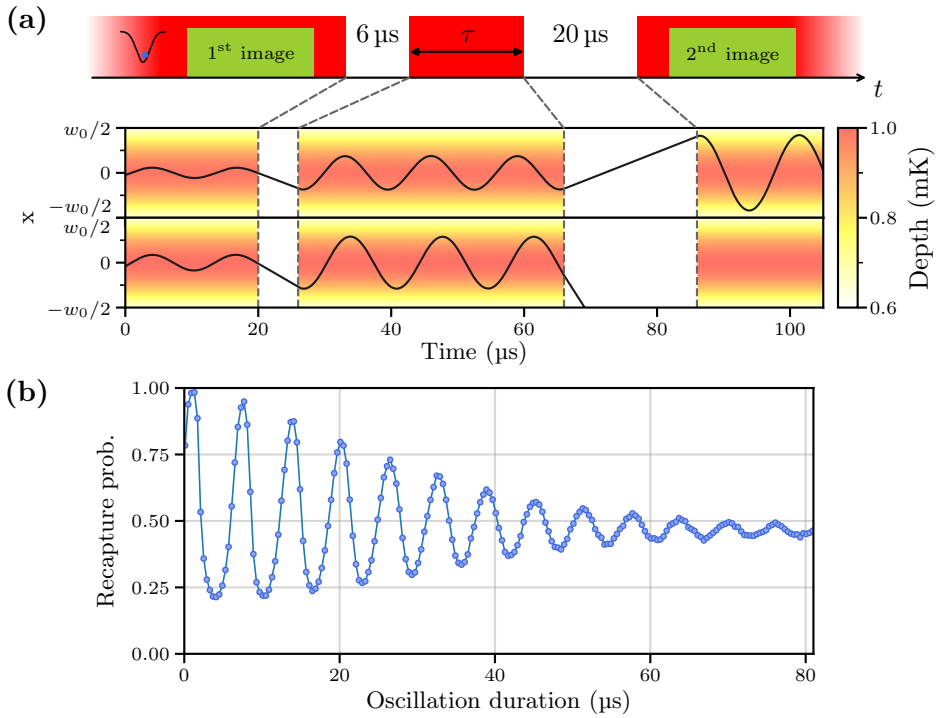

Figure 3.5: Measurement of the trap frequencies. (a) Top: Scheme of the sequence. Bottom: simulated trajectories highlighting the behavior of the atoms (only the evolution of the x coordinate is shown). Trapped atoms are first released for 6 µs, then recaptured for a variable time, during which they oscillate in the trap. A second release for 20 µs allows fast atoms to leave while short enough to keep the slow atoms. The simulations were carried with the measured trap parameters (eq. (3.19)) and temperature $T = 14\,\mu\text{K}$). (b) Measured recapture probability averaged over all trapping sites.

amplitude in the bottom panel. The accumulation of a phase is manifest and yields two completely different outcomes when released.

The regularity of the averaged recapture probability hides the important heterogeneity of oscillations observed in individual traps. This is highlighted in figure 3.6 (a) in which we present the array of 9×9 individual signals. We identified three general main oscillation patterns and selected archetypal signals that appear framed with a red box. Those are reported in large in the top panels of figure 3.6 (b), along with the corresponding Fourier power spectra[2] in the bottom panels. The left graph shows a regular oscillation slowly damping toward 50 % recapture probability over more than 100 µs, with a sharp peak at 164 kHz on the corresponding spectrum. The signal of the central graph shows a beat pattern with an envelope similar to the left graph, that manifests itself as two peaks at 163 and 176 kHz in the Fourier spectrum. This can be interpreted *a priori* as an anisotropy of the trap (giving rise to an elliptic beam), having slightly different transverse frequencies. The last signal presented on the right graph decays in less than 50 µs, with weak oscillations persisting for more than 100 µs. The corresponding Fourier spectrum is harder to interpret, having three peaks at 157, 163 and 168 kHz. Let us mention that none of the signals yield a peak around 20 kHz, the expected axial frequency, on the Fourier spectra.

[2]The signal has its mean subtracted before taking the Fourier transform to suppress an otherwise dominant (and irrelevant) component at zero frequency.

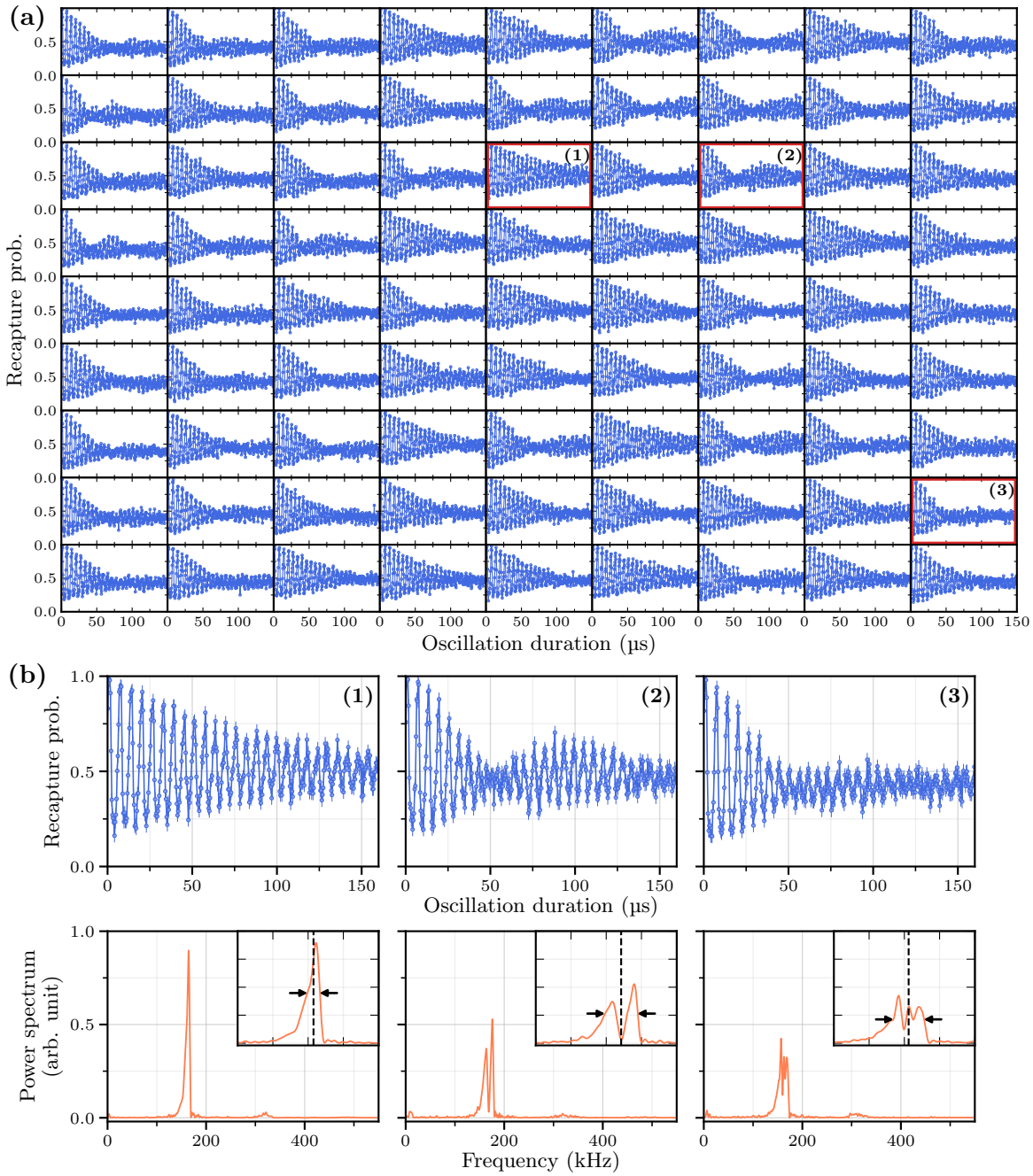

Figure 3.6: Site-resolved oscillations in the traps. (a) Detail of the individual oscillation signals, with three archetypal behaviors highlighted with a red box. (b) The selected signals are magnified in the top panels. They show from left to right a damped oscillation at a single frequency, a damped oscillation with two beating frequencies and a quickly decaying oscillation. We recover an effective frequency from the discrete Fourier power spectra (bottom panels) by the method given in the text.

A more detailed analysis of these results, with attempts to account for the observed behaviors with Monte-Carlo simulations, is given in appendix D.

Let us now describe the retained analysis procedure for such complex signals. The data indicate that the exact shape of the tweezers is only approximately gaussian and an exhaustive

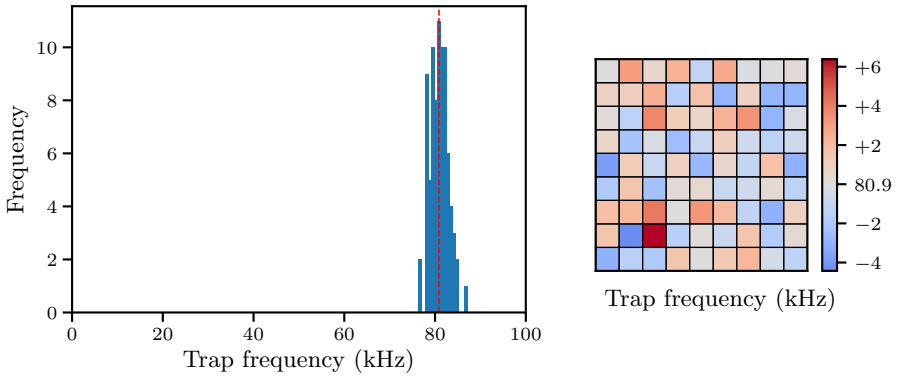

Figure 3.7: Histogram and color map of the individual trap frequencies. Note that the outlier observed in figures 3.2 and 3.4 also presents a higher trap frequency.

description of the latter is out of reach. We therefore focus on getting the best gaussian approximation of the traps to estimate their spatial extension and power. This amounts to reduce the oscillation to a single frequency from which we deduce the waist according to equation 3.14.

A radial trap frequency is obtained from the power spectrum $S(f)$ of the oscillations by computing $f_{\min}$ and $f_{\max}$ as:

$$f_{\min} = \min_f \left\{ S(f) = \frac{\max S}{2} \right\}, \quad f_{\max} = \max_f \left\{ S(f) = \frac{\max S}{2} \right\}. \tag{3.16}$$

Intuitively, these quantities point at the half maximum of the peak structure, to which we associate an effective full width at half maximum $f_{\max} - f_{\min}$. The values are pointed by arrows on the magnified peaks in the insets of the spectra of figure 3.6. The effective oscillation frequency f_{osc}, indicated as a dotted line, is then set as the average of $f_{\min}$ and $f_{\max}$:

$$f_{\text{osc}} = \frac{f_{\min} + f_{\max}}{2}. \tag{3.17}$$

We thus obtain the desired trap frequency $f_{\text{trap}} = f_{\text{osc}}/2$. The individual values are presented figure 3.7 with $\langle f_{\text{trap}} \rangle = 80.9\,\text{kHz}$, $\text{Std}(f_{\text{trap}}) = 2.0\,\text{kHz}$.

3.2.3 Trap parameters

From the knowledge of the maximum intensity I_0 and the radial frequency f_{trap} of a gaussian tweezer, we recover the waist w_0 and total power P_0 as:

$$w_0 = \sqrt{\frac{\beta_0 I_0}{m\pi^2 f_{\text{trap}}^2}}, \quad P_0 = \frac{\pi}{2} I_0 w_0^2. \tag{3.18}$$

Using the measurements of the previous sections, we obtain:

$$\langle w_0 \rangle = 1.21\,\mu\text{m}, \quad \text{Std}(w_0) = 0.01\,\mu\text{m}, \tag{3.19a}$$
$$\langle P_0 \rangle = 2.62\,\text{mW}, \quad \text{Std}(P_0) = 0.12\,\text{mW}. \tag{3.19b}$$

The waists thus obtained are effective parameters encompassing the spatial extension of the tweezers. Nevertheless, they show very little dispersion of less than 1 %. This uniformity

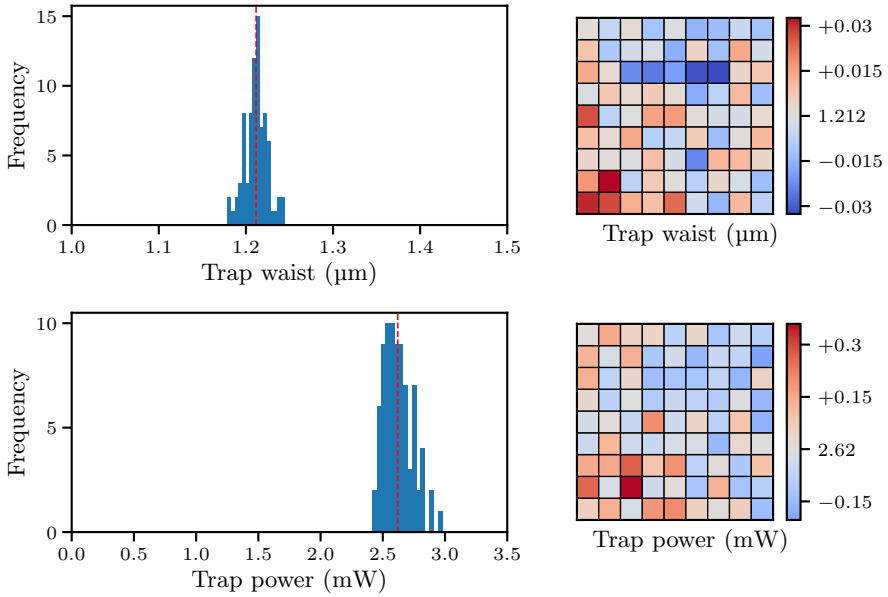

Figure 3.8: Histogram and color map of the individual trap parameters computed from equation 3.19.

in size indicates that the aberrations are well compensated over the explored lens field of 80 µm. Indeed, aberrations tend to deform the traps, effectively increasing their size. This effect being more pronounced at the edges of the lens field, improper aberrations correction would is expected to lead to higher dispersion in the traps size. The power per trap shows more dispersion, of the order of 5 %.

Inspection of the individual trapping site data presented in figure 3.8 shows that the waists are higher than average in the lower left corner of the array. This can be interpreted in view of the previous remark as an imperfect correction of aberrations in this region. The power per trap shows the same tendency to increase in the lower left corner. The outlier trapping site mentioned throughout this chapter appears to have more than 10 % higher power than the others, with average waist.

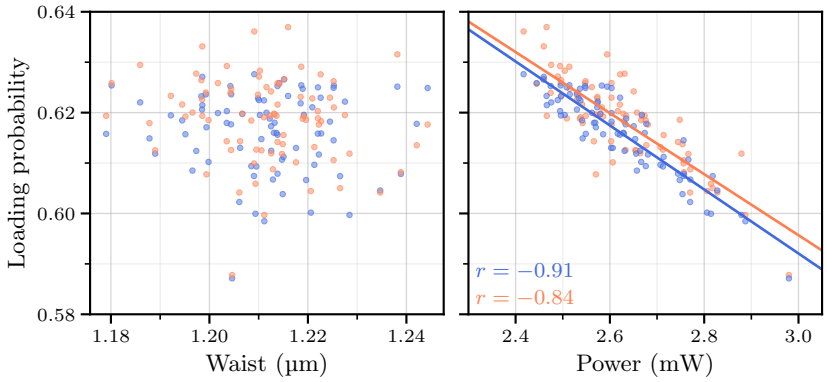

Figure 3.9: Correlation between the trap parameters and the loading probability obtained from the measurement of oscillation in the traps (blue) and light-shift spectroscopy (orange). The loading probability is well correlated to the trap power but not to the waist. The solid lines indicate the linear relationship between the power and the loading probability. We also indicate the corresponding Pearson's correlation coefficients.

To conclude, let us mention the correlation between the loading probability and the trap power. Figure 3.9 shows scatter plots of the loading probability versus the waist (left panel) and the power (right panel). Since the trap characterization involves two distinct measurements, we have two sets of loading probabilities, one from the light shift spectroscopy (light green) and one from the trap oscillation measurement (magenta). Although there is clearly no correlation between the waist and loading probability, a linear regression reveals a strong correlation between the power and the loading probability for the spectroscopy and the trap oscillation data. The respective (Pearson's) correlation coefficients are -0.83 and -0.91.

3.3 Atoms in tweezers

We turn to the two measurements pertaining to the behavior of atoms in tweezers: the lifetime and temperature. The latter is usually determined on a day-to-day basis and depends on the experimental conditions. The results of this section rather serve to illustrate the methodology.

3.3.1 Lifetime in the trap

We measure the lifetime of atoms in the trap by simply waiting for a variable delay between the two fluorescence images, as described in figure 3.10 (a). Two main mechanisms affect the lifetime of atoms in the trap [131]. The first mechanism is the heating of atoms inside the trap. Many factors influence this heating, including the scattering of the light that generates the trap (and also near-resonant residual light) and fluctuations of the trap intensity and position. The second mechanism is the collision with surrounding atoms. Assuming only collisions at a rate $1/\tau$ with the residual gas, this leads to a survival probability at time t:

$$P_{\text{surv}}(t) = \exp(-t/\tau). \tag{3.20}$$

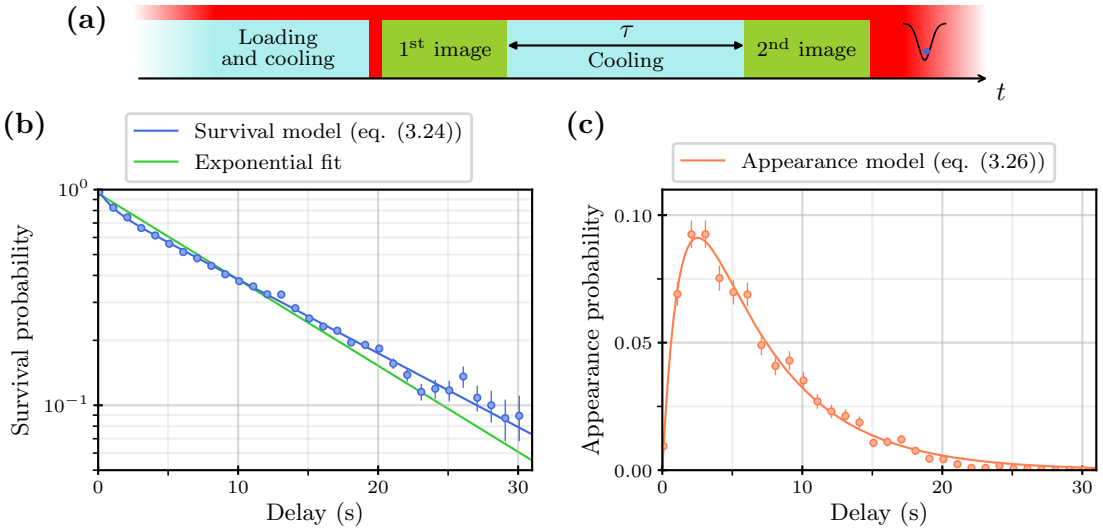

Figure 3.10: Lifetime measurement experiment. (a) Scheme of the sequence. (b) Average recapture probability. (c) Average appearance probability.

We maintain the molasses cooling during the experiment to suppress the contribution of atomic heating to the lifetime. The measured recapture probability $P_{\text{recapture}}$ is presented in

figure 3.10 (b). A simple fit with the model of eq. (3.20) is only in qualitative agreement with the data, especially at short delays when the recapture probability decreases faster than expected. This can be understood by taking into account the contribution from surrounding molasses-cooled atoms which can be captured in a trap. This leads to two phenomena: the discharge due to light-assisted collisions [136, 137] of a trap that was already loaded and the loading of a trap that was empty.

To get a more quantitative insight, let us first assume that the atomic density $n_{\mathrm{mol}}(t)$ in the molasses surrounding the tweezers is proportional to a decaying exponential. This results in a probability density $p_{\mathrm{load}}(t)$ to load an atom at time t:

$$n_{\mathrm{mol}}(t) \propto e^{-\frac{t}{\tau_{\mathrm{load}}}}, \quad p_{\mathrm{load}}(t) = \frac{A}{\tau_{\mathrm{load}}} e^{-\frac{t}{\tau_{\mathrm{load}}}}, \tag{3.21}$$

where τ_{load} is the lifetime of the molasses and $0 < A \leq 1$ is an empirical parameter to be fitted from the data.

In the case of a loaded trap, such an event in which an additional atom gets trapped leads to the emptying of the trap. The infinitesimal variation of P_{surv} is

$$P_{\mathrm{surv}}(t + \mathrm{d}t) = P_{\mathrm{surv}}(t) \left(1 - \frac{\mathrm{d}t}{\tau} - \mathrm{d}t \frac{A}{\tau_{\mathrm{load}}} e^{-\frac{t}{\tau_{\mathrm{load}}}}\right), \tag{3.22}$$

where the first contribution to the variation comes from the possible collision with the residual gas and the second contribution stems from the loading of an atom from the molasses. This yields the following differential equation satisfied by P_{surv}:

$$\frac{\mathrm{d}P_{\mathrm{surv}}}{\mathrm{d}t}(t) = \left(-\frac{1}{\tau} - \frac{A}{\tau_{\mathrm{load}}} e^{-\frac{t}{\tau_{\mathrm{load}}}}\right) P_{\mathrm{surv}}(t). \tag{3.23}$$

After integration and proper normalization, we obtain:

$$P_{\mathrm{surv}}(t) = \exp\left(-\frac{t}{\tau} + A(e^{-\frac{t}{\tau_{\mathrm{load}}}} - 1)\right). \tag{3.24}$$

The data of figure 3.10 (b) are in very good agreement with eq. (3.24), with fitted survival time $\tau = 12.6 \pm 0.2\,\mathrm{s}$ and loading time $\tau_{\mathrm{load}} = 0.84 \pm 0.18\,\mathrm{s}$. The fit also gives a value $A = 0.166 \pm 0.013$ for the empirical parameter introduced.

In the case of an empty trap, the loading of an atom leads to an atom appearance event, as described in section 3.1.2. The probability of such an event is presented figure 3.10 (c). Qualitatively, we observe an initial increase as the surrounding atoms get more time to load the trap, followed by an exponential decay with a characteristic survival time. The observation of an atom at time t (conditioned to the absence at $t = 0$) is therefore the combination of two events: the loading of an atom at time t' such that $0 < t' < t$ and its survival from t' to t. This gives, after integrating over t',

$$P_{\mathrm{gen}}(t) = \int_0^t p_{\mathrm{load}}(t') P_{\mathrm{surv}}(t, t') \mathrm{d}t'. \tag{3.25}$$

Substituting $P_{\mathrm{surv}}(t, t') \simeq \exp\left(-\frac{t-t'}{\tau}\right)$ and integrating we get:

$$P_{\mathrm{gen}}(t) = A \frac{\tau}{\tau - \tau_{\mathrm{load}}} \left(e^{-\frac{t}{\tau}} - e^{-\frac{t}{\tau_{\mathrm{load}}}}\right). \tag{3.26}$$

Fitting the probability of appearance with the model of eq. (3.26) yields $A = 0.140 \pm 0.005$ and $\tau_{\text{load}} = 1.28 \pm 0.11\,\text{s}$, which are close to the values obtained from the measured recapture probability, 0.166 ± 0.013, and $0.84 \pm 0.18\,\text{s}$, respectively. We however get $\tau = 5.81 \pm 0.28\,\text{s}$, two times smaller than the value of $12.6 \pm 0.2\,\text{s}$ found previously. This indicates another loss mechanism for those atoms that are loaded in the trap during the delay between the two images.

3.3.2 Atom temperature

A last experiment pertaining to the behavior of the atoms trapped in gaussian tweezers is the measurement of their temperature. This is done with a *release-recapture* [134] experiment depicted in figure 3.11 (a)-(b). The atoms are first prepared and cooled by an optical molasses before switching the tweezers off for a variable delay, during which the atoms move freely. At the end of the delay, the tweezers are switched on, recapturing those atoms which are close to the center of the trap, thus having low enough energy.

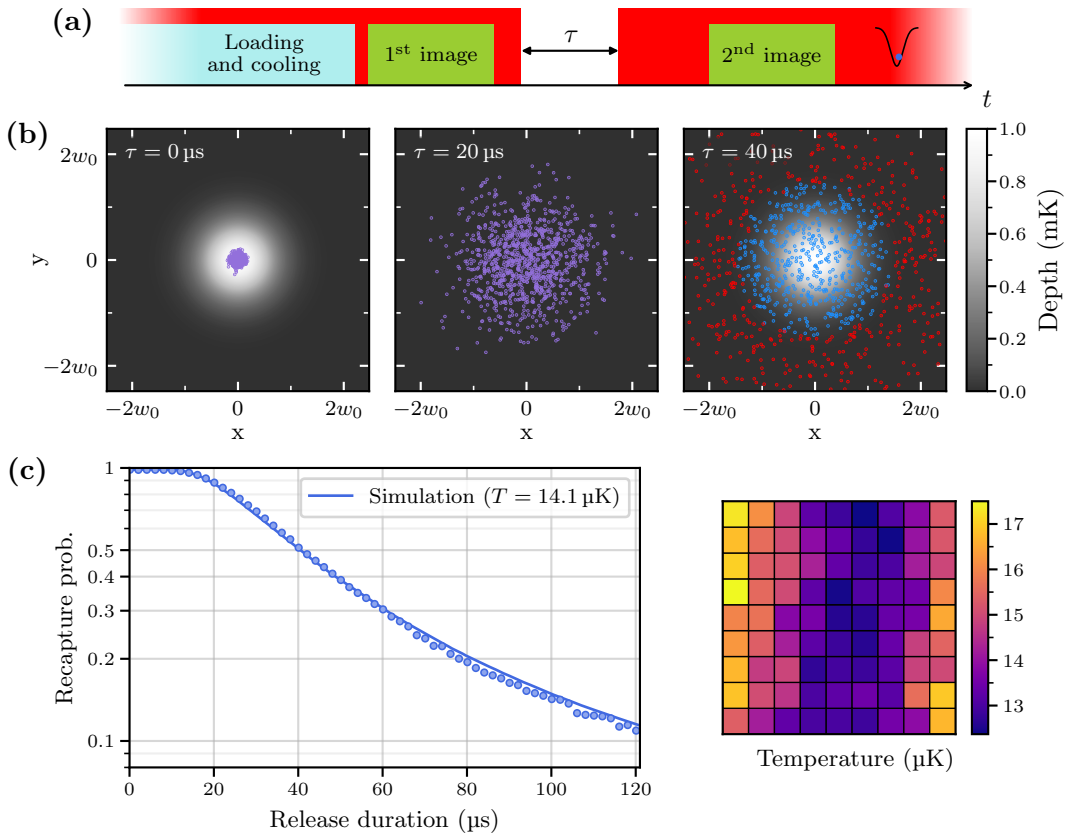

Figure 3.11: Release-recapture experiment for temperature measurement. (a) Scheme of the sequence. (b) Snapshots of a sample of 1000 atomic positions obtained from Monte-Carlo simulations for various release durations, from left to right: 0 µs, 20 µs, 40 µs. At the end of the release period, the tweezers recapture only those atoms depicted in blue. The simulations were carried with the measured trap parameters (eq. (3.19)) and temperature. (c) Experimental results. Left: measured average recapture probability as a function of the release duration; the simulated curve shown corresponds to a fitted temperature of $14.1 \pm 0.1\,\mu\text{K}$. Right: site-resolved temperatures obtained from the Monte-Carlo fitting procedure of individual trapping sites data, revealing a significant inhomogeneity in atomic temperatures.

Monte-Carlo simulations of the atom dynamics are carried to fit the temperature of the atoms. Samples of initial atomic positions and velocities are drawn according to a Maxwell-Boltzmann distribution:

$$\rho_{\mathbf{r}}(x,y,z) \propto \exp\left(-\frac{V(x,y,z)}{k_{\mathrm{B}}T}\right), \quad \rho_{\mathbf{v}}(v_x,v_y,v_z) \propto \exp\left(-\frac{m(v_x^2+v_y^2+v_z^2)}{2k_{\mathrm{B}}T}\right). \tag{3.27}$$

We use the harmonic approximation of eq. (3.13) for the trap potential, which we parameterize by the average values of the waist and depth found previously:

$$w_0 = 1.21\,\mu\mathrm{m}, \quad V_0 = k_B \times 990\,\mu\mathrm{K}. \tag{3.28}$$

The determination of the temperature thus assumes that the different trapping sites are the same and correspond to the average "best gaussian" approximation. After evolution in free space for a duration τ, the fraction of recaptured atoms is determined. The recapture condition is that the mechanical energy is negative:

$$E_{\mathrm{m}} = \frac{1}{2}m\mathbf{v}^2(\tau) + V[\mathbf{r}(\tau)] < 0. \tag{3.29}$$

The recapture probabilities $p_{\mathrm{sim}}(t_i)$ simulated at various delays t_i for a given temperature T can be compared with experimental recapture probabilities $p_{\mathrm{exp}}(t_i)$ (having estimated uncertainties $\sigma_{\mathrm{exp}}(t_i)$) by computing the χ^2 distance:

$$\chi^2 = \sum_i \frac{(p_{\mathrm{exp}}(t_i) - p_{\mathrm{sim}}(t_i))^2}{\sigma^2_{\mathrm{exp}}(t_i)}. \tag{3.30}$$

To estimate the temperature, simulations are carried for a list of temperatures T_i to obtain values $\chi^2(T_i)$. The non-negligible sampling noise in the latter is mitigated by fitting with a polynomial to obtain the position of the minimum, $\hat{T}$. The uncertainty in the estimated temperature, $\hat{\sigma_T}$, is given by the formula [138]:

$$\hat{\sigma}_T^2 = 2\left[\frac{\mathrm{d}^2\chi^2}{\mathrm{d}T^2}\right]^{-1}_{\hat{T}} \frac{\chi^2(\hat{T})}{k}, \tag{3.31}$$

where k is the number of degrees of freedom, that is, $k = n - p$ with n the number of data points taken and $1 \leq p \leq 3$ is the number of fitted parameters (the temperature, along with optional global scale and offset). The detail of the simulations and fitting procedure, along with a discussion on the validity of the previous approximations, is given in appendix D.

The results are presented figure 3.11 (c). Despite the averaging over many trapping sites (and many trap shapes), the global recapture probability is well fitted with the Monte-Carlo procedure, yielding a temperature of $14.1 \pm 0.1\,\mu\mathrm{K}$. The fitting of individual trapping site data gives a temperature $\langle T \rangle = 14.3\,\mu\mathrm{K}$, $\mathrm{Std}(T) = 1.4\,\mu\mathrm{K}$, revealing significant inhomogeneity in the fitted temperatures. The latter inhomogeneity is further highlighted by the mosaic plot of the temperatures shown in the right panel of figure 3.11 (c). There is a clear tendency to have cooler atoms along the vertical in the center of the array. The reason for this pattern is unclear, and does not correlate to any of the trap parameters studied previously[3].

[3]One could think that the observed pattern is an artifact from the compensation of trap parameters inhomogeneity by the fitting procedure.

Conclusion

The preparation of optical tweezers being new to our team, we described here the characterizations carried on the gaussian traps for ground-state atoms. The results presented in this chapter were obtained with an array of 9×9 traps with 10 µm spacing.

The fluorescence signal emitted by trapped atoms allowed us to discriminate their presence at each trapping site. In the 25 ms of imaging, we detect approximately 300 photons scattered from one atom. This allowed us to establish detection thresholds and binarize the data. We obtained an average loading probability of 60% per trap. From the comparison of frames acquired before and after the actual experiment, our analysis procedure consists in computing basic statistics such as the probability of recapture for an atom at each trapping site.

We characterized the gaussian traps by measuring on the one hand the light-shift induced on the transition $\left|5\mathrm{S}_{1/2}, F = 1\right\rangle \longrightarrow \left|5\mathrm{P}_{3/2}, F' = 2\right\rangle$ by spectroscopy and on the other hand the trap frequency from a release-recapture experiment. The spectroscopy gave a depth (averaged over all trapping sites) $\langle V_0 \rangle = 990\,\mu\mathrm{K}$. We measured (also on average) a trap frequency of $\langle f_{\mathrm{trap}} \rangle = 80.9\,\mathrm{kHz}$. From these values we recovered the waist w_0 and the power P_0:

$$\langle w_0 \rangle = 1.21\,\mu\mathrm{m}, \quad \langle P_0 \rangle = 2.62\,\mathrm{mW}.$$

These values were found to be relatively homogeneous among the 81 traps, with a dispersion of about 1% for the waist and 5% for the power.

We reported lifetime of $12.6 \pm 0.2\,\mathrm{s}$ for ground-state atoms in the tweezers. To conclude we determined the temperature with a release-recapture experiment: we measured the recapture probability after releasing the atoms for a variable time. The data was fitted by running a series of Monte-Carlo simulations for a sequence of temperatures and computing the mean squared error. A polynomial fit of the latter yielded the temperature at its minimum. We thus obtained an average temperature $\langle T \rangle = 14.3\,\mu\mathrm{K}$. The spatially-resolved map of temperatures revealed a strong inhomogeneity, the atoms being cooler along a vertical band located at the center.

These characterizations, and most notably the temperature measurement, set the stage for circular states trapping. We therefore turn to the topic of their preparation.

Chapter 4

Preparation of circular states

"Would you tell me, please, which way I ought to go from here?"
"That depends a good deal on where you want to get to," said the Cat.
"I don't much care where -" said Alice.
"Then it doesn't matter which way you go," said the Cat.
"- so long as I get SOMEWHERE," Alice added as an explanation.
"Oh, you're sure to do that," said the Cat, "if you only walk long enough."

— Lewis Carroll, *Alice in Wonderland*

We now turn to the preparation of circular Rydberg states from ground state atoms trapped in gaussian tweezers. Previous calculations [90] have shown the levels $|48\mathrm{C}\rangle$ and $|50\mathrm{C}\rangle$ to be good candidates to embody the spin states of the prospected quantum simulator. However, in line with previous work [96], we choose to prepare the $n = 52$ circular state to demonstrate the trapping and in the longer term study dipole-dipole interaction with $|50\mathrm{C}\rangle$. Although the circularization procedure has previously been described extensively [98, 96], we adapted it and optimized each step to maximize the preparation efficiency. The latter must be as high as possible to improve the signal and in the longer term minimize the occurrence of defects in the simulator. This involves careful control of each of the four steps of the new preparation process depicted in figure 4.1:

(1) We introduced in this work a first stage of optical pumping to transfer the initial atomic populations to the state $\left|5\mathrm{S}_{1/2}, F = 2, m_F = 2\right\rangle$. This step is of paramount importance for the circularization efficiency since only the pumped state is addressed by the excitation lasers of the second stage.

(2) The Rydberg excitation to the state $\left|52\mathrm{D}_{5/2}\right\rangle$ is carried via a two-photon excitation. However, we now use $\left|6\mathrm{P}_{3/2}\right\rangle$ as the intermediate state instead of $\left|5\mathrm{P}_{3/2}\right\rangle$, which allows us to reach higher Rabi frequencies and perform coherent excitation.

(3) The third stage consists in the transfer of population from $\left|52\mathrm{D}_{5/2}\right\rangle$ to the state $|52\mathrm{F}\rangle$ that branches, when the electric field is applied, to the state suitable for the last step.

(4) The fast adiabatic transfer, introduced in chapter 1, is carried in the same way as we used to, yet with a new radio-frequency setup.

The directing magnetic field (along the x direction) is set constant during the whole sequence. Its orientation defines the quantization axis for the ground state and low-l Rydberg

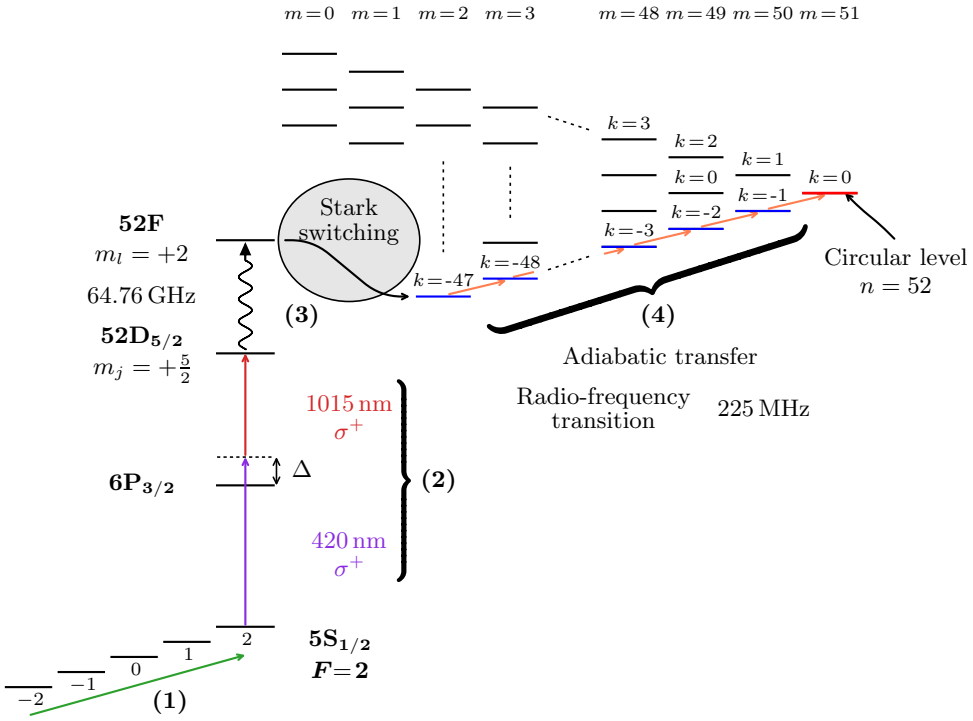

Figure 4.1: Preparation of circular states. (1) Optical pumping; (2) Laser excitation; (3) Microwave transfer; (4) Adiabatic transfer.

states. The electric field is applied before the circularization and defines the quantization axis during the circular Rydberg experiment.

We take advantage of the two detection methods at our disposal for the optimization of each step. Fluorescence imaging gives us spatially resolved information and is insensitive to the presence of surrounding atoms potentially excited to Rydberg state. In practice, we use imaging to probe the first preparation steps and to demonstrate the trapping of Rydberg states, as it requires prior information on the localization of atoms. State-selective field ionization, on the other hand, gives us a snapshot of the populations of different Rydberg states in the experiment at any given time. It is therefore involved in the detection of circular states, be it for various optimizations or lifetime measurements presented in the next chapter.

We conclude the chapter with the characterization of the state purity and the estimation of the preparation efficiency in our room temperature environment. This is done with the help of a spectroscopy measurement between circular states.

4.1 Preparation of 52D

The first step toward the preparation of circular states is the laser excitation from the state $\left|5S_{1/2}, F = 2, m_F = +2\right\rangle$ to $\left|52D_{5/2}, m_j = +5/2\right\rangle$. The degeneracy between the different m-sublevels is lifted by a constant magnetic field present during the whole sequence. The Rydberg excitation is done by addressing a two-photon transition with $\left|6P_{3/2}\right\rangle$ as the intermediate state. To maximize the transfer efficiency, we first pump ground state atoms into the $m = +2$ sub-level. The optical pumping is optimized by probing the Zeeman levels population using Raman spectroscopy. Figure 4.2 shows the optical setup involved in the preparation of $|52D\rangle$.

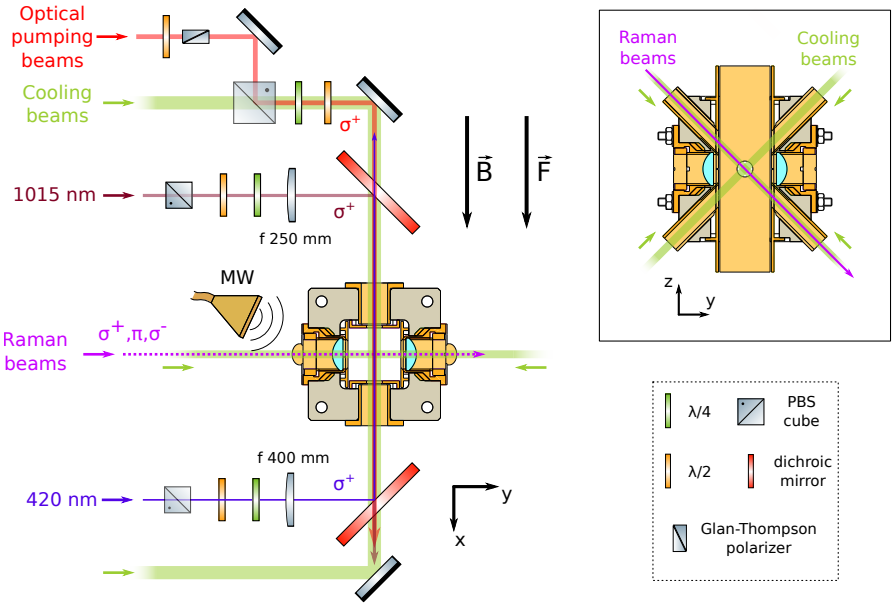

Figure 4.2: Optical setup for the optical pumping and Rydberg excitation. The microwave horn involved in further state manipulations is also shown.

We keep the 9×9 array of tweezers used for the characterizations described in the previous chapter to optimize both optical pumping and Rydberg excitation. The optical pumping benefits from the improved statistics offered by a larger number of atoms, while the Rydberg excitation takes advantage of the larger spatial extension to ease proper alignment of the lasers. We then switch to a 6×3 array that matches the BoB traps introduced in the next chapter for an in-depth characterization of the Rydberg excitation.

4.1.1 Optical pumping

The optical pumping is done by illuminating the atoms with the "repumper" and "probe" beams[1], referred to as optical pumping beams on figure 4.2. They are respectively tuned to the repumping transition $\left|5S_{1/2}, F=1\right\rangle \longrightarrow \left|5P_{3/2}, F'=2\right\rangle$ and the cycling transition $\left|5S_{1/2}, F=2\right\rangle \longrightarrow \left|5P_{3/2}, F'=3\right\rangle$ in the presence of the directing magnetic field. They come out of the same optical fiber with parallel polarization, further purified by a Glan-Thompson polarizer, and adjusted with a pair of half and quarter waveplates to be σ^+ at the atoms position.

The optical pumping efficiency is probed by two-photon Raman spectroscopy as described in figure 4.3 (a). The sequence proceeds as follows. After imaging and cooling the atoms, the repumper is applied for 400 µs to empty the population in $F=1$. The two Raman lasers couple the $F=1$ and $F=2$ levels through the states[2] $5P_{3/2}$ $F'=1$ and $F'=2$, with respective (blue) detunings $\Delta_1 = 759\,\text{MHz}$ and $\Delta_2 = 602\,\text{MHz}$. Shining the Raman beams during approximately 4 µs transfers the population from the resonant Zeeman sub-levels from $F=2$ to $F=1$. Residual population in $F=2$ is kicked out of the trapping region in the same manner as for light shift spectroscopy: the tweezers are switched off and the pushing beam is applied for 4 µs. We therefore observe the absence of recaptured atoms except at the

[1] Those are the same as the beams involved in light shift spectroscopy.

[2] The hyperfine levels $F'=0$ and $F'=3$ do not intervene since the selection rule $|\Delta F| \leq 1$ cannot be satisfied for both $F=1$ and $F=2$.

Raman resonances that transfer the population to $F = 1$, which is insensitive to the kick.

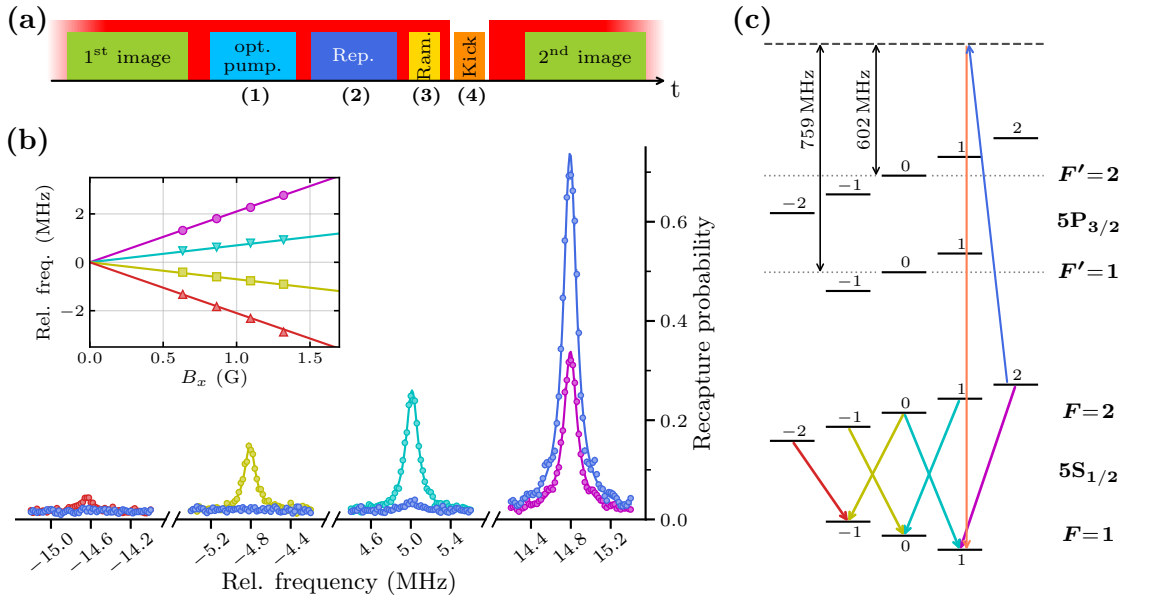

Figure 4.3: Raman spectroscopy. (a) Experimental sequence. (1) The optical pumping lasts 400 µs; (2) The repumper pulse lasts 400 µs; (3) The Raman pulse lasts ~ 4 µs; (2) The kick lasts 4 µs;. (b) Spectra obtained with (blue) and without (various colors) optimized optical pumping. The zero corresponds to the frequency where the peaks coalesce as the magnetic field vanishes. The inset shows the position of the peaks as a function of the magnetic field, solid lines correspond to the theory. (c) Scheme of the levels indicating the observed Raman transitions.

Figure 4.3 (b) presents Raman spectra with and without optical pumping, after optimization. The measurements are carried at our working magnetic field $B = 7\,\mathrm{G}$. Each transition has its pulse duration and laser power adjusted to reach a π-pulse at the peak frequency, the intensities are approximately $200\,\mathrm{mW\,cm^{-2}}$ and $100\,\mathrm{mW\,cm^{-2}}$ for the beam tuned to $F = 1$ and $F = 2$ respectively.

The Raman beams come out of the same optical fiber and have the same circular polarization at the atoms location. The quantization axis being orthogonal to the direction of propagation of the beams, the Raman field is a mixture of 25% σ^+, 25% σ^- and 50% π-polarized light. We only observe peaks corresponding to four of the seven possible transition frequencies, as indicated in the level scheme figure 4.3 (c).

The peaks are evenly spaced and their dependence in the magnetic field agrees very well with the theory as seen in the inset of figure 4.3 (b). At a given magnetic field B, the peak frequencies are offset from their zero-field value by[3] $\nu_k = \frac{k}{2}\mu_\mathrm{B} B$, $k = \pm 1, \pm 3$, where μ_B is Bohr magneton. The splitting $\Delta\nu = \mu_\mathrm{B} B$ between two adjacent peaks allows for the precise measurement of the magnetic field. From measured $\Delta\nu = 9.81 \pm 0.02\,\mathrm{MHz}$, we infer a magnetic field $B_x = 7.01 \pm 0.02\,\mathrm{G}$.

The drawback of our optical pumping scheme is the heating of atoms from the cycling transition. We want to maximize the population in the state $\left|5\mathrm{S}_{1/2}, F = 2, m = 2\right\rangle$ without

[3]Here and in the following we assume that the electron, orbital and nuclear g-factors have their approximate integer value 2, 1 and 0 respectively. This approximation is valid to about 0.1%, which is good enough for our purposes. Note that this also is the order of the uncertainty of our magnetic field measurement, which is thus limited by this approximation.

excessively heating the atoms. The optimization is done on these criteria by adjusting the polarization of the beams, their power and duration. We settled on a duration of 400 µs with respective intensities of the order of $0.02\,\mathrm{mW\,cm^{-2}}$ and $200\,\mathrm{mW\,cm^{-2}}$ for the probe and the repumper beam. This leads to an increase of atomic temperature from 14 µK to 25 µK. We can get a rough estimate of the purity of the population from the spectra of figure 4.3 (b) where some residual population in $m = 1$ can be seen from the peak at 5 MHz. Fitting the two high-frequency peaks (corresponding to the cyan and purple transitions) with lorentzian profiles we get respective amplitudes $A_{m=1} = 0.018 \pm 0.002$ and $A_{m=2} = 0.72 \pm 0.01$ from which we evaluate the optical pumping efficiency η_{OP} as:

$$\eta_{\mathrm{OP}} = \frac{A_{m=2}}{A_{m=1} + A_{m=2}} = 0.97 \pm 0.01. \tag{4.1}$$

4.1.2 Laser excitation

The excitation to the Rydberg state $\left|52\mathrm{D}_{5/2}, m_j = +5/2\right\rangle$ takes place after the optical pumping. We proceed via a two-photon process with $\left|6\mathrm{P}_{3/2}\right\rangle$ as the intermediate state (see figure 4.1). The low-lying transition $5\mathrm{S}_{1/2} \longrightarrow 6\mathrm{P}_{3/2}$ is addressed by a 420 nm laser, blue-detuned by $\Delta = 500\,\mathrm{MHz}$. A second laser, with a wavelength of 1015 nm, completes the excitation scheme to the Rydberg state. To reach the $m_j = +5/2$ sub-level, the two excitation beams propagate in opposite directions, parallel to the magnetic field along the x-direction, with σ^+-polarizations (see figure 4.2). In the presence of lasers with Rabi frequencies Ω_{420} and Ω_{1015}, the three-level system in the far detuned regime $\Delta \gg \Omega_{420}, \Omega_{1015}$ is equivalent to a two-level system with effective Rabi frequency and detuning:

$$\Omega = \frac{\Omega_{420}\Omega_{1015}}{2\Delta}, \quad \delta = \delta_0 + \frac{1}{4\Delta}\left(\Omega_{1015}^2 - \Omega_{420}^2\right). \tag{4.2}$$

The detuning Δ limits the maximum allowable Rabi frequency Ω_{420}: we must stay in the $\Delta \gg \Omega_{420}$ regime to avoid populating the intermediate $\mathrm{P}_{3/2}$ state. Therefore, the two-photon Rabi frequency that we can achieve is essentially limited by the laser power at 1015 nm.

The excitation takes place at zero electric field. In doing so we minimize the broadening of the transition due to the large quadratic Stark shift of the target state: $140\,\mathrm{MHz\,V^{-2}\,cm^2}$. We identified the transition to address among the many possibilities by performing Zeeman spectra with and without the optical pumping. The latter is then always present in subsequent experiments.

The excitation lasers

The laser emitting at 420 nm is composed of a titanium-sapphire laser (SolsTiS, M-squared) emitting 6 W of power at 840 nm and a frequency-doubling cavity from which we can get up to 2 W of output power. The titanium-sapphire laser is pumped with approximately 18 W of 532 nm light with dedicated pump (Equinox, M-squared). Initially, the laser light at 1015 nm was obtained from a similar assembly: a pump at 532 nm and a titanium sapphire laser from which we got 2 W of output power at 1015 nm (again, a commercial Equinox and SolsTiS apparatus from M-squared). Unfortunately, the 1015 nm laser pump got defective, and we had to use a diode laser instead (DL Pro, Toptica) with 120 mW of output power. Technical details on the laser setup are gathered in appendix B.

In our conditions, we have approximately 50 mW of power at 1015 nm focused on the atoms with a waist of 140 µm, hence a Rabi frequency $\Omega_{1015} \approx 2\pi \times 10\,\mathrm{MHz}$. With a power

estimated to be 55 mW and a size[4] of $\sim 100\,\mu$m at the atoms location for the 420 nm beam, we get a Rabi frequency $\Omega_{420} = 2\pi \times 160\,$MHz. This leads to an expected two-photon Rabi frequency $\Omega \approx 2\pi \times 1.7\,$MHz.

The 9×9 array

We begin by showing in figure 4.4 an excitation spectrum obtained on the 9×9, $10\,\mu$m spacing array of tweezers described in chapter 3. As indicated earlier, the spectrum is taken in a magnetic field $B = 7\,$G and at zero electric field: $F = 0\,\mathrm{V\,cm^{-1}}$. The tweezers, that would otherwise undesirably light-shift the Rydberg transition, are switched off during the laser pulse and re-established just after. Atoms thus excited to the Rydberg state are subject to the repulsive ponderomotive potential of the gaussian tweezers and expelled from the trapping region, while those atoms still in the ground state are recaptured and detected by fluorescence imaging. To complement the optical detection, we ionize the Rydberg atoms still present in the environment and count the total number of ions detected during the ionization ramp. The obtained spectra show good complementarity and fit well with the theoretical line shape for a square pulse of duration T:

$$p(\omega) = y_0 + A\frac{\sin^2(\pi(f - f_0)T)}{(\pi(f - f_0)T)^2}, \tag{4.3}$$

where f is the frequency of the pulse and f_0 is the transition frequency. The offset y_0 and amplitude A have been included as necessary parameters for proper fitting of experimental data.

There is a noticeable decrease in the number of ions detected as compared to the lost atoms. This difference is due to the delay between laser excitation and ionization. In the case of fluorescence detection, the atoms transferred to the Rydberg state are necessary lost as they are repelled by the tweezers. Fluorescence detection is therefore, once corrected from background losses, quantitative in terms of excitation efficiency. Ionization detection can, however, only detect atoms in the Rydberg state, yet does so independently of their position.

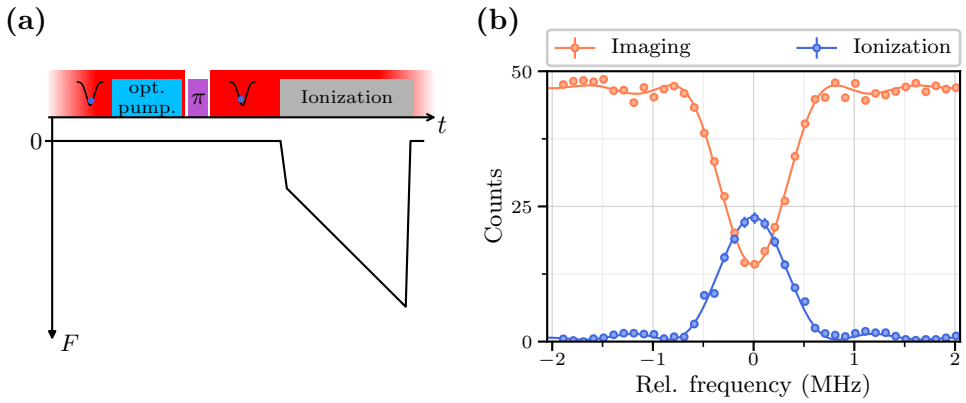

Figure 4.4: Two-photon laser spectrum on the large 9×9 array. (a) Scheme of the sequence. In addition to the usual fluorescence imaging, ionization detection is triggered $40\,\mu$s after laser excitation. (b) Corresponding laser spectrum, showing on the same scale the average number of recaptured atoms on the whole array from fluorescence imaging and the detected ion counts. Note the complementarity between the two signals.

[4]The beam does not look gaussian at the focus.

Owing to the delay between excitation and detection, a significant fraction of the Rydberg population decays to the ground state. We estimated, using the Alkali Rydberg Calculator package [122], this decay rate to be 150 µs. Most ions being produced 70 µs after the excitation, we expect the loss of 33 atoms from optical detection to translate into $33 \times e^{70/150} = 21$ detected ions. This result is very close to the measured value of 22.5 ions, especially considering the fact that untrapped surrounding atoms excited to the Rydberg state also contribute to ion counts.

The size of the excitation lasers is comparable to that of our array of tweezers, 80 µm. Figure 4.5 (a) presents spatially-resolved Rabi oscillations with the laser frequency at the peak of the average spectrum of figure 4.4 (b). The results make the inhomogeneity of the laser excitation manifest. There is a clear tendency towards higher Rabi frequencies at the center of the array, where the laser intensity is maximal, as highlighted in the color map of figure 4.5 (b). Assuming the lasers are aligned with waists w_1 and w_2, we have, according to eq. (4.2)

$$\Omega \propto e^{-x^2\left(\frac{1}{w_1^2}+\frac{1}{w_2^2}\right)},$$

where x is the distance to the propagation axis. With our measured values $w_1 = 100\,\mu\text{m}$ and $w_2 = 140\,\mu\text{m}$, this yields an expected ratio of Rabi frequencies $\Omega(x = 50\,\mu\text{m})/\Omega(x = 0\,\mu\text{m}) \simeq 0.69$. This value is in reasonable agreement with the measured ratio $\frac{250}{420} = 0.6$.

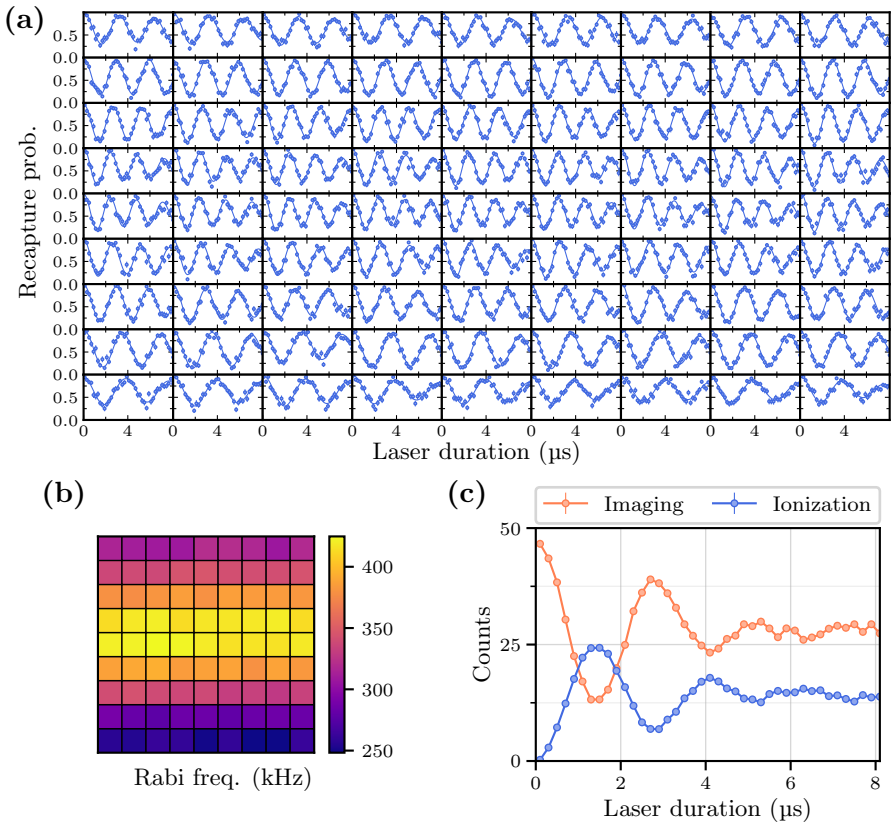

Figure 4.5: Rabi oscillations of the two-photon laser transition on the large 9×9 square array, with 10 µm spacing. (a) Individual oscillation signals. (b) Map of fitted Rabi frequencies. (c) Number of recaptured atoms summed on all trapping sites and ion counts. The laser powers here differ from the ones announced earlier and correspond to pre-optimized settings, with lower values.

The number of recaptured atoms summed over the whole array (see figure 4.5 (c)) shows a quick damping due to the dephasing between individual Rabi oscillations which, again, reflects itself in the ionization detection signal. This damping is non-negligible even at short pulses durations, and is the cause of the reduced contrast observed in the spectrum of figure 4.4 (b).

The 6×3 array

The above Rabi signal is very useful to properly align the excitation lasers. However, to ensure homogeneous Rydberg excitation, we must restrict ourselves to a horizontal band of at most 30 µm vertical extension. This, together with the fact that we are limited by the power at our disposal to produce BoB traps, leads us to switch to a smaller array of traps. Hence, from now on and for the rest of this manuscript, we use an array of 6×3 traps, spaced by 15 µm to rule out the possibility of any interaction between neighboring atoms. This corresponds to a spatial extension of 75×30 µm for the new array.

We present the results obtained for the laser spectroscopy averaged over all trapping sites in figure 4.6. Along with the usual excitation spectrum, figure 4.6 (a) shows the light-shifted spectrum in the presence of the tweezers light. The dispersion of tweezer light intensity causes a significant broadening and a drop of the maximum achievable Rydberg transfer from 90% to 30%. Comparing with figure 3.4 (c), we see that in the latter case the light-shifted spectrum in not significantly broadened. On the contrary, the broadening observed on the Rydberg transition in figure 4.6 (a), with a full width at half maximum (FWHM) of 2.14 ± 0.05 MHz, is much smaller than the 6 MHz of the D_2 line. This opens the perspective of a much higher resolution on the measurement of the traps intensity profile, by using the Rydberg transition instead of the D_2 line. In figure 4.6 (b), we plot the excitation spectrum in terms of counts and compare optical and ionization detection. For this purpose, the delay between the laser excitation and the triggering of ionization detection is reduced to the minimum: 5 µs. The arrival times of figure 4.6 (c) show a peak of ions produced 35 µs after the laser pulse, to be contrasted with the $\sim$ 80 µs delay in the case of the large array. This shorter delay translates into a higher ratio of detected ions over lost atoms as compared to the spectrum of figure 4.4 (b).

The number of atoms measured in the Rydberg state can be estimated from fits of the data with the theoretical line shape. This yields an average loss of $n_{\text{img}} = 10$ atoms from the tweezer array and 8.5 ions detected. Spectroscopy in the presence of the tweezers has

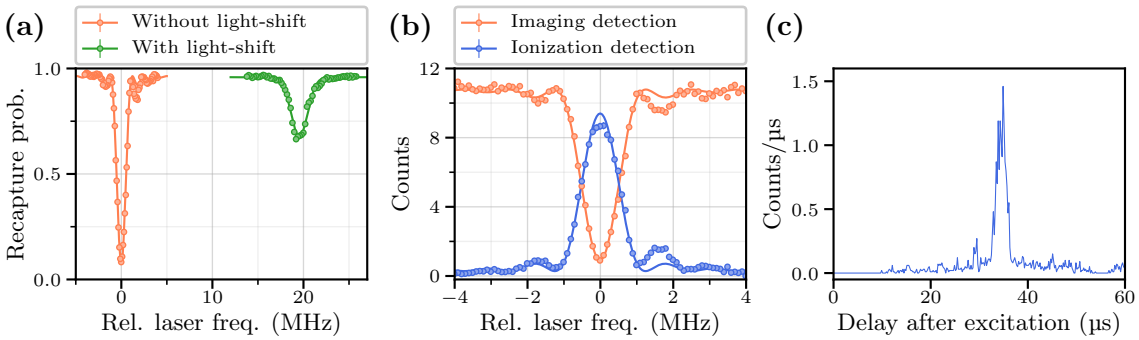

Figure 4.6: Laser spectroscopy on the small 6×3 array of tweezers. (a) Laser spectra obtained from the recapture probability averaged on all trapping sites, with and without the light-shift induced by the tweezers. (b) Total number of recaptured atoms and ion counts. (c) Ion arrival times at the peak frequency.

shown the ion background, resulting from the excitation of surrounding untrapped atoms) to be approximately 0.5 atoms. We thus get an estimated $n_{\text{ion}} = 8$ ions produced from the excitation of trapped atoms. This number is very close to the value expected from the decay rate to the ground state: $10 \times e^{-35/150} = 7.9$. We conclude to a near-unity efficiency of our ionization detection setup.

Spatially-resolved spectra and Rabi oscillations are presented in figure 4.7. The spectra are measured with a π-pulse duration of 0.8 µs. The individual peak amplitudes, with value $\langle A \rangle = 0.925$, $\text{Std}(A) = 0.013$, are all superior to that of the averaged data, $A = 0.89 \pm 0.01$. The reason for this reduction of contrast appears on the inspection of the peak frequencies map. They fluctuate by 100 kHz around the average position, causing a mean decrease of the Rydberg transfer of 3% for each trapping site. The global efficiency $\eta_{52\text{D}}$ of the laser excitation corresponds to the peak amplitude A of the averaged data:

$$\eta_{52\text{D}} = A = 0.89 \pm 0.01. \tag{4.4}$$

The map of Rabi frequencies of figure 4.7 (b) reveals another mechanism leading to the decrease of excitation efficiency. The atoms are subject to large variations of Rabi frequencies Ω along the vertical, with $\langle \Omega \rangle = 2\pi \times 660\,\text{kHz}$, $\text{Std}(\Omega) = 2\pi \times 50\,\text{kHz}$. The laser pulse is therefore not a perfect π-pulse, causing an additional peak amplitude reduction of 1% on average.

The two effects described above clearly share a common origin given the strong anti-correlation between the position of peak frequency and the Rabi frequency. The observed

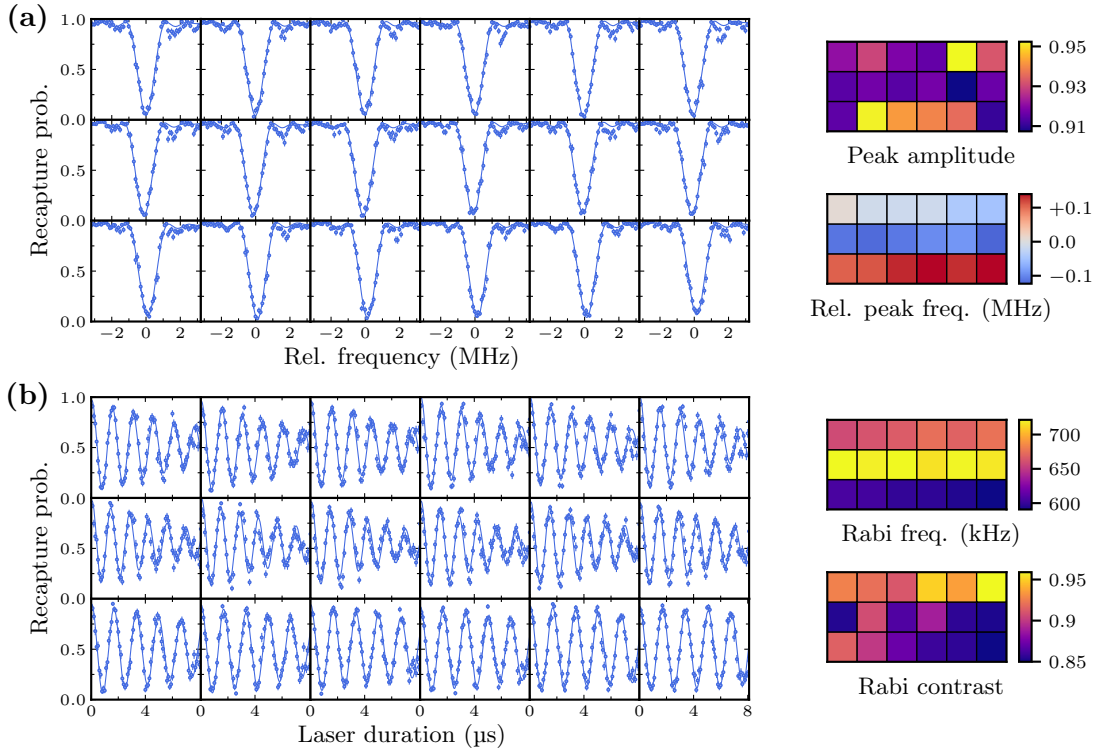

Figure 4.7: Spatially-resolved laser spectra and Rabi oscillations. (a) Laser spectroscopy with corresponding peak amplitudes and frequencies maps. The reference frequency is that of the average spectrum (see figure 4.6). (b) Rabi oscillations with corresponding Rabi frequencies and contrasts maps. Note the anti-correlation between the peak frequencies and the Rabi frequencies.

behavior can therefore be attributed to spatial variations of the intensity of the 420 nm laser beam, in accordance with eqs. 4.3. The Rabi frequency inhomogeneities cannot be accounted for by assuming a gaussian shape with waist $\sim 100\,\mu$m for the lasers. This would lead to a Rabi frequency ratio of 0.96 at a 15 µm distance, in contrast with the measured values of 0.85-0.93 for the bottom and top pairs of lines, respectively.

The measured Rabi frequency is significantly lower than the value announced in the beginning of this section, by a factor of approximately 2.5. This can be due to an imprecision in the measurement of laser powers, with a possibly large difference between continuous and pulsed values. There is also the possibility of an imperfect alignment of the 420 nm laser, with a beam profile that cannot be considered gaussian.

To conclude, let us emphasize that the possibility of measurements on individual trapping sites is a powerful tool to analyze and optimize the experimental conditions. The Rydberg excitation spectra and Rabi oscillations presented in this section illustrate the use of spatially-resolved information to get the beams characteristics at the atoms location.

4.2 Preparation of circular states

Further state manipulation from $\left|52\mathrm{D}_{5/2}, m_j = +5/2\right\rangle$ in the Rydberg manifold is done with the help of microwave (MW) and radio-frequency (RF) fields by taking advantage of the sensitivity of the Rydberg levels to the electric field. As indicated in chapter 1, the D state cannot be involved directly in the circularization process. The energy shift caused by its large quantum defect displaces it far off-resonance with the harmonic ladder that we go through during the adiabatic transfer. The preparation of circular states thus involves an intermediate step consisting in the microwave transfer of $\left|52\mathrm{D}_{5/2}, m_j = +5/2\right\rangle$ to a $|52\mathrm{F}\rangle$ state. The latter branches, after switching on a directing electric field parallel to the magnetic field, to the state from which we carry out the adiabatic transfer.

Although it is possible to detect each population transfer optically by going backwards to the ground state, this is of limited use, especially as we add up experimental steps. Indeed, fluorescence imaging essentially requires to double the number of necessary steps, thus squaring the total efficiency and leading to a non-negligible loss of contrast on the signal. Moreover, without ponderomotive trapping, the necessary delays for each preparation step would lead to the loss of a significant fraction of atoms. For these reasons, the results presented in this section involve only state-selective field ionization as the detection method.

4.2.1 Microwave transition

The frequency of the transition $|52\mathrm{D}\rangle \longrightarrow |52\mathrm{F}\rangle$ is 64.76 GHz in zero field. To address it, microwave at 16.2 GHz is generated by a signal generator (MG3692C, Anritsu), amplified and converted with a frequency quadrupler (AMC-15-RFH00, Millitech). The MW field is emitted in free space by a pyramidal horn located outside the UHV chamber, close to the outgoing tweezers beam opening (see figure 4.2). A PIN diode allows us to control the timing and duration of the MW pulse with a digital gating signal.

The target $|52\mathrm{F}\rangle$ state is particularly sensitive to the electric field. We therefore work at zero electric field to minimize the broadening of the transition from field inhomogeneity or noise, the quantization axis being still maintained by the magnetic field. Figure 4.8 (a) shows the energy of the levels $|52\mathrm{F}\rangle$ as a function of the magnetic field B. These states correspond to the quantum numbers $l = 3$ and $s = \frac{1}{2}$, hence a total of $(2l+1)(2s+1) = 14\ m$ sub-levels. The spin-orbit coupling dominates at low magnetic fields ($B \lesssim 1\,\mathrm{G}$), the spin and

angular momenta add-up to form m_j levels with $j = \frac{5}{2}, \frac{7}{2}$. The level structure, magnified in the inset of figure 4.8 (a), is that of the Zeeman splitting proper. The coupling to the magnetic field dominates for higher field values, in particular at our working field $B = 7\,\mathrm{G}$. The structure here corresponds to the Paschen-Bach effect, with levels $|l = 3, s = \frac{1}{2}, m_l, m_s\rangle$ perturbed by the residual spin-orbit coupling. Neglecting the latter, the eigenenergies at field B are $-\mu_\mathrm{B} B(m_l + g_s m_s)$, where μ_B is Bohr's magneton and $g_s \approx 2$ is the electron g-factor.

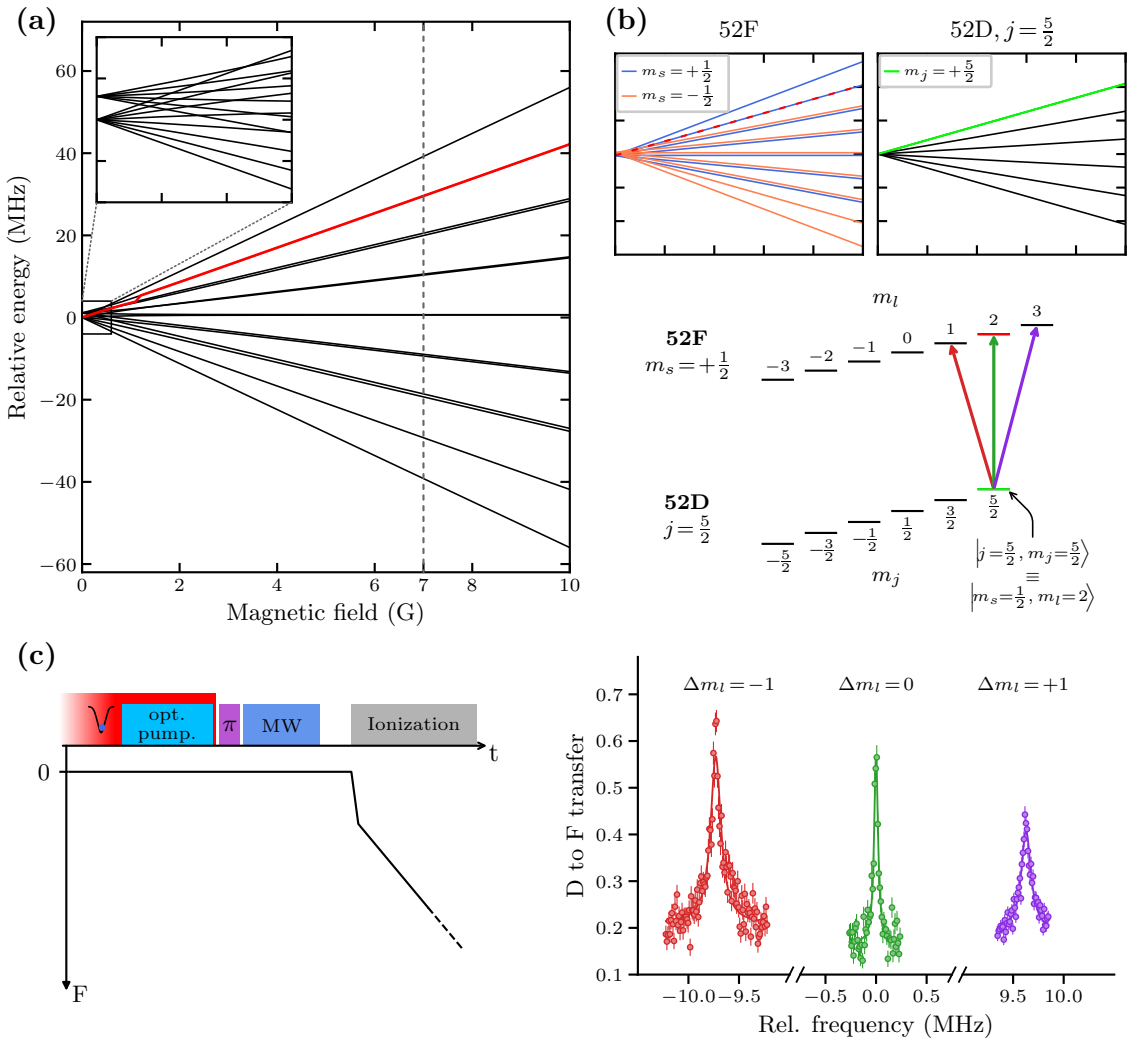

Figure 4.8: Level structure and spectroscopy of the 52F states. (a) Eigenenergies of the $|52\mathrm{F}\rangle$ as a function of the magnetic field. The level indicated in magenta is the target state for the circularization. The dashed line corresponds to the working magnetic field. The inset shows the L-S mixing at low magnetic field. (b) Level structure of $|52\mathrm{D}\rangle$ and $|52\mathrm{F}\rangle$. Top left: scheme of the levels of $|52\mathrm{F}\rangle$ highlighting the two subsets with $m_s = +\frac{1}{2}, -\frac{1}{2}$; the target state is indicated as a dashed magenta line. Top right: Zeeman splitting of the $|52\mathrm{D}\rangle$ levels; the Rydberg excitation prepares the state indicated in green. Bottom: Representation of the levels as a function of m with allowed transitions; the m_l levels of $|52\mathrm{F}\rangle$ are shifted by $m_s = +\frac{1}{2}$ to make manifest the $\Delta m_l = 0, \pm 1$ selection rules. (c) Experimental sequence and related spectra obtained for the three allowed transitions. The zero of frequency is set at the peak position of the $\Delta m_l = 0$ line, with value given in the text.

This level structure is schematized in the upper left panel of figure 4.8 (b) with two sets distinguished that correspond to $m_s = +\frac{1}{2}, -\frac{1}{2}$. The right panel shows the $\left|52\mathrm{D}, j = \frac{5}{2}\right\rangle$ levels, for which the stronger spin-orbit coupling still dominates in our experimental conditions. The state $\left|52\mathrm{D}, j = \frac{5}{2}, m_j = +\frac{5}{2}\right\rangle$ which constitutes the initial state for the microwave transfer can be written $\left|52\mathrm{D}, m_l = +2, m_s = +\frac{1}{2}\right\rangle$. As we address a dipolar electric transition, hence with forbidden spin flip, we are coupled to the $m_s = +\frac{1}{2}$ subset of F levels, with three transitions allowed by the selection rules: $\Delta m_l = 0, \pm 1$.

The spectra for these three transitions are shown in figure 4.8 (c), along with the experimental sequence for their measurement. We apply a 30 µs MW pulse after the laser excitation described in the previous section and detect the $|52\mathrm{D}\rangle$ and $|52\mathrm{F}\rangle$ populations by ionization. We plot the transfer from $|52\mathrm{D}\rangle$ to $|52\mathrm{F}\rangle$, which is computed as $n_\mathrm{F}/(n_\mathrm{D} + n_\mathrm{F})$, where n_F and n_D are the ion counts corresponding respectively to $|52\mathrm{F}\rangle$ and $|52\mathrm{D}\rangle$. The zero of the frequency scale corresponds to the peak of the central line, that we measure at $64755.1529 \pm 1.4 \times 10^{-3}$ MHz.

Assuming negligible spin orbit coupling, the splitting between successive transitions is equal to $\mu_\mathrm{B} B$, where B is the magnetic field. We measure an average splitting of 9.68 ± 0.05 MHz, from which we recover a magnetic field of 6.92 ± 0.04 G, close to the value of 7.01 G obtained by Raman spectroscopy. The discrepancy between the two estimations is due to the spin-orbit coupling that still affects the F levels. Let us also mention the possible presence of a residual electric field to which the F levels are very sensitive.

For the preparation of circular states, we address the $\Delta m = 0$ transition. Rabi oscillations along with the spectrum in the conditions of a π-pulse at resonance are presented in figure 4.9. The microwave power corresponds to a Rabi frequency of 277.5 ± 0.2 kHz which gives a maximal detected population transfer of 80% with a π-pulse lasting 1.8 µs. It must be noted that this estimation of the efficiency is only approximate, since the ionization signals have significant noise as can be seen in the arrival times of figure 4.9. In the absence of MW (top plot) we observe residual counts in the detection window of the F state, hence a non-zero background transfer. Reciprocally, at the π-pulse (bottom plot), ions are detected in the detection window of the D state, thus reducing the transfer. It is not possible to determine precisely the origin of these ions.

For the reasons given above, the use of raw ion counts is not well suited to the quantitative

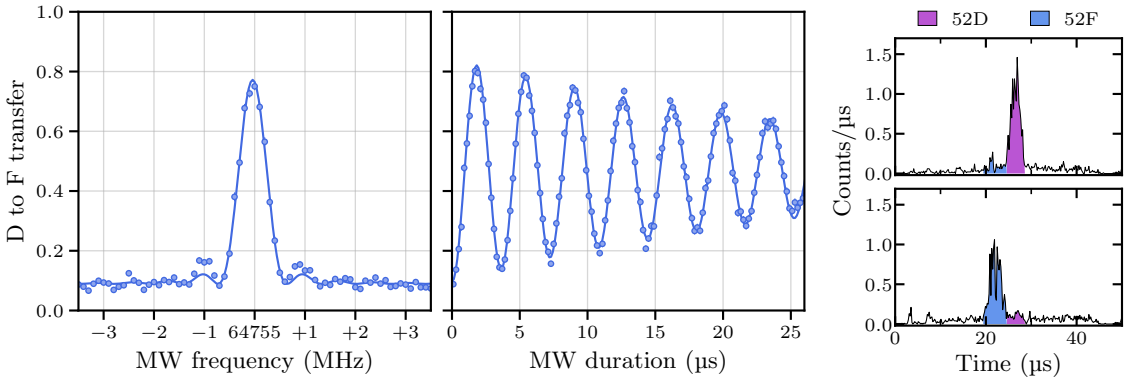

Figure 4.9: The $\Delta m = 0$ DF transition: spectrum, Rabi oscillations and ion arrival times. The spectrum is recorded with a MW pulse of 1.6 µs, slightly shorter than the π pulse duration of 1.8 µs, hence the reduced transfer at the peak. The arrival times without (top) and with (bottom) DF transfer show residual population in the detection windows of 52F and 52D respectively, causing the observed reduction of contrast.

measurement of the microwave transfer efficiency. Its determination is done from the MW spectrum obtained by optical detection, as shown in figure 4.10. The sequence begins identically as when using ionization detection (see figure 4.8 (c)). After the MW pulse, however, instead of triggering the ionization ramp we apply a second laser π-pulse to send back the remaining 52D population to the ground state followed by the switching-on of the tweezers. The state manipulation takes 5 µs, during which the atoms are not trapped. This duration is short enough to ensure *a priori* negligible mechanical losses from the free flight of atoms (see figure 3.11).

The individual spectra and averaged recapture probability presented in figure 4.10 (a) are fitted by the line shape (4.3). Some quantitative insight is provided by the mosaic plots of figure 4.10 (b). A first remark comes from the dispersion of peak frequencies, that lie in a 40 kHz-range, much smaller than the approximately 400 kHz FWHM of the peak. We can conclude that there is no significant reduction of transfer efficiency from the dispersion of resonance frequencies. The most striking feature of the data is the inhomogeneity of the out-of-resonance baseline y_0, with a 10% difference between the central horizontal line and the side lines. This is associated to similar variations of the peak amplitude (the presence of the outlier value makes the visualization difficult though). The efficiency η_{DF} is computed from the baseline y_0 and amplitude A of the peak as

$$\eta_{\text{DF}} = \frac{|A|}{y_0}. \tag{4.5}$$

We thus obtain the efficiency η_{DF} for each individual trapping site,

$$\langle \eta_{\text{DF}} \rangle = 0.884, \quad \text{Std}(\eta_{\text{DF}}) = 0.045. \tag{4.6}$$

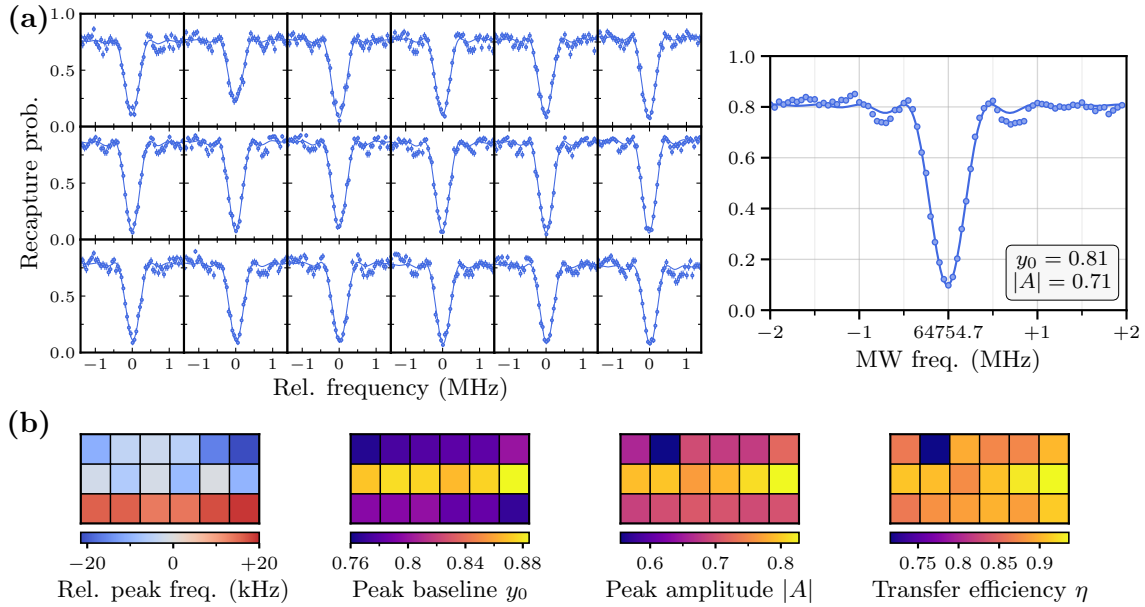

Figure 4.10: Spatially-resolved MW spectroscopy of the 52D to 52F transition. (a) Individual trapping sites spectra (left) and corresponding average recapture probability (right). (b) Maps of relevant parameters (see text for discussion). Note the large inhomogeneity of the baseline y_0.

As a global efficiency, we retain that deduced from the average signal,

$$\eta_{\text{DF}} = 0.878 \pm 0.013. \tag{4.7}$$

The structured spatial variations of baseline, with higher values along the central line, are unlikely to be caused by inhomogeneity in the laser excitation. The laser frequency, power and pulse duration tend to favor the excitation on the upper and lower lines. This suggests another mechanism for the decreased baseline at the edges. One possibility is the expulsion of atoms from the trapping region due to Rydberg-Rydberg interactions. Qualitatively, this would lead to the observed pattern. By symmetry, the atoms along the central line are on a potential extremum, with a vanishing force exerted on them, and therefore, minimal displacement during the trap-off duration. However, the interaction is one-sided for edge atoms, which may move significantly during the 5 µs period.

4.2.2 Circularization

The last step of circular Rydberg states preparation requires the presence of pure σ^+-polarized radiofrequency (RF) on the atoms. The RF field is produced by the circuit schematized in figure 4.11. Two phase-coherent RF signals are emitted by a PCI-interfaced signal generator (Synth-300, Acquitek). The subsequent circuitry is identical for both channels. Two mixers in series shape the RF into a smooth pulse with the help of an arbitrary waveform generator (33521A, Agilent Technologies). The RF signal is then split in two, with a voltage-controlled phase shifter on one line to adjust the relative phase on the two RF lines. The power is controlled individually by an additional mixer connected to a voltage source, and is subsequently amplified. A RF circulator is present at the output of the amplifier to transfer the reflection from the high impedance electrodes into a 50 Ω termination to protect the circuitry. DC voltages are superimposed to the RF via bias tees installed just before the electrodes. Each of the 10 applied voltages (2 for phase control, 4 for power control and 4 for the DC bias voltage) comes from a computer-controlled DAC. The four lines are connected to the

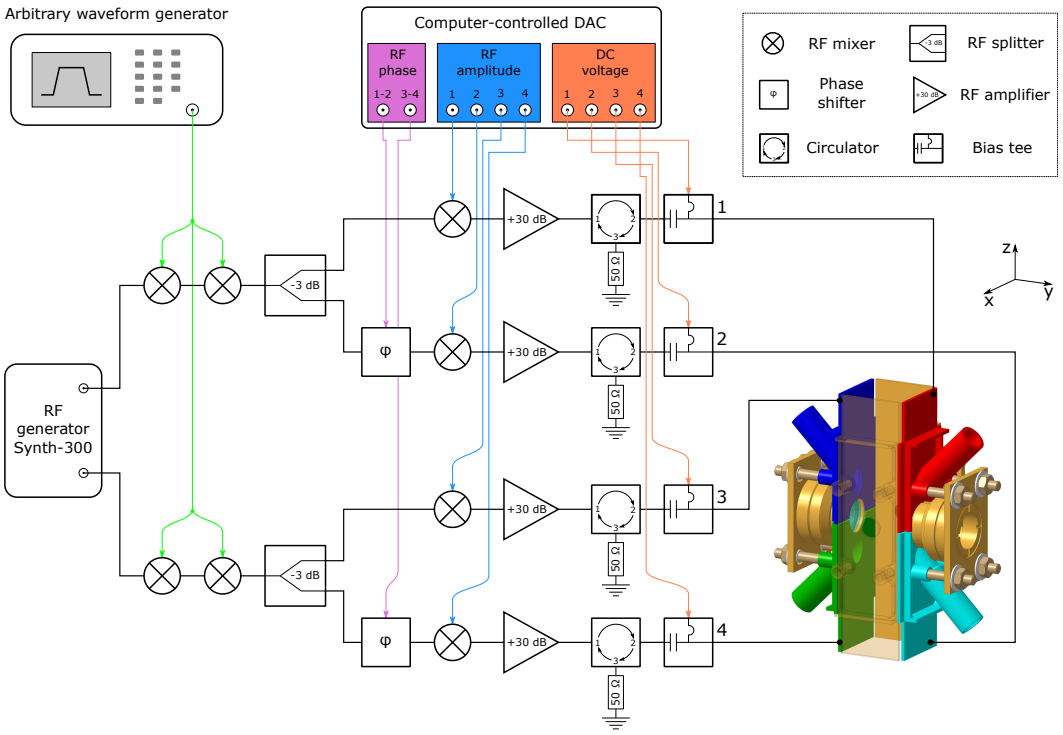

Figure 4.11: Scheme of the RF circuit used for the circularization.

RF electrodes as indicated in the figure and generate a field orthogonal to the quantization axis (set along the x-direction).

The course of events leading to the preparation of 52C is summarized in figure 4.12 (a). The electric field comes into play just after the transfer to $|52\mathrm{F}\rangle$ (step (4)). It is switched along the x direction, parallel to the magnetic field, to approximately $2.25\,\mathrm{V\,cm^{-1}}$. Figure 4.12 (b)

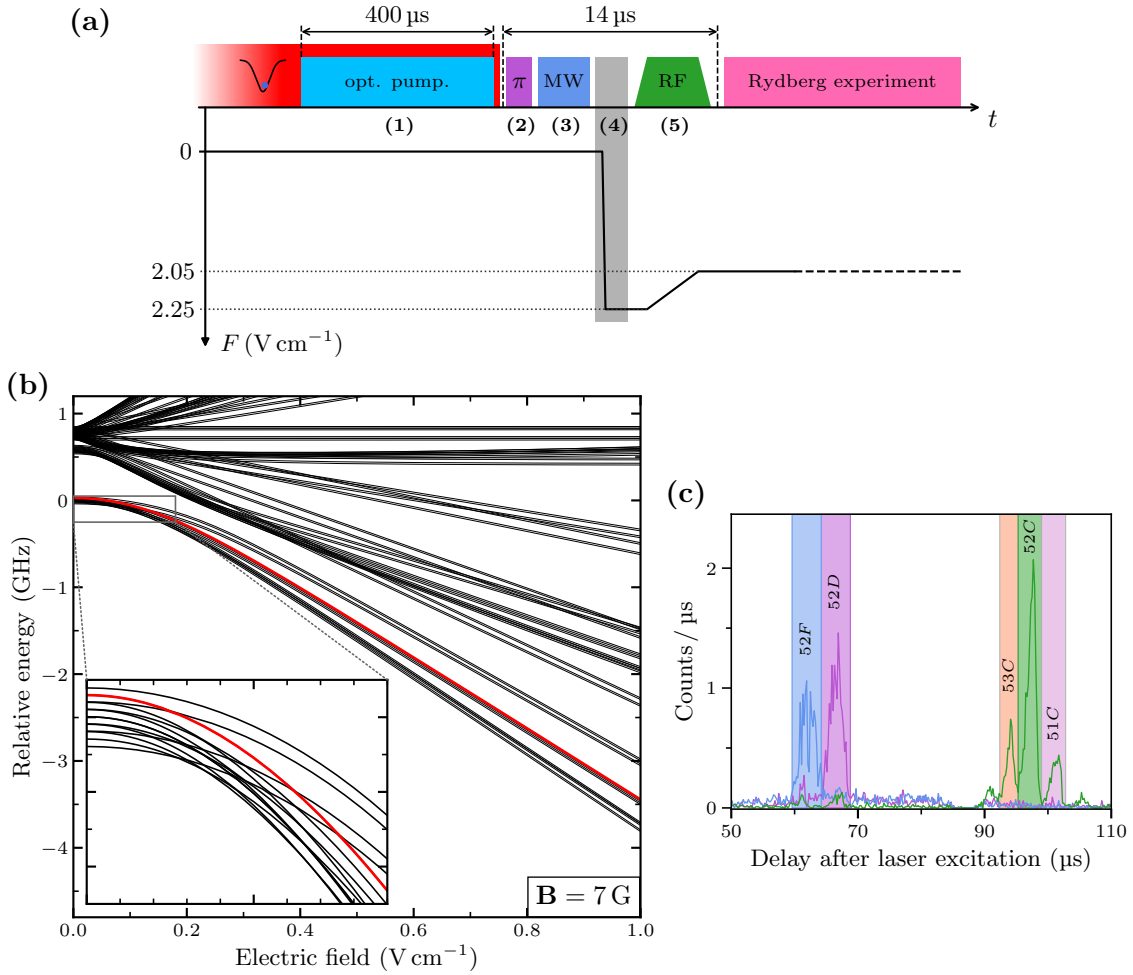

Figure 4.12: Circularization procedure. (a) Complete circular Rydberg state preparation sequence. Atoms are prepared and cooled to 14 µK in gaussian optical tweezers; (1) the optical pumping lasts 400 µs, in the presence of the tweezers, and results in the heating of atoms to 25 µK; (2) the tweezers are switched off for the laser excitation, with a π-pulse lasting 0.8 µs; (3) the DF transfer ensues with a MW pulse of 1.8 µs; (4) we apply the electric field and reach a value of $2.25\,\mathrm{V\,cm^{-1}}$ in 0.5 µs; (5) after a settling delay of a few µs, we apply a trapezoidal RF pulse while decreasing the electric field from $2.25\,\mathrm{V\,cm^{-1}}$ to $2.05\,\mathrm{V\,cm^{-1}}$ in 4.7 µs. The circularization (steps (2)-(5)) takes 14 µs and is followed by the actual experiment. (b) Stark map of the F levels. The evolution of the state $|52\mathrm{F}\rangle$ when the electric field is applied in step (4) is indicated as a red line. The inset shows three anti-crossings at low field that we must go through fast enough. (c) Arrival times of ions obtained after each of the three population transfer stages (2), (3), (5). Note the appearance of peaks corresponding to the states 51C and 53C, that result from the decay of 52C population during the 80 µs delay between preparation and detection.

shows the Stark map of neighboring states at our working magnetic field of 7 G, and the red line indicates the evolution of the $|52\mathrm{F}\rangle$, that branches to the state $|n = 52, m = 2, n_1 = 1\rangle$, as the electric field increases. The electric field is switched in 0.5 µs to allow for diabatic transfer through the early anticrossings shown in the inset of figure 4.12 (b). The adiabatic condition is fulfilled for the rest of the evolution, with electric field $F \gtrsim 0.2\,\mathrm{V\,cm^{-1}}$. The transfer to the circular state follows in the presence of RF at 225 MHz with the electric field decreasing from $2.25\,\mathrm{V\,cm^{-1}}$ to $2.05\,\mathrm{V\,cm^{-1}}$ in 4.7 µs. The RF pulse is trapezoid, lasts a total of 6 µs with 1 µs rising and falling edges to ensure adiabatic switching. The RF comes resonant with the ladder of levels during the electric field ramp, resulting in the desired population transfer.

The difficulty in optimizing the circularization lies in the optimization of the RF polarization. Indeed, the σ^--polarized component must be suppressed to avoid population loss to resonant neighboring states during the adiabatic transfer, as indicated in figure 4.13. This can be achieved using only a pair of adjacent electrodes, which is what we do due to a defect in one of the four RF lines. We thus only use electrodes 1 and 2 of figure 4.11 to generate the RF field for circularization. Using the four electrodes would improve the homogeneity of the RF field and suppress the σ^- component over a larger range. The RF optimization procedure that we follow can be found in [96].

4.3 Purity of the circular states and de-circularization

To conclude on the preparation of circular states, we determine their purity and describe the de-circularization procedure. Deviations from an optimal circularization will transfer a fraction of the initial population to levels in the vicinity of the circular state. We assess the purity of the latter by probing the populations of the surrounding states with microwave spectroscopy.

Optical detection of atoms is at the core of the demonstration of trapping and associated characterizations. This requires to follow the circularization procedure backwards to the ground state, which is not as efficient as the forward part. We conclude by wrapping up the efficiencies of each step, which will give us an estimation of the global efficiency of the whole procedure. This sets a limit on the signal that we can expect from the measurements performed in BoB traps.

4.3.1 Purity

The local level structure near 52C is represented in figure 4.13, including levels down to $m = n - 3$ for each multiplicity. Closest to the circular state (characterized by $m = n - 1$), two elliptical levels, denoted by $|52\mathrm{E}^+\rangle$ and $|52\mathrm{E}^-\rangle$ have angular momentum $m = n - 2$. Those states are of primary importance for fine tuning of the parameters and determining the efficiency of the circularization. Indeed, they are the first states to get populated in case of an imperfect (yet already good) adjustment of the parameters. We determine the population of the three levels mentioned by the two-photon MW spectroscopy from $n = 52$ to $n = 50$. We probe the transitions indicated as colored arrows in figure 4.13. Circular states are subject to the Stark effect only to the second order, with coefficients $2.03\,\mathrm{MHz\,V^{-2}\,cm^2}$ and $2.57\,\mathrm{MHz\,V^{-2}\,cm^2}$ for 50C and 52C respectively. First order Stark effect dominates for elliptic states with $\pm 95.97\,\mathrm{MHz\,V^{-1}\,cm}$ and $\pm 95.97\,\mathrm{MHz\,V^{-1}\,cm}$ for $50\mathrm{E}^\pm$ and $52\mathrm{E}^\pm$, respectively. The MW transition is only sensitive to differential effects, with the corresponding splitting of the three lines shown in figure 4.13.

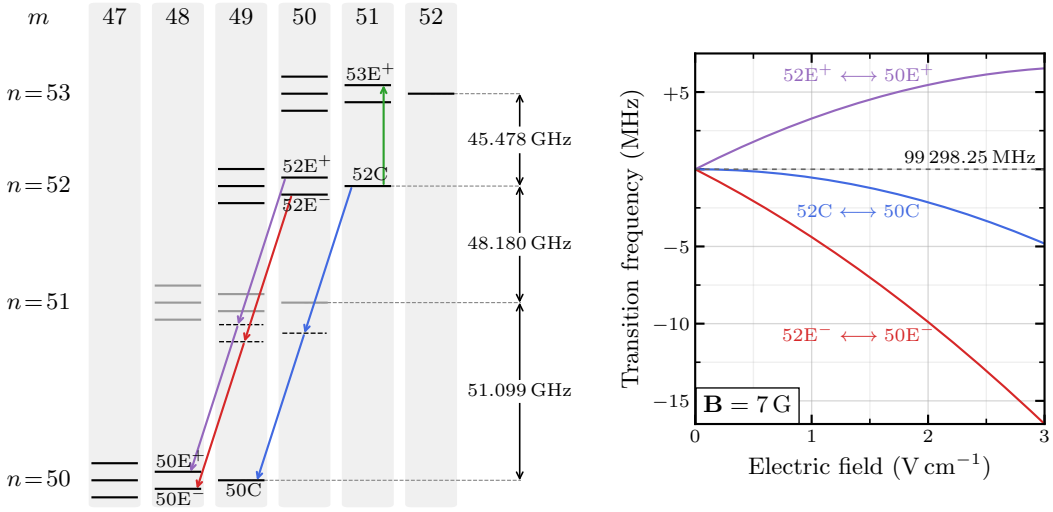

Figure 4.13: Level structure in the vicinity of 52C. We address the downward two-photon transitions indicated as colored arrows. The upwards one-photon transition to the elliptical state is described in section 4.3.2. The right panel shows the Stark splitting of the two-photon transitions.

The reason to choose a two-photon transition rather than the apparently simpler single photon transition from $n = 52$ to $n = 51$ is twofold. First, the spin levels of the prospected quantum simulator are implemented with states having $\Delta n = 2$, hence we conveniently anticipate the necessity of a two-photon transition to probe coherence between the spin states. The second, and more important reason is specific to our room temperature setup. As shown in the arrival times of figure 4.12, the delay between MW transfer and detection is non-negligible as compared to the lifetime of circular states. That would lead to significant transfer $n = 52 \longrightarrow n = 51$ and $n = 51 \longrightarrow n = 52$ and a reduction of contrast if we were to probe these transitions. In choosing the two-photon transition, we also free ourselves from the consideration of the strong dipole interaction between $\Delta n = 1$ circular states, which would potentially complicate the interpretation of the spectra.

Figure 4.14 shows the spectra obtained for the three transitions described above. The elliptical transitions appear as large peaks in case of an improperly adjusted RF (in red and purple). Only small peaks remain after optimization. Fitting these residual peaks yields amplitudes

$$A_0 = 0.71 \pm 0.02, \quad A_- = 0.05 \pm 0.01, \quad A_+ 0.031 \pm 0.007,$$

for the circular, E^- and E^+ transitions, respectively. We estimate the purity η_{circ} as

$$\eta_{\text{circ}} = \frac{A_0}{A_0 + A_- + A_+} = 0.90 \pm 0.02. \tag{4.8}$$

We also present the sharp circular to circular transition obtained with a 50 µs long MW pulse. The line shape fits well to a Voigt profile, giving a FWHM of 28 ± 4 kHz for a peak centered at $99\,295.432\,18 \pm 0.000\,55$ MHz. The width is not limited by MW the pulse length, but potentially by non-intrinsic processes. For instance, the sequence was not triggered on the power line, potentially causing a broadening due to magnetic field variations between the repetitions. The presence of 50 Hz current noise in the coils would be a likely cause.

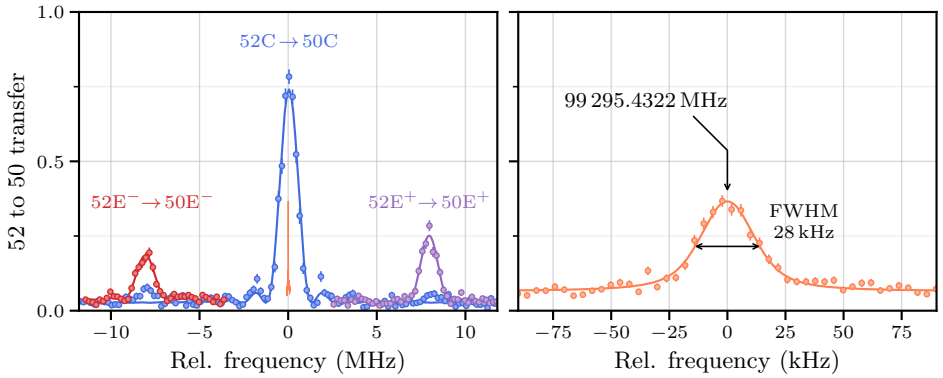

Figure 4.14: Two-photon circular to circular spectroscopy. Left: spectrum measured with a 0.8 µs π-pulse; the elliptical to elliptical transitions that appear with an imperfect adjustment of the RF are also shown. Right: spectrum measured with 50 µs-long pulse. Note the difference of frequency scales between left and right panels.

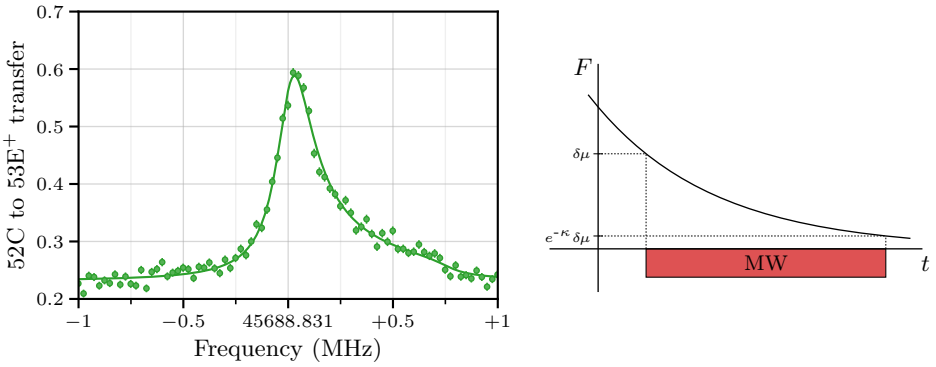

Figure 4.15: $|52C\rangle$ to $|52E^+\rangle$ spectroscopy, with a marked asymmetry towards high frequencies (*i.e.* higher electric fields). The scheme on the right illustrates the exponential decay of the electric field leading to the model of eq. (4.9).

4.3.2 Electric field measurement

The circular to circular spectroscopy is not convenient to measure the electric field. On the one hand, it is only second-order sensitive. On the other hand, having $\Delta m = 2$, it is also sensitive to the magnetic field. We get rid of this dependence by measuring the frequency of the $\Delta m = 0$ transition between $|52C\rangle$ and $|52E^+\rangle$ (green arrow on figure 4.13). The large linear Stark shift of the elliptical state, about 100 MHz V^{-1} cm, makes for an accurate measurement. The corresponding spectrum, presented in figure 4.15 (a), has an asymmetric line shape, with a larger tail at high frequencies. The scheme of figure 4.15 (b) illustrates the underlying mechanism. The 12 µs-long MW pulse takes place 3.5 µs after the target value of the potential is set by the AWG (see figure 4.12 (a), at the end of the RF pulse). At this time, the electrode voltage (and thus the electric field) has not completely settled down and slowly drifts down towards its steady value. The electric field consequently decreases, which translates into a shift of the spectral line and causes its asymmetry. Additional details on the circuitry involved in the electric field control are given in appendix C.

Assuming an exponential decay of the electric field toward its steady value and a propor-

tional transition frequency (linear Stark shift), the line shape has the form

$$f(\nu) = y_0 + \frac{A\gamma}{\kappa} \int_{e^{-\kappa}\delta\mu}^{\delta\mu} \frac{1}{\gamma^2 + (x - \mu - y)^2} \frac{\mathrm{d}y}{y}. \tag{4.9}$$

In this formula, the parameters μ and γ represent respectively the peak frequency and width of the lorentzian line shape, which is the limit at steady field. The parameters y_0 and A represent the offset and scale of the peak experimentally measured. The effect of drift is encompassed in the two parameters κ and $\delta\mu$, which are represented on the graph in figure 4.15 (b). The deviation of the field from its steady value at the beginning of the MW pulse corresponds to $\delta\mu$. The decay towards the steady value is characterized by the non-dimensional parameter κ. The latter is linked to the decay time τ of the field by the relation $\tau = T_0/\kappa$, where $T_0 = 12\,\mu\mathrm{s}$ is the MW pulse duration.

The fit of the data with the formula (4.9) gives $\mu = 45\,688.831 \pm 0.006\,\mathrm{MHz}$. From this value we recover, by inverting the Stark shift formula up to 3$^{\mathrm{rd}}$ order perturbation, a steady electric field $F_0 = 2.0887 \pm 0.0001\,\mathrm{V\,cm^{-1}}$. The width $\gamma = 89 \pm 5\,\mathrm{kHz}$ corresponds to field fluctuations of approximately $0.9\,\mathrm{mV\,cm^{-1}}$, hence an estimated[5] differential voltage noise of 1.6 mV on the electrodes. This value is consistent with the 1.2 mV precision of our waveform generator[6].

The fitted drift parameters $\delta\mu = 751 \pm 44\,\mathrm{kHz}$ and $\kappa = 5.5 \pm 0.4$ correspond to an initial field deviation of $7.51 \pm 0.44\,\mathrm{mV\,cm^{-1}}$ and a characteristic decay time $\tau = 2.2 \pm 0.2\,\mu\mathrm{s}$. The capacitance of the line is 2.7 nF, in parallel with a $60\,\Omega$ resistance (see appendix C), which gives a characteristic time of 160 ns, one order of magnitude below the value estimated from the spectroscopy.

4.3.3 Circularization and de-circularization efficiency

The demonstration of circular states trapping requires the spatially-resolved detection of those atoms that stayed in the trapping region during the whole sequence. Our approach consist in following the circularization procedure backwards and eventually catch ground-state atoms back in gaussian tweezers. The recorded arrival times corresponding to each step are shown in figure 4.16, towards the circular state (left), and backwards to 52D (right). Qualitatively, we observe that the 52F and 52D counts obtained after de-circularization are reduced as compared to the initial counts. Moreover, some population remains in the peak corresponding to the 52F after optimized MW transfer to 52D.

The determination of the efficiency of steps (4-5) is indirect. We cannot use fluorescence imaging since the free flight of atoms would result in a very weak signal. Neither can we use the raw counts as low-l-states evolution during the delay between preparation and ionization changes the populations and makes their interpretation difficult. We instead rely on ionization spectra for the 52F to 52D transfer, as shown in the right panel of figure 4.16. The latter essentially represents the combined efficiency of steps (3-5). The population in the state 52F gets transferred to 52c with elliptical impurities. The de-circularization brings back both circular and elliptical states to levels that appear in the same ionization peak as our desired 52F level. The latter gets transferred back to 52D with finite efficiency. What remains in the ionization peak of the state 52F is thus the residual population that has accumulated from the imperfections of the stages (3-5), as shown in the arrival times of figure 4.16 (curve in cyan). However, as mentioned earlier, the ion signal is by itself insufficient and must be

[5]The field response of each Stark electrode is 0.4 (V/cm)/V.

[6]This corresponds to a precision of 14 bits over a voltage range of $\pm 10\,\mathrm{V}$.

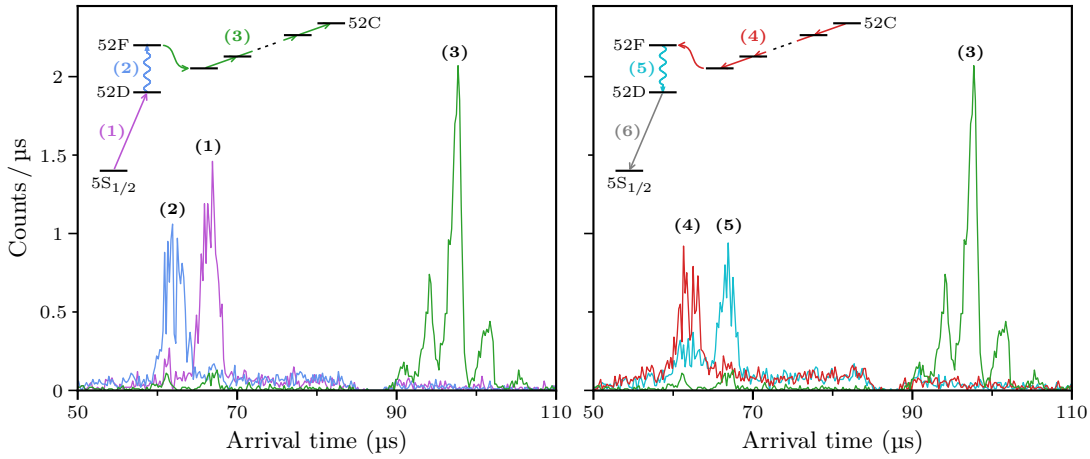

Figure 4.16: Arrival times corresponding to each step of the circularization (left) and de-circularization (right) procedure.

compared to a reference for which the efficiency is known. For this purpose, we use the signal pertaining to the 52D to 52F transfer, described in section 4.2.1, of which we know the efficiency. Thus, for 52D $\rightarrow$ 52F and 52F $\rightarrow$ 52D peaks of respective amplitudes A_{DF} and A_{FD}, the efficency $\eta_{\text{F-C-F-D}}$ is

$$\eta_{\text{F-C-F-D}} = \eta_{\mathrm{DF}} \frac{A_{\mathrm{FD}}}{A_{\mathrm{DF}}}. \tag{4.10}$$

We show in figure 4.17 the transfer 52D $\rightarrow$ 52F for both steps (2) and (5). To record the spectrum of step (5), we used another MW source which frequency was scanned (while the frequency for the 52D $\rightarrow$ 52F transition was kept fixed). Rather than adjusting the power to have a π-pulse at the same duration, we choose to adjust the pulse duration for an optimum at 1.1 µs. On these spectra note that step (5) leads to a less efficient de-population of the 52F state. From a fit of the two curves, we obtain

$$\eta_{\text{F-C-F-D}} = 0.49 \pm 0.04. \tag{4.11}$$

Table 4.1: Relevant quantities characterizing the BoB trapping potential. The potential was computed with the circular state oriented along the x direction.

Step	Detection method	Efficiency	Ref. eq.
$5S_{1/2} \rightarrow 52D$ (1)	Optical	0.89 ± 0.01	(4.4)
$52D \rightarrow 52F$ (2)	Optical	0.88 ± 0.01	(4.7)
$52F \rightarrow 52C$ (3)[a]	Ionization	0.90 ± 0.02	(4.8)
$52F \rightarrow 52C \rightarrow 52D$ (3-5)	Ionization	0.49 ± 0.04	(4.11)
$52D \rightarrow 5S_{1/2}$ (6)	Optical	0.89 ± 0.01	(4.4)
Total		0.34 ± 0.04	

[a] Not included in the computation of the total efficiency.

The results are summarized in table 4.1. They suggest that the backward population transfer from 52C to 52D (steps (4-5) on figure 4.16 (a)) is the bottleneck of the whole procedure.

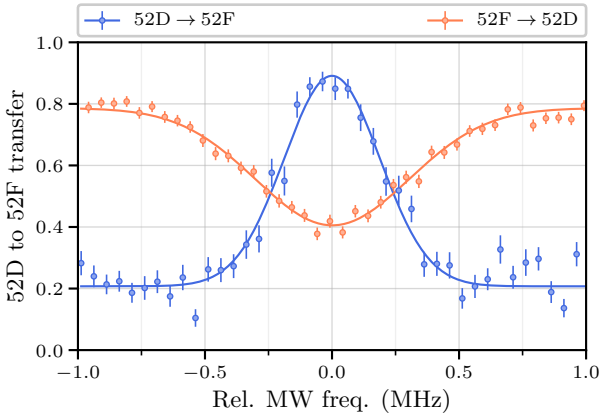

Figure 4.17: Spectroscopy of the 52D → 52F (step (2)) and 52F → 52D (step (5)) transitions. The latter is measured using a different MW source with more power, hence the shorter 1.1 µs-long pulse as compared to 1.8 µs for the former.

Conclusion

The transfer from the ground state to the circular state takes place in four stages. Although the general methodology is the same as in our previous works, some improvements have been made. Moreover, the use of optical tweezers, along with optical detection, brings new insights on the process.

The initial state is not well defined, it consists in a mixture of Zeeman sublevels of $\left|5S_{1/2}, F = 2\right\rangle$. The first step is the optical pumping to the state $\left|5S_{1/2}, F = 2, m_F = 2\right\rangle$. This was done with a σ^+-polarized laser tuned on the $\left|5S_{1/2}, F = 2\right\rangle \longrightarrow \left|5P_{3/2}, F' = 3\right\rangle$ transition. The hyperfine sub-levels of the ground state $\left|5S_{1/2}\right\rangle$ were probed by Raman spectroscopy. The spacing between the different peaks allowed us to determine the magnetic field $B = 7.01 \pm 0.02\,\mathrm{G}$. After optimization of the optical pumping, we obtained a state purity $\eta_{\mathrm{OP}} = 0.97 \pm 0.01$.

The next step is the laser excitation to the Rydberg state $\left|52D_{5/2}, m_j = +5/2\right\rangle$, for which we address a two-photon transition with $6P_{3/2}$ as the intermediate state. We recorded site-resolved spectra and Rabi oscillations on both the large 9×9 array used for the measurements presented in the previous chapter, and on a smaller 6×3 array of 18 traps having now a 15 µm spacing. This latter array was kept for the rest of the experiments and matches with the maximum number of BoB traps we were able to prepare, with large enough spacing to ensure weak interactions between Rydberg states. We used both ion and optical detection in these experiments, but the latter turned out to be more reliable for quantitative analysis. We obtained an excitation efficiency $\eta_{52\mathrm{D}} = 0.89 \pm 0.01$ for a π-pulse with an average Rabi frequency $\langle\Omega\rangle = 2\pi \times 660\,\mathrm{kHz}$. Our main limitation was the laser power at our disposal.

The third step consists in a microwave transfer to the state $|52\mathrm{F}, m_l = +2\rangle$. An analysis similar to that of the previous step concluded to a transfer efficiency $\langle\eta_{\mathrm{DF}}\rangle = 0.88$.

When we apply an electric field, the state 52F branches to the level that constitutes our starting point for the adiabatic transfer to the circular state 52C, as detailed in chapter 1. We proceeded in practice by ramping down the electric field from $2.25\,\mathrm{V\,cm^{-1}}$ to $2.05\,\mathrm{V\,cm^{-1}}$ in the presence of σ^+-polarized radio-frequency (RF) at 225 MHz. The RF signal was generated with an improved which we described.

After the transfer, we carried spectroscopic measurements to nearby states for further characterizations. We estimated the purity from the two-photon transition 52C ⟶ 50C.

The presence of lateral peaks corresponding to the transitions $52E^{\pm} \longrightarrow 50E^{\pm}$ indicated an imperfect adiabatic transfer. We nevertheless obtained a good purity, estimated as $\eta_{\mathrm{circ}} = 0.90 \pm 0.02$. The transition $52C \longrightarrow 53E^{+}$ is insensitive to the magnetic field, and allowed us to determine the electric field $F_0 = 2.0887 \pm 0.0001\,\mathrm{V\,cm^{-1}}$.

Finally, the optical detection of circular states currently requires us to de-excite them to the ground state, which appeared to be less efficient than the excitation. Combining the total efficiencies we obtained a global value $\eta_{\mathrm{tot}} = 0.34 \pm 0.04$.

The optical detection proved a valuable tool for the diagnostic of the experimental conditions pertaining to the processes presented in this chapter. The trapping of circular states, which we describe in the next chapter, will continue in this direction by offering the possibility for optical detection over long timescales.

Chapter 5

Ponderomotive trapping of circular states

How long is forever?
Sometimes just one second.

— Lewis Carroll, *Alice in Wonderland*

Having prepared cold ground-state atoms in tweezers and described the procedure to transfer them to the (circular) Rydberg state with good efficiency, we are ready to tackle the problem of the trapping of atoms in the Rydberg state. We thus present here the main results of this thesis, and pave the way for subsequent work on inter-atomic interactions and, in the longer term, on quantum simulation.

The topic of Rydberg atom trapping is not new and some strategies have already been proposed and implemented. One approach consists in using the second valence electron of alkali-earth atoms for dipole trapping. This has been achieved for instance with strontium in [52, 53] and ytterbium in [54]. The second approach takes advantage of the ponderomotive force exerted on the Rydberg electron. Successful implementations of three-dimensional trapping include [69] (with an optical lattice) and [84] with one or two individual bottle-beam (BoB) traps. Here we extend the latter method to produce not only one or two but arrays of ponderomotive BoB traps, allowing for more flexibility than a definite regular lattice.

Before describing the traps in detail, we begin by demonstrating the ponderomotive trapping of circular Rydberg states with our setup. We anticipate the full presentation and analysis for both low-l and circular states by reporting in figure 5.1 the early demonstration of circular states trapping. The data were obtained before the failure of one of our Rydberg excitation lasers, as mentioned in section 4.1.2. We observed no atomic loss apart from the natural thermal decay of the population over 1 ms of trapping. Some analysis of these data is provided in appendix E.

The detailed description of the traps follows in the next section, where we also introduce the experimental characterization of the traps. Although, as we will show, the trapping potential to which the circular states are subject is complex, the characterization is limited to the transverse trap frequency.

The trapping of atoms in the Rydberg state is, of course, paramount to the control of the inter-atomic distance, and, *in fine*, to that of the interactions. However, in this work, the

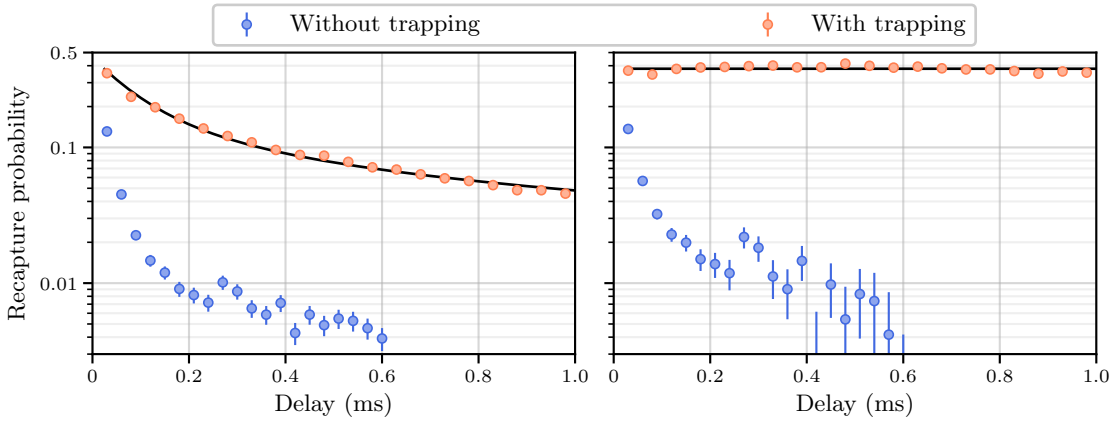

Figure 5.1: Early demonstration of circular states trapping. Left panel: raw data. Right panel: data corrected from natural population decay at 300 K.

interactions are not studied and even avoided by imposing a spacing of 15 µm between traps. We recall from chapter 1 that the interaction nC–nC is in the kHz-range (with a difference of about 100 Hz between $n = 50$ and $n = 52$). The exchange interaction, with $\Delta n = 1$ is three orders of magnitude larger and lies in the range 0.5–1 MHz in our geometric configuration.

We take advantage of Rydberg trapping in the majority of the experiments described in this chapter. Indeed, the trapping makes it possible to use optical detection even when running 100 µs-long sequences that would otherwise lead to the loss of almost all atoms from free flight out of the trapping region. As it was the case in the two previous chapters, the spatially-resolved measurements of the chapter give useful information on the experimental conditions and open the possibility for the fine-tuning of the parameters. This is illustrated in the last section, devoted to the study of the effect of trapping on thermal population transfer and coherent state manipulation.

5.1 Ponderomotive trapping of Rydberg states

The trapping of Rydberg states is achieved by producing an array of hollow bottle beams overlapped with the gaussian tweezers. A false-color camera picture of both arrays is shown in figure 5.2. The figure also shows the theoretical BoB intensity profile, the Rydberg atoms being contained in the low intensity region. Mechanical losses of atoms are most likely along the escaping directions indicated as dashed lines on the yz-section of the profile.

In this section, we keep an empirical approach to the trapping and its study is reduced to the investigation of mechanical losses. The detailed structure of the potential is not considered here, as this will be the topic of the next section. We first describe the trapping of the 52D level prepared by laser excitation. Elements of analysis are introduced in this simpler context before moving on to the more complex case of circular states.

In probing the trapping, we are primarily limited by the lifetime of the considered state. In the case of 52D, this limits us to a maximal trapping duration of 400 µs. For 52C, despite a room temperature lifetime of ~ 130 µs, we are able to probe the trapping for 5 ms thanks to the specific state dynamics of thermal transfers between circular levels that maintains a fraction of the initial population over an extended timescale. Let us note that this is still a short duration as compared to what is possible in a cryogenic environment [94], where the lifetimes have been observed to be longer by a factor of approximately 30.

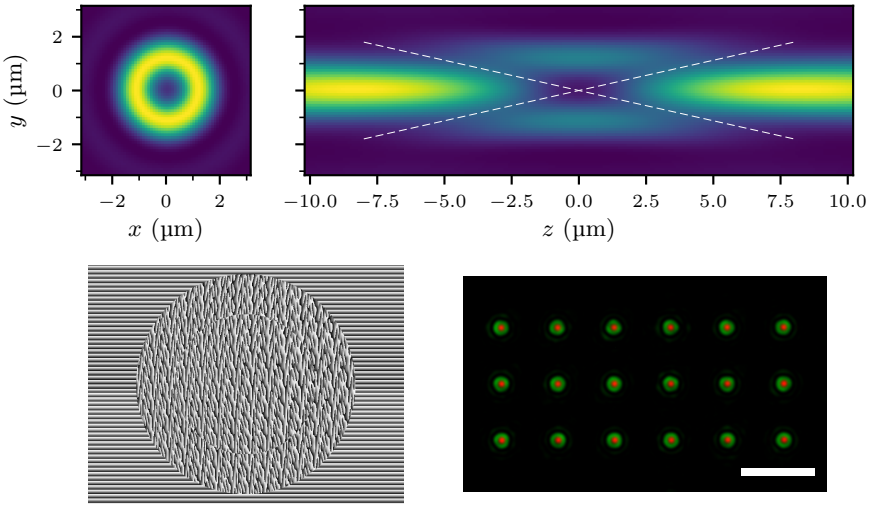

Figure 5.2: BoB traps for Rydberg trapping. Top: xy and yz-cuts of the theoretical profile of a single BoB trap; the escaping directions are shown as dashed line on the yz section. Bottom: phasemask used to generate the 6×3 array of BoBs presented in the right panel; the gaussian tweezers (in red) overlap the BoB traps (in green). White scale bar: 20 µm.

Let us recall that due to the laser power limitation, we work with a rectangular array of 6×3 trapping sites spaced by 15 µm. We have approximately 20 mW of laser power per BoB trap.

5.1.1 Trapping of 52D

We begin by demonstrating the trapping of atoms in the state 52D obtained after laser excitation. This allows us to get more signal by getting rid of the technical aspects and imperfections of the circularization and de-circularization process. Moreover, the possible outcomes leading to the recapture or loss of an atom at the end of the sequence are simpler for the state 52D than for circular states.

Indeed, the many decay channels available to low-l states essentially make the decay of 52D irreversible. On the one hand, the radiative decay towards low-n states via optical transitions is one-way as there is no light at these wavelength in the environment. On the other hand, the black-body radiation induced decay brings the atoms to nearby Rydberg states that in turn have many possible decay channels, hence a negligible probability of return. The evolution of the 52D population can be considered as an exponential decay, with its characteristic time as a single parameter. This leads to an easier interpretation of the results and serves as a good preliminary study before introducing the more complex evolution of circular states.

The experimental sequence, shown in figure 5.3 (a), consists in switching on the BoB traps for a variable duration Δt after the laser excitation, followed by another laser pulse to send the remaining 52D population back to the ground state. Gaussian tweezers are present before and after the two π-pulses with minimal delay to release and recapture ground-state atoms. The results are presented in figure 5.3 (c), in which we compare the recapture probabilities with or without BoB trapping as a function of the delay Δt. We observe a fast decay in the absence of BoB traps (blue discs) as compared to the trapping condition (orange discs), which is the signature of Rydberg-state trapping.

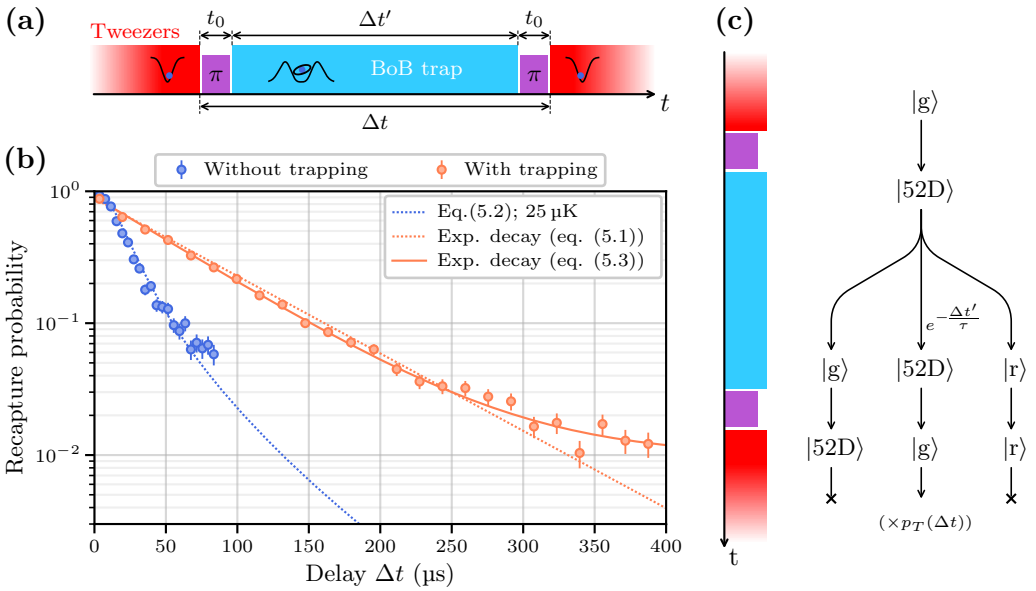

Figure 5.3: Ponderomotive trapping of atoms in the state 52D. (a) Scheme of the experimental sequence. The laser excitation is indicated as purple rectangles, during which both types of traps are off for a duration $\sim 2\,\mu s$. (b) Averaged recapture probability with and without trapping. The lines corresponds to the various models described in the text. (c) Simplified scheme for the possible outcomes during the sequence. The population in the state 52D decreases due to its finite lifetime, and additional losses occurs when the traps are off.

To understand the qualitatively different data obtained in the two conditions, we must consider the evolution of the states during the sequence. We schematize it in figure 5.3 (c) We begin with atoms in the optically-pumped state $|5S_{1/2}, F = 2, m_F = +2\rangle$, denoted $|g\rangle$. The Rydberg excitation transfers the population to the state $|52D\rangle$. The latter subsequently evolves for a duration $\simeq \Delta t' = \Delta t - 2t_0$, where t_0 represents the duration of the Rydberg excitation. At the end of this period and just before the second laser pulse, the initial state may have decayed either to another Rydberg state $|r\rangle$ through a transition (or more) induced by black-body radiation or to the ground state $|g\rangle$. The second π pulse then exchanges $|52D\rangle$ and $|g\rangle$ populations but does not affect $|r\rangle$. For the sake of simplicity, we assume here that the optical pumping is perfect and that the Rydberg excitation has unit efficiency.

The presence of optical traps leads to mechanical losses depending on the atomic state. First, Rydberg states are expelled by the gaussian tweezers that we switch back at the end of the sequence. Second, when present, the BoB traps capture ground state atoms in their high intensity lobes far from the focus of gaussian tweezers. This leads to the loss of most atoms independently of their state, but it also acts as a reservoir of atoms for the gaussian tweezers that get populated with a small probability at the end of the sequence. We also assume this process to be negligible.

With these simplifications, the interpretation of the data is straightforward. The recapture probability in the presence of the traps is essentially the surviving fraction of $|52D\rangle$ at the end of the delay, combined with possible mechanical losses. In the absence of trapping, we must also take into account the free flight of atoms.

We now introduce some notations to get quantitative formulas for the recapture probability in both conditions. We denote by τ the lifetime of $|52D\rangle$ at 300 K, and $p_T(\Delta t)$ the recapture probability after a free flight of duration Δt for an atom initially trapped at a

temperature T. Assuming that the atoms do not escape from the BoB traps, the recapture probability $p_{\text{trap}}(\Delta t)$ in their presence is simply

$$p_{\text{trap}}(\Delta t) = e^{-\frac{\Delta t'}{\tau}} = e^{-\frac{\Delta t - 2t_0}{\tau}}. \tag{5.1}$$

In the absence of BoB traps, we have

$$p_{\text{free}}(\Delta t) = p_T(\Delta t) e^{-\frac{\Delta t'}{\tau}}. \tag{5.2}$$

The parameters of our models are fixed. The Rydberg excitation duration t_0 is a sequence setting. The lifetime $\tau = 74\,\mu\text{s}$ is computed using the Alkali Rydberg Calculator package [122]. Finally, the quantity $p_T(\Delta t)$ is computed from Monte-Carlo simulations (see section 3.3.2), with a measured temperature $T = 25\,\mu\text{K}$.

In order to partially account for imperfections of the experimental steps such as the optical pumping and laser excitation, we include a global scaling factor to both[1]. The contribution from t_0 can be included in this factor, hence we also remove this parameter. These models are plotted as dashed lines on figure 5.3 (b). The free flight model of eq. (5.2) fits the data well, with a scale factor equal to 0.94. A discrepancy nevertheless is discernible at the final delays, around 80 µs, yet not precise enough to be analyzed.

The data in the presence of trapping is in good agreement with the constrained model of eq. (5.1), represented as a dashed orange line on figure 5.3 (a). Further insight can be obtained by fitting the data with an exponential decay

$$p_{\text{trap}}(\Delta t) = A e^{-\frac{\Delta t'}{\tau}} + y_0, \tag{5.3}$$

with amplitude A, offset y_0 and decay time τ kept as free parameters. The fitted curve is represented as a dashed orange line on figure 5.3 (b). The fit gives an offset of approximately 1%, possibly due to the BoB traps acting as a reservoir of decayed ground-state atoms, as mentioned above.

We note a difference between the fitted and theoretical decay times $\tau_{\text{fit}} = 66 \pm 1\,\mu\text{s}$ and $\tau = 74\,\mu\text{s}$. Assuming that the fitted values encompasses another loss mechanism, the corresponding characteristic time is $\tau' = \tau\,\tau_{\text{fit}}/(\tau - \tau_{\text{fit}}) = 600 \pm 90\,\mu\text{s}$. This value is larger than the maximum trapping duration in the above experiment, which shows its limitations to probe the possible loss mechanisms. The increased decay can originate from mechanical losses, but also from photo-ionization processes to which low-l states are possibly subject to.

We can use the photo-ionization cross sections measured in [139] to get a more quantitative insight on this process. From figure 14 of [139], we extract a cross-section $\sigma_{\text{pi}} \simeq 1.2 \times 10^{-24}\,\text{m}^2$ for 50D and a trapping laser wavelength $\lambda_{\text{L}} = 1.01\,\mu\text{m}$. Using the order of magnitude $\sigma_{\text{pi}} \sim 10^{-24}\,\text{m}^2$ for 52D at our trapping laser wavelength $\lambda_{\text{L}} = 821\,\text{nm}$ (thus a pulsation $\omega_{\text{L}} = 2\pi \times 365\,\text{THz}$), we estimate the photo-ionization rate

$$\Gamma_{\text{pi}} = \frac{I_0 \sigma_{\text{pi}}}{\hbar \omega_L} \sim 430\,\text{s}^{-1}, \tag{5.4}$$

where we used the laser intensity at the bottom of our traps $I_0 = 1.04 \times 10^8\,\text{W m}^{-2}$. The associated characteristic time is about 2.3 ms, not far from the value $\tau' = 600\,\mu\text{s}$ found above. This is especially true considering that the average laser intensity seen by the atoms is larger due both to the spatial extension of the Rydberg wavefunction and to the residual atomic motion.

[1] A more detailed analysis would show that the experimental imperfections have a more complex effect than a simple rescaling. However, our data are not precise enough to be sensitive to such effects.

5.1.2 Trapping of circular states

We now describe the trapping of circular Rydberg atoms, which is our ultimate goal in the context of this work. The experimental sequence is reported in figure 5.4 (a). It is similar to that of 52D trapping, yet was subject to one adjustment in order to improve the signal. After the optical pumping, we further cool down the atoms by decreasing the tweezers power from a depth of 1 mK to approximately 100 µK. This is done by filtering the stepping down of the control voltage with an RC filter having a damping time of 500 µs. Through this procedure, we reduce the atomic temperature to 4 µK. The sequence also adds-up an incompressible duration to circularize at the beginning and de-circularize at the end of BoB trapping. The sensitivity of states to the BoB traps light within the Rydberg manifold is weak enough to allow us to perform the circularization in the presence of the BoBs. The whole circularization (including the laser excitation) takes approximately 15 µs, hence a minimal delay of 30 µs.

Figure 5.4 (b) presents the averaged recapture probability, again, with or without BoB trapping. A first remark concerns the recapture at minimal delay. Contrary to the case of 52D trapping, we only reach $\sim 36\%$ recapture at minimal delay with trapping. This is in good agreement, albeit slightly higher than the efficiency $\eta \simeq 34\%$ of the whole circularization and de-circularization procedure obtained in section 4.3.3. Despite this, the occurrence of trapping is manifest, with a significant fraction of recaptured atoms, even after a trapping duration of a few ms.

The analysis of the recapture is analogous to that of the previous section, except that we must consider the more complex evolution of 52C instead of the simple exponential decay of 52D. We thus introduce $\rho_{52C}(t)$ the fraction of the population in the state 52C after a delay t, assuming a pure 52C state at $t = 0$. The expected recapture probability in the presence of trapping is then

$$p_{\text{trap}}(\Delta t) = \eta\, \rho_{52C}(\Delta t'), \tag{5.5}$$

and without trapping, is

$$p_{\text{free}}(\Delta t) = p_T(\Delta t)\eta\, \rho_{52C}(\Delta t'). \tag{5.6}$$

In the same manner as in the previous section, the relevant evolution duration $\Delta t'$ is shorter than the delay Δt. We have $\Delta t' = \Delta t - 2t_0$, where $t_0 = 12$ µs now represents the time not spent in the circular state during the circularization and de-circularization processes[2]. The quantity ρ_{52C} is obtained by solving the master equation described in [95] with the black-body temperature, 300 K, as the only parameter.

We first discuss the data obtained without Rydberg trapping. The recapture probability drops quickly and reaches 0.25% in approximately 500 µs. This value essentially corresponds to the probability $p_{\text{gen}} = 0.16 \pm 0.08\%$ of appearance of an atom in an initially unloaded trap, which indicates that essentially all atoms are lost at this delay. To get a quantitative description, we use the model of eq. (5.6) to fit the temperature T and efficiency η, yielding respectively $T = 18 \pm 3$ µK and $\eta = 0.50 \pm 0.01$. The fitted temperature is significantly higher than that measured on ground-state atoms, 4 µK. On the left panel of figure 5.4 (a), we show two simulated curves, with $T = 18$ µK and $T = 4$ µK, the latter being normalized by imposing that it crosses the experimental data at minimal delay ($\Delta t = 30$ µs). The curves both take into account the 52C population decay, itself shown as a black solid line on the figure (with appropriate normalization, which will be discussed later). The mismatch between the data and the simulation with $T = 4$ µK indicates that the atoms are expelled faster than expected from the trapping region, and suggests an effect of interactions.

[2] This is shorter than the 15 µs-long procedure as the latter includes some field settling time and additional delays to re-initialize the voltages sources.

The recapture probability is significantly higher at all times in the presence of BoB traps, which is a clear signature of circular states trapping. The data overlaps well at moderate delays $\lesssim$500 µs with the properly scaled theoretical population. However, the two curves separate at higher delays, indicating an additional loss of population in the traps. Nevertheless,

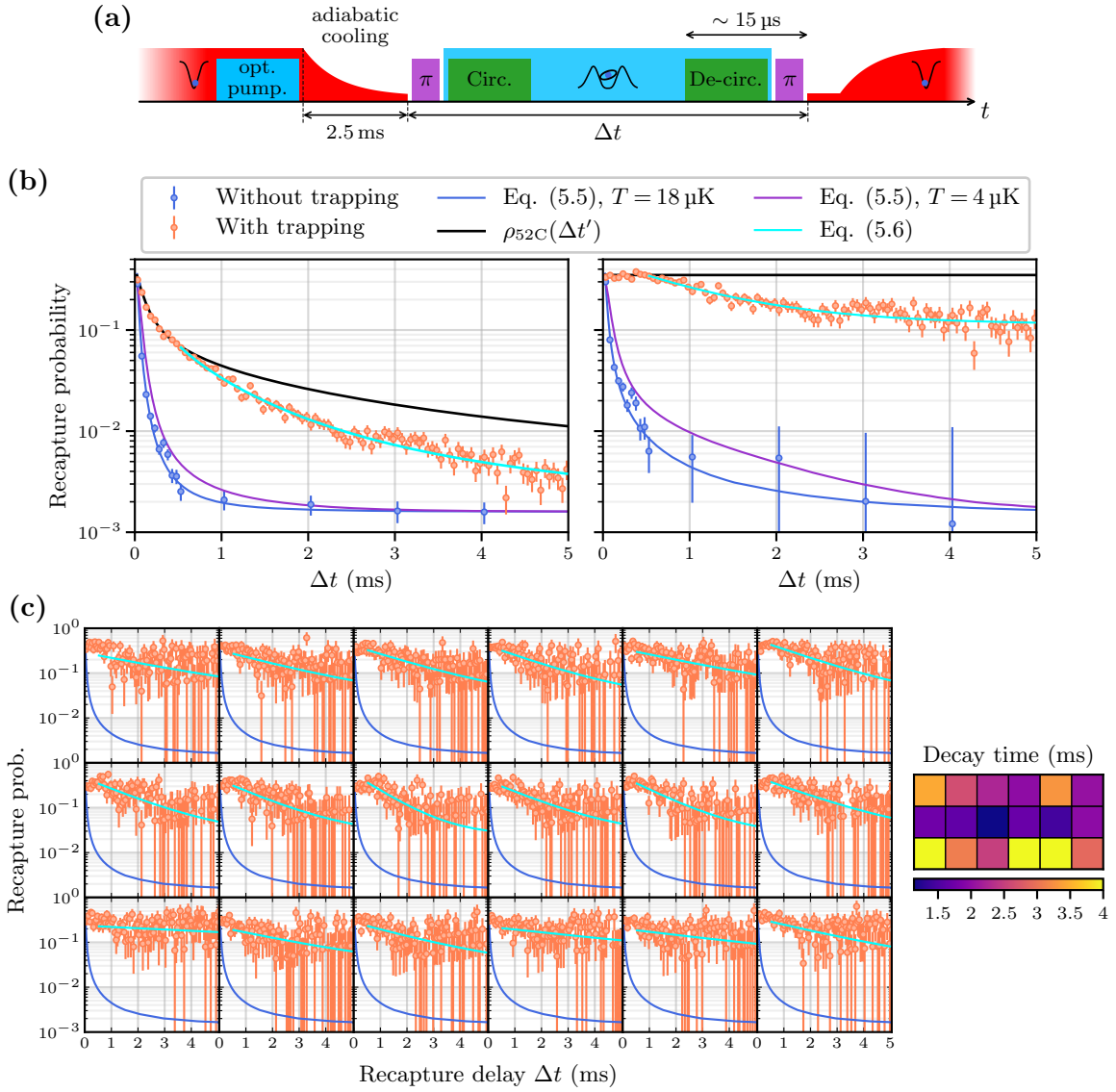

Figure 5.4: Ponderomotive trapping of circular Rydberg atoms. (a) Scheme of the experimental sequence. (b) Average recapture probability obtained without (blue discs) and with (orange discs) trapping. Left: raw data. The black solid line corresponds to the theoretical population of the state 52C, at 300 K, according to [95], properly scaled to the data. Right: data corrected by the theoretical population of 52C. The two panels also show various models used to fit the data; they are detailed in the main text. (c) Recapture probability for individual trapping sites. The data is re-scaled by the theoretical population as in the right panel of (b). The statistics in the absence of trapping are not good enough to allow for a good visualization. Accordingly, we plot instead the curve fitted on the averaged data for a clearer comparison. We show on the right panel the map of characteristic times from exponential fits of the decaying portion of the curve, after 500 µs.

this reduction is only partial even at the maximal delay of 5 ms. This is highlighted in the right panel of figure 5.4 (b), where we present the recapture probability corrected from the 52C population decay. In order to analyze this decay more quantitatively, we empirically model the excess losses $p_{\mathrm{trap}}/\rho_{52\mathrm{C}}$ by a decaying exponential:

$$\frac{p_{\mathrm{trap}}}{\rho_{52\mathrm{C}}}(\Delta t > \Delta t_0) = Ae^{\frac{-\Delta t-\Delta t_0}{\tau}} + y_0, \tag{5.7}$$

where $\Delta t_0 = 500\,\mu\mathrm{s}$ is the time at which the decay begins. As an illustration we obtain, for the averaged signal, $\tau = 1.1 \pm 0.1\,\mathrm{ms}$, with a significant offset $t_0 = 0.114 \pm 0.007$. These values are difficult to interpret for the averaged data, but the model 5.7 is nevertheless useful to compare the decay for different trapping sites. We thus obtain the color map presented in the right panel of figure 5.4 (c). The decay, $\langle\tau\rangle = 3.3\,\mathrm{ms}$, $\mathrm{Std}(\tau) = 2.9\,\mathrm{ms}$ is skewed by three outliers having values of 14 ms, 6 ms and 5 ms. Moreover, the fits suffer from a large uncertainty in the optimal decay time. Let us limit ourselves to the qualitative observation from the individual plots (with population decay correction) of figure 5.4 (c) that the trapping efficiency seems homogeneous over the whole array of BoBs. With all due reservations on the soundness of the fitting procedure, the color map indicates a possible excess loss from the traps that lie in the center of the array. These sites corresponds to atoms having the most neighbors, which hints, again, at a possible effect of the interactions.

Let us finally mention a mechanism through which the interactions are likely to play a role in the atomic motion, leading to the fast drop of recapture probability without trapping, and to the excess loss of atoms in the presence of the traps. A heating mechanism[3] may originate from the stochastic evolution of circular states, together with the dipole interaction. The interaction between two circular states is strong when we have $\Delta n = \pm 1$, and rather weak otherwise. Starting with a pair of $n = 52$ circular states, the interaction becomes stronger when one of them decays thermally, say, to $n = 51$. We now have $\Delta n = 1$, which causes the atoms to be attracted or repelled more strongly, and pushes them to regions of higher trapping potential. However, any subsequent thermal decay will lead to $\Delta n = 0$ or 2 and thus the force holding them on the edges of the trap will vanish. The atoms may gain mechanical energy through this mechanism.

Order of magnitude estimation of the effect of the exchange interaction

We gave in chapter 1 an order of magnitude estimate of the interaction energy for a first-order dipole coupling. We have $A_3/R^3 \sim 1\,\mathrm{MHz}$ for an inter-atomic distance of $R = 15\,\mu\mathrm{m}$. This added potential has an effect of both free atoms (no trapping condition) and on trapped atoms.

Free atoms subject to this interaction are pushed outside the trapping region. This leads to a faster decay of the recapture than what would be expected if the atoms simply had a velocity corresponding to their initial temperature. Using the above interaction energy, we get a corresponding acceleration

$$\frac{3}{M}\frac{A_3}{R^4} \sim 10^{-3}\,\mu\mathrm{m}\,\mu\mathrm{s}^{-2}, \tag{5.8}$$

where M denotes the mass of ^{87}Rb. With this acceleration, atoms initially at rest are displaced by 1 µm in approximately 50 µs, and acquire a kinetic energy that corresponds to a temperature of $\sim 10\,\mu\mathrm{K}$.

[3] Or at least an increase in average mechanical energy.

For trapped atoms, the interaction adds up a term to the trapping potential, causing the minimum to shift slightly in position. This displacement in turn induces atomic motion in the trap, increasing the mechanical energy of atoms. We can estimate the displacement of the potential (assumed harmonic) by linearizing the interaction near the inter-atomic distance R. The potential thus becomes, along the interatomic distance denoted x,

$$\begin{aligned} V(x) &= \frac{1}{2}M\omega^2 x^2 - 3\frac{A_3}{R^4}x \\ &= \frac{1}{2}M\omega^2(x-x_0)^2 + C, \end{aligned}$$

with

$$x_0 = \frac{3A_3}{M\omega^2 R^4}. \tag{5.9}$$

For a trap frequency $\omega = 2\pi \times 16\,\mathrm{kHz}$, we get $x_0 \sim 90\,\mathrm{nm}$ associated to an energy shift $\frac{1}{2}M\omega^2 x^2 \sim k_\mathrm{B} \times 0.5\,\mu\mathrm{K}$. Such a displacement following random thermal population transfers between circular state is indeed likely to effectively "heat-up" the atoms. However, the above quick estimation does not give the precise rate and dynamics of this mechanism, which should be studied through more refined simulations.

5.2 Characterization of the traps

The trapping of a Rydberg atom relies on the ponderomotive force exerted by the oscillating laser field on the Rydberg electron. We recall from chapter 1 the formula for the ponderomotive potential generated by a laser of intensity $I(\mathbf{r})$ and pulsation ω_L:

$$V(\mathbf{r}) = \frac{e^2}{2m_e\varepsilon_0\, c\omega_L^2} I(\mathbf{r}), \tag{5.10}$$

with e the elementary charge, m_e the electron mass, ε_0 the vacuum permittivity and c the speed of light.

The trapping potential exerted on the Rydberg atoms in our experiment cannot be reduced (up to a proportionality constant) to the simple theoretical intensity profile of the BoB traps. An intrinsic reason for this is that the laser intensity must be averaged over the electron orbit to get the trapping potential at a given point [82]. This, together with the strong anisotropy of the circular Rydberg electron wavefunction, leads to a non-trivial trapping potential, dependent on the orientation of the circular orbit.

Extrinsic factors also influence the trapping potential by causing deviations of the light intensity profile from the ideal case. Among these factors we can cite interferences between neighboring traps, optical aberrations introduced by the setup (to which the BoBs are very sensitive) and the limitation of the SLM itself. In particular, the fact that the SLM cell must be used to prepare not only one but the 6×3 array of BoBs leads to the appearance of speckle light that deforms the intensity pattern.

In order to properly describe the BoB traps, we begin by giving a theoretical description of the trapping potential, for an ideal BoB. We cannot directly measure the intensity profile in the experiment since the second lens of the sapphire cube adds up aberrations that deform the beam. Our only possibility to probe the actual trap profile is to perform *in situ* measurements. The theoretical discussion is thus followed by an experimental characterization of the traps. In doing so, we limit ourselves to a measurement of the transverse trap frequency by inducing oscillations in the trap.

5.2.1 Description of the traps

Using the ponderomotive force to trap circular Rydberg atoms imposes us to prepare light patterns consisting in a low intensity region surrounded by light. This requirement strongly constrains the shape of the potential, and in particular that of BoB traps which were the retained solution for trapping circular states.

We describe here the important features of the BoB traps, that are essential to interpret the experimental results that follow. A more detailed study is provided in appendix D, where we analyze among other things the impact of the trapping on the coherence, which is of primary importance in the prospect of quantum simulation.

Principle of BoB preparation

A bottle beam intensity pattern is obtained by making two beams of differing size interfere [140]. In the context of optical tweezers preparation, we achieve this by imprinting a π phase shift to the central part of the SLM. The incoming beam can be split in two components, with a π phase shift between the two. The inner part produces a beam with a large extension at the lens focus, in which the more tightly focused outer part digs a dip because of the destructive interference.

To make a more quantitative description, let us introduce some notations for the parameters used. We thus define

- k, the wavenumber of the laser beam;
- $a = 5.5\,\mathrm{mm}$, the pupil radius;
- f, the focal length of the lens;
- s, the radius of the disc on which a π phaseshift is applied for BoB preparation;
- I_{prof}, the intensity profile of the beam hitting the SLM.

The phase mask imprinted on the SLM only depends on the distance r to the center of the pupil. To produce a single BoB, it consists in a phase shift of π for $r < s$ and zero for $r > s$. The expression of the bottle beam amplitude at a distance ρ from the optical axis and z from the focal plane $z = 0$ is

$$A(\rho, z) = A_0 \mathcal{F}\left[\mathbf{1}_{r<a} I_0(r) e^{ikz\frac{r^2}{2f^2}} e^{i\pi \mathbf{1}_{r<s}}\right]. \tag{5.11}$$

Here A_0 is a complex scaling factor, and $\mathbf{1}_X$ denotes the characteristic function of the set X:

$$\mathbf{1}_X(x) = \begin{cases} 1, & \text{if } x \in X \\ 0, & \text{otherwise.} \end{cases} \tag{5.12}$$

The intensity profile corresponds *a priori* to a gaussian beam clipped at the pupil radius. However, a more refined analysis yields the following empirical formula

$$I_{\mathrm{prof}}(r) = I_0\left(\alpha + e^{-\frac{2r^2}{w^2}}\right). \tag{5.13}$$

The intensity offset α and waist w were fitted to give $\alpha = 0.1$ and $w = 4\,\mathrm{mm}$. A few words are in order to explain and justify the difference with respect to an ideal gaussian beam. Despite the fact that our aspheric lenses have an anti-reflection coating, the latter is optimized at normal incidence. However, albeit valid at the center of the lens, this normal incidence

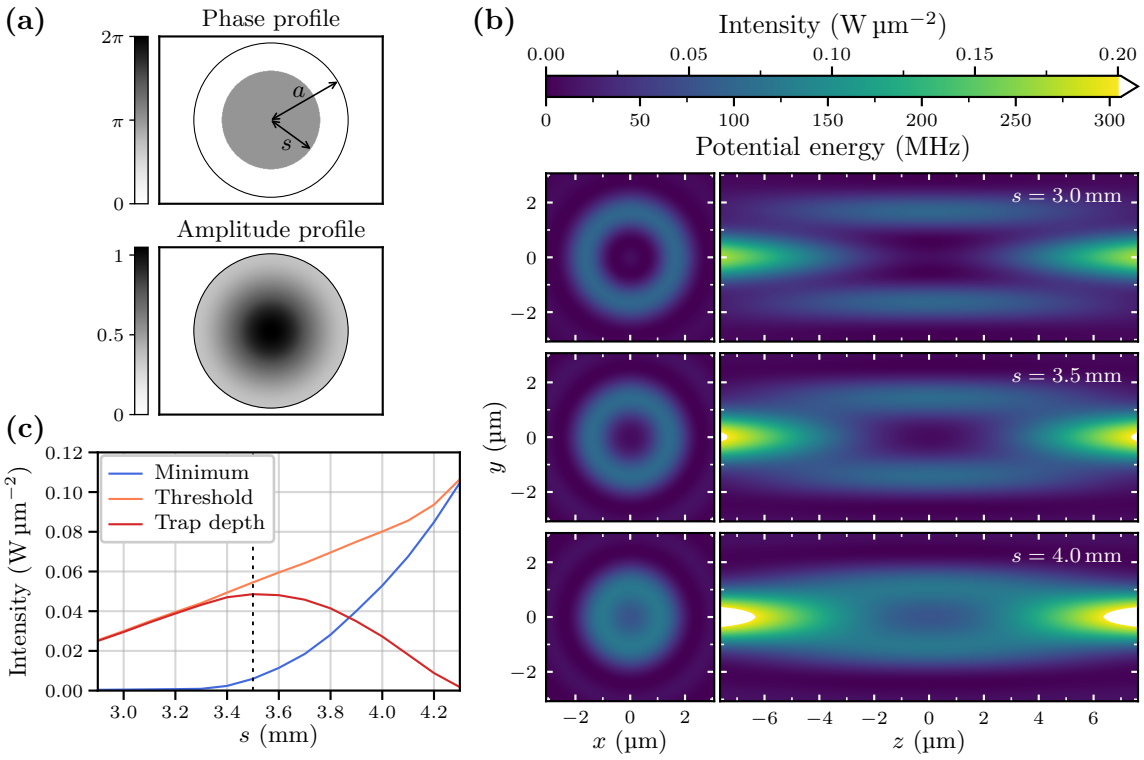

Figure 5.5: Description of the BoB intensity profile. (a) Representation of the phase and amplitude profiles pertaining to our experimental conditions for single BoB generation. We have $a = 5.5\,\text{mm}$ and $r = 3.5\,\text{mm}$. (b) Sections of the corresponding BoB intensity profile for (from top to bottom) $r = 3,\ 3.5$ and $4\,\text{mm}$. The scale is normalized to $1\,\text{W}$ total power in the beam. (c) Minimum and threshold intensity defining the trapping region as a function of the phase shift radius r. The trap depth is the difference between the threshold and the minimum.

condition is not satisfied for the outer part of the incident beam, hence some undesired reflection occurs. The latter leads to a reduction of the intensity at the edge of the beam, that we effectively describe by a modified intensity profile on the SLM.

This empirical amplitude profile $\sqrt{I_{\text{prof}}}$, along with the phasemask used are presented in figure 5.5 (a). We show, in figure 5.5 (b), cuts of the resulting BoB intensity profiles for different values of the parameter s. When the value is too low (upper panel), the BoB is open on the sides and non-trapping. On the contrary, when too high, the BoB becomes tight and shallow with significant light intensity at the center.

We report on figure 5.5 (c) the residual light intensity at the bottom of the BoB trap, along with the threshold intensity (the light intensity at the saddle points of the trapping walls). We also plot the corresponding trap depth, which is the difference between the threshold and minimum intensity. The trap depth is maximal for $s = 3.5\,\text{mm}$, the retained value for our experiments. The residual light intensity at this value is of the order of 10% of the threshold intensity, which is not a problem given that circular states are insensitive to photo-ionization. *Dark BoBs*, having zero intensity at their center, correspond to $s = 3.3\,\text{mm}$ and suffer from a lower trap depth.

In contrast with the theoretical idea behind the preparation of a bottle beam, our actual implementation differs significantly. Apart from the subtleties related to the effective intensity

on the SLM, the main difference lies in the more complex mask required to prepare not only a single trap but a whole array. Insights from section 3.2 hints at the possibly important fluctuations of BoB trap shapes as we explore a large field of the lens with higher sensibility to aberrations.

The trapping potential

The ponderomotive force is exerted on the electron, itself bound to the Rb^+ core. Under the Born-Oppenheimer approximation [82], the resulting atomic trap potential U is the convolution between the Rydberg electron wavefunction and the potential of eq. 5.10. For an atom located at position $\mathbf{R}$, we thus have

$$U(\mathbf{R}) = \int V(\mathbf{R}+\mathbf{r})|\psi(\mathbf{r})|^2 \,\mathrm{d}^3\mathbf{r}, \tag{5.14}$$

where $\psi(\mathbf{r})$ denotes the Rydberg electron wavefunction evaluated at relative position $\mathbf{r}$ from the ion core.

In the case of circular states, the charge density $|\psi_n(\mathbf{r})|^2$ of the Rydberg electron (see eq. 1.45) is a torus whose axis is parallel to the quantization axis (set by the electric field). The trapping potential of a circular Rydberg atom in a BoB trap thus depends on the orientation of the quantization axis. This is illustrated with the sections presented in figure 5.6 (a). We computed the convolution (5.14) of the theoretical BoB intensity profile with the charge density corresponding to the circular state $|52C\rangle$ for the three quantization axes x, y and z. We present the difference with the effective potential for a point-like Rydberg orbit $|\psi(\mathbf{r})|^2 = \delta^{(3)}(\mathbf{r})$, which is directly proportional to the light intensity. In the case of a transverse quantization axis, the real potential is not cylindrically symmetric anymore.

To further quantify this, the convolution was computed with the circular states nC for $48 \leq n \leq 54$. Some characteristics of the trapping potentials thus obtained are reported in figure 5.6 (b). We compare the values with those of the reference point-like orbit introduced above. The reference values are indicated as a red horizontal line on each panel and are approached asymptotically as $n \to 0$. The trap potential is slightly shallower by approximately 1% with respect to the reference. This tendency is more pronounced when the quantization axis is axial (along the z-axis), and the effect increases with n. This is expected as the intensity pattern gets more averaged-out as the wavefunction extension increases.

In addition to the minimum energy and trap depth introduced previously, we also plot the trap frequencies along the three spatial directions x, y and z. We distinguish two cases, depending on the orientation of the quantization axis: axial or transverse. Their behavior is more complex. The axial frequency essentially decreases, which reflects the increase of the minimum energy: the potential gets more "flat" along the z-axis. On the contrary, the transverse frequency increases as the charge distribution gets closer to the lateral walls.

The results presented in this chapter were obtained with a transverse quantization axis, set along x. The corresponding data is indicated as discs on the plots of figure 5.6 (b-c). The experimental results presented in the next sections involve the state 52C or transitions between 52C and 50C. To this end, we present in tables 5.1 and 5.2 some relevant quantities that characterize the trapping potential under our experimental conditions for these two states. In particular we compare the values with the reference point-like Rydberg state.

The important energy scales of the BoB traps are reported in 5.1, for a BoB trap produced with 1 W laser power. They are represented by the trap depth and the energy shift at the center. The state dependence, in the 0.1% range, is essentially unimportant, save for the

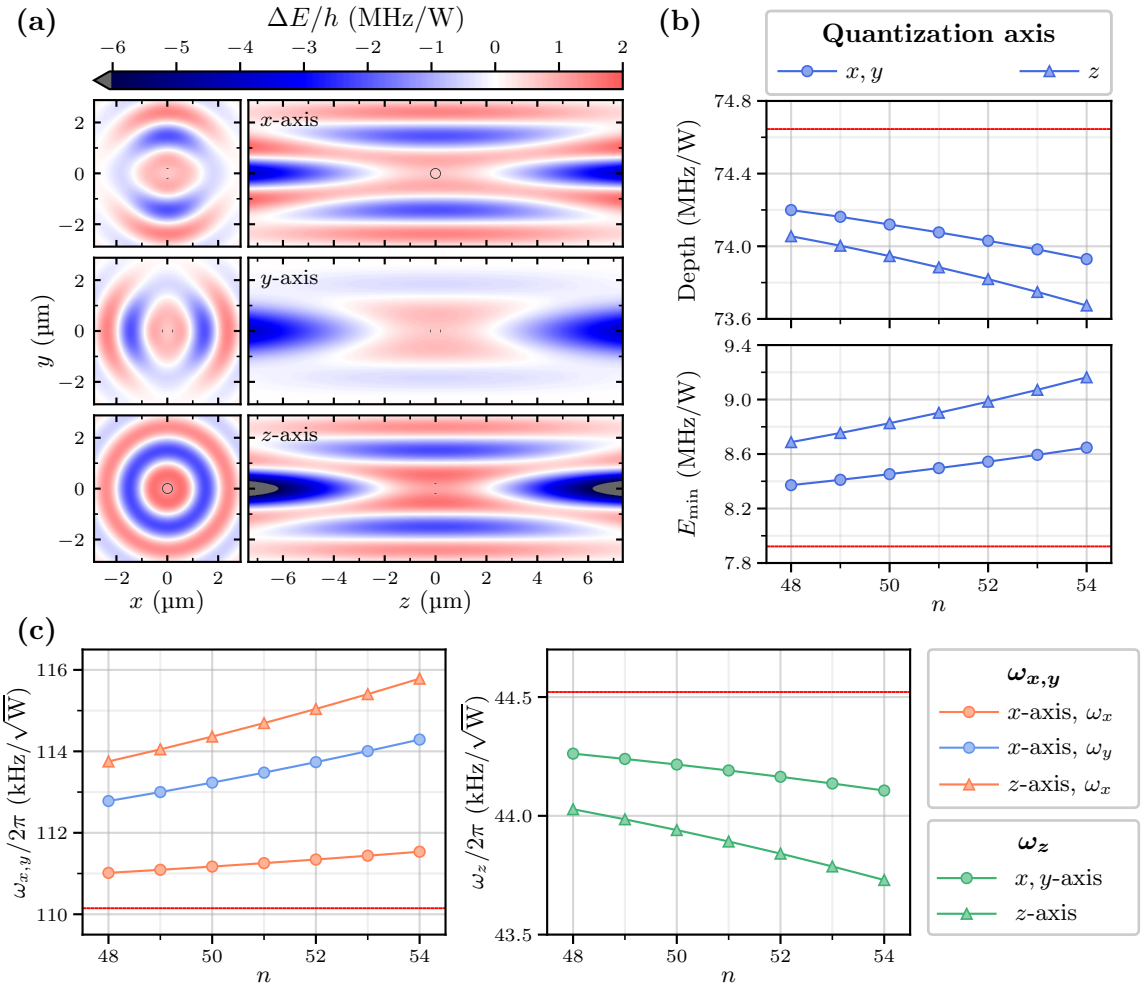

Figure 5.6: Characterisation of the theoretical trapping potential. (a) Cut of the difference between the actual and effective trapping potential for a point-like charge. Results are presented for $|52C\rangle$ oriented along x, y and z. The anisotropy of the charge density breaks the cylindrical symmetry for the trapping potential when the quantization axis is transverse. On-scale cuts of the charge density are superimposed on the trapping potential section. They appear as a pair of dots or as a circle depending on the quantization axis. (b) Corresponding minimum energy and trap depth of the trapping potential for a transverse or axial quantization axis as a function of the principal quantum number n. (c) Trap frequencies as a function of the principal quantum number n. The quantization axis is set along the x-direction in our experiment. The red horizontal line on each plot is the corresponding value obtained for a reference point-like charge.

difference of energy at the center which causes a shift of the transition. A more detailed description of this energy difference is given in appendix D, where we also discuss its spatial variations.

Those spatial variations are described locally by the trap frequencies, shown in table 5.2. The frequency difference between 52C and 50C lies in the range 0.1–0.5%. However, the difference of potential is not accurately described by an quadratic polynomial. We provide an extensive description of the potential difference in appendix D, along with its main consequence: motion-induced decoherence in the trap.

Table 5.1: Trap depth and minimum light shift. The quantization axis is set along x.

State	$E_{\min}$ (MHz W^{-1})	Depth (MHz W^{-1})	Depth (mK W^{-1})
Reference	7.9219	74.645	3.58
$(n = 50)$	8.4522	74.12	3.55
$(n = 52)$	8.5438	74.03	3.56
$(n = 52) - (n = 50)$	0.092	0.009	0.004

Table 5.2: Trap frequencies (in kHzW$^{-\frac{1}{2}}$). The quantization axis is set along x.

State	$\omega_x/2\pi$	$\omega_y/2\pi$	$\omega_z/2\pi$
Reference	110.15	110.15	44.52
$n = 52$	111.3	113.7	44.2
$n = 50$	111.2	113.2	44.2
$(n = 52) - (n = 50)$	0.17	0.5	-0.05

We measured an incident power of about 400 mW shared between 18 BoB traps, hence approximately 20 mW per trap. This gives, according to table 5.1 a depth of about 70 µK, almost 15 times less than the gaussian tweezers. We also expect a shift of the transition due to the difference of minimum energy $E_{\min}$, which we estimate to be 1.8 kHz. With such power, we also expect a trap frequency of about 16 kHz.

5.2.2 Trap frequency measurement

The most important characterization of the BoB traps is their frequency, which we measure by inducing oscillations of atoms in the traps as we did for gaussian tweeezers. However, the method to induce these oscillations differs from the latter case. Indeed, simply releasing the atoms from BoB traps did not give rise to a detectable oscillation signal in our setup. To ensure that the various atomic trajectories start in phase, the solution that we found consisted in a circular states preparation offset with respect to the trap center.

The sequence used for the trap frequency measurement is detailed in figure 5.7 (a). We initially prepare the array of BoB traps with a lateral x-offset of 0.3 µm with respect to the gaussian tweezer array. The usual trapping sequence follows, with BoB traps switched on immediately after the laser excitation. The lateral offset of position with respect to the BoBs center causes atoms to oscillate in-phase. We then wait until the completion of the circularization to release the atoms. The rest of the experimental sequence is comparable to that of the analogous experiment for ground-state atoms presented in section 3.2.2. If the atoms have minimal velocity, *i.e.* they are at the edge of the trap, their displacement during the release is minimal and they recaptured in BoB traps. However, if they are at the bottom of the trap, hence with maximal velocity, they drift out of the trapping region and are lost. The BoB traps are subsequently switched back on until the end of the de-circularization. The latter takes place at a constant delay after circularization to ensure that the reference recapture probability is constant. We found an optimal release duration of 15 µs for our trap parameters and atomic temperature (22 µK). No adiabatic cooling of the atoms is carried during the sequence since the atoms must have significant motion amplitude to be able to leave the trap during the release.

The averaged recapture probability is reported in figure 5.7 (c), where a clear oscillation

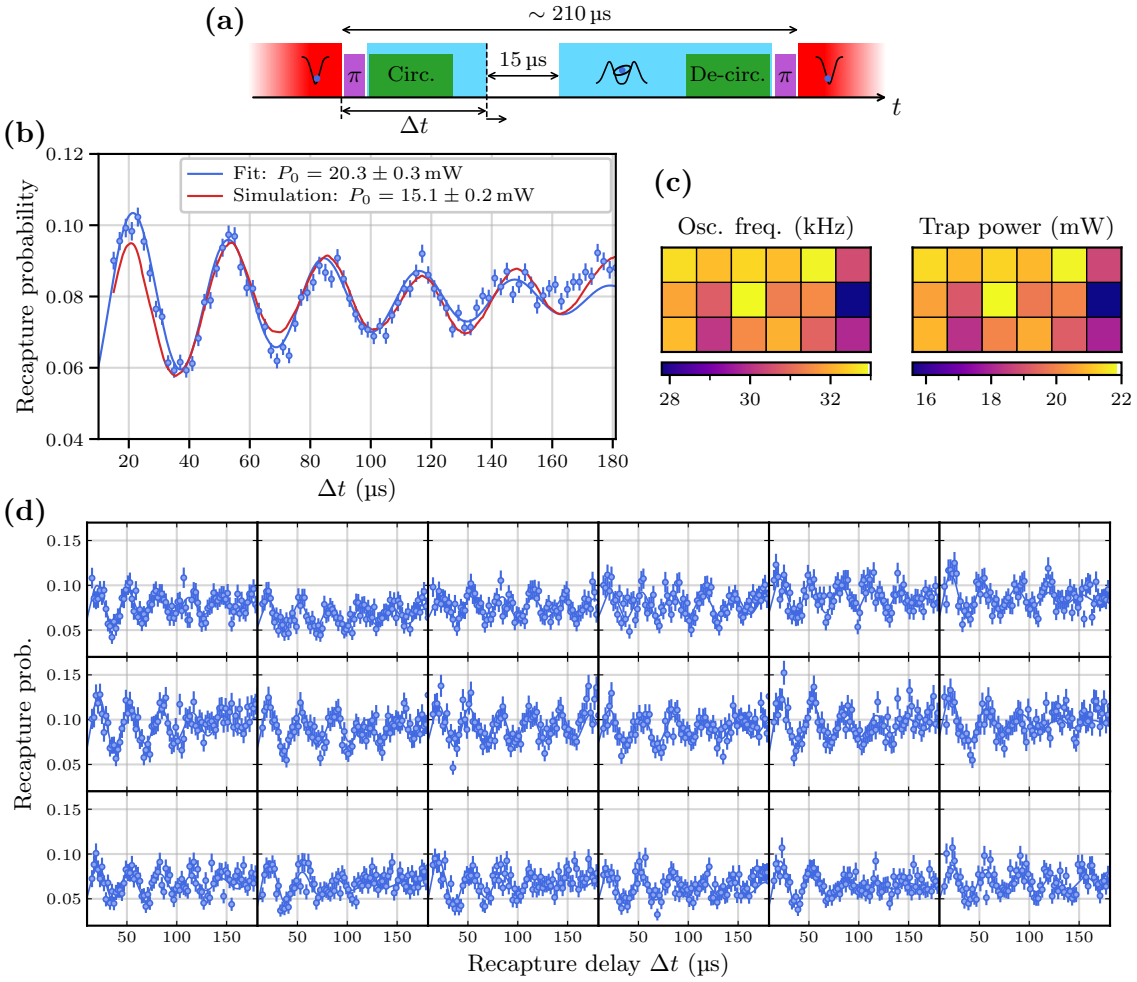

Figure 5.7: Measurement of the transverse trap frequency. (a) Scheme of the experimental sequence. (b) Oscillation signal from the averaged recapture probability, with corresponding damped-sinus fit and Monte-Carlo simulation. (c) Color map of the fitted oscillation frequency and associated trap power determined using the data of 5.2 for each trap. (d) Individual trap oscillation signals. The signals appear relatively homogeneous, with a lower signal amplitude along the bottom line.

signal is manifest. A damped sinus fit yields a frequency of 31.7 ± 0.2 kHz thus a trap frequency $\omega_{\text{trap}} = 2\pi \times 15.8 \pm 0.1$ kHz. According to the results of table 5.2 and assuming that we measure the frequency along the x-axis, the measured value corresponds to an average power of $P_0 = 20.3 \pm 0.3$ mW. This result is compatible with an estimated 400 mW of power shared between 18 traps.

We can also compute atom dynamics over the whole sequence to determine the power in the trap. For this purpose, we use a Monte-Carlo fitting procedure similar to that used for the temperature, which we describe in more detail in appendix D. The simulation uses the theoretical trapping potential introduced in the previous section, and fits well to the data. A global scale was left as a free parameter in the fitting procedure. The value thus recovered, 0.122 ± 0.001 is in good agreement with the one measured from the recapture data of figure 5.4, 0.13. The fitted trap power, $P_0 = 15.1 \pm 0.2$ mW, is significantly lower than the one obtained from the trap frequency. Such a difference, pointing towards lower trap

frequencies, is consistent with the anharmonicity of the BoB trap. With a positive quartic coefficient, the frequency of oscillations is larger than the pure harmonic case (and increases with the amplitude), hence a lower power required to reach a lower frequency.

We report in figure 5.7 (d) the recapture probability for individual traps. The signal appears quite homogeneous across the various sites, with only one outlier at the edge of the array. We carried only the fitting with a damped sinus to recover the trap frequency and deduce the power. We thus obtained a trap frequency $\langle\omega_{\text{trap}}\rangle = 2\pi \times 15.7\,\text{kHz}$, $\text{Std}(\omega_{\text{trap}}) = 2\pi \times 0.6\,\text{kHz}$, with corresponding power (within the harmonic approximation) $\langle P_0\rangle = 19.9\,\text{mW}$, $\text{Std}(P_0) = 1.6\,\text{mW}$. The individual powers sum up to a total value $P_{\text{tot}} = 359 \pm 3\,\text{mW}$, which is, again, compatible with 400 mW of total incident power.

5.3 Lifetime measurement and coherent state manipulation

For the purpose of quantum simulation, the traps must not affect the properties of our circular states. This section introduces three characterizations of single atom properties of the trapped circular states in our room temperature setup.

The room temperature radiative lifetime of circular states sets the limit on what can be achieved with our new setup. We present here its measurement [96, 94], with a comparison between the trapped and free conditions.

Coherent control of the states is required to perform quantum simulation and is also a limiting factor for the duration of any simulation protocol. We operate between the two states 52C and 50C, as we did in section 4.3.1, for essentially the same reasons. First, we show the measurement of spatially-resolved Rabi oscillations, from which we probe the mode structure of the microwave. Then, we describe Ramsey interferometry experiments from which we recover a coherence time. In addition, the Ramsey signal is sensitive enough to detect the effect of trapping and inter-atomic interactions, which makes it a promising tool to probe them.

5.3.1 Lifetime measurement

Circular states have no allowed optical transition but are sensitive to radiation in the radio-frequency and microwave domain. Thus, the main factor influencing their lifetime is the temperature through black-body radiation. The lifetime measurement is possible because circular states only decay to nearby levels that are still detectable by ionization, allowing us to measure the spreading-out of the initial population to these states. The evolution of a given state corresponds to a series of stochastic transfers to accessible levels which is well described by a master equation for the various populations.

The experimental sequence is depicted in figure 5.8 (a). It essentially consists in waiting a variable delay before applying the ionization ramp and recording the arrival times of the ions. However, the non-circular Rydberg states remaining in the environment after an imperfect circularization process might alter the population measurements. Moreover, contrary to the cryogenic environment, the low-l states have a lifetime comparable to that of circular states and thus are also present on ionization signals. Before the introduction of the variable delay, we clear the environment of non-circular states by transferring the population from 52C to 50C, followed by the application for a short duration of a high voltage on the ionization electrodes to ionize the states up to 51C. We reach approximately $140\,\text{V}\,\text{cm}^{-1}$ in $8\,\mu\text{s}$ in what we refer to as a "broom ramp". In figure 5.8 (b) we show the effect of the broom ramp, that clears residual low-l states and elliptic states visible at $20\,\mu\text{s}$ and $30\,\mu\text{s}$ respectively.

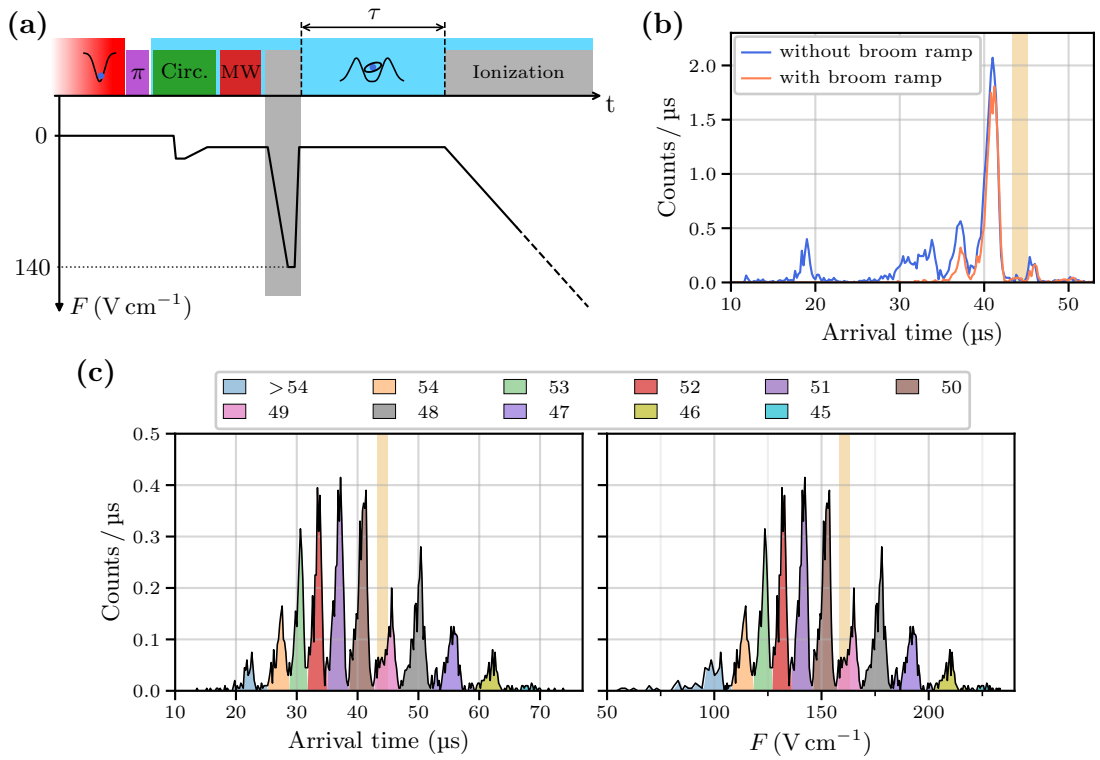

Figure 5.8: Timing of the lifetime measurement experiment. (a) Experimental sequence. After the preparation of 52C, the population is transferred to 50C and the Rydberg atoms with $n > 50$ are ionized with a "broom ramp". Ionization is then triggered after a variable delay. (b) Effect of the broom ramp on the ionization signal at zero delay. (c) Ionization signal at 800 µs delay. The populations nC for $45 \leq n \leq 54$ correspond to the colored areas under the curve. Note the "detection shadow" indicated as a light beige rectangle on the ionization signals.

The detected ions at a delay of 800 µs are reproduced in figure 5.8 (c), versus both the arrival time and ionization field. The detail of the ionization setup and electronics is given in appendix C. An important remark must be made on these ionization signals. In performing the measurements, we noticed a dip of ion counts at the location of the 49C peaks. This "detection shadow" is of unknown origin, but is consistent throughout the lifetime measurements. It prevents us from normalizing the data with the total population, as the amount of 49C atoms not detected is time-dependent. The population analysis is therefore carried without normalization at each time step, and does not take into account the 49C state. Nevertheless, we can still compare the results in the presence and absence of BoB trapping.

Figure 5.9 (a) illustrates the evolution of the populations by showing the arrival times at different delays, with 200 µs steps, with and without trapping. We see that after a transient spread of the initial 50C population between neighboring circular states, the system reaches a quasi-steady distribution characterized by the stochastic diffusion within the local set of states. This is further highlighted in figure 5.9 (b), where the integrated population show little evolution for delays > 1000 µs. The evolution of the initial 50C population is only approximately described by an exponential decay.

Finally, in figure 5.9 (b), we compare the populations measured in the presence or absence

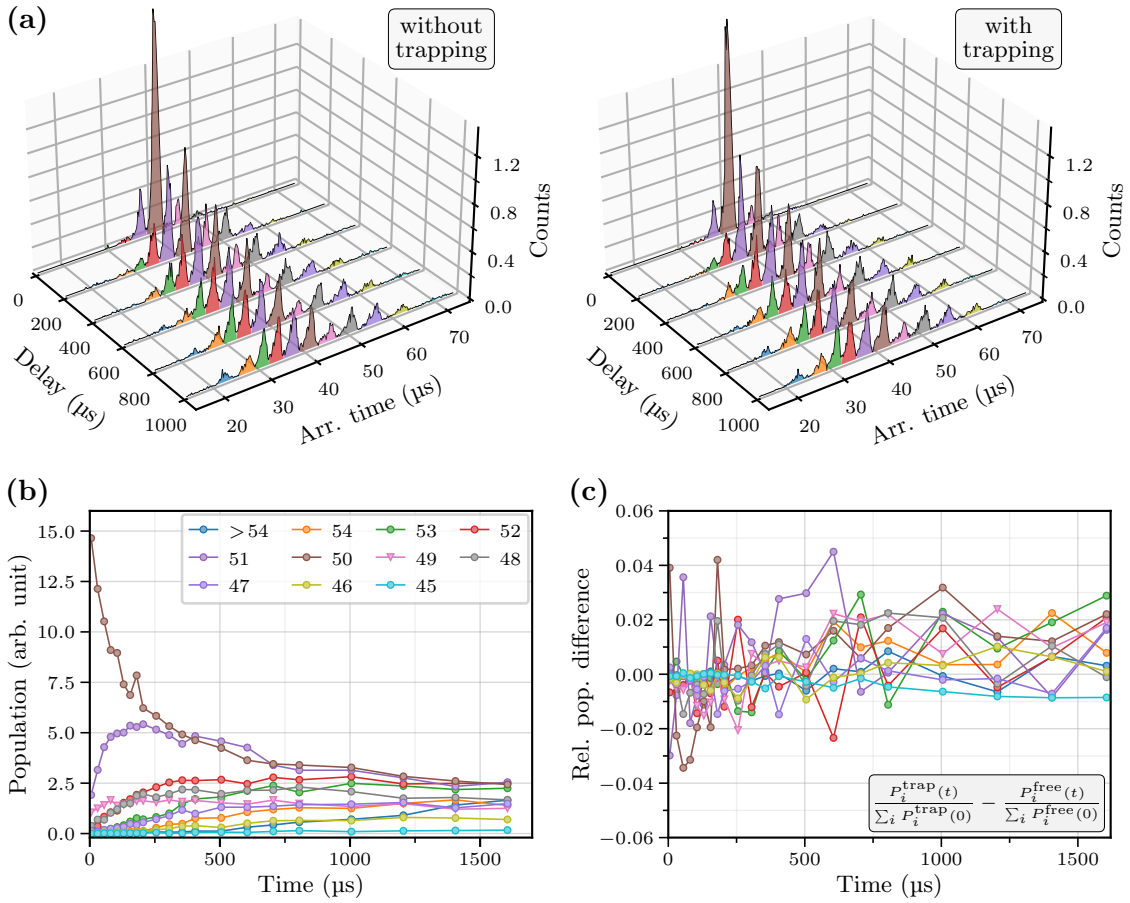

Figure 5.9: 50C lifetime measurement. (a) Ionization signals plotted as a function of the delay, without (left) and with (right) trapping. Each colored area corresponds to the population of a given state. (b) Time evolution of the detected states populations. (c) Relative population difference computed from (5.15).

of the BoB traps by computing the relative difference between the two:

$$\Delta_{\mathrm{rel}} P_i(t) = \frac{P_i^{\mathrm{trap}}(t)}{\sum_i P_i^{\mathrm{trap}}(0)} - \frac{P_i^{\mathrm{free}}(t)}{\sum_i P_i^{\mathrm{free}}(0)}, \tag{5.15}$$

where $P_i^{\mathrm{trap}}(t)$ and $P_i^{\mathrm{free}}(t)$ are the integrated populations of state i at delay t, with and without trapping, respectively. We normalize by the population at zero delay in each trapping condition to compare similar quantities. The relative population difference is relatively small, between $\pm 4\%$, and is essentially random. The effect of the traps on the lifetime can therefore be considered negligible. Let us however mention a pitfall of the previous comparison. The trapping measurements of section 5.1.2 have shown that the atoms tend to escape from the traps at moderate delays. The ionization detection being insensitive to this effect, it is safe to assume that a fraction of the detected populations corresponds to untrapped atoms, even when the BoB traps are present. Nevertheless, the atoms are likely to still be trapped at short delays. The data is therefore not sensitive enough to conclude on any detrimental effect of the trap on the lifetime at these timescales.

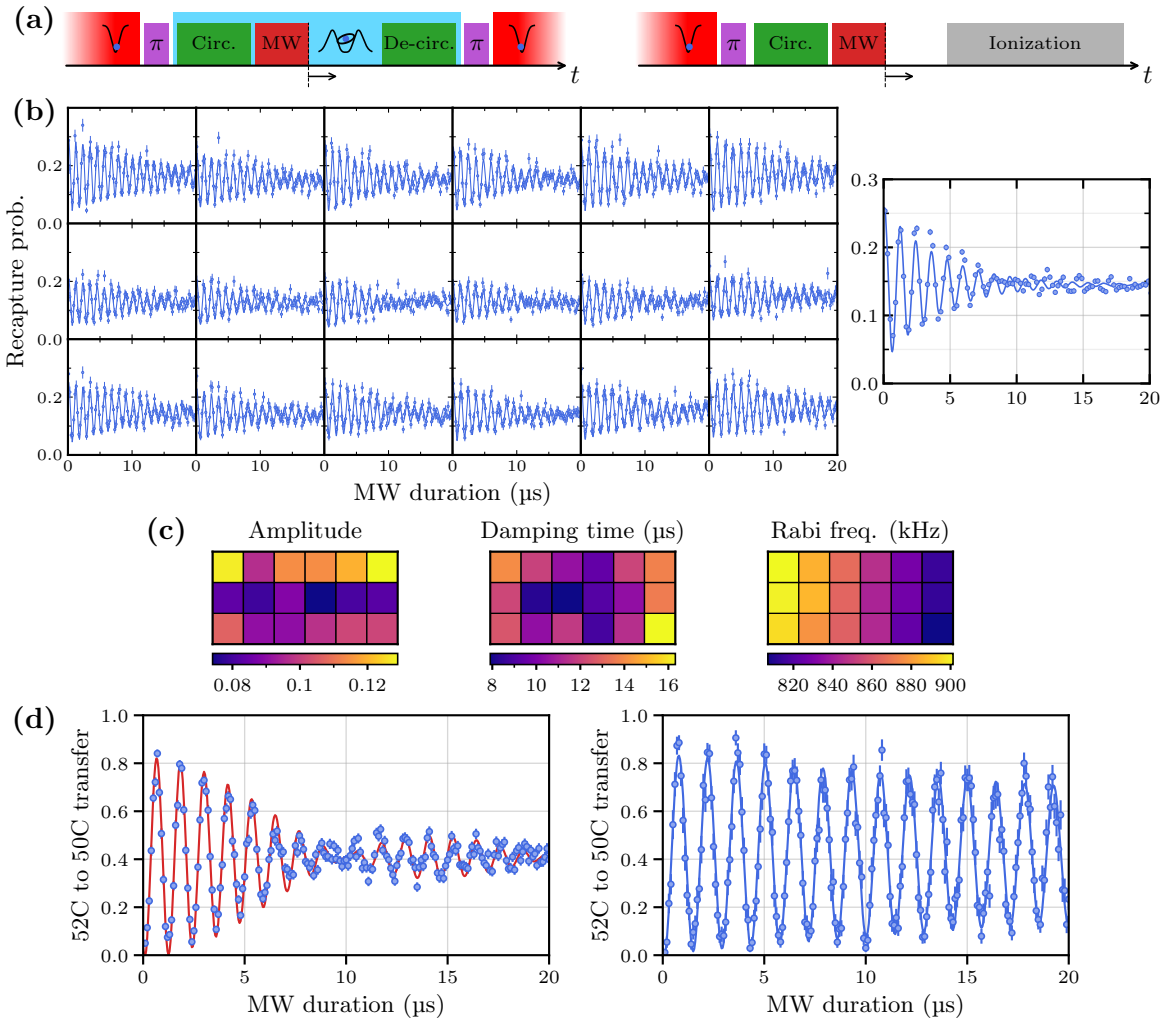

Figure 5.10: Rabi oscillations between 52C and 50C. (a) Experimental sequences for the measurement of Rabi oscillations, with optical detection (left) or ionization detection (right). (b) Optically-detected oscillations with BoB trapping. Left panels: individual Rabi oscillation signals. Note the lower contrast and faster decay in the center of the array. Right panel: averaged Rabi oscillation signal. (c) Color map of the fitted amplitude, damping time and Rabi frequencies. The map of Rabi frequencies reveals the inhomogeneity of the microwave, with a conspicuous linear gradient of approximately $1.2\,\mathrm{kHz\,\mu m^{-1}}$. (d) Rabi oscillations measured by ionization detection. Left: data from the 6×3 array; the red line is a (rescaled) sum of exponentially damped sinus with frequencies from the spatially-resolved measurement, and decay time from the single-atom measurement. Right: oscillations measured with a single atom, without trapping.

5.3.2 Rabi oscillations

The Rabi oscillations between circular states 52C and 50C presented here take advantage of the trapping to allow for the optical detection of circular states. Both spatially-resolved measurements and ionization signals are shown in figure 5.10.

The Rabi oscillations experiment simply consists in applying a MW pulse of variable duration after the preparation of circular states. We proceed in the presence of trapping for optical detection, but not when we detect the states by ionization. The MW frequency is set at

49.647 716 GHz (at resonance with the transition of figure 4.14). The individual oscillations are shown in figure 5.10 (b), each fitted with an exponentially-damped sinus. The most striking feature of these signals is the lower contrast in the middle horizontal line, concomitant with a faster decay in the center of the array. Before discussing these features, we remark that, albeit hardly visible to the eye, the spatial variation of Rabi frequencies is manifest from the color mapping of the values. It reveals a linear gradient of MW amplitude of approximately $1.2\,\mathrm{kHz\,\mu m^{-1}}$, oriented mainly along the $+x$-direction but also with a component along the $+z$-direction. We therefore have a variation $\pm 45\,\mathrm{kHz}$ across the $75 \times 30\,\mu\mathrm{m}$ tweezer array. This corresponds to a relative difference of $\pm 5\%$, around the mean value 855 kHz.

We can now interpret the corresponding ionization signal presented in figure 5.10 (d) as the sum of individual Rabi oscillations with different Rabi frequencies. Such a sum can be written:

$$p_{\mathrm{ion}}(t) = y_0 + A \sum_i \sin(2\pi f_i t + \varphi_i + \pi) e^{-\frac{t}{\tau}}, \tag{5.16}$$

with f_i, φ_i the Rabi frequency and oscillation phase[4] of trapping site i and τ the characteristic damping time of single-atom Rabi oscillations shown in the right panel of figure 5.10 (d). The (properly scaled) sum $p_{\mathrm{ion}}(t)$ is plotted in red on the figure and fits well to the data.

The single-atom Rabi oscillation signal is recorded without trapping. Fitting with an exponentially decaying oscillation, we recover the characteristic single-atom damping time $\tau = 51.2 \pm 5.8\,\mu\mathrm{s}$. The microwave power and frequency are slightly different for these data, resulting in a Rabi frequency of $703.9 \pm 0.5\,\mathrm{kHz}$. Note that the measurements involving ionization detection are carried without BoB trapping. With a temperature of $25\,\mu\mathrm{K}$, the average displacement over the $15 + 20\,\mu\mathrm{s}$ duration of circular state preparation and Rabi oscillation is $\sim 1.7\,\mu\mathrm{m}$. This value corresponds to a Rabi frequency shift of 2 kHz, not detectable over the $20\,\mu\mathrm{s}$ of MW probing.

The faster damping of oscillations observed with optical detection could have two origins.

- The traps could induce, together with the microwave, some additional population transfer, thus leading to faster losses.
- The atoms could be expelled faster from the traps due to a combination of the interactions and the microwave.

In favor of the latter possibility, we insist on the fact that the damping time used in eq. (5.16) comes from the fit of the single-atom measurement rather than from the optically-detected signal. The revival of oscillations indeed seems more pronounced on the ionization signal than on the averaged fluorescence signal, although this may be due to the improved contrast of ionization detection. An effect of the interactions also tends to be supported by the spatial distribution of the decay times and oscillation amplitudes. Lower values are located in the center of the array, where atoms are on average more subject to interactions. The mechanism by which the MW could induce these excess losses is nevertheless unclear.

5.3.3 Ramsey interferometry

We conclude with the measurement of the coherence time T_2 of the superposition $(|52\mathrm{C}\rangle + |50\mathrm{C}\rangle)/\sqrt{2}$. We proceed by performing Ramsey interferometry, which allows us to quantify the decoherence including both homogeneous and inhomogeneous processes.

[4] A maximum of detected ions corresponds to a minimum of recaptured atoms, hence the additional π phase-shift.

We first prepare a superposition $(|52\mathrm{C}\rangle + |50\mathrm{C}\rangle)/\sqrt{2}$ by applying a $\pi/2$ MW pulse at a frequency ν_{MW} with a two-photon detuning Δ_0 from the transition frequency ν_{CC}: $\nu_{\mathrm{MW}} = (\nu_{\mathrm{CC}} + \Delta_0)/2$. This leads, after a delay τ, to a dephasing $\phi = 2\pi\Delta_0\tau$ which is converted to a population difference by a second $\pi/2$-pulse in phase with the first one. For a proper measurement, the MW Rabi frequency Ω_{MW}, the detuning and the coherence time must satisfy the hierarchy $\Omega_{\mathrm{MW}} \gg 2\pi \times \Delta_0 \gg 1/T_2$. The left inequality amounts to require a hard $\pi/2$-pulse, while the right inequality is the condition for the detection of many Ramsey oscillations and the precise measurement of the decay time T_2. Taking into account the damping of the oscillations, we expect a signal:

$$p(\tau) = y_0 + Ae^{-\frac{\tau^2}{2T_2^2}} \sin(2\pi\Delta_0\tau + \phi_0). \tag{5.17}$$

Measurements on the 6×3 array

The actual experimental sequences are depicted in figure 5.11 (a) and (b). After the preparation of circular states, a $\pi/2$-pulse of 0.4 µs duration is applied, followed by another one after a variable delay τ. We proceed in the presence of BoB trapping using imaging detection (figure 5.11 (a)) or without trapping using ionization (figure 5.11 (b)). We present spatially-resolved data in figure 5.11 (c) from the imaging experiment. The MW frequency is set at $\nu_0^{\mathrm{img}} = 49.647\,839\,\mathrm{GHz}$, hence an expected detuning $\Delta_0 = +246\,\mathrm{kHz}$ from the measured 52C to 50C transition (see section 4.3.1). We measure a Ramsey frequency of $\Delta_0^{\mathrm{trap}} = 236.4 \pm 0.4\,\mathrm{kHz}$ for the averaged data (see figure 5.11 (a)), and for individual trapping sites $\langle\Delta_0^{\mathrm{trap}}\rangle = 236.5\,\mathrm{kHz}$, $\mathrm{Std}(\Delta_0^{\mathrm{trap}}) = 1.2\,\mathrm{kHz}$. The standard deviation given above is comparable to the uncertainity resulting from the fitting procedure ($\sim 1\,\mathrm{kHz}$), and significantly smaller than the Fourier-limited width $1/(2\pi \times \tau) = 5\,\mathrm{kHz}$ for a maximal delay $\tau = 30\,\mu\mathrm{s}$. In the case of free atoms (figure 5.11 (b)) the measured Ramsey frequency is $\Delta_0^{\mathrm{free}} = 243.0 \pm 0.4\,\mathrm{kHz}$. Here, the MW frequency was set at $\nu_0^{\mathrm{ion}} = 49.647\,840\,\mathrm{GHz}$, hence an expected frequency shift of $2 \times (\nu_0^{\mathrm{ion}} - \nu_0^{\mathrm{img}}) = +2\,\mathrm{kHz}$ with respect to the optical measurement.

Three contributions can affect the measured Ramsey frequencies:

- Electric field gradients. These affect both trapped and free atoms, yet we could expect a faster decoherence in the latter case as atoms are allowed to drift.
- The differential energy shift induced by the BoB traps (see figure 5.6-(b)). Obviously, it affects only trapped atoms.
- Inter-atomic interactions. They are expected to affect both trapped and free atoms, albeit differently since free atoms can move in response.

The average frequency difference between trapped and free atoms is $4.6 \pm 0.6\,\mathrm{kHz}$. At least part of this difference is attributable to the BoB trap. Its curvature at the bottom causes the differential energy shift between 50C and 52C discussed in section 5.2.1. This causes the transition frequency to increase and in turn yields a decrease in the detuning Δ_0^{trap}, as observed. According to table (5.2), the measured shift corresponds to, on average, $50 \pm 7\,\mathrm{mW}$ power per BoB trap, more than a factor of 2 off from the trap power given in section 5.2.2, about 20 mW. This suggests that other mechanisms intervene to cause this frequency difference, although these are unclear.

We also note that the spatial structure of Ramsey frequencies is incompatible with the rather homogeneous distribution of trap powers seen on figure 5.7. We observe a tendency towards lower Ramsey frequencies along the central row, with an average of $235 \pm 0.4\,\mathrm{kHz}$ as

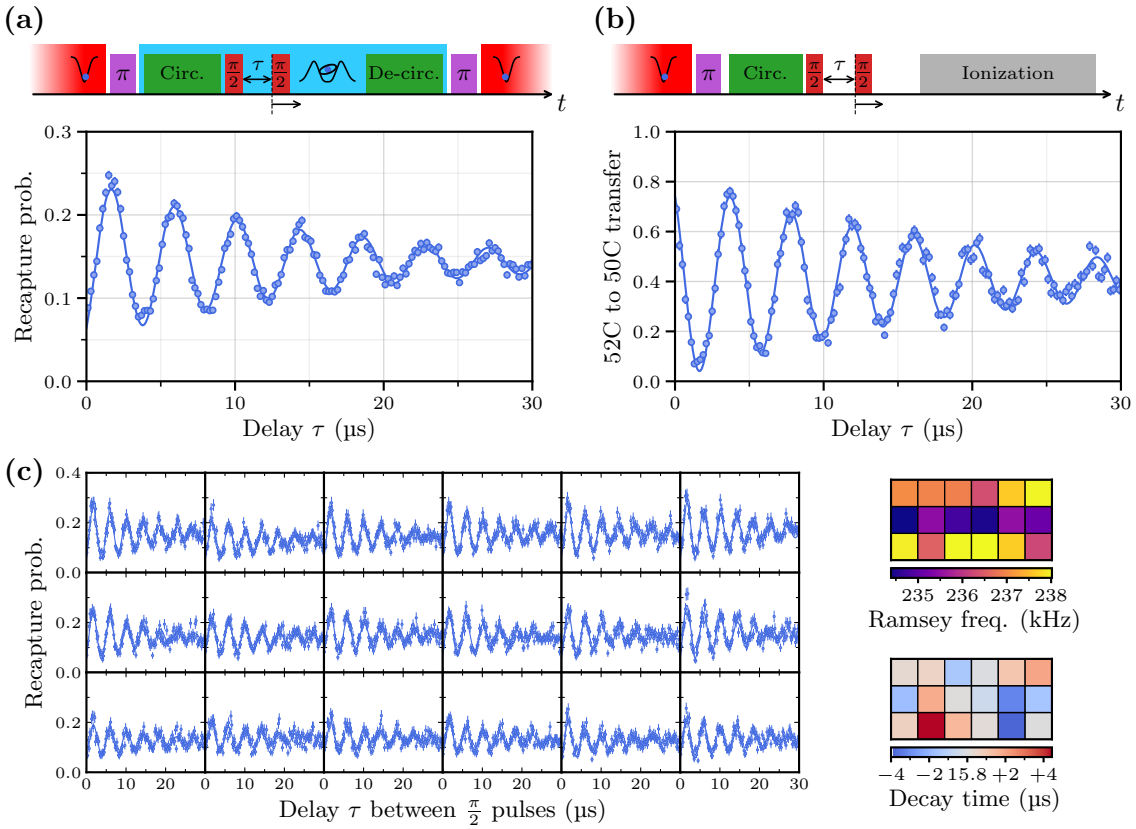

Figure 5.11: Ramsey interferometry on the 6×3 array of tweezers. (a) Experimental sequence in the presence of trapping with corresponding averaged recapture probability. (b) Experimental sequence carried in the absence of trapping with ionization detection. (c) Ramsey oscillations measured in individual trapping sites. The data is fitted with an exponentially-damped sinus (eq. 5.18) with corresponding Ramsey frequency and damping time shown as color maps on the right.

compared to $237.3 \pm 0.7\,\mathrm{kHz}$ on the upper and lower rows. This difference corresponds to a shift of approximately $2\,\mathrm{kHz}$ towards higher frequencies for the transition. The sign of this difference is the same as that of the differential of the $C_6^{n,n}$ coefficients given in section 1.2.3, although the numerical value $\sim +100\,\mathrm{Hz}$ for the latter quantity differs by more than one order of magnitude.

At our working electric field of $2.09\,\mathrm{V\,cm^{-1}}$, a variation of $1\,\mathrm{mV\,cm^{-1}}$ is expected to cause a frequency shift of $2.2\,\mathrm{kHz}$ on the two-photon transition. The field being directed along x, only the x-component of the gradient is significant. Although the data is not very precise, from the spatial distribution of Ramsey frequencies, we can safely conclude that the electric field variation is below $1\,\mathrm{mV\,cm^{-1}}$ over the $75\,\mu\mathrm{m}$ extension of the array. This gives an order of magnitude for an upper bound to electric field gradients of $10\,\mu\mathrm{V\,cm^{-1}}$ per $\mu\mathrm{m}$, or equivalently $0.1\,\mathrm{V\,cm^{-2}}$.

The Ramsey oscillations damping times of individual trapping sites suffer from significant fluctuations, with a value $\langle\tau\rangle = 15.8\,\mu\mathrm{s}$, $\mathrm{Std}(\tau) = 1.9\,\mu\mathrm{s}$. Nevertheless, this damping time is close to the value $\tau_{\mathrm{img}} = 15.6 \pm 0.6\,\mu\mathrm{s}$ fitted from the averaged data presented in figure 5.11 (a). With ionization detection (and without the BoB traps), we get similar oscillations with a fourfold increase in contrast. In this case, we obtain a damping time $\tau_{\mathrm{ion}} = 18.7 \pm 0.9\,\mu\mathrm{s}$.

This value is larger than τ_{img} and suggests an additional coherence loss mechanism in the presence of the traps, possibly linked to the position-dependent differential shift between 52C and 50C.

In the above treatment, the oscillation signals were not fitted with the model of eq. (5.17), but rather with an exponentially decaying sinus:

$$p(t) = y_0 + Ae^{-t/\tau} \sin(2\pi\Delta_0 t + \phi_0). \tag{5.18}$$

This choice is justified by the following semi-quantitative argument, from which we can recover the announced decay times. Owing to their rather short lifetime at room temperature, some atoms might decay either to 53C or 51C during the delay between the two MW pulses. When that occurs, the strong dipole-dipole interaction that appears ($\sim 1\,\text{MHz}$ at $15\,\mu\text{m}$) causes the 52C to 50C transition of nearby atoms to shift far from its initial value. In this case, the second MW pulse is off-resonant and does not affect the populations, yielding the observed damping. We assume, for the sake of simplicity, that the process described above is the dominant mechanism for the loss of coherence and that the decay to 53C or 51C shifts all the remaining atoms off resonance. Under these approximations, the decay is roughly $n_{52\text{C}}/T_{52\text{C}}$, where $n_{52\text{C}}$ is the number of 52C atoms prepared and $T_{52\text{C}} \simeq 130\,\mu\text{s}$ is the lifetime of 52C at room temperature. We noted earlier that approximately $n_{52\text{C}} = 7$ circular states are produced per experimental run. We therefore expect $\tau \sim 7/130 \approx 19\,\mu\text{s}$, which is close to the measured value, especially considering that other decoherence processes were neglected.

Single-atom measurements

To free ourselves from the complexity brought by inter-atomic interactions, we measure Ramsey oscillations with a single atom. The results are reported in figure 5.12. The electric field is kept at the same value of $2.09\,\text{V}\,\text{cm}^{-1}$ as before, hence the same transition frequency. However, to circumvent the problem of reduced statistics, we restrain ourselves to ionization detection. In the single-atom case, this essentially gives the same information as imaging. The bare detuning is reduced to $\Delta_0 = +86\,\text{kHz}$ by setting the microwave frequency at $49.647\,759\,\text{GHz}$, allowing us to reduce the sampling frequency and further improve the statistics.

The Ramsey interference signals are presented in figure 5.12, both without (left panel) and with (right panel) BoB trapping. We found it necessary to trigger the whole sequence

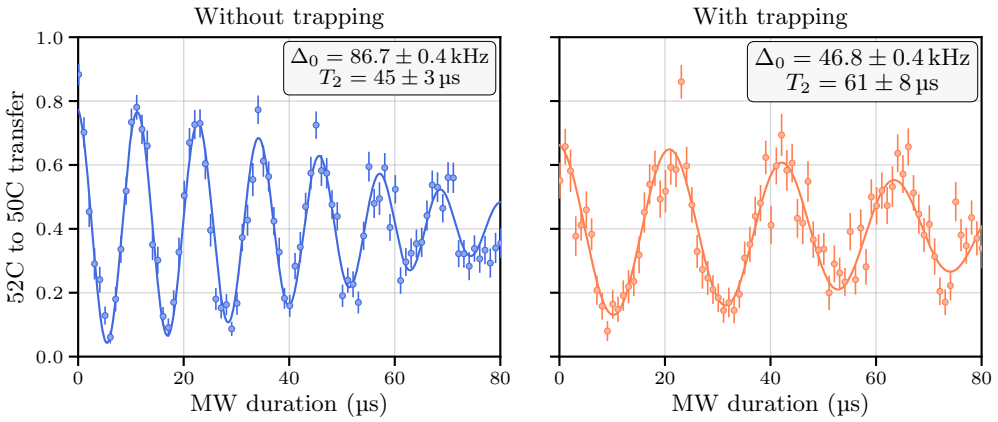

Figure 5.12: Single-atom Ramsey oscillations. In the trapping condition (right), all the available power was used in the single BoB trap.

on the power line in order to avoid the convolution of the signal with 50 Hz power line noise picked-up by the experiment.[5] The most striking feature of the two signals is the difference of Ramsey frequencies. With free atoms, we have $\Delta_0^{\text{free}} = 86.7 \pm 0.4\,\text{kHz}$, in very good agreement with the expected value $\Delta_0 = +86\,\text{kHz}$. The Ramsey frequency in the trap, $\Delta_0^{\text{trap}} = 46.8 \pm 0.4\,\text{kHz}$, is 40 kHz below. To observe such an energy shift, all the available laser power was used to prepare the single trap. According to table (5.1), we estimate that the trap was produced with a laser power of $436 \pm 7\,\text{mW}$. In contrast with the value deduced from the measurement carried on the 6×3 array, this result is in good agreement with our estimation of 400 mW for the total available power. This is expected, as the other frequency shifting mechanisms are dwarfed by the large differential shift at the bottom of the BoBs.

The damping of the signal is fitted according to the model of eq. (1.112). It is interesting to note that the decay of the coherence appears slower when the atom is trapped, with $T_2^{\text{trap}} = 61 \pm 8\,\mu\text{s}$, as compared to $T_2^{\text{free}} = 45 \pm 3\,\mu\text{s}$ for the free atom. The uncertainty in the fitted value is large and one cannot rule out the possibility of specific effects appearing at high trapping power[6].

Overall, the coherence times are compatible with the electric field noise of $0.9\,\text{V cm}^{-1}$ determined in section 4.3.2. Indeed, this noise is associated to fluctuations of $\delta\Delta_0 \simeq 2\,\text{kHz}$ of the transition, with corresponding timescale $T_2 = 1/(2\pi\delta\Delta_0) \simeq 80\,\mu\text{s}$.

Conclusion

In order to consistently describe the subsequent results, we first studied the trapping of Rydberg states. We kept an empirical approach and did not consider in detail the atom dynamics in the traps. We first demonstrated the trapping of the laser-accessible 52D state, allowing us to free ourselves from the complexity brought by circular states. The data were found to be consistent with an exponential decay at a rate of $66 \pm 1\,\mu\text{s}$, close to the theoretical value of 74 µs.

The analysis of the data pertaining to circular states was more difficult, mostly due to the complex dynamics of circular states, subject to stochastic thermal transfers to nearby levels. The population evolution is governed by a master equation that we did not detail here. By scaling the data with the theoretical 52C population expected at room temperature, we observed a residual decay, associated to a timescale in the ms range. The precise origin of these losses is not clear, yet we conjectured an effect of the strong first-order dipole interactions that appear when an atom decays to a nearby state such as 51C or 53C.

We then gave a theoretical description of the trap: the preparation of bottle-beams and their convolution with the charge distribution of various circular states. We obtained in particular the light-shift at the bottom of the trap (along with the differential value between 50C and 52C), and the trap frequencies. We subsequently used these values to confront the theory with the experiments to come.

This was first illustrated with the measurement of the transverse trap frequency. We thus obtained a mean value of $15.8 \pm 0.1\,\text{kHz}$ that corresponds, assuming harmonic motion within the traps, to a power per trap of 20 mW. This was found to be in good agreement with our estimations of 400 mW shared between 18 traps. However, a simulation of the atom dynamics inside the traps yielded a significantly lower trap power, of about 15 mW. Such a difference appeared in qualitative agreement with the trap anharmonicity.

[5] The data measured without power line triggering are presented in appendix E.

[6] In particular, the circularization efficiency dropped by a factor 1.5 in the presence of the high power trap.

We verified that the presence of the traps does not affect the states evolution by measuring the various populations with ionization detection. The resulting plots are close to each other and prevented us from detecting an effect of the traps at our level of precision.

Rabi oscillations benefited from the spatially-resolved optical detection. It allowed us to interpret the ionization signal as resulting from a gradient of Rabi frequencies over the 75 µm-large array of atoms.

We concluded with a Ramsey interferometry experiment on the 52C $\leftrightarrow$ 50C transition. The measurement realized with the 6×3 array of atoms revealed two things. First, we observed a difference of 4.6 ± 0.6 kHz between the frequencies obtained without and with trapping, corresponding to a transition displaced towards high frequencies. About half of this difference could be attributed to the differential light-shift of the trap. Second, the signal showed a rather quick decay, in the 15–20 µs range. Echoing to the mechanism suggested when we discussed circular state trapping, we interpreted this as a consequence of the interactions. An atom decaying to a nearby state could induce an important shift on the transition due to the first-order dipole-dipole interaction.

This hypothesis seemed confirmed by the significant increase in coherence time when we repeated the experiment with a single atom. The coherence time increases to 61 ± 8 µs in the presence of the trap and 45 ± 3 µs for free atoms. The precision of the measurements prevented us from concluding on the origin of this difference. All the available power was used in the single BoB trap, that resulted in a significant frequency difference of approximately 40 kHz between the two conditions. This led us to another estimation of the power for the single BoB trap. The obtained value of 440 mW was found to be in good agreement with our estimation. In this case the other processes that shift the transition were likely to be dwarfed by the large light shift.

Conclusion and outlook

Have I gone mad?
I'm afraid so. But I'll tell you a secret. All the best people are.
— Lewis Carroll, *Alice in Wonderland*

The work presented in this manuscript introduced a new experimental setup operated at room temperature and dedicated to the preparation of arrays of circular Rydberg states trapped in optical "bottle-beam" tweezers. We detailed the design of this new setup, which encompasses the constraints imposed by both the preparation of optical tweezers and by the preparation and manipulation of circular Rydberg states. We recalled the procedure to prepare a cloud of cold rubidium atoms from a "hot" vapor to a $\sim 10\,\mu K$ optical molasses by going through two stages of magneto-optical trapping. We presented the methodology to prepare optical tweezers: the phase modulation techniques with SLMs, the algorithms for phase retrieval and the aberration correction procedure. This topic is however only partially covered in this manuscript since most of the work on optical traps preparation and characterization has been done by another PhD student of our team, Yohann Machu. An extensive coverage of tweezers will be given in his thesis.

The loading of gaussian optical tweezers with rubidium atoms is the starting point of all the experiments described in this thesis. We first went through an extensive description of the fluorescence imaging of the atoms and data analysis methodology, as they are involved in most of the subsequent experiments. With these tools in hand, we moved on to the characterization of the tweezers, assuming a gaussian intensity profile. We thus obtained the trap depth from light-shift spectroscopy and the trap frequency by recording an atomic oscillation signal. From these two parameters we recovered the average waist $\langle w_0 \rangle = 1.21\,\mu m$ and power $\langle P_0 \rangle = 2.62\,mW$ at each trapping site of a large 9×9 array of tweezers. Among the 81 sites, we obtained a waist inhomogeneity of about 1% and a power inhomogeneity of approximately 5%. This validates the methodology used for tweezers preparation. The study pertaining to trapped ground-state atoms concluded with the measurement of their lifetime in the tweezers and of their temperature by a release-recapture experiment. We obtained a lifetime of $12.6 \pm 0.2\,s$, and an average temperature $\langle T \rangle = 14.3\,\mu K$. The measurement carried on individual trapping sites revealed a specific pattern for the distribution of temperatures: atoms along a vertical band in the center of the array were found cooler. The temperature is however dependent on the experimental conditions. For instance, our optical pumping scheme increases it to a value in the range 20 to $25\,\mu K$, which we can then reduce to $4\,\mu K$ with adiabatic cooling of the atoms. Let us stress the fact that the preparation of optical tweezers is new to our group, hence the necessity to detail the associated experimental procedures and methodologies.

The next step consists in the preparation of circular Rydberg states from trapped atoms, with notable differences with respect to previous works. Each of the many stages leading to the target state $|52\mathrm{C}\rangle$ was thus described. In doing so, we switched to an array of 6×3 tweezers, which corresponds to the maximal number of BoB traps that we are able to prepare with effective trapping. The inter-atomic distance was also increased to 15 µm to mitigate the interactions between neighboring Rydberg atoms.

We begin by optically pumping our atoms to the proper Zeeman sublevel. We determined a state purity of $97 \pm 1\%$ by Raman spectroscopy. The laser excitation to the Rydberg state $|52\mathrm{D}\rangle$ follows. We proceed via a two-photon transition through the intermediate state $\left|6\mathrm{P}_{3/2}\right\rangle$ with a 420 nm-laser and a 1015 nm-laser. The average efficiency for this transition was found to be $89 \pm 1\%$, mainly limited by the laser power at our disposal. This is followed by a microwave transition to the state $|52\mathrm{F}\rangle$, for which we estimated an efficiency of $88 \pm 1\%$. The adiabatic transfer to the circular state $|52\mathrm{C}\rangle$ constitutes de last step of the process. It has been covered extensively in a previous work [96], and was therefore only briefly discussed.

From that point, we described microwave spectroscopy experiments between $|52\mathrm{C}\rangle$ and nearby states, which we used as a diagnostic tool for the circularization procedure. We first probed the transition from $|52\mathrm{C}\rangle$ and neighboring elliptical states to $|50\mathrm{C}\rangle$ and its corresponding elliptical levels. This transition echoes the embodiment of spin-1/2 qubits by circular states with $\Delta n = 2$ in the proposed quantum simulation platform. We used it to determine the state purity after the adiabatic transfer, which we estimated to be $90 \pm 2\%$. This transition was later involved both in lifetime measurements as a way to get rid of undesired states to get a pure lifetime signal, and for coherence measurements by Ramsey interferometry. We determined the electric field in the environment using the transition between $|52\mathrm{C}\rangle$ and $|53\mathrm{E}^{\pm}\rangle$. Having $\Delta m = 0$, this transition is insensitive to the magnetic field, yet is very sensitive to the electric field, owing to the strong first order Stark shift of the elliptical state. We thus obtained a value of $2.0887 \pm 0.0001\,\mathrm{V\,cm^{-1}}$ for the electric field. The width of the line indicated field fluctuations of $0.9\,\mathrm{mV\,cm^{-1}}$, which are most likely attributable to voltage noise on the electrode rather than field inhomogeneity at the atoms location. We concluded with a summary of the efficiency of each preparation step, including the de-circularization procedure, and estimated a total efficiency $\eta = 0.34 \pm 0.04$ for the round trip from the ground state to the circular state and back to the ground state. At this stage of the experiment, we focused on the demonstration of trapping and the various preparation steps were not thoroughly optimized.

We took advantage of both the spatially-resolved fluorescence imaging and the state-selective field ionization detection throughout the preparation of circular states. In particular, it was possible to obtain most of the presented data pertaining to Rydberg states (with the exception of lifetime measurements) using both detection methods. Yet the reader must be aware that the optimizations were usually more conveniently carried using ionization detection. This is especially true when adjusting the adiabatic transfer parameters, because ionization detection still brings information even if the atoms are completely lost in the Rydberg manifold, a situation that would prevent going backward to the ground state as required by fluorescence detection.

We finally demonstrated Rydberg state ponderomotive trapping in bottle-beam traps. Since all Rydberg states are subject to the ponderomotive potential, we began by showing the trapping of the state $|52\mathrm{D}\rangle$. This simple experiment showed good agreement with a model involving only the decay of the Rydberg state, without mechanical losses. We then described the main result of this thesis: the trapping of atoms in the circular state. Despite the rather short lifetime of circular states at room temperature, we were able to observe trapping over

a 5 ms timescale. This is due to the fact that circular states mainly decay to nearby circular states, which not only are trapped, but also repopulate the initial state.

The trapping potential generated by the BoBs is not exactly proportional to the light intensity but must be convolved with the Rydberg electron wavefunction. Such convolution was carried numerically with the charge distribution of circular states of interest. We studied the resulting theoretical trapping potential, that was characterized by its depth, along with its energy shift and curvature at the minimum. These values depend on the quantization axis of the circular state. In our experimental conditions, with the quantization axis orthogonal to the propagation axis, we computed a differential energy shift of $92\,\mathrm{kHz\,W^{-1}}$ between the states 52C and 50C. The trap frequencies associated to the curvature at the minimum are also dependent on the principal quantum number, with relative variations found to be about 1%. The transverse frequencies (whose degeneracy is lifted by the orientation of the circular orbit) were found to be around $112\,\mathrm{kHzW^{-\frac{1}{2}}}$.

We confronted the theory to the experiment by measuring the transverse trap frequency. We obtained a value of $15.8 \pm 0.1\,\mathrm{kHz}$, which, according to our prediction on the frequency, corresponds to a power per trap of $20.3 \pm 0.3\,\mathrm{mW}$, compatible with our expectations of 20 mW per trap. However, a more refined analysis through the complete atom dynamics simulation yielded an estimated power of $15.1 \pm 0.2\,\mathrm{mW}$, significantly lower than the value obtained using the trap frequency. This indicated that the anharmonicity of the trap could not be neglected at this level.

To get some insight on the evolution of circular states in our room temperature setup, we performed a lifetime measurement, both with free and trapped atoms. The results showed little incidence of the trapping on the lifetime.

The trapping proved itself a valuable tool to perform coherent state manipulation for extended duration, with optical detection, as illustrated by Rabi oscillations and Ramsey interferometry. As for rabi oscillations, we were able to detect a significant inhomogeneity in the microwave intensity, that translated into a gradient of Rabi frequencies. The corresponding ionization signal, showing some beating, would be difficult to interpret without the spatially-resolved measurement. Ramsey fringes are quite sensitive to the frequency of the probed transition. Here, we were able to detect a shift of $4.6 \pm 0.6\,\mathrm{kHz}$ in the frequency of the $|52\mathrm{C}\rangle$ to $|50\mathrm{C}\rangle$ transition caused by the trapping. The measurement was also sensitive enough to reveal a spatial distribution of Ramsey frequencies which hinted at the presence of interactions between circular states despite the large distance separating them. We observed a fast damping of the oscillations, with an average characteristic time of $15.8 \pm 1.9\,\mu\mathrm{s}$. We interpreted this as the effect of the strong first order dipole coupling that appears when an atom is transferred thermally to a neighboring state.

To circumvent this phenomenon of interactions-mediated coherence loss, we realized single-atom experiments. Using the full power available for trapping, approximately 400 mW, we detected a large shift of the transition that was found to be compatible with the power available. We obtained a coherence time of $61 \pm 8\,\mu\mathrm{s}$ for a trapped atom, higher than that of a free atom. The significance of this difference was difficult to interpret owing to the large uncertainties in the fitted values. These coherence times were nevertheless compatible with the measured temporal electric field noise, with a possible, yet unlikely, effect of field gradients.

The results reported here essentially relate to single-atom physics but pave the way toward our proposed quantum simulation platform. The experiment is now turning to many body systems, which will require to go though several stages. The improvement of holographic trap generation algorithms will increase the spatial extension of the trap array, and *in fine*

the number of traps that we are able to produce. An atom rearrangement setup is being installed to prepare defect-free arrays of atoms and significantly improve our control over the experiment. Finally, a necessary step before diving into the complexity of many-body systems is to understand the simplest of them: a pair of interacting atoms. The experimental measurement of the dipole-dipole interaction between circular states is thus the object of current studies.

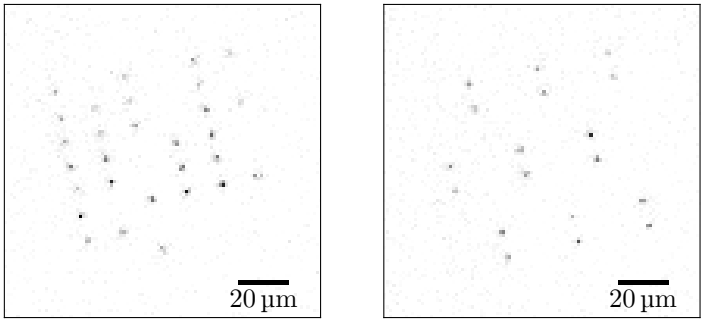

Figure 5.13: Successful rearrangement of a partially loaded array of tweezers to prepare pairs of atoms for dipole-dipole interaction measurement.

The study of many-body physics with a small number of atoms can also be considered in the current experimental setup. This will require to improve the efficiency of circular states preparation. The de-circularization to the ground state was shown to be an important limiting factor to the total efficiency for optical detection. It would also need to be improved, or could possibly be abandoned in favor of a non-destructive optical detection scheme [89].

Finally, as already mentioned, exploiting the full potential of circular states requires a cryogenic environment to benefit from their extended lifetime. However, this will require a much tighter control of the technical aspects that affect the coherence of the system, of which we can cite the the electric and magnetic field noise along with electric gradients. The transition from our room-temperature setup to a cryostat, which adds another layer of complexity and technical difficulties, is thus the last step before the implementation of the proposed quantum simulation platform.

Appendix A

The Kramers relation

A.1 The Kramers recurrence relation

We start from the radial equation[1] (1.6):

$$\left[a^2\frac{\mathrm{d}^2}{\mathrm{d}r^2} - l(l+1)\frac{a^2}{r^2} + 2\frac{a}{r} - \frac{1}{n^2}\right] y_{nl}(r) = 0. \tag{A.1}$$

The normalization condition on the radial wavefunctions R_{nl} is

$$\int_0^\infty r^2 R_{nl}^2(r)\ \mathrm{d}r = \int_0^\infty y_{nl}^2(r)\ \mathrm{d}r = 1, \tag{A.2}$$

and we therefore have

$$\langle r^s\rangle = \int_0^\infty y_{nl}(r)\, r^s\, y_{nl}(r)\ \mathrm{d}r. \tag{A.3}$$

The idea behind the derivation of the Kramers relation is to apply successive integrations by parts, substituting (A.1) whenever possible. The formula states, for well-behaved functions u and v:

$$\int_a^b u(x)\, v'(x)\ \mathrm{d}x \ = \ \Big[u(x)\, v(x)\Big]_a^b - \int_a^b u'(x)\, v(x)\ \mathrm{d}x. \tag{A.4}$$

In the derivation, we will use this notation and identify the functions u and v when integrating by parts. We first multiply (A.1) by $r^s y_{nl}$ and integrate to get:

$$a^2 \int y_{nl}\, r^s\, y_{nl}''\ \mathrm{d}r \ = \ l(l+1)\, a^2\, \langle r^{s-2}\rangle - 2\, a\, \langle r^{s-1}\rangle + \frac{1}{n^2}\langle r^s\rangle, \tag{A.5}$$

where the primes denote the derivative of the function. For the sake of clarity, the integration bounds and the r-dependence of y_{nl} have been omitted. We now turn to the evaluation of the right hand side of the above equation. Integrating by parts, with $u = y_{nl} r^s$ and $v' = y_{nl}''$ yields

$$\int y_{nl}\, r^s\, y_{nl}''\ \mathrm{d}r \ = \ \Big[y_{nl} r^s y_{nl}'\Big]_0^\infty - \int (y_{nl}\, r^s)'\, y_{nl}'\ \mathrm{d}r. \tag{A.6}$$

We first consider the first term of the right hand side. The functions y_{nl} decay exponentially as $r \to \infty$, hence the evaluation at infinity is always zero. We also have $y_{nl} \sim r^{l+1}$ for $r \to 0$, hence the evaluation at zero vanishes as long as

$$s > -(2l+1), \tag{A.7}$$

[1] We substitute a for a_0 to alleviate the notations.

which we assume verified in all the following computations. Computing the derivative in the second term yields

$$\int y_{nl}\, r^s\, y''_{nl}\, \mathrm{d}r \;=\; -\int y'_{nl}\, r^s\, y'_{nl}\, \mathrm{d}r - s\int y_{nl}\, r^{s-1}\, y'_{nl}\, \mathrm{d}r. \tag{A.8}$$

We want to express the first term of the right hand side in the same form as the second therm. For this we again integrate by parts with $u = (y'_{nl})^2$ and $v' = r^s$ so that

$$\int y'_{nl}\, r^s\, y'_{nl}\, \mathrm{d}r \;=\; \frac{1}{s+1}\Big[(y'_{nl})^2 r^{s+1}\Big]_0^\infty - \frac{2}{s+1}\int y''_{nl} y'_{nl}\, r^{s+1}\, \mathrm{d}r, \tag{A.9}$$

where the first term evaluates as zero by virtue of the same argument as above. We can substitute the second derivative y''_{nl} that appears using eq. (A.1) and we obtain

$$\int y'_{nl}\, r^s\, y'_{nl}\, \mathrm{d}r \;=\; -\frac{2}{s+1}\int y_{nl}\, \left[l(l-1)r^{s-1} - \frac{2}{a}r^s + \frac{1}{a_0^2 n^2} r^{s+1}\right] y'_{nl}\, \mathrm{d}r. \tag{A.10}$$

Combining this equation with eq. (A.8) gives:

$$\int y_{nl}\, r^s\, y''_{nl}\, \mathrm{d}r \;=\; \int y_{nl}\, f(r)\, y'_{nl}\, \mathrm{d}r, \tag{A.11}$$

$$f(r) = \left[\frac{2l(l+1)}{s+1} - s\right] r^{s-1} - \frac{4}{a(s+1)} r^s + \frac{2}{a_0^2 n^2 (s+1)} r^{s+1}. \tag{A.12}$$

Noting that $(y_{nl}^2)' = 2y'_{nl} y_{nl}$ and integrating by parts with $u = f$ and $v' = y'_{nl} y_{nl}$, we get

$$\int y_{nl}\, r^s\, y''_{nl}\, \mathrm{d}r \;=\; -\frac{1}{2}\int y_{nl}\, f'(r)\, y_{nl}\, \mathrm{d}r = -\frac{1}{2}\langle f'(r)\rangle, \tag{A.13}$$

with

$$f'(r) = (s-1)\left[\frac{2l(l+1)}{s+1} - s\right] r^{s-2} - \frac{4s}{a(s+1)} r^{s-1} + \frac{2}{a_0^2 n^2} r^s. \tag{A.14}$$

Substituting in eq. (A.5) and summing the common terms yields

$$\frac{2a^2}{s+1}\left[(2l+1)^2 - s^2\right]\langle r^{s-2}\rangle - \frac{2a}{s+1}(2s+1)\langle r^{s-1}\rangle + \frac{2}{n^2}\langle r^s\rangle = 0, \tag{A.15}$$

from which we recover the announced Kramers relation after multiplying by $(s+1)/2$:

$$\frac{s+1}{n^2}\langle r^s\rangle - (2s+1)\, a\, \langle r^{s-1}\rangle + \frac{s}{4}\left[(2l+1)^2 - s^2\right] a^2\, \langle r^{s-2}\rangle = 0. \tag{A.16}$$

To conclude, let us make an important remark on the validity of the Kramers relation. In the above derivation, no assumption has been made on the values of n and l, which is valid as long as the solutions y_{nl} exist and are square-integrable. The latter condition is verified as long as $l > 0$ and $n > 0$, without the restriction to integers values. In particular, this holds true for Rydberg states withing the context of quantum defect theory, where n is replaced with $n^* = n - \delta_{nlj} > 0$ (see eqs. (1.40-1.41)). To sum up, the conditions of validity of the Kramers relation are:

$$n > 0, \quad l > 0, \quad s > -(2l+1). \tag{A.17}$$

A.2 Computation of the average values $\langle r^s \rangle$

We now turn to the computation of the average values $\langle r^s \rangle$ used in chapter 1. The Kramers relation above allows for the immediate determination $\langle r^s \rangle$ for $s \leq -1$. More work is required to compute $\langle r^{-2} \rangle$, which is necessary to apply the recurrence relation to get those values corresponding to $s \leq -3$.

Case $s \geq -1$

Setting $s = 0$ in the Kramers relation (A.16), we get, using the normalization relation $\langle r^0 \rangle = 1$:

$$\frac{1}{n^2} - a\langle r^{-1} \rangle = 0, \tag{A.18}$$

hence

$$\langle r^{-1} \rangle = \frac{1}{n^2 a}. \tag{A.19}$$

We can get higher exponents s recursively. For instance, setting $s = 1$ yields

$$\frac{2}{n^2}\langle r \rangle - 3a + l(l+1)a^2\langle r^{-1} \rangle = 0, \tag{A.20}$$

hence

$$\langle r \rangle = \frac{a}{2}\left[3n^2 - l(l+1)\right]. \tag{A.21}$$

We also make use of $\langle r^2 \rangle$, which we get by setting $s = 2$ in the Kramers relation:

$$\frac{3}{n^2}\langle r^2 \rangle - 5a\langle r^2 \rangle + \left[2l(l+1) - \frac{3}{2}\right] a^2 = 0, \tag{A.22}$$

which finally gives

$$\langle r^2 \rangle = \frac{a^2}{2} n^2 \left[5n^2 + 1 - 3l(l+1)\right]. \tag{A.23}$$

These results extend *without restriction* to the case of Rydberg atoms simply by using $n - \delta_{nlm}$ in place of n.

Case $s \leq -2$

The Kramers relation alone is not sufficient to determine $\langle r^s \rangle$ for $s \leq -2$. We therefore must determine $\langle r^{-2} \rangle$ by another method to initiate the recurrence towards negative values. The method shown here is based on the application of the Hellmann-Feynmann theorem [141]. We note that the quantum number l appearing in the radial equation (1.6) is only a mere parameter and is not bound to be integer. The equation has solutions also for non-integer[2] l, which allows for the derivation with respect to l. Multiplying (1.6) by y_{nl}, taking the derivative with respect to l and integrating with respect to r, we get:

$$\int \mathrm{d}r \left[\frac{\partial y_{nl}}{\partial l}\mathcal{H} y_{nl} + y_{nl}\frac{\partial \mathcal{H}}{\partial l} y_{nl} + y_{nl}\mathcal{H}\frac{\partial y_{nl}}{\partial l}\right] = 0, \tag{A.24}$$

with

$$\mathcal{H} = a^2 \frac{\mathrm{d}^2}{\mathrm{d}r^2} - l(l+1)\frac{a^2}{r^2} + 2\frac{a}{r} - \frac{1}{n^2}. \tag{A.25}$$

[2]The solutions y_{nl} can actually be made analytical in l by replacing the factorials with the Gamma function.

The left term is essentially the radial equation multiplied by $\frac{\partial y_{nl}}{\partial l}$, thus vanishes. The same goes for the right term, which corresponds to the conjugate of the radial equation. We therefore have

$$\int \mathrm{d}r \; y_{nl} \frac{\partial \mathcal{H}}{\partial l} y_{nl} = 0, \tag{A.26}$$

which we can write as

$$\frac{\partial}{\partial l} \left\langle a^2 \frac{\mathrm{d}^2}{\mathrm{d}r^2} - l(l+1)\frac{a^2}{r^2} + 2\frac{a}{r} - \frac{1}{n^2} \right\rangle = 0. \tag{A.27}$$

Before computing the derivative, note that n has a hidden dependency in l. Indeed, we have the constraint $n \geq l+1$, which can be accounted for by writing $n = l + k$, with $k \geq 0$. We now have, retaining only those terms dependent on l:

$$\frac{\partial}{\partial l} \left[l(l+1)a^2\langle r^{-2}\rangle - \frac{1}{(l+k)^2} \right] = 0, \tag{A.28}$$

which yields

$$\langle r^{-2}\rangle = \frac{2}{(2l+1)n^3a^2}. \tag{A.29}$$

From this point we can compute the remaining $\langle r^s \rangle$ using the Kramers relation. In particular, we obtain $\langle r^{-3}\rangle$ by setting $s = -1$ in the latter:

$$\langle r^{-2}\rangle - l(l+1)a\langle r^{-3}\rangle = 0. \tag{A.30}$$

Finally, we have:

$$\langle r^{-3}\rangle = \frac{1}{a^3n^3} \frac{1}{l(l+1/2)(l+1)}. \tag{A.31}$$

Contrary to the previous section, the derivation of $\langle r^{-2}\rangle$ does *not* extend to the Rydberg case. Indeed, we assumed a relation $n = l + k$ between n and l, which is valid only for the hydrogen atom. The relation writes $n = l + k - \delta_{nlj}$ for Rydberg atoms, with a non-trivial (and unknown) dependence to l of δ_{nlj}. This prevents the direct computation of values such as $\langle r^{-3}\rangle$, though the knowledge of $\langle r^{-2}\rangle$ (for instance from a numerical computation) would still allow to determine them by use of the (still valid) Kramers relation.

Summary of the results

The quantities computed in this section are relevant to the calculations carried in chapter 1. We summarize them here:

$$\langle r^{-3}\rangle = \frac{1}{n^3a^3} \frac{1}{l(l+1/2)(l+1)}, \tag{A.32}$$

$$\langle r^{-2}\rangle = \frac{2}{n^3a^2(2l+1)}, \tag{A.33}$$

$$(*) \quad \langle r^{-1}\rangle = \frac{1}{n^2a}, \tag{A.34}$$

$$(*) \quad \langle r\rangle = \frac{a}{2}\left[3n^2 - l(l+1)\right], \tag{A.35}$$

$$(*) \quad \langle r^2\rangle = \frac{a^2}{2}n^2\left[5n^2 + 1 - 3l(l+1)\right]. \tag{A.36}$$

Those preceded with $(*)$ are also valid for non-hydrogenic Rydberg states.

Appendix B

Laser setup and frequencies

Many laser beams are involved during operation of the experiment. Almost all must have specific and stable frequencies, They are described in detail here.

We can categorize the lasers in three classes, depending on their role in the experiment. This entails different constraints and requirements that are shared within a given class. We thus can distinguish:

(1) "Ground-state lasers". Those are mostly involved in the manipulation of atoms in their ground state. They are tuned to the D_2 line of ^{87}Rb. They are characterized by the number of beams involved to address the various hyperfine levels.

(2) "Rydberg lasers". As their name suggest, they serve to excite atoms to the Rydberg state. They require high power and high frequency stability to maximize the transfer efficiency.

(3) The "tweezers laser". Its purpose is the generation of optical traps in the experiment. Its power is, in our conditions, the limiting factor to the number of traps we can prepare. The power fluctuations should also be controlled to prevent the heating of atoms.

In comparison to previous work, the Rydberg and tweezers laser setups are completely new, and the ground state lasers setup has been entirely rebuilt. This is also true of the laser locking scheme, that has been improved to fulfill the stronger constraints imposed by the new experimental setup. In this perspective, we describe here the "ground-state lasers" and "Rydberg lasers" setups. The "tweezers laser" has been described in chaper 2. We also briefly describe the frequency stabilization setup.

B.1 Ground-state laser setup

The ground-state laser setup is constituted by three lasers. The "spectro" laser, the "repumper" laser, and the "MOPA" laser. The schemes of the optical setups associated to each of them is shown in figure B.1.

The "spectro" laser is a Toptica DL pro laser diode emitting $\sim 60\,\mathrm{mW}$ of power. It is tuned to the $5S_{1/2}, F = 2 \leftrightarrow 5P_{3/2}$ hyperfine transition and is locked on an external cavity. It serves as a reference for the locking of the other two lasers. In addition to the beams involved in the frequency lock, we derive from it:

- The "probe" beam, tuned to the $F = 2 \rightarrow F' = 3$ transition. Its main role is to optically pump the atoms to the $m_F = 2$ Zeeman level, but it also serves as a kick beam in light-shift and Raman spectroscopy experiments.

- The "Raman F2" beam, involved in Raman spectroscopy.

Each of these two beams can have its frequency tuned with a $\sim 40\,\mathrm{MHz}$ bandwidth using a double-pass AOM system [142].

The "repumper" laser is also a Toptica DL pro laser diode. It is tuned to the $5S_{1/2}, F = 1 \leftrightarrow 5P_{3/2}$ hyperfine transition. We derive from it:

- Two static "repumper" beams, tuned to the $F = 1 \rightarrow F' = 2$ transition. Their role is to re-pump the atoms from the $F = 1$ to the $F = 2$ hyperfine level. Those beams overlap with the cooling beams of the MOT/molasses.
- One frequency-tunable "repumper", thanks to an AOM in double-pass configuration. The beam is overlapped with the probe beam of the spectro laser (they also share the same polarization). It is the repumper beam dedicated to the tweezers-trapped atoms. It is also involved more specifically in the light-shift spectroscopy experiment.
- The "Raman F1" beam, involved in Raman spectroscopy.

The "MOPA" laser is a Toptica TA 100 tapered amplifier system emitting $\sim 1\,\mathrm{W}$ of power. It is tuned to the $5S_{1/2}, F = 2 \leftrightarrow 5P_{3/2}$ hyperfine transition. We derive from it:

- Two "2D-MOT" beams, in charge of the first cooling stage of the atoms: the 2D-MOT.
- One "3D-MOT" beam, in charge of the 3D-MOT/molasses cooling in the sapphire cube. For this purpose, the beam is split in six with the help of a Schäfter+Kirchhoff cluster system, also shown in figure B.1.

The level structure of ^{87}Rb D_2-line along with the relative frequencies of the various beams described above are represented in figure B.2. The "probe", "Raman F2", "Raman F1" and "scanned repumper" beams can have their frequency tuned using a double-pass AOM configuration. The corresponding frequencies are indicative and may vary in actual experiments.

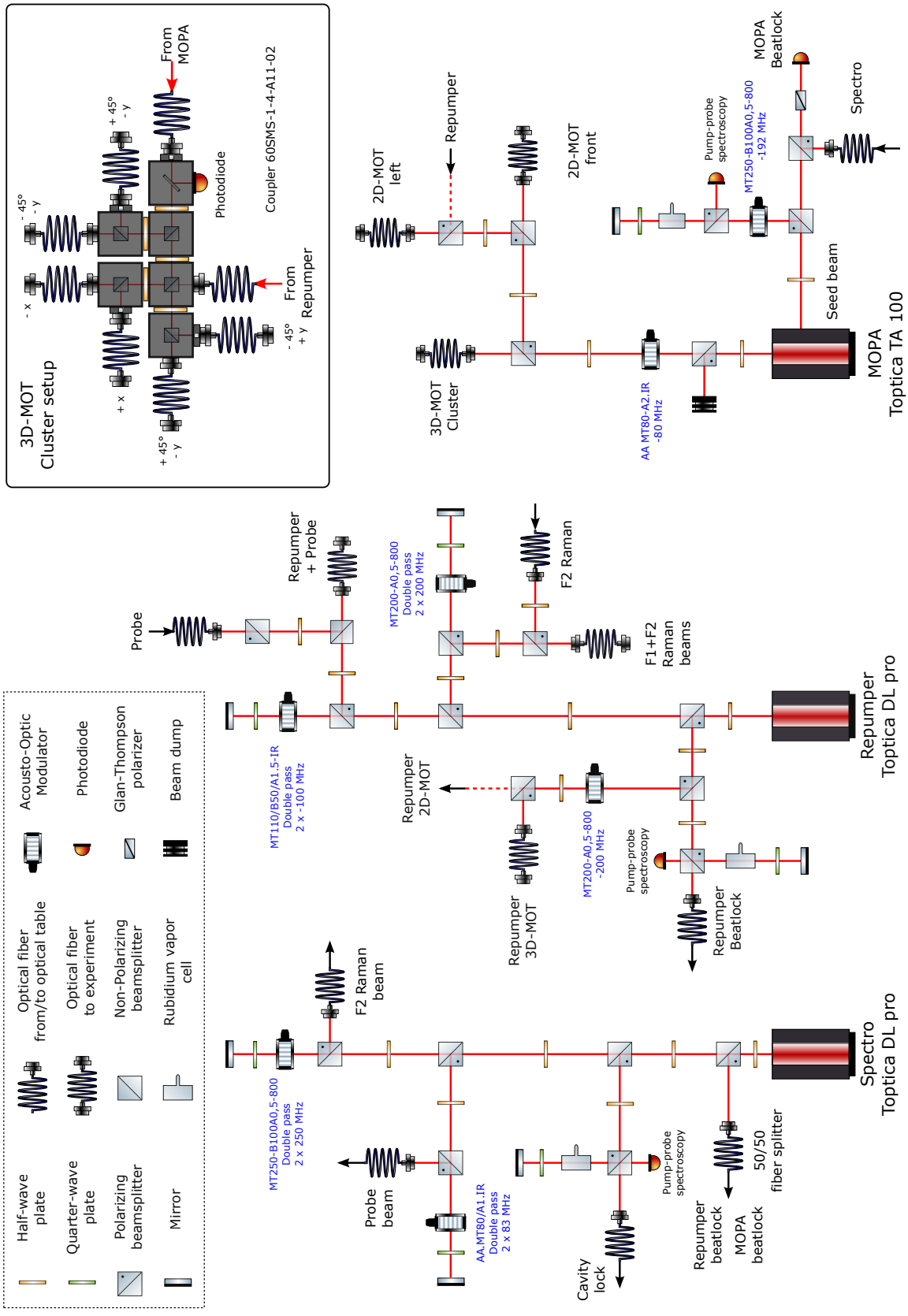

Figure B.1: Optical schemes of the ground-state lasers.

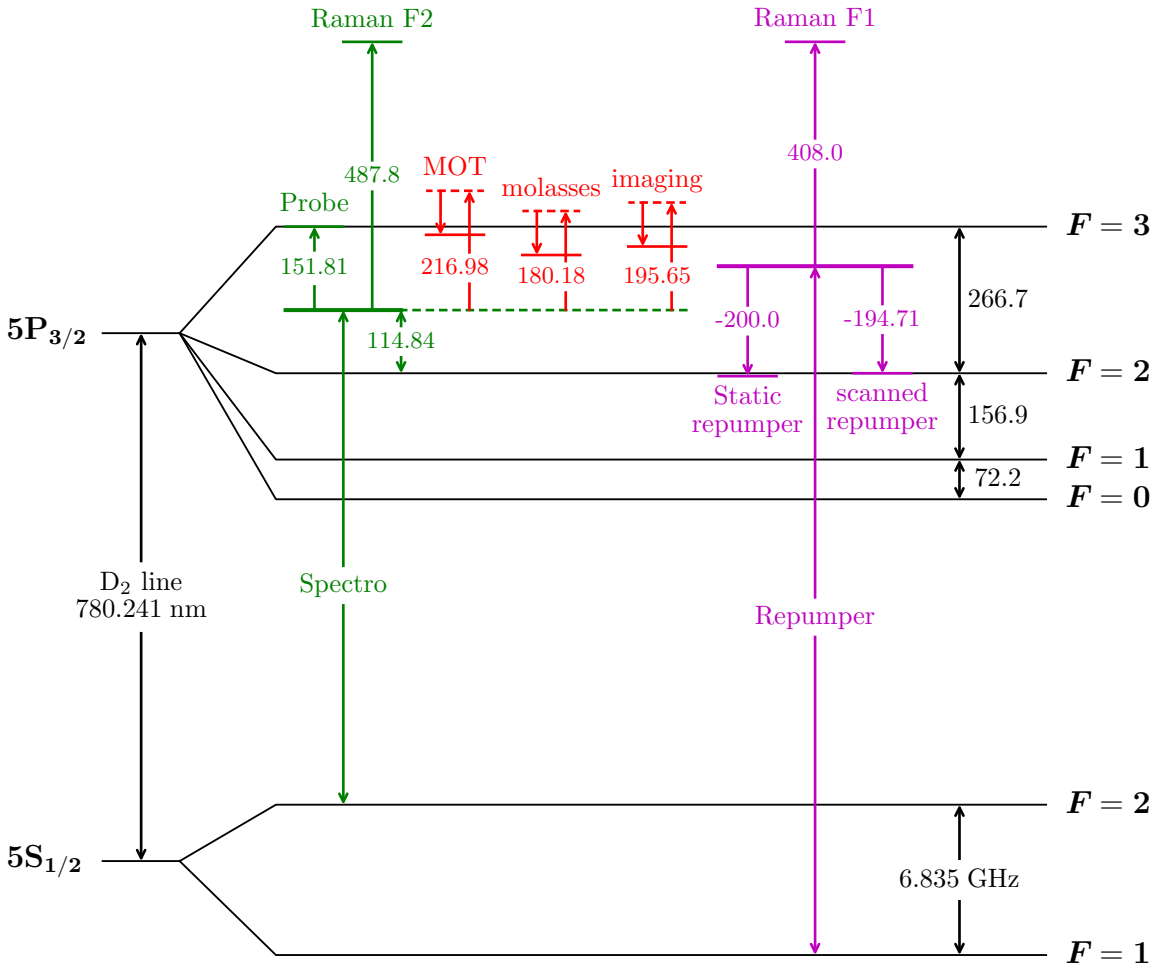

Figure B.2: Level structure of ^{87}Rb D_2-line and relative frequencies of the "Ground-state lasers". Owing to its particular locking scheme, the main MOPA laser beam (represented with a dashed red line) has its frequency tuned dynamically during the experimental sequence. We represent the frequency (relative to the "spectro" laser) of the relevant beams during the corresponding parts of the sequence as a solid red line. Unless otherwise specified, the frequencies are expressed in MHz.

B.2 Rydberg lasers setup

Two lasers are dedicated to the Rydberg excitation by a two photon transition at 420 nm + 1015 nm. However, the laser emitting at 1015 nm that we used initially went defective and was replaced by another one. We present in figure B.3 the optical setup of the three lasers, with the one corresponding to the defective laser (on the right) shaded.

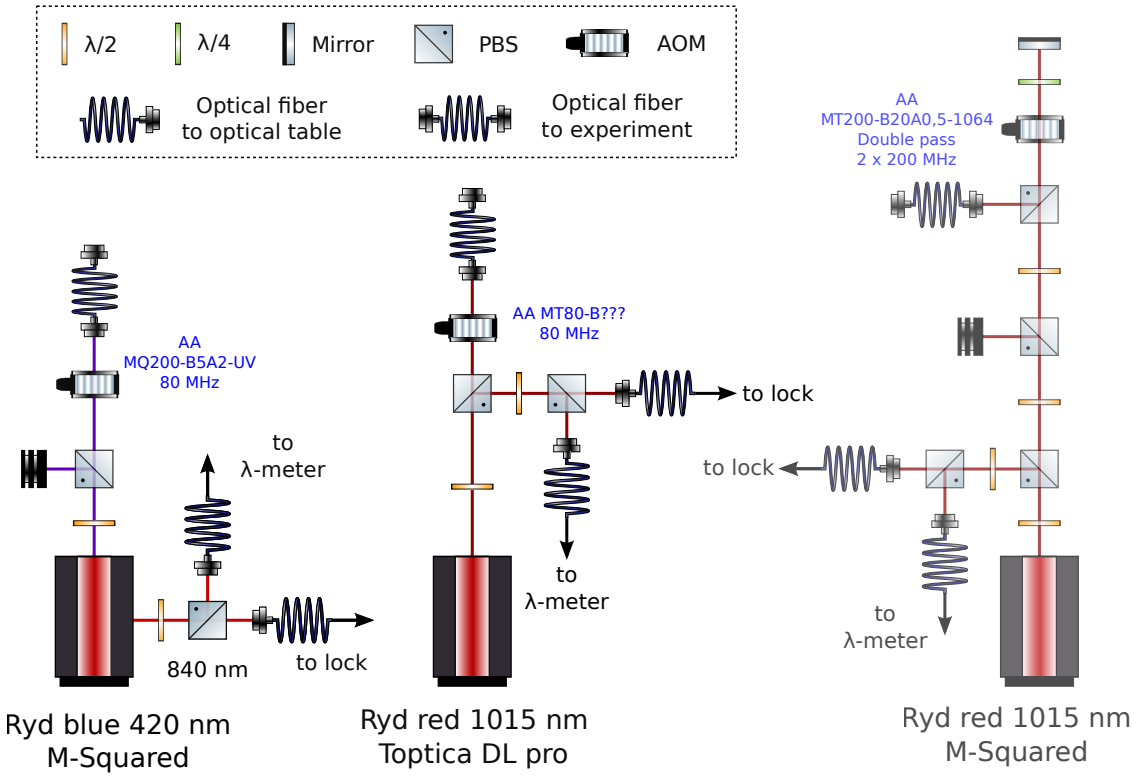

Figure B.3: Optical schemes of the Rydberg lasers. The titanium-sapphire laser emitting at 1015 nm (shaded center scheme) went defective and was replaced by a laser diode setup (right scheme).

The laser emitting at 420 nm (left scheme, referred to as "Ryd blue") is produced by a titanium-sapphire (TiSa) laser (SolsTiS, M-squared) pumped at 532 nm with a pump laser (Equinox, M-squared). The TiSa laser emits ~ 6 W of power at 840 nm, and is frequency-doubled (ECD-X, M-squared) to yield ~ 2 W of power at 420 nm. We use a fraction of the seed beam at 840 nm to lock the laser and monitor its frequency on a wavelength-meter. The frequency of the beam cannot be scanned.

The original laser emitting ~ 2 W of output power at 1015 nm (right scheme, referred to as "Ryd red") was prepared using a similar TiSa laser assembly (Equinox + SolsTiS, M-squared). A fraction of the output was used for the lock and to monitor the frequency. The beam frequency could be tuned thanks to a double-pass AOM system.

The current laser beam at 1015 nm (middle scheme, also referred to as "Ryd red") is produced by a Toptica DL pro laser diode. Contrary to the TiSa laser, the output power is only 130 mW. The setup is similar to the original laser except for the AOM that operates in single-pass. The beam frequency is tuned by changing the lock point of the laser.

B.3 Laser locking setup

The optical setup for the lock of the Rydberg and "spectro" lasers is presented in figure B.4. We lock the three lasers on a Stable Laser Systems ultrastable caity using the Pound-Drever-Hall (PDH) method [143]. Each beam has its frequency modulated by a fiber-coupled Electro-Optical Modulator (EOM) in order to shift the beam frequency and produce the modulation required for the PDH lock. The three beam are then overlapped before being sent to the cavity. The reflection from the cavity is then collected by a photodiode and sent to the locking electronics.

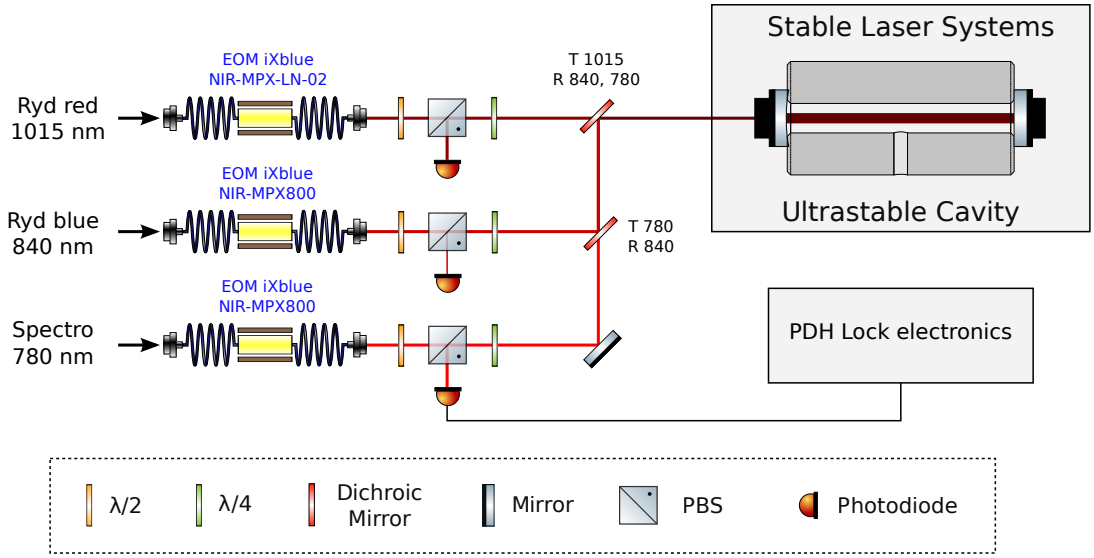

Figure B.4: Optical scheme of the PDH lock of the Rydberg lasers and the "spectro" laser on a Stable Laser Systems cavity.

The "repumper" laser is phase-locked to the "spectro" laser with a frequency offset of $32 \times 216.08 = 6914.56\,\text{MHz}$. The "MOPA" laser is beat-locked to the "spectro" laser with a variable frequency of approximately $+200\,\text{MHz}$. The frequency offset is controlled by a Voltage-Controlled Oscillator which frequency is tuned dynamically during the experiment (see figure B.2).

Appendix C

Electric field control in the experiment

The control of the electric field in the experiment is paramount to its proper operation, be it for the results presented here, those next to come or in the longer term for quantum simulation. Significant work has been done to ensure a good control of the electric field despite the strong constraints imposed by the setup:

(1) The minimization of electric field gradients over the $\sim 100\,\mu m$ spatial extension of atoms, in particular those possibly arising from charge accumulation on nearby dielectric surfaces.

(2) The necessity to switch between low voltages during the Rydberg sequence and high voltage for state-selective field ionization.

(3) Although this is not an actual limitation for the results shown in this manuscript, voltage noise from the sources can possibly be a limiting factor to the achievable coherence times in the prospect of long simulation times.

We first detail in this appendix the sapphire cube electrodes, their electrical connections and some of their characteristics. We follow with the description of the low-to-high voltage switching electronics that proved itself to be a significant improvement over the previously used devices [98, 96].

C.1 The sapphire cube electrode system

The Simion simulations carried for the design of the ionization detection setup give the field response at any point of the simulation domain for a given potential applied to an electrode. For this purpose, we simulated a set of 12 electrodes: 2 Stark electrodes, 2 Stark holders, 4 RF electrodes[1], 2 lens holders and 2 lenses. This can be used to determine the field with high precision when given the potential applied to each electrode.

To do this, we simplify the problem and consider only the 6 electrodes covering the interior of the sapphire cube: 2 Stark electrodes and 4 RF electrodes. Furthermore, instead of considering each electrode independently for its field response, we consider linear combinations of voltages applied to each electrode. These combinations, depicted in figure C.1, benefit from a simple physical interpretation. The reference V_{ref} essentially represents a global shift of the

[1]The reader must be aware that mechanical constraints prevent the tube-shaped part of the RF electrodes to be mechanically attached to the plate part (see figure fig:SapphireCube (d), yellow electrodes). The simulation actually takes both parts as separate electrodes, for a total of 16 electrodes rather than 12. The two parts are nevertheless electrically connected in the UHV setup and are considered as one in what follows.

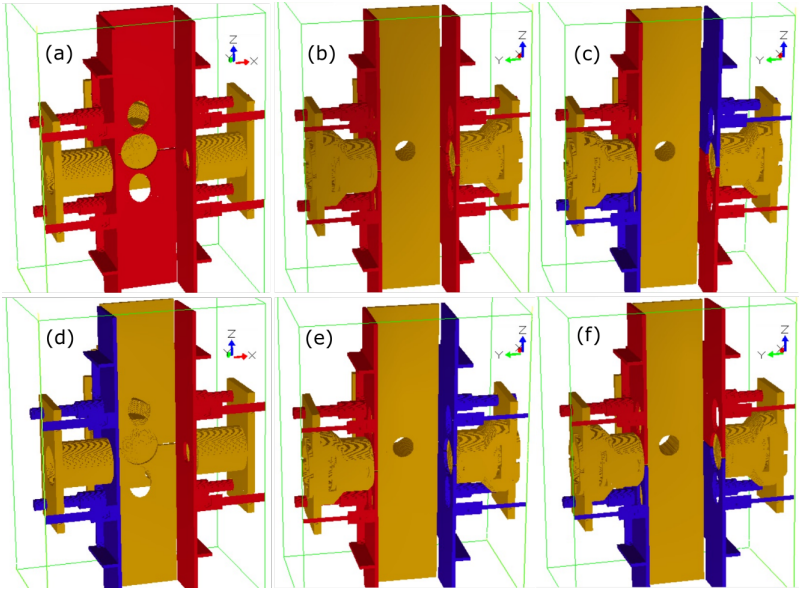

Figure C.1: Scheme of the sapphire cube electrodes highlighting the main voltages components. Red electrodes have positive voltage, blue electrodes have negative voltage, and yellow electrodes are grounded. (a) V_{ref}. (b) V_0. (c) V_+. (d) V_x. (e) V_y. (f) V_z.

potential. The component V_0 produces a quadrupolar field in the (x, y)-plane. V_+ produces a quadrupolar field in the (y, z)-plane. The three components V_x, V_y, and V_z are the most important and produce an electric field along the x-, y- or z-direction respectively.

The situation is made more complex, however, due to the Indium-Tin Oxide (ITO) coating of the lenses. Indeed, we must take into account the difference of work function ϕ between ITO and the gold-coated electrodes. Although we can take the value $\phi_{\text{ITO}} = 4.45\,\text{eV}$ [144] with a reasonable degree of confidence, the work function of gold is more variable an depends on the actual sample preparation and history [145].

The following tables show the field and gradient response to a potential of 1 V applied to each main voltage component (see figure C.1). Except for the ITO-coated lenses, the other electrodes are set to 0 V.[2] In table C.1 we provide the values in the condition $\phi_{\text{gold}} = \phi_{\text{ITO}}$. In table C.2 we set $\phi_{\text{gold}} = 5.15\,\text{eV}$, which is approximately the value for a clean sample of Au according to [145]. This translates respectively into an intrinsic potential difference $V_{\text{ITO}} = 0\,\text{V}$ and $+0.7\,\text{V}$ between the lenses and the lens holder (that is, the lens voltage is 0.7 V *higher* than the lens holder voltage in the latter case).

The simulation gives an electric field of $2.068\,\text{V cm}^{-1}$ when set with the voltages applied on the electrodes during the Rydberg experiments. This is in very good agreement with the measured value $F = 2.09\,\text{V cm}^{-1}$. Assuming $V_{\text{ITO}} = +0.7\,\text{V}$, we get a field gradient $\|\nabla F\| = -0.138\,\text{V cm}^{-2}$ directed along the x-direction. This represents a field variation of approximately $1\,\text{mV cm}^{-1}$ over the 75 µm-lateral extension of our 6×3 array of atoms, or $15\,\mu\text{V cm}^{-1}$ over the trapping region of our BoB traps. The effect of gradients is therefore much weaker than the temporal noise of the electric field, which we evaluated as $0.9\,\text{mV cm}^{-1}$ (see subsection 4.3.2).

[2]The other electrodes have little effect on the electric field and mainly produce gradients. As such, they could have their potential adjusted for precise field control at the atoms location. Although this might be necessary in the future, it was not done for the experiments presented and is out of the scope of this thesis.

Table C.1: Field response at the center of the cube to 1 V applied on the indicated voltage component. We set $V_{\mathrm{ITO}} = +0\,\mathrm{V}$ for the ITO-coated lens potential; other electrodes are grounded.

Voltage component	Field response ($\mathrm{V\,cm^{-1}}$)			Gradient response ($\mathrm{V\,cm^{-2}}$)		
	F_x	F_y	F_z	$\partial_x \lVert\mathbf{F}\rVert$	$\partial_y \lVert\mathbf{F}\rVert$	$\partial_z \lVert\mathbf{F}\rVert$
V_{ref}	0	0	0	−0.021	0.002	0
V_0	0	0	0	−0.777	0.654	0
V_+	0	0.142	0	0	0	1.149
V_x	−0.818	0	0	0	0	0
V_y	0	−0.787	0	0	0	0
V_z	0	0	−0.548	0	0	−0.163

Table C.2: Field response at the center of the cube to 1 V applied on the indicated voltage component. We set $V_{\mathrm{ITO}} = +0.7\,\mathrm{V}$ for the ITO-coated lens potential; other electrodes are grounded.

Voltage component	Field response ($\mathrm{V\,cm^{-1}}$)			Gradient response ($\mathrm{V\,cm^{-2}}$)		
	F_x	F_y	F_z	$\partial_x \lVert\mathbf{F}\rVert$	$\partial_y \lVert\mathbf{F}\rVert$	$\partial_z \lVert\mathbf{F}\rVert$
V_{ref}	0	0	0	0.145	−0.111	0
V_0	0	0	0	−0.857	0.849	0
V_+	0	0.142	0	0	0.252	1.149
V_x	−0.818	0	0	0.138	0	0
V_y	0	−0.787	0	0	0.252	0
V_z	0	0	−0.548	0	0	−0.049

C.2 Electric field control in the experiment

We present in figure C.2 a scheme of the electrical connections and instruments involved in the control of the electric field in the experiment.

The electric field is during Rydberg manipulation is set by a Keysight 33612A Arbitrary Waveform Generator (AWG) with 14 bit precision over the −10 to 10 V range. The two output of the AVG generate opposite voltages, each one being sent to a Stark electrode according to the circuit of figure C.2. To detect the Rydberg states by ionization, we switch the electrodes connection to high-voltage (HV) circuits. One of them (Stanford Research Systems PS310) is a static source. The other two are composed of an AVG and a HV amplifier and generate the ionization ramps.

The switching circuit and electrodes setup impose an important capacitive load of 2.7 nF to the voltage sources. This is significant for the negative HV amplifier that we use (Trek 2205) which has a low current capability. The corresponding (negative) ionization ramp gets deformed by the capacitive load.

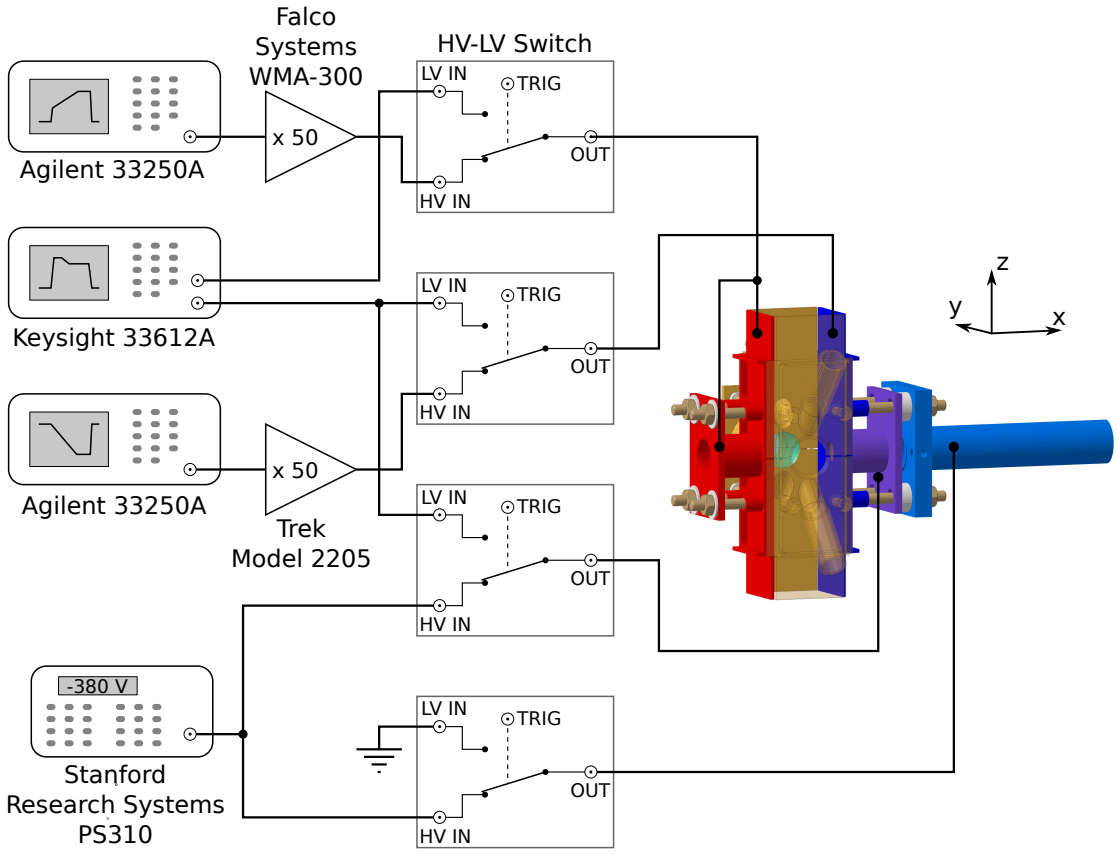

Figure C.2: Scheme of the electric circuit and connections for electric field control. The low-to-high voltage switch circuit is described in a dedicated section.

C.3 Voltage switching electronics

The electric fields involved in the ionization of Rydberg states are incompatible with those applied during the experimental sequence. Electronic circuits for HV to LV switching were thus designed to conciliate both voltage ranges. We distinguished two cases, depending on the sign of the high voltage, and designed a circuit to switch to high *negative* voltage and one to switch to high *positive* voltage. The essential components of the circuit are schematized in figure C.3, where we focus on the switching between LV and *negative* HV.

The isolation between the low voltage line and the output when connected to HV is done by a high-voltage p-channel MOSFET (FQB1P50), maintained closed with a voltage of $+12\,\mathrm{V}$ applied on the gate. When switching to LV, the gate is set at a voltage of $-15\,\mathrm{V}$, thus allowing for a full -10 to $+10\,\mathrm{V}$ range of low voltages. The transistor gate presents a rather large capacitance and is conveniently driven with a gate driver optocoupler (FOD3182) for shorter switching times. The connection to the HV line is established with the help of a high-voltage phototransistor optocoupler (MOC8204) able to withstand collector-to-emitter voltage up to $400\,\mathrm{V}$. When switching from HV to LV, it is important to discharge the electrode before connecting to LV. For this purpose, a second optocoupler connects the output to the $+15\,\mathrm{V}$ power supply for a few µs.

For proper operation, the activation of the various components must be controlled precisely. For this purpose, some timing and synchronization circuitry converts the LV-to-HV triggering gate into three signals that command each of the three components described

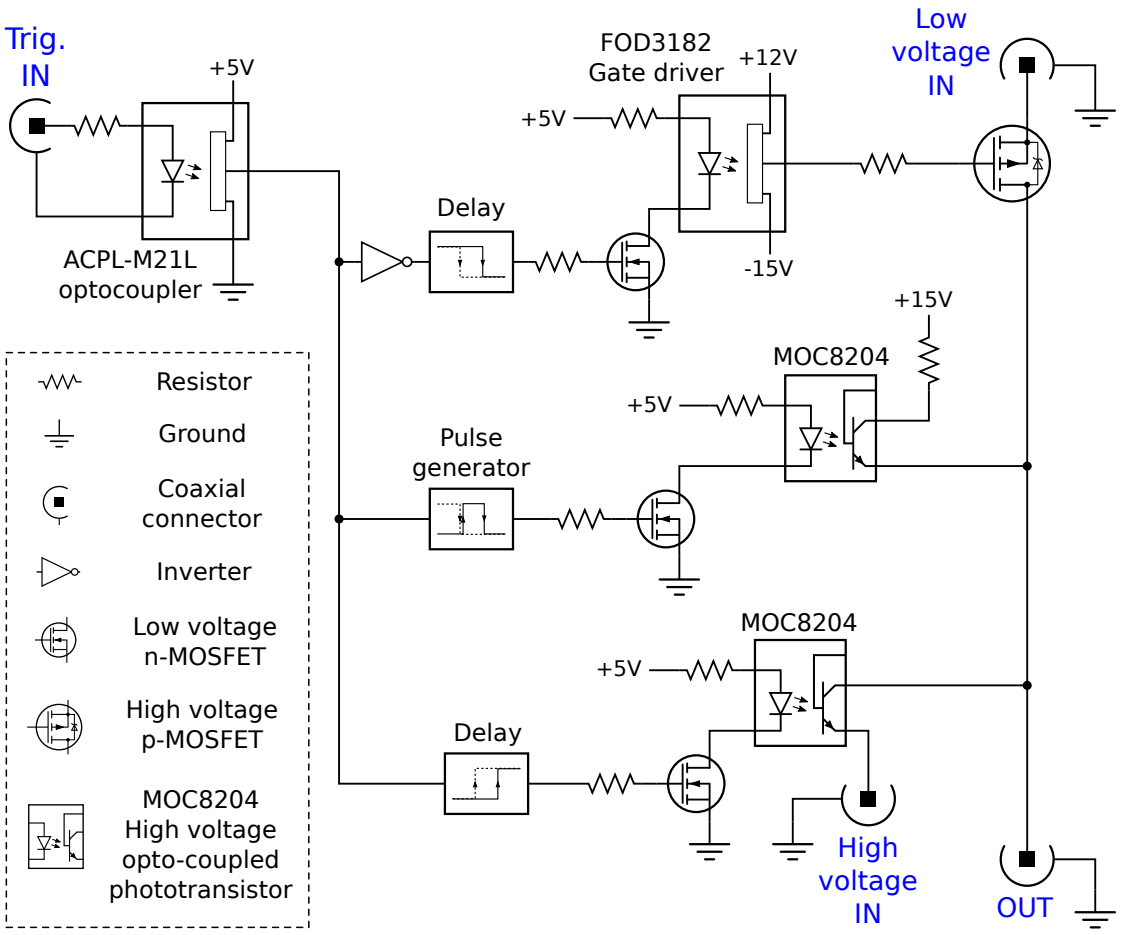

Figure C.3: Simplified scheme of the electronic circuit designed to switch between low voltage and high *negative* voltage. The circuitry essentially consists in three components: voltage regulation (not shown for simplicity); shaping of the trigger pulse to generate the control signals (boxes "Delay" and "Pulse generator"); high voltage switching proper. The operation is detailed in the text. The circuit differs slightly for *positive* voltage switching. Most notably the high-voltage p-channel MOSFET is be replaced by a n-channel MOSFET and the connections to the MOC8204 emitter and collector are adapted.

above. The timings are set by the intermediate of trimmers in the circuit. The triggering gate, coming from the computers, is a potential source of noise. It is isolated from the remaining circuitry with the help of another optocoupler (ACPL-21ML). The switching is therefore current-controlled rather than voltage-controlled. The whole circuit is powered with $\pm 15\,\mathrm{V}$, with intermediate voltages produced by regulators. The corresponding circuitry is not shown in figure C.3.

A LV to HV to LV switching cycle proceeds as follows.

- No current flows in the trigger circuit. The HV MOSFET connects the LV input to the output.
- The trigger is activated. A command to close the MOSFET channel is sent immediately. A delay of a few us is waited before sending a command to set the HV optocoupler into conduction. This is to ensure that the LV line does not get connected to the HV input.
- This state is maintained as long as current flows in the triggering circuit.

- The trigger is deactivated. The HV input is isolated from the output immediately. After a short delay, a control pulse is sent to the other HV optocoupler to discharge of the electrode. Only after this optocoupler goes back to non-conductive mode is the HV MOSFET channel opened to connect the LV line to the output.

The following pages show the complete circuits for both negative (1st page) and positive (2nd page) high voltage switching. In addition to the high-voltage control, they detail the pulse shaping logic, and the voltage regulation circuitry. The circuits may appear significantly more complex than the simplified scheme of figure C.3. They include some circuit protection devices, along with other tricks to improve the response time of the circuit. These, along with useful components miscellany, are described in great detail in [146, 147].

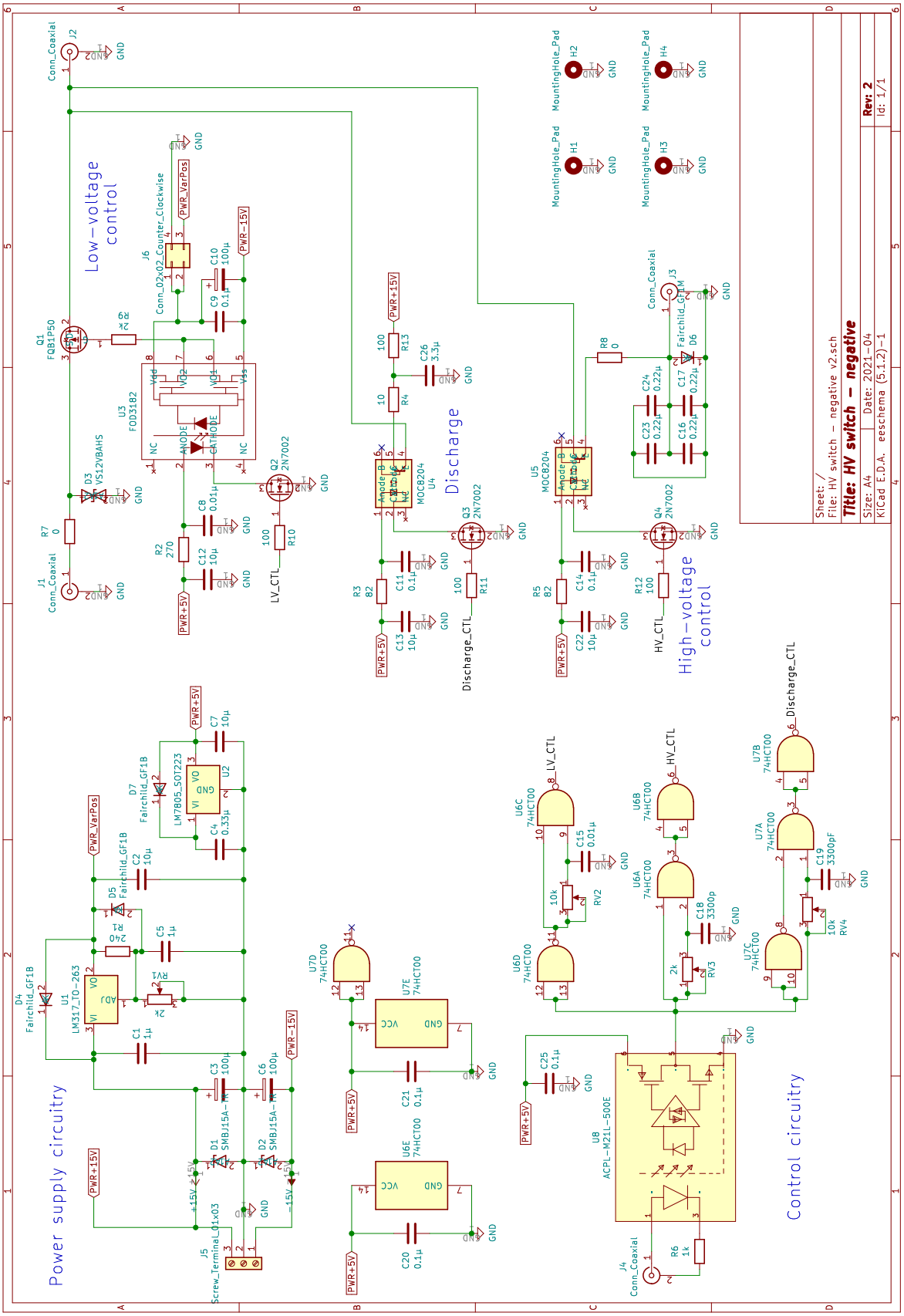
Low-voltage control
Discharge
High-voltage control
Power supply circuitry
Control circuitry
Sheet: /
File: HV switch - negative v2.sch
Title: HV switch - negative
Size: A4
Date: 2021-04
KiCad E.D.A. eeschema (5.1.2)-1
Rev: 2
Id: 1/1

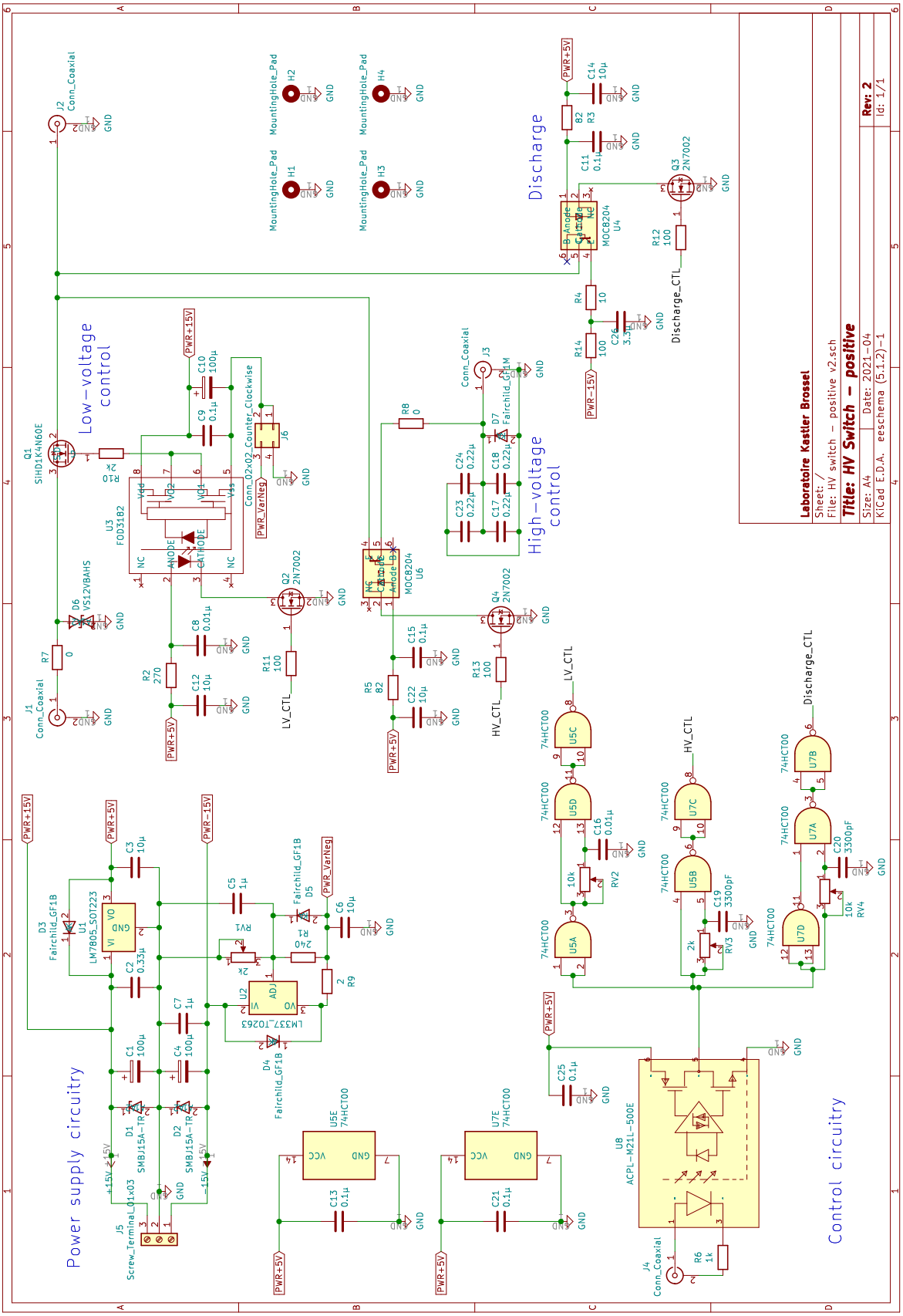
Power supply circuitry
Low-voltage control
High-voltage control
Discharge
Control circuitry
Laboratoire Kastler Brossel
Title: HV Switch – positive
Rev: 2
Size: A4
Date: 2021-04
KiCad E.D.A. eeschema (5.1.2)-1
Id: 1/1
LV_CTL
HV_CTL
Discharge_CTL
PWR+15V
PWR-15V
PWR+5V
PWR_VarNeg
GND

Appendix D

Numerical simulations of atomic dynamics

Atomic dynamics in the traps has an incidence on many aspects of our experimental results. Most notably, we discussed in chapter 5 the mechanical losses and the transition frequencies shift due to the residual light at the bottom of the trap. We also have seen in chapter 3 that our measurement of the oscillation of atoms in optical tweezers is sensitive enough to probe the trap shape beyond the gaussian approximation. In this appendix, we detail the methods used for classical atomic dynamics simulations in various trap potentials and use them to investigate its impact on various experimental observations.

The simulations begin with the sampling of atomic positions and velocities in a given potential, that corresponds to (or approximates) the gaussian tweezer potential. We provide some technical details on the potential and sampling method that are involved in all subsequent atomic dynamics simulations. We also discuss in some detail the Monte-Carlo fitting procedure involved in the atom temperature measurement. Simulations of the atomic motion in the traps, together with this methodology, are used to get an insight on the trapping potential beyond the gaussian approximation.

The ponderomotive trapping potential produced by the bottle beams presents additional features as compared to the ground-state traps. Indeed, contrary to the latter, the BoB potential is not simply proportional to the light intensity. We discussed some of the consequences in chapter 5 and most notably its variation with respect to the circular level considered. Here, we extend on the topic and investigate the origin of this difference and the consequences on the light-shift and coherence.

D.1 Gaussian traps

Gaussian optical tweezers are based on gaussian beams, the simplest solution of the paraxial Helmoltz equation for the propagation of light. These solutions are analytical, and the corresponding trapping potential (for ground-state atoms) is directly proportional to the light intensity at the atomic position, which simplifies greatly the study of these traps and the associated numerical simulations of atomic dynamics. Moreover, our experimental results obtained in chapter 3 allow us to get some insight on their deviation from the ideal gaussian trap.

D.1.1 Gaussian trap potential

The idealized trapping potential is generated by a gaussian beam produced by focusing a collimated monochromatic laser beam (wavelength λ) to a waist w_0 with a lens having a focal length f. The resulting potential is cylindrically symmetric and its value at a distance r from the optical axis and z from the lens focal plane is

$$V(r,z) = -\frac{V_0}{1+(z/z_\mathrm{R})^2}\exp\left[-2\frac{r^2}{w_0^2\left(1+(z/z_\mathrm{R})^2\right)}\right], \tag{D.1}$$

where $z_\mathrm{R} = \pi w_0^2/\lambda$ is the Rayleigh length. The potential amplitude V_0 is proportional to the maximum intensity I_0 (see chapter 1). It is often useful to consider the harmonic approximation to the above potential, retaining the curvature at the minimum as the only spatial dependence. The trapping potential thus becomes, for an atomic mass m,

$$V(r,z) \simeq -V_0 + \frac{1}{2}m\omega_r^2 r^2 + \frac{1}{2}m\omega_z^2 z^2, \tag{D.2}$$

associated to the axial and radial trap frequencies

$$\omega_z = \sqrt{\frac{2V_0}{mz_\mathrm{R}^2}}, \quad \omega_r = \sqrt{\frac{4V_0}{mw_0^2}}. \tag{D.3}$$

Cut views of the potential and corresponding plots of the trap depth are represented in figure D.1. Also depicted is the profile of the harmonic approximation (D.2), which is valid for $r \lesssim w_0/2$ and $z \lesssim z_\mathrm{R}/2$. An important remark is that the gaussian potential is sub-harmonic in the sense that it is always inferior to its harmonic approximation.

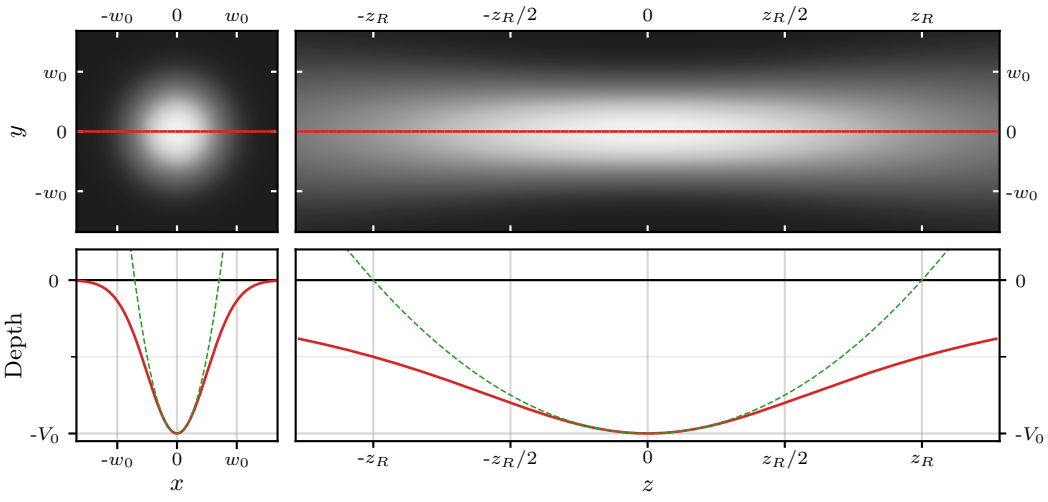

Figure D.1: Vizualization of the gaussian trap potential. Top: cut views of the potential. Bottom: transverse profile of the potential at the focal plane (left) and axial profile along the optical axis (right). The green dashed line corresponds to the harmonic approximation.

As we will now see, the gaussian potential is not only used to numerically solve the equations of motion and compute the dynamics, but also to sample atomic positions as the initial conditions for dynamics computation.

D.1.2 Sampling in phase space

The sampling of atomic coordinates in phase space assumes that the energies are Boltzmann-distributed, which is regarded as a valid hypothesis [134]. We also restrain ourselves to *classical* motion: position and momentum commute and are therefore independent. For a position $\mathbf{r}$ and velocity[1] $\mathbf{v}$, the mechanical energy E_m is

$$E_\mathrm{m} = \frac{1}{2} m \left\|\mathbf{v}\right\|^2 + V(\mathbf{r}). \tag{D.4}$$

As mentioned above, the velocity and position are independent and the join equilibrium probability distribution ρ can be factored in two terms

$$\rho(\mathbf{r}, \mathbf{v}) = \rho_r(\mathbf{r})\rho_v(\mathbf{v}). \tag{D.5}$$

At thermodynamic equilibrium, with a temperature T, the corresponding probability densities are

$$\rho_r(\mathbf{r}) = \mathcal{N} \exp\left[-\frac{V(\mathbf{r})}{k_\mathrm{B}T}\right], \tag{D.6}$$

$$\rho_v(\mathbf{v}) = \left[\frac{m}{2\pi k_\mathrm{B}T}\right]^{3/2} \exp\left[-\frac{m\left\|\mathbf{v}\right\|^2}{2k_\mathrm{B}T}\right], \tag{D.7}$$

where we introduced the Boltzmann constant k_B, and an unspecified normalization factor $\mathcal{N}$.

Each component of the velocity follows a normal distribution with standard deviation $\sqrt{k_\mathrm{B}T/m}$. Sampling the velocity numerically therefore does not pose any problem. However, the distribution of positions is not trivial, and even ill-defined. To see this, we remark that the exponential in eq. (D.6) does not vanish at infinity:

$$\exp\left[-\frac{V(\mathbf{r})}{k_\mathrm{B}T}\right] \xrightarrow[\left\|\mathbf{r}\right\|\to\infty]{} \epsilon > 0, \tag{D.8}$$

and hence the integral over all space is infinite (and so is the normalization factor in eq. (D.6)). To circumvent this problem, the retained approach consists in confining the atomic positions to a finite volume in space.

However, the difficulty of position sampling is not completely solved. Indeed, contrary to the case of velocities, the potential of eq.(D.1) does not lead to a distribution (eq. (D.6)) for which a sampling algorithm is immediately available. We followed two approaches to samples positions despite these difficulties.

- Simplify the potential. With the harmonic approximation of eq.(D.2), the positions become normally-distributed and are easily sampled.
- Use a general sampling method. The *rejection sampling* method [148] applies well to our case.

Our rejection sampling algorithm proceeds as follows.

(1) We first add the constant energy V_0 to the potential: $V(\mathbf{r}) \longrightarrow V'(\mathbf{r}) = V(\mathbf{r}) + V_0$. The resulting potential is always positive. Therefore, introducing $\tilde{V}_T(\mathbf{r}) = V(\mathbf{r})/(k_\mathrm{B}T)$, we have $0 < \exp\left(-\tilde{V}_T(\mathbf{r})\right) \leq 1$ at any position.

[1] We favor velocity over momentum as it is more convenient to work with in addition to being more intuitive.

(2) We define a region of space in which raw positions are sampled by the condition $\exp\left(-\tilde{V}_T(\mathbf{r})\right) < 10^{-3}$. The value 10^{-3} was chosen empirically and works fine for temperatures up to 150 µK.
(3) Draw atomic positions $\mathbf{r}_i$ in the selected spatial volume, along with a number $0 \leq p_i < 1$. Position $\mathbf{r}_i$ is accepted if $p_i < \exp\left(-\tilde{V}_T(\mathbf{r}_i)\right)$. This is done until the desired number of values is obtained.

The rejection sampling is precise, but computationally intensive and hence rather slow. Normal sampling from the harmonic approximation of eq.(D.2) is significantly faster (about 20 times), but less precise. The harmonic approximation is valid as long as $r << w_0$, the natural radial length scale, and $z << z_R$, the natural axial length scale. Assuming that the harmonic approximation is valid, we get, for a thermal distribution at temperature T,

$$\frac{\langle r_{\mathrm{rms}}\rangle}{w_0}, \frac{\langle z_{\mathrm{rms}}\rangle}{z_{\mathrm{R}}} = \sqrt{\frac{k_{\mathrm{B}}T}{2V_0}}. \tag{D.9}$$

Thus, for trap depths of the order of 1 mK, the condition is verified if $T \lesssim 20$ µK (giving a ratio of 1/10).

We compare the two sampling methods in figure D.2. We used the gaussian beam parameters obtained in chapter 3 (see eq. 3.28), and show scatter plots for 500 samples at temperatures $T = 10,\ 60$ and 120 µK. As expected from the above argument, the distributions are hardly distinguishable at $T = 10$ µK, but start to differ significantly for $T \gtrsim 60$ µK. The difference lies mainly in the underestimation of the axial extension $\langle z_{\mathrm{rms}}\rangle$ by the normal sampling method.

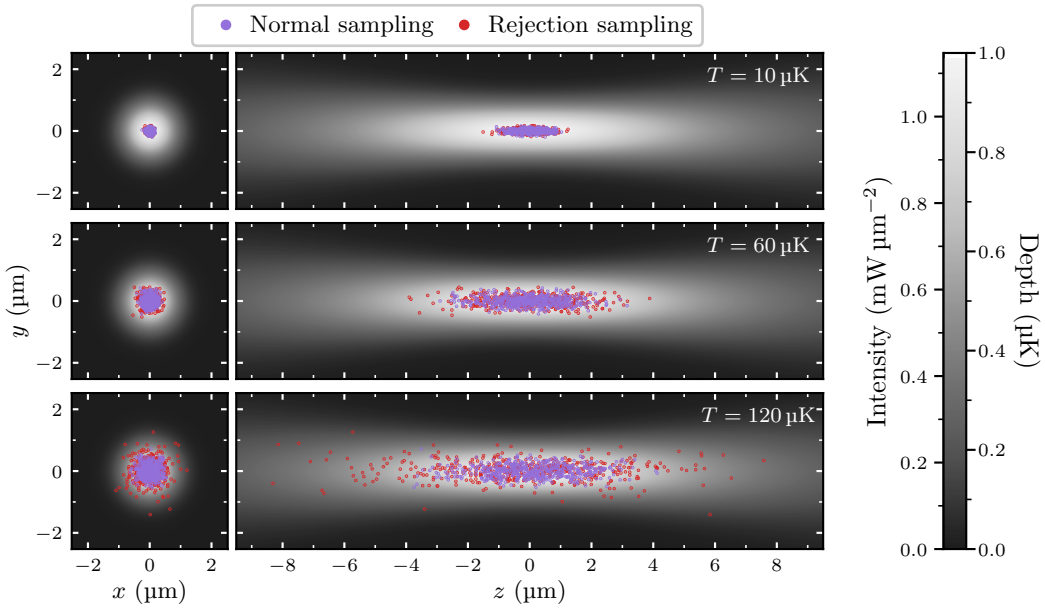

Figure D.2: Comparison between normal and rejection sampling of atomic positions. 500 samples were drawn by both methods at indicated temperatures using the tweezers parameters found in chapter 3. The panels show the (x, y)-coordinates of the samples (left), and the (z, y)-coordinates (right).

None of the experimental results presented in this manuscript involves atomic temperatures higher[2] than 30 µK. We therefore choose the faster normal sampling in all our fitting

[2]Higher temperatures nevertheless occur in pre-optimized conditions.

procedures and simulations described hereafter.

D.1.3 Monte-Carlo fitting procedure: temperature measurement

Our Monte-Carlo fitting procedures are based on the simulation of an experimental sequence and its comparison with the data. Repeating this by varying the fitted parameter lead to the determination of the best value. We illustrate this with the simplest simulations involved in this thesis: the release-recapture experiment for temperature measurement.

The release-recapture sequence measures the fraction $p_{\mathrm{exp}}(t_i)$ (with standard deviation σ_{exp})of atoms that get recaptured after releasing them for variable delays t_i, which depends on their temperature. Knowing the beam parameters, the procedure to compare how a given temperature fits to the experimental data goes as follows.

- Draw N atomic position and velocity samples in the tweezer potential. For the temperature measurement, we usually take $N \sim 100\,000$.
- Simulate the recaptured fraction $p_{\mathrm{sim}}(t_i)$ at each recapture delay. To gain in computational speed, we use the same N atomic samples for all experimental points.
  - Compute the atomic positions and velocities after free flight for a duration t_i (we take the gravity $\mathbf{g}$ into account).

$$\mathbf{r}(t_i) = \mathbf{r}(0) + \mathbf{v}(0)\, t_i + \mathbf{g}\frac{t_i^2}{2} \tag{D.10}$$

$$\mathbf{v}(t_i) = \mathbf{v}(0) + \mathbf{g}\, t_i \tag{D.11}$$

  - Determine the recapture probability. Atoms are recaptured if their mechanical energy is negative:

$$E_{\mathrm{m}} = \frac{1}{2}m\mathbf{v}^2(t_i) + V[\mathbf{r}(t_i)] < 0. \tag{D.12}$$

- Take into account additional loss mechanisms, such as the finite lifetime of the atomic species considered (see for instance sections 5.1.1 and 5.1.2). Mathematically we do the transform $p_{\mathrm{sim}}(t_i) \to \hat{p}_{\mathrm{sim}}(t_i) = p_{\mathrm{sim}}(t_i)\rho(t_i)$, where $\rho(t)$ represents the population decay at delay t.
- Scale the simulated curve to the data. The scale A accounts for baseline losses of atoms, and y_0 corresponds to the atom background. This values can be set constant or fitted to the experimental data, that is by fitting to p_{exp} the parameters (A, y_0) of the function $f(A, y_0; t) = A\hat{p}_{\mathrm{sim}}(t) + y_0$. Although these parameters can be estimated from the data in some situations (for instance in chapter 3, see figure 3.11), this is not always the case (see chapter 5, figures 5.3 and 5.4). In the latter case, the fitting procedure is necessary.
- Compute the χ^2 distance using the transformed simulated curve

$$\chi^2 = \sum_i \frac{(p_{\mathrm{exp}}(t_i) - A\hat{p}_{\mathrm{sim}}(t_i) - y_0)^2}{\sigma^2_{\mathrm{exp}}(t_i)}. \tag{D.13}$$

The whole fitting procedure involves repetitions of the above algorithm for different temperatures. We first get a rough estimate of the temperature by performing quick simulations with a reduced number of samples, retaining the temperature T_0 that minimizes the χ^2 distance (D.13). More precise simulations are run for temperatures near T_0, from which we determine the distance $\chi^2(T)$. The resulting curve is fitted with a 4^{th}-degree polynomial, from which we recover the temperature at the minimum $\hat{T}$.

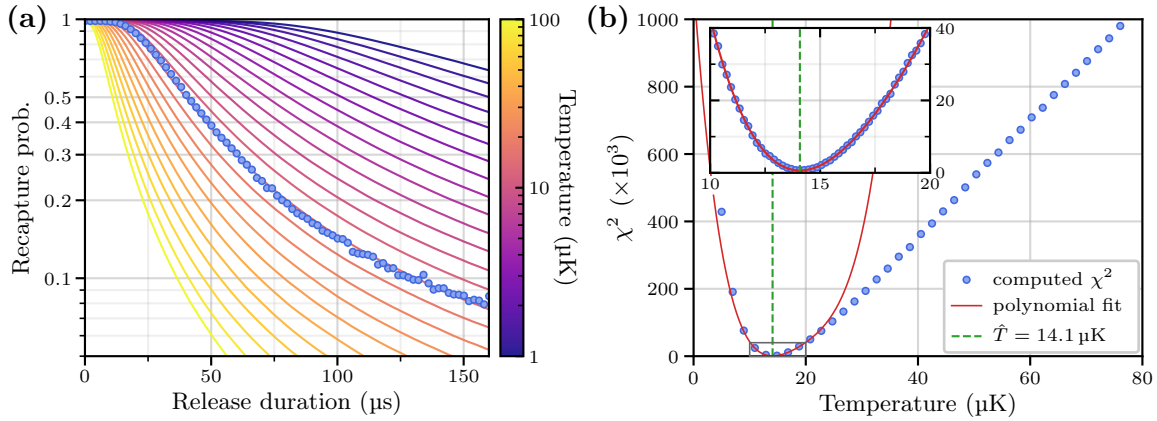

Figure D.3: Monte-Carlo fitting procedure for the temperature. (a) Simulated recapture curves for various temperatures. The simulations were run with 400 000 samples and scaled to the data (scaling factor $A = 0.985$) (b) Calculated χ^2 distance as a function of the temperature for the preliminary estimation (large panel) and for precise determination (inset). The solid red line is a 4^{th}-degree polynomial fit of the inset data. The simulations were carried with 400 000 samples. The optimal temperature is $\hat{T} = 14.1\,\mu\text{K}$, that corresponds to $\chi^2 = 656$.

The uncertainty in the fitted temperature is determined using the formula [138]:

$$\hat{\sigma}_T^2 = 2\left[\frac{\mathrm{d}^2\chi^2}{\mathrm{d}T^2}\right]^{-1}_{\hat{T}} \frac{\chi^2(\hat{T})}{k}, \tag{D.14}$$

where k is the number of degrees of freedom. We have $k = n - p$ with n the number of data points taken and $1 \leq p \leq 3$ the number of fitted parameters (the temperature, along with optional global scale and offset). We have included the factor $\chi^2(\hat{T})/k$ so that the weights $1/\sigma^2_{\text{exp}}(t_i)$ are considered as relative rather than absolute. This behavior is consistent with all the fits carried throughout this thesis. One could nevertheless argue that the interval $[0, 1]$ is the natural scale for Monte-Carlo simulations and thus the weight should be considered as absolute. In the data presented on figure D.3, we have[3] $k = 81 - 2 = 79$, and $\chi^2(\hat{T}) = 656$. Hence considering the weights as absolute would reduce the uncertainty by a factor of ~ 8.

To conclude, let us mention some limitations in the procedure. They represent functionality that is currently not implemented rather than fundamental limitations.

- We do not take into account the uncertainty in the position of the minimum of the polynomial fit of χ^2. The difficulty lies in the fact that we do not fit the roots of the polynomial but its coefficients, which are harder to link to the roots.
- When the scaling parameters are fitted, the covariance with the temperature is not determined.

D.1.4 Classical dynamics in gaussian tweezers

The atomic dynamics in BoB traps does not corresponds to that of atoms at thermal equilibrium. Instead, the dynamics is inherited from the atomic motion in gaussian tweezers. The oscillation signals described in section 3.2.2 are actually an indirect probe of the latter. Hence, in order to get some insight on the dynamics in gaussian tweezers, we analyze here

[3] we fix $y_0 = 0$ and fit A and T so that $p = 2$.

these signals beyond the simple Fourier analysis described in the main text. To this end, we carry simulations of the atomic motion during the whole experimental sequence to compare with the measurements.

Atomic motion in gaussian traps

We show five classical atomic trajectories simulated for a total duration of 100 µs in figure D.4. The trapping potential is that of eq.(D.1), with the trap parameters and temperature obtained in chaper 3, namely:

$$w_0 = 1.21\,\mu\text{m}, \quad V_0 = k_\text{B} \times 990\,\mu\text{K}, \quad T = 14.1\,\mu\text{K}. \tag{D.15}$$

To improve on the precision, we sampled the initial positions using rejection sampling.

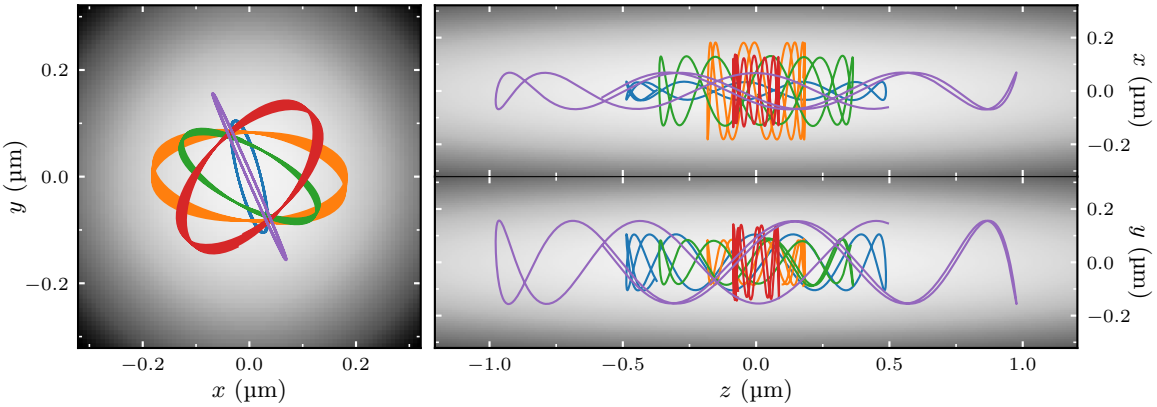

Figure D.4: Simulated trajectories in gaussian tweezers. The left panel shows the (x, y) coordinates of the trajectories; the right panels show the (z, x) (top) and (z, y) (bottom) coordinates. The background shading indicates the trapping potential (compare with figure D.2). The motion was calculated for a duration of 100 µs.

We note that the typical transverse motion is elliptical rather than simply linear. This is in contrast with the picture of a one-dimensional oscillating motion, in which the kinetic and potential energies necessarily oscillate. Here, situations occur in which both energy terms stay relatively constant along the trajectory.

The time-averaged kinetic energy $\bar{E}_c$ and potential energy $\bar{E}_p$ along the trajectories (we take the mean over 150 000 trajectories, hence the brackets) are

$$\langle \bar{E}_c \rangle = h \times 440\,\text{kHz} = \frac{3}{2} k_\text{B} T, \quad \langle \bar{E}_p \rangle = h \times 453\,\text{kHz} \approx \frac{3}{2} k_\text{B} T. \tag{D.16}$$

The potential energy deviates slightly from the expected value $\frac{3}{2} k_\text{B} T$ in the case of an harmonic potential. This indicates an effect of the trap anharmonicity, to which the atoms are sensitive even at such low temperatures. This effect is nevertheless very small, and the potential can safely be assumed harmonic for the purpose of semi-quantitative analysis. We also note that such a thermal shift cannot be detected with the light-shift spectroscopy discussed in section 3.2.1 since its value is 10 times smaller than the natural width of the probed transition. However, we could expect to observe it on the sharper Rydberg transition.

Let us conclude with a word of caution on the validity of these simulations. The trap parameters used above correspond to transverse and axial trap frequencies $\omega_r \approx 2\pi \times 80\,\text{kHz}$

and $\omega_z \approx 2\pi \times 12\,\mathrm{kHz}$, respectively. Those values must be compared to the atomic temperature, that corresponds to a frequency[4] $\omega_T \approx 2\pi \times 300\,\mathrm{kHz}$. On the one hand, we have $\hbar\omega_z/k_\mathrm{B}T \sim 25 \gg 1$, and the axial motion can therefore safely be assumed to be in the classical regime. On the other hand, we have $\hbar\omega_r/k_\mathrm{B}T \sim 4 \sim 1$, which implies that the transverse motion is still in the quantum regime.

As we will now see, our classical simulations, albeit limited in precision, allow us to grasp the essential features of atoms dynamics in the traps.

Simulations of release-induced oscillations

The variety of oscillations signals observed in the experiment dedicated to the trap frequency measurement (see figure 3.6) forced us to go beyond the simple damped sinus model for the analysis of oscillations. Before justifying the choice retained to recover the trap parameters from those signals, we describe here some of the features observed and characterize them with simulations.

In order to get an insight on the variety of oscillation signals observed, we introduce a generalized potential

$$V(x,y,z) = -\frac{V_0 w_{0x} w_{0y}}{w_x(z), w_y(z)} \exp\left[-2\frac{r^2}{w_x(z)w_y(z)}\right]. \tag{D.17}$$

Apart from V_0, this potential is now dependent on three parameters rather than one: w_{0x}, w_{0y} and δz. The first two parameters correspond to the beam waist along the x- and y-direction respectively. The dependence on δz lies in the functions $w_x(z)$ and $w_y(z)$:

$$w_x(z) = w_{0x}\sqrt{1 + ((z-z_0)/z_{\mathrm{R}x})^2}, \quad w_y(z) = w_{0y}\sqrt{1 + ((z+z_0)/z_{\mathrm{R}y})^2}, \tag{D.18}$$

where $z_{\mathrm{R}x}$ and $z_{\mathrm{R}y}$ are the corresponding Rayleigh lengths. These parameters emulate the deformation of gaussian tweezers by optical aberrations. for instance, the difference $w_{0x} - w_{0y}$ can be associated to coma, resulting in an elliptical beam. A non-zero δz can be associated to astigmatism, that makes the two axes of the beam focus at different positions.

We present, in figure D.5, simulations of the experimental sequence leading to the recorded oscillation signal. We reproduce in the top panels the selected signals of figure 3.6. The middle panel show simulated curves that qualitatively replicate the selected signals.

To obtain those curves, we simulate the whole experimental sequence (see figure 3.5):

- sample atomic positions using rejection sampling;
- compute free-flight evolution for a duration of 6 µs;
- compute the evolution in the trapping potential for a variable delay;
- compute free-flight evolution for a duration of 20 µs;
- determine the recapture probability.

The potential used to sample atomic position and to compute the dynamics is the same. It is set using the trap depth V_0 obtained for the corresponding trapping site (the same is done for the sampling temperature T). The remaining parameters w_{0x}, w_{0y} and δz are set manually.

The three oscillation behaviors are archetypal and each of the 81 signals can be related to one of them. On the left, we have a slowly decaying oscillation, which we can reproduce by setting $w_{0x} = w_{0y} = 1.16\,\mu\mathrm{m}$ and $\delta z = 0$. In the middle panel, we observe a beating occurring

[4]The value $\frac{k_\mathrm{B}}{h} \simeq 21\,\mathrm{kHz}\,\mu\mathrm{K}^{-1}$ is useful for quick order-of-magnitude estimates.

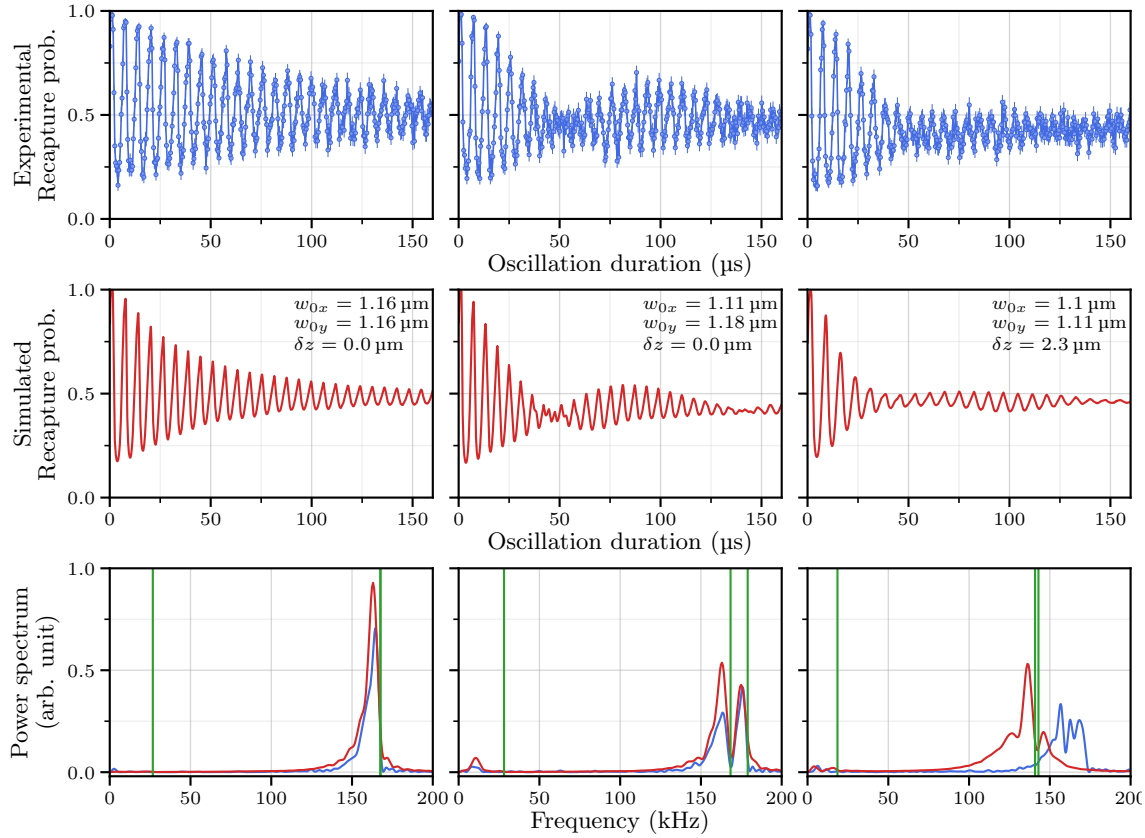

Figure D.5: Simulation of atomic oscillations in the traps. Top panels: selected signals exhibiting the three archetypal oscillation behaviors (see figure 3.6). Middle panels: simulated curves obtained with 50 000 atomic samples using the indicated trap parameters. Bottom panels: Corresponding Fourier power spectra of the experimental data (blue) and of the simulated curve (red). The green vertical lines are the trap frequencies associated to the trapping potential used in the simulations. Note that they appear systematically at frequencies higher than the peak(s) of the power spectrum.

with a node at 50 µs. This can be interpreted as resulting from two distinct transverse frequencies which we reproduce by setting $w_{0x} = 1.11\,\mu m$ and $w_{0y} = 1.11\,\mu m$. The signal on the left shows a quick decay, with persistent residual oscillations. Simulating this behavior proved more difficult. Albeit less convincing, we obtain a similar oscillation decay by setting $\delta z = 2.3\,\mu m$. Its relevance to the actual trap shape is questionable, yet it illustrates that a large variety of oscillation dynamics can take place when the traps are deformed.

Some features of the experimental data are shared by all simulations. For instance, we recover a minimal recapture probability of 20% and the particular shape of oscillations, sharp at the top and smooth at the bottom, that was discussed in section 3.2.2. This is in good agreement with the experimental data. However, a notable difference is the decay of the simulated curves, which is significantly faster than that of the experimental curves. No obvious reason appears for this discrepancy, but we can make the following remarks:

- The switching of the optical tweezers is not instantaneous, but takes a few hundreds ns. This is not taken into account and might alter the atomic dynamics.
- As mentioned in the previous section, the initial cloud expansion (1^{st} release) takes places in the quantum regime. This might cause the oscillatory motion to be more

coherent and result in a slower decay of the signal.

We plot on the bottom panels of figure D.5 the power spectra of both the experimental data and the simulation. Except for the rightmost data set, the spectra of the simulated curve overlap well with those of the experimental data. We also plot the trap frequencies of the trap potentials used in the simulations as vertical green lines. They appear systematically $\sim 5\,\mathrm{kHz}$ above the peak(s) of the spectra. This indicates an effect of the trap anharmonicity and a possible bias in our estimation of the waist, as we will now see.

Monte-Carlo fitting of the waist

Using the Monte-Carlo fitting procedure described above to systematically fit the trap parameters is not possible. As we have seen, many parameters are required to accurately describe the trap shape. This would in turn necessitate an intractable exploration of the parameter space with simulations for proper fitting. Nevertheless, it is possible to fit those signals that are accurately described by one parameter. This is the case of the rightmost signal of figure D.5, which can be described with the beam waist w_0 as the single trap parameter.

In figure D.6 we show, along with the experimental data, a simulated curve corresponding to the fitted value $w_0 = 1.167 \pm 0.001\,\mu\mathrm{m}$ of the waist. The fitting procedure is the same as described for the temperature, except that we simulate the oscillation sequence with the waist as the varying parameter. Apart from the faster decay of the simulation, the agreement between the two is good, as evidenced by the good overlap of the Fourier power spectra (right panel of figure D.6).

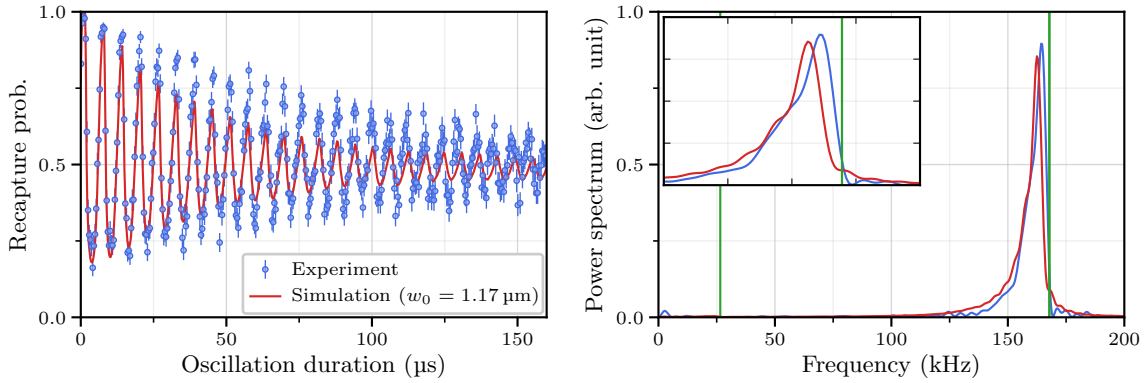

Figure D.6: Monte-Carlo fitting of the trap waist. Left panel: selected oscillation data used for fitting and simulated curve with the trap potential parameterized with the fitted value of the waist. Right panel: Corresponding power spectra (the colors match the data). The inset details the peaks in the range 140 – 180 kHz. The green lines represent the trap frequencies of the potential used in the simulation.

The waist obtained from the Monte-Carlo procedure differs slightly (but significantly) from the value $w_0 = 1.192 \pm 0.004\,\mu\mathrm{m}$ obtained in section 3.2.3. This overestimation of the waist from the identification of the oscillation frequency with the trap frequency (that is, its curvature at the minimum) is compatible with the sub-harmonic character of the gaussian potential (see figure D.1). Indeed, for a given motion amplitude, the oscillation frequency is inferior to what it would be with the corresponding harmonic potential. The discrepancy of about 2% is nevertheless very small and does not affect much the distribution of positions used in the simulations.

Choice of the analysis method

The bias in the waist estimation mentioned above is difficult to avoid. This is due to the impossibility to directly fit the atom dynamics to the data in most cases, where the oscillations are more complex than the simple decay. Even then, the variety of signals make difficult the recovery of the trap parameters. They do not convey enough information to get the detailed structure of the trap and require us to make the simplification of reducing the data to a single trap frequency from which we deduce the waist.

The question of how to compute a trap frequency is thus not trivial. For this purpose we selected three methods, which we illustrate in figure D.7 with a selected signal[5]. This data set, plotted of the left panel of figure D.7 (a), was chosen because it shows pronounced beating and a complex power spectrum (right panel), with three peaks.

(1) Fitting with a damped sinus function, shown in the left panel of figure D.7 (a). This solution is the simplest, yet is not completely satisfactory. First, it does not grasp some features of the signal such as the nonzero minimum recapture probability. Second, and most importantly, the beating of the signal is associated to a phase inversion, which is deleterious to the fit. To compensate for this, the decay time is reduced so as to make the oscillations collapse at the first beating node. This can be seen as an algorithmic way to get rid of a part of the data, which is not desirable.

(2) Compute the frequency that corresponds to the maximum of the power spectrum $S(f)$. Mathematically, we compute $\arg\max S$. This method is not satisfactory either since when we are in the presence of multiple peaks, there is no apparent reason to favor one over another.

(3) Take the center of the peak structure. As detailed in section 3.2.2, we set

$$f_{\text{osc}} = \frac{f_{\min} + f_{\max}}{2}, \tag{D.19}$$

with

$$f_{\min} = \min_f \left\{ S(f) = \frac{\max S}{2} \right\}, \quad f_{\max} = \max_f \left\{ S(f) = \frac{\max S}{2} \right\}. \tag{D.20}$$

This method has the disadvantage of being somewhat arbitrary in the definition of $f_{\min}$ and $f_{\max}$.

The frequencies determined with the three methods are shown as vertical lines on the power spectrum of figure D.7 (a).

To compare the three methods and select the best, we determine the trap parameters with each method and look at the correlation between the trap power and the loading probability. We report in figure D.7 (b) the loading probability vsthe trap power of each trapping site as determined by the three methods. We have two set of loading probabilities, one from the light-shift spectroscopy (violet) and one from the trap frequency measurement (green). A linear regression for each set is shown as a solid line, along with the corresponding Pearson's r coefficient. The "arg max" method is clearly the worst, while the "peak center" method appears to give the best correlation with $r = -0.84$ and $r = -0.91$ for the light-shift spectroscopy data set and the trap frequency measurement data set, respectively.

Although the exact origin of this correlation is unknown, it is unlikely that it occurs randomly out of a given analysis method. On this basis, the "peak center" method (3) was retained to get the trap parameters.

[5]Visible on figure 3.6 (a), 3$^{\text{rd}}$ column from the left, 2$^{\text{nd}}$ line from the top.

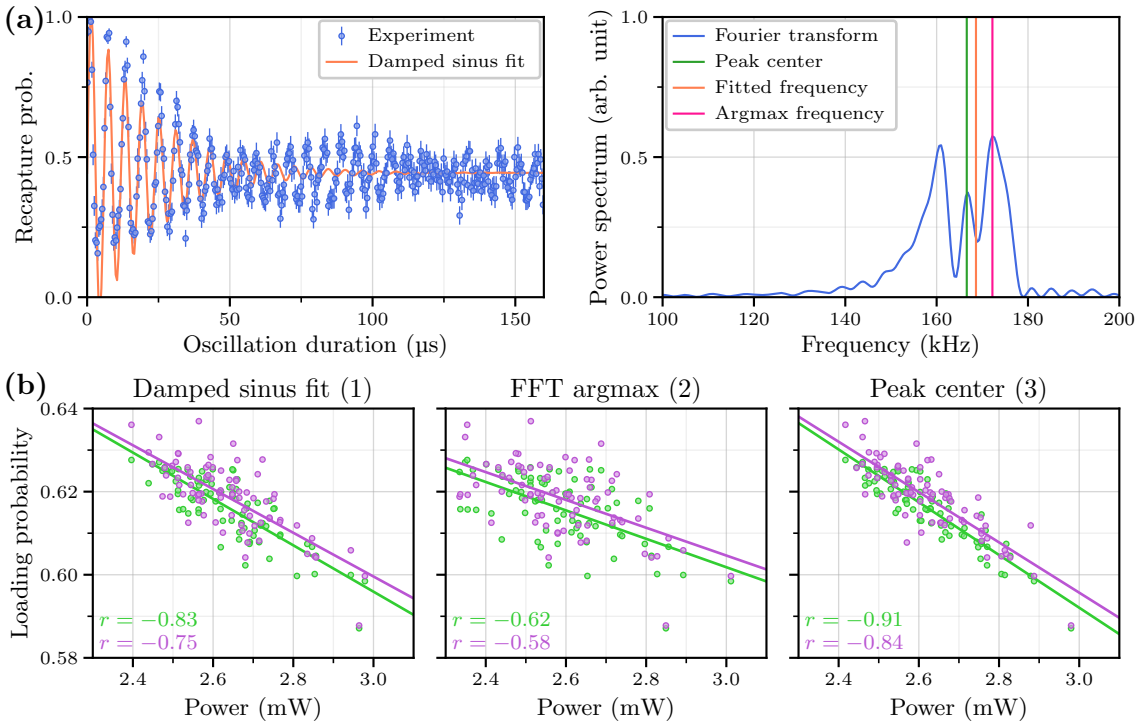

Figure D.7: Benchmarking analysis procedures to get the trap frequency from the oscillation signals. (a) Left panel: selected data set fitted with a damped sinus. Right panel: Corresponding Fourier power spectrum. The vertical lines corresponds to the frequencies determined by the three methods described in the text. (b) Correlation between the trap power and the loading probability from the frequency measurement (green) and the light-shift spectroscopy (violet).

The average waist thus obtained is used to parameterize the gaussian trapping potential that is involved in the simulation of atom dynamics in BoB traps, which is the topic of the next section.

D.2 BoB traps

Due to the repulsive nature of the ponderomotive force, the BoB traps are much more complex than the gaussian traps discussed above. In addition to the fact that the intensity pattern has no analytic expression, the exact potential is not directly proportional to the intensity but a convolution with the Rydberg wavefunction charge density. This has important consequences that we study in this section.

We thus first briefly describe the anharmonicity of the BoB intensity profile and show that it is at the heart of the trapping potential deformation from the convolution with the charge distribution of the trapped state. The transfer of atoms from gaussian traps has an impact on the subsequent dynamics in the shallower BoB traps, which we discuss together with the transfer efficiency. Finally, the state-dependent deformation of the potential leads to a position-dependent shift of the transition. We study the decoherence induced by this effect, using classical Monte-Carlo simulations.

D.2.1 BoB traps anharmonicity

We present in figure D.8 cut views of the BoB intensity profile along with corresponding plots of the intensity. This is similar to and should be compared with figure D.1 for the gaussian traps.

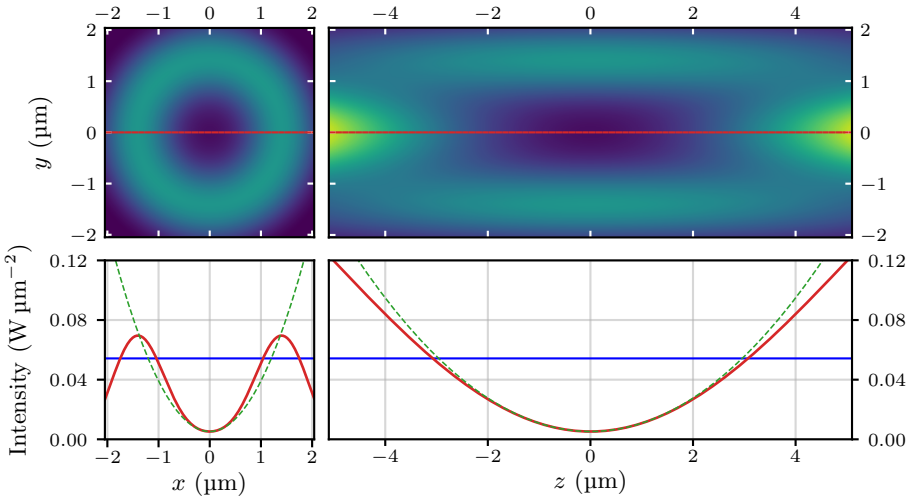

Figure D.8: Vizualization of the BoB intensity profile. Top: cut views of the BoB. Bottom: transverse profile at the focal plane (left) and axial profile along the optical axis (right). The blue line indicates the trapping threshold; atoms with an energy above this threshold are able to escape from the trap. The green dashed line corresponds to the harmonic approximation; note that the transverse profile is above its harmonic approximation.

There is one notable difference between the BoB traps and their gaussian counterpart. Although both are sub-harmonic along their propagation axis (the z-direction), the BoB intensity profile differs from the gaussian beam in that it is above its harmonic approximation along the transverse direction.

As we indicated in section 5.2.1, the BoB profile is parametrized by the radius s of the disc on which we apply a π phase shift (see figure 5.5). The retained value, $s = 3.5\,\mathrm{mm}$ for our experimental settings, not only maximizes the trap depth as already discussed, but also corresponds to a maximization of the harmonic character of the BoB profile. The quadratic coefficients of the series expansion of the BoB profile in the vicinity of the center is thus maximized. In contrast, a dark BoB, having no residual light intensity at its center, is also completely anharmonic. This means that the quadratic coefficients of its power series expansion (at the center) vanish.

As we will now see, the intensity profile anharmonicity is at the origin of the deformation of the trapping potential occurring from the convolution with the charge density of the state.

D.2.2 Convolution with a charge density

We mentioned in chapter 5 that the convolution of the BoB intensity profile with the charge density of the Rydberg electron causes a deformation of the trapping potential. This leads to a state-dependent potential not only leading to a global energy offset but also to a position-dependent shift.

In order to analyze the effect of the convolution in general terms, we rewrite eq. (5.14)

with an arbitrary probability distribution $\rho(\mathbf{r})$:

$$U(\mathbf{R}) = \int V(\mathbf{R}+\mathbf{r})\rho(\mathbf{r})\,\mathrm{d}^3\mathbf{r}. \tag{D.21}$$

A qualitative difference arises when comparing quadratic and quartic potentials. We thus first study these two simple cases to obtain analytical results and get some insight on the occurrence of this state-dependent potential variation. We proceed by describing the potential difference that pertains to our experiments: between 52C and 50C in the BoB trap. In that case, the intensity distribution $V(\mathbf{R})$ is that of the BoB traps and the probability distribution is that of the Rydberg electron of the circular state 52C or 50C.

Quadratic intensity profile

We first consider the simple case of a one-dimensional quadratic potential $V(X) = \alpha X^2$. Denoting $\mathbf{r} = (x, y, z)$, we can simplify the convolution of eq. (D.21) by integrating over the y and z coordinates. This yields

$$U(X) = \alpha \int (X+x)^2 p(x)\,\mathrm{d}x, \tag{D.22}$$

where

$$p(x) = \int \rho(x,y,z)\,\mathrm{d}y\mathrm{d}z. \tag{D.23}$$

The above convolution can be further integrated with respect to the x coordinate to give

$$U(X) = \alpha(X^2 + 2X\langle x\rangle + \langle x^2\rangle) = \alpha(X - \langle x\rangle)^2 + \alpha(\langle x^2\rangle - \langle x\rangle^2), \tag{D.24}$$

where $\langle x^k\rangle = \int x^k p(x)\mathrm{d}x$ is the k-th moment[6] of x. The convolved potential is thus essentially the original potential $V(X)$, shifted in position by $\langle x\rangle$ and with the variance $\langle x^2\rangle - \langle x\rangle^2$ of the distribution as a global offset. The shift $\langle x\rangle$ makes the result D.24 essentially invariant under a change of coordinates. The latter can be conveniently chosen so as to have $\langle x\rangle = 0$, in which case only the offset remains.

The above result obtained for a one-dimensional potential generalizes without restriction to three dimensions. Indeed, in the latter case there always exists a system of coordinates (X, Y, Z) in which the potential can be written $V(X,Y,Z) = \alpha X^2 + \beta Y^2 + \gamma Z^2$. Each term of the sum can then be treated independently as above and will give a contribution analogous to that of eq. D.24. In particular, for a probability distribution $\rho(\mathbf{r})$ such that $\langle\mathbf{r}\rangle = \mathbf{0}$, we have $U(\mathbf{R}) = V(\mathbf{R}) + \langle\,\|\mathbf{r}\|^2\rangle$.

A word of caution is nevertheless in order when comparing the convolution with two different probability distributions. In this situation, the convolution must be computed *in the same coordinates* for both distributions. However, it is quite possible that (the indices denote the two distinct distributions) $\langle x\rangle_1 \neq \langle x\rangle_2$. This leads to a position-dependent potential difference

$$U_1(X) - U_2(X) = 2\alpha X(\langle x\rangle_1 - \langle x\rangle_2) + \alpha(\langle x^2\rangle_1 - \langle x^2\rangle_2)^2. \tag{D.25}$$

Focusing on circular states, this situation may occur when the atoms are subject to a strong electric field. In this case, the ion core is displaced in the direction of the electric field while the Rydberg electron wavefunction is displaced in the opposite direction. This effect being stronger for higher circular levels, we could expect such a state-dependent shift of the potential to occur. The effect might as well be negligible, and in any case would benefit from a quantitative study.

[6] Here and in the following, we assume that p and ρ are regular enough so that the moments of any order k are well defined. This is the case for instance of atomic orbitals which decay exponentially as $r \to \infty$.

Quartic intensity profile

We now consider the simple quartic potential $V(X) = \alpha X^4$ to highlight the qualitatively different effect of the convolution as compared to a quadratic potential. Keeping the above notations, the convolution yields

$$U(X) = \alpha(X^4 + 4X^3\langle x\rangle + 6X^2\langle x^2\rangle + 4X\langle x^3\rangle + \langle x^4\rangle). \tag{D.26}$$

Similarly to the quadratic potential, the cubic term $\propto X^3$ can be removed by choosing the appropriate coordinates. In addition, the odd moments $\langle x^{2k+1}\rangle$ vanish for a symmetric probability distribution, thus further simplifying the convolved potential. This is the case of circular states wavefunctions (save for the last remark of the previous section on the necessity to keep the same coordinates when comparing two convolutions), for which we get

$$U(X) = \alpha(X^4 + 6X^2\langle x^2\rangle + \langle x^4\rangle). \tag{D.27}$$

In addition to the original potential $V(X)$ and the global offset $\alpha\langle x^4\rangle$, a quadratic term $6\alpha\langle x^2\rangle X^2$ appears that changes the shape of the potential. Furthermore, the quadratic coefficient $\propto \langle x^2\rangle$ is dependent on the atomic state considered which leads to a state-dependent change of the potential shape.

This analysis extends to the three-dimensional case and to more complex potentials. The potential can in general be expanded as a power series in which each term of the sum will be treated independently as above. The convolution basically leads to the apparition of lower order terms proportional to the moments of the probability distribution. Even though the odd terms vanish in the case of a symmetric probability distribution (such as for circular states), position-dependent terms remain that change the shape of the potential. The only exception is the quadratic potential, which degree as a polynomial is too low to make non-constant terms appear.

Potential difference between 52C and 50C

Our BoB traps fall in the category of complex potentials which cannot be assumed quadratic. The convolution with the circular state charge density causes a state-dependent deformation of the trapping potential. This is illustrated in figure D.9, in which we show cut views of the potential energy difference $U_{52} - U_{50}$ between 52C and 50C. This potential energy difference can be interpreted as the light-shift of the 50C $\rightarrow$ 52C transition.

The individual potentials U_{52} and U_{50} were obtained by directly computing the convolution between the BoB intensity profile and the corresponding circular state probability density (both evaluated on a discrete mesh). The quantization axis was set along the x-direction, which corresponds to our experimental configuration.

We define the *trapping region* as the part of the trap, where the potential is lower than the threshold energy necessary to escape from the trap. Its boundary is indicated on the cut views by a gray line[7].

The color map is split in three parts. The dashed lines are the isocontours corresponding to a zero light-shift. The regions in blue (negative light-shift) lie mostly outside of the trapping region, albeit not entirely. The dotted lines correspond to the light shift at the center of the trap, $94.32\,\mathrm{kHz\,W^{-1}}$, that delimitate regions of positive yet lower light-shift (cyan to yellow) and larger light-shift (red). The situation is quite complex here as the trap center is actually

[7]The trapping region is found to be the same for both 52C and 50C within a spatial resolution of $10 \times 10 \times 40\,\mathrm{nm}$.

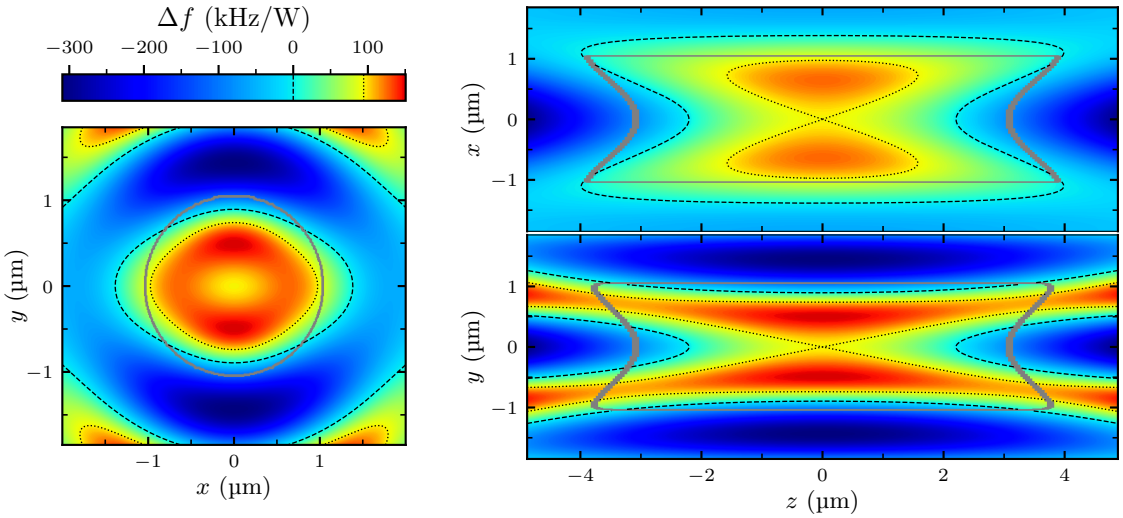

Figure D.9: Cut views of the difference of potential between 52C and 50C. The trapping region is delimited by the gray line. The dashed lines correspond to the isocontours of zero transition light-shift. The dotted lines correspond to the isocontours at the trap center light-shift of $94.32\,\mathrm{kHz\,W^{-1}}$.

a saddle point for the transition light-shift, which increases in the transverse direction and decreases along the propagation axis. We also note a strong anisotropy that appears as a result of the quantization axis being transverse.

D.2.3 Classical dynamics in BoB traps

Although it can be safely assumed that thermal equilibrium is reached for atoms in gaussian traps [134], this is not the case in BoB traps. The atoms are "dropped" in BoB traps with their position and velocity inherited from the gaussian trap. This has consequences on their dynamics, that we discuss here.

In the remaining of this section, we consider a BoB trap with 20 mW total power, corresponding to a trap depth of $\sim 80\,\mu\mathrm{K}$ with respective radial and transverse frequencies $\omega_r \simeq 2\pi \times 16\,\mathrm{kHz}$ and $\omega_z \simeq 2\pi \times 6.4\,\mathrm{kHz}$. Note that these trap frequencies correspond to excitation quanta $\hbar\omega_r \simeq k_\mathrm{B} \times 0.75\,\mu\mathrm{K}$ and $\hbar\omega_z \simeq k_\mathrm{B} \times 0.3\,\mu\mathrm{K}$. The classical treatment of the atomic motion is therefore justified in the 10 µK-range of temperatures considered here.

We show in figure D.10 five trajectories of atoms in the circular state 52C computed for a duration of 200 µs. To obtain these, the atoms are initially sampled in the gaussian beam potential with the parameters of eq. (D.15) and left to evolve in the 52C BoB potential. These trajectories exhibit some differences with respect to those in the gaussian traps (compare with figure D.4).

The radial extension of the trajectory is much larger in BoB traps, getting close to the boundary in some cases. This is can be understood by considering the respective trap frequencies of the gaussian beam and BoB potentials. In our conditions, the gaussian beam has a radial frequency $\omega_{r,\,\mathrm{gauss}} \simeq 80\,\mathrm{kHz}$, hence a ratio

$$\frac{\langle r\rangle_\mathrm{BoB}}{\langle r\rangle_\mathrm{gauss}} \approx \frac{\omega_{r,\,\mathrm{gauss}}}{\omega_{r,\,\mathrm{BoB}}} = 5. \tag{D.28}$$

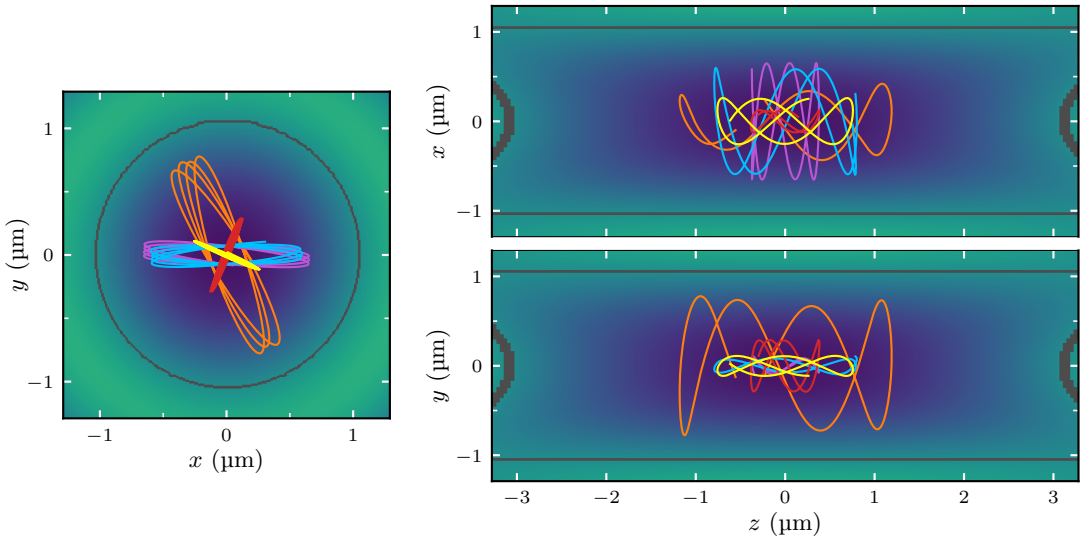

Figure D.10: Simulated trajectories for 52C atoms in a BoB trap with 20 mW total power. The trapping potential is represented in the background, along with its boundary (gray line). The initial position and velocities correspond to the thermal equilibrium in gaussian traps with the parameters of eq. (D.15), and the atoms were left to evolve for a duration of 200 µs.

As for the axial motion, from eq. 3.14 and table 5.2 we have

$$\omega_{z,\,\mathrm{gauss}} \simeq 2\pi \times 12.4\,\mathrm{kHz}, \quad \omega_{z,\,\mathrm{BoB}} \simeq 2\pi \times 6.3\,\mathrm{kHz}. \tag{D.29}$$

This leads to an axial extension $\langle z \rangle$ in the BoB traps only about 2 times larger than in the gaussian traps.

The fact that the atoms are "dropped" in BoB traps with their position and velocity inherited from the tighter gaussian trap causes the initial atomic positions to be distributed closer to the center of the BoB trap than the corresponding thermal distribution. This is illustrated in the xy components of the trajectories (left panel of figure D.10) which always get close to the center of the trap. As a consequence, the initial atomic velocities look almost radial, and in contrast with what was seen for gaussian traps, the xy motion is almost linear, without elliptical trajectories (compare with the left panel of figure D.4)).

Transferring atoms from gaussian to BoB traps amounts to replace the potential energy in the gaussian trap by that of the BoB trap. The latter being shallower than the former, the initial potential energy is significantly reduced. As a consequence, the atoms are not anymore in thermal equilibrium, and the evolution in BoB traps will cause a periodic (and partial) redistribution of energies. From 200 000 trajectories we obtain, for the time-averaged kinetic and potential energies along the trajectory,

$$\langle \bar{E}_c \rangle = h \times 235\,\mathrm{kHz}, \quad \langle \bar{E}_p \rangle = h \times 238\,\mathrm{kHz}. \tag{D.30}$$

These values are in good agreement with the rough estimate $\frac{3}{4} k_\mathrm{B} T = h \times 220\,\mathrm{kHz}$ obtained by assuming that the transfer to the BoB traps amounts to suppress the potential energy term. The only contribution is thus the kinetic energy $\langle E_c \rangle = \frac{3}{2} k_\mathrm{B} T$ that redistributes equally between the kinetic and potential terms when averaging over the trajectory.

Let us finally make clear that this reduction of the mechanical energy is not equivalent to a decrease of temperature. The distribution of atomic positions and velocities in the BoB trap does not correspond to that of the thermal equilibrium at any time.

Atomic losses in the trap

The BoB traps being shallower than their gaussian counterpart, a fraction of the trapped atoms may actually have enough energy to escape the BoB traps after switching the traps.

The remarks of the previous section allow us to get some quantitative insight on the efficiency of this transfer process. Indeed, we noted that the transfer from gaussian to BoB traps is well approximated by the suppression of the potential energy of the atoms. With this approximation, the initial energy distribution of the atoms is that of an ideal gas. The dispersion relation is

$$E(\mathbf{k}) = \frac{\hbar^2 \|\mathbf{k}\|^2}{2m}, \tag{D.31}$$

with $\hbar\mathbf{k} = \mathbf{p}$ the atomic momentum and m the atomic mass. The energy is solely a function of $k = \|\mathbf{k}\|^2$, and the equilibrium probability distribution of the latter is

$$p(k) = \sqrt{\frac{2}{\pi}} \lambda_T^3 k^2 e^{-\frac{\lambda_T^2 k^2}{2}}, \quad \lambda_T = \sqrt{\frac{\hbar^2}{m k_\mathrm{B} T}}. \tag{D.32}$$

The transfer efficiency p_capture corresponds to those atoms whose energy is lower than the trap depth, that is $\frac{\hbar^2 k^2}{2m} < k_\mathrm{B} T_\mathrm{thr}$. We therefore have

$$p_\mathrm{capture} = \int_0^{k_\mathrm{thr}} p(k)\mathrm{d}k, \quad k_\mathrm{thr} = \sqrt{\frac{2 m k_\mathrm{B} T_\mathrm{thr}}{\hbar^2}} = \sqrt{2}/\lambda_{T_\mathrm{thr}}. \tag{D.33}$$

After integration of the above expression, we finally obtain

$$p_\mathrm{capture}(T) = \mathrm{erf}\left(\sqrt{\frac{T_\mathrm{thr}}{T}}\right) - \frac{2}{\sqrt{\pi}} \sqrt{\frac{T_\mathrm{thr}}{T}} e^{-\frac{T_\mathrm{thr}}{T}}. \tag{D.34}$$

We present in figure D.11 (a) the efficiency of the transfer process from gaussian to BoB traps as a function of the temperature of atoms initially in gaussian traps. The BoB trap depth is $k_\mathrm{B} T_\mathrm{thr} = k_\mathrm{B} \times 71\,\mu\mathrm{K}$, and is indicated by a dashed vertical line. The simple analytical model of eq. D.34 is plotted as a red line. The agreement with the simulation is very good, and its departure at high temperatures is interpreted as a contribution of the initial potential energy, which becomes non-negligible and causes more atomic losses.

In order to avoid some problematic side effects, the characterization of an atomic loss must be conservative. It is therefore different from determining whether the atom is located inside or outside the trapping region introduced in the previous section. The retained loss condition is thus

$$r > 1.4\,\mu\mathrm{m} \text{ or } |z| > 4\,\mu\mathrm{m}. \tag{D.35}$$

The radius of 1.4 µm defines the annulus where the BoB potential is maximal: atoms farther than 1.4 µm from the trap axis are expelled (see figure D.8). The axial distance of 4 µm corresponds approximately to the axial position of the saddle region of the trap (that can be visualized on the right panels of figure D.9).

The two characterizations of atomic losses given above did not yield significantly different gaussian-to-BoB transfer efficiencies. However, the choice of an appropriate atomic loss condition is important when computing the escape time of atoms from the traps, which is presented in figure D.11 (b). The escape time is defined as the lowest time of the trajectory for which the loss condition (D.35) is satisfied. When running simulations, cases occur in which an atom has a enough initial radial velocity to go outside the trapping region yet not

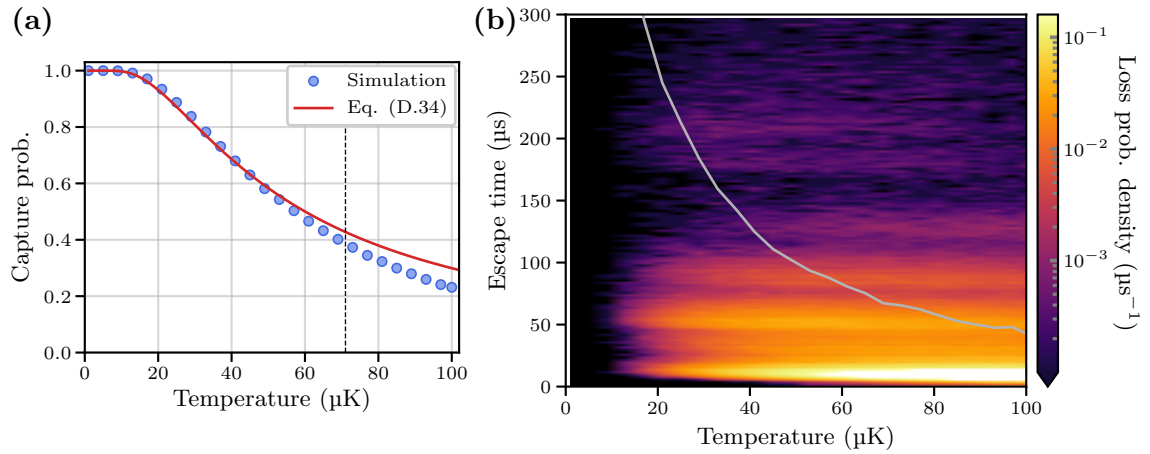

Figure D.11: Transfer efficiency from gaussian to BoB traps. (a) Transfer efficiency as a function of the initial temperature of the atoms. (b) Distribution of the escape times of atoms; the gray line represents the mean.

enough to go through the maximum of potential and escape immediately. The atom has the possibility to escape the trap but will only do so when reaching the saddle region of the trap, which might take a significant amount of time. This is the reason why the conservative loss condition of eq. (D.35) is preferred over the lenient condition based on the trapping region, that would lead to an underestimation of the escape times.

The color map presents the probability density of an atom escaping at a given time as a function of the temperature. The gray line represents the mean of this distribution, conditioned to the fact that atoms are lost at the end of the 6 ms simulation time. We see that the probability density is skewed towards large escape times, with the mean located well above the mass of the distribution. This reflects the fact that although most losses occur rather quickly, in the first 100 μs of the trajectory, there are also outliers that escape the trap after several ms.

Thermal energy shift and coherence loss

Apart from the atomic losses potentially occurring due to a lower trap depth, the BoB traps also affect the coherence of a superposition of (circular Rydberg) states. This is due to the small state dependence of the trapping potential discussed in section D.2.2. This causes a spatially variable light-shift of the transition frequency, which in turn leads to decoherence when averaging over possible trajectories.

To characterize and quantify this effect further, we simulated sets of 50 000 trajectories at various initial atomic temperatures in the gaussian trap for a total duration of 6 ms (with a time step of 200 ns). The atoms evolve in the potential U_{52} of the state 52C, and we record the light-shift on the transition by computing the potential energy difference $U_{52} - U_{50}$ at each time step. We thus obtain the light-shift frequencies $\delta f_i(t_j)$ for each trajectory i and time step t_j.

We report in figure D.12 the distribution of these frequencies δf as a function of the temperature. More precisely, the color map represents the fraction of the time spent with a given light-shift along a trajectory, and averaged over the trajectories for which atoms are still trapped at the last time step. The solid white line corresponds to the mean of this distribution, and the dashed black line is the trap center light-shift, $\delta f = 1.89$ kHz (for a trap

power $P_0 = 20\,\mathrm{mW}$, see figure D.9).

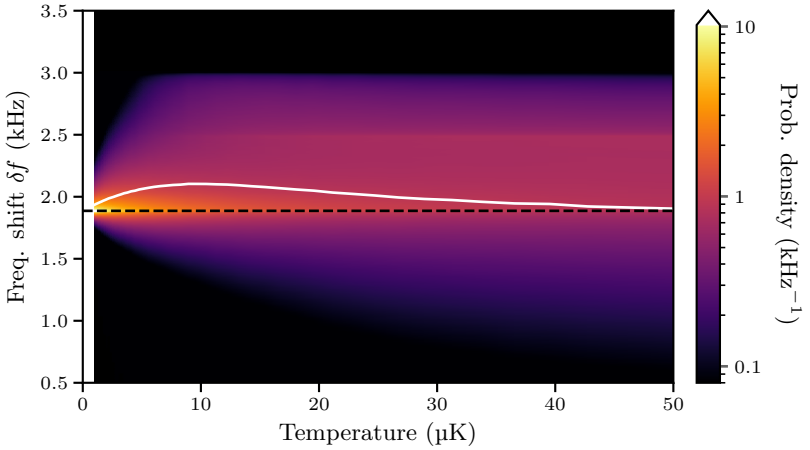

Figure D.12: Probability distribution of the light shift of the 50C $\rightarrow$ 52C transition as a function of the initial atomic temperature in gaussian traps. The dashed black line represents the light shift at the center of the trap; the solid white line corresponds to the mean light-shift.

The atoms are located in the center of the trap in the limit of zero temperature, and the light-shift distribution (thus also the mean) concentrates around the corresponding light-shift. The distribution quickly expands as the temperature increases, and the maximum light-shift of about 3 kHz (see figure D.9) is reached at moderates temperatures of approximately 10 µK. This is associated to an increase of the mean light-shift (of 10%).

A further increase of the temperature causes the distribution to expand towards lower light-shifts as the axial extension of the trajectories increase, with the mean correspondingly decreasing, and a slower evolution above 10 µK. To interpret that, it is important to remember that the data presented here is conditioned to the fact that atoms are kept trapped in the BoBs. Such post-selection effectively imposes a cutoff on the mechanical energy of the trajectories that are involved in the computation of the light-shift distribution. In other words, only the trajectories with an energy inferior to the trap depth are used to compute the light-shift distribution. This is the cause of its slow evolution above 10 µK, the temperature at which some atoms begin to be lost from the BoB traps (see figure D.11 (a)).

We now consider the effect of such a variation of the light-shift along a given trajectory on the single-atom coherence. The atom is initialized in a superposition $|\psi_0\rangle = (|50\mathrm{C}\rangle + |52\mathrm{C}\rangle)/\sqrt{2}$, with corresponding density matrix

$$\rho(0) = \frac{1}{2}\begin{pmatrix} 1 & 1 \\ 1 & 1 \end{pmatrix}. \tag{D.36}$$

The evolution of such state corresponds to the accumulation of a phase associated to the frequency shift between the two atomic levels of the superposition, and we have, after a given delay t:

$$\rho(t) = \frac{1}{2}\begin{pmatrix} 1 & \exp\left(-i\omega_0 t - i\int_0^t \delta\omega(t')\mathrm{d}t'\right) \\ \exp\left(i\omega_0 t + i\int_0^t \delta\omega(t')\mathrm{d}t'\right) & 1 \end{pmatrix}, \tag{D.37}$$

where $\hbar\omega_0$ is the bare energy difference between 50C and 52C, and $\hbar\delta\omega(t')$ is the light-shift induced by the trap on the transition. We define the coherence $\gamma(t)$ as the norm of the

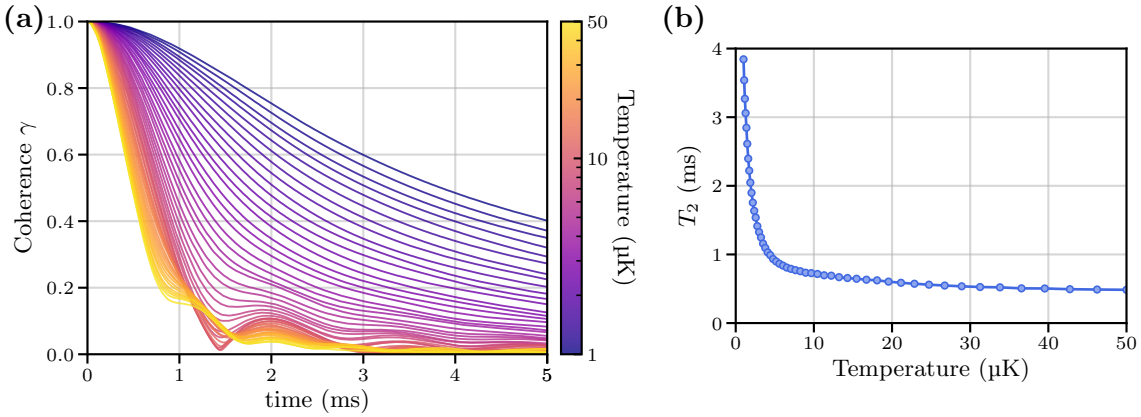

Figure D.13: Decoherence of the $(|50\mathrm{C}\rangle + |52\mathrm{C}\rangle)/\sqrt{2}$ superposition in the BoB traps. (a) Coherence plots (eq. D.38) for various initial temperatures in the gaussian trap. (b) Corresponding coherence time T_2 (defined in eq. D.39) as a function of the temperature.

off-diagonal terms of the density matrix, averaged over all possible atomic trajectories:

$$\gamma(t) = \left| \left\langle \exp\left(i \int_0^t \delta\omega(t')\mathrm{d}t' \right) \right\rangle_{\delta\omega} \right|. \tag{D.38}$$

We report in figure D.13 (a) the coherence $\gamma(t)$ of eq. (D.38) computed from the sets of trajectories described above. Again, only those trajectories corresponding to trapped atoms are used for the computation. We define the coherence time T_2 such that

$$\gamma(T_2) = \frac{1}{2}. \tag{D.39}$$

The latter is plotted as a function of the atomic temperature in figure D.13 (b).

Decoherence occurs rather quickly in the BoB traps, even at very low temperatures (we have $T_2 \simeq 4\,\mathrm{ms}$ at $T = 0.1\,\mu\mathrm{K}$). Moreover, the coherence time drops to about 1 ms as the temperature increases to 5 µK, with further yet slower decrease at higher temperatures. At large temperatures, a plateau at about 0.5 ms is reached. This stabilization at high temperatures is due to the energy cutoff imposed by the post-selection of trajectories corresponding to trapped atoms. However, the situation is not as bad as it may seems for temperatures $T \gtrsim 5\,\mu\mathrm{K}$. Indeed, we observe rebounds of the coherence for such values (see figure D.13 (a)), echoing to the periodicity of atomic trajectories. This hints at the possibility to improve coherence by methods such as dynamical decoupling [149, 150].

In the 5 – 20 µK atomic temperature range involved in our experiments, we expect a BoB-limited coherence time of about 500 – 1000 µs. This value is much larger than our measurement of $\sim 60\,\mu\mathrm{s}$ (see section 5.3.3), and indicates that we are not sensitive to the trap-induced decoherence at the probed timescales. This might however become a serious limitation to the realization of quantum simulation in a context in which the lifetime of circular Rydberg atoms is extended (such as a cryogenic environment).

We conclude this section with final cautionary notes on the validity of these simulations.

- The simulated trajectories are classical, therefore effects of quantum nature such as spin-motion entanglement are completely overlooked.
- Rydberg interactions are not taken into account, and their effect on the motion and decoherence of an atomic ensemble as a whole is also neglected.

Appendix E

Supplementary material to chapter 5

This appendix constitutes supplementary data to the chapter 5.

In the first part, we provide additional data pertaining to the trapping of circular states and trap frequency measurement. The signal was recorded a few days before the failure of our titanium-sapphire laser emitting at 1015 nm. As such, it is only partial: the trapping is only probed for a duration of 1 ms and the oscillation signal is only visible on the averaged data.

In the second part, we present Ramsey fringes that were obtained without triggering the sequence of the power line. We found out that the signal was deformed due to the magnetic field fluctuations oscillating at the power line frequency, 50 Hz. We present a quantitative evaluation of this "noise" from the data.

E.1 Trapping of circular states: early demonstration

E.1.1 Trapping signal

Analogously to section 5.1.2, we present in figure E.1 the recapture signal both with and without the BoB traps. The sequence, depicted in figure E.1 (a), differs from that shown in figure 5.4 (a): there was no adiabatic cooling after the optical pumping and prior to the trapping. The average recapture probability, both with and without trapping, is reported in figure E.1 (b). We also show the theoretical thermal population decay ρ_{52C} scaled to the data (solid black line). The decay in the presence of the traps agrees very well to the theory. This translates into an almost flat signal when normalized to the thermal population decay, as shown on the right panel of figure E.1 (b).

Because of the absence of adiabatic cooling, the initial atomic temperature $T_0 = 25\,\mu\text{K}$ is significantly higher than the $4\,\mu\text{K}$ obtained after the adiabatic cooling. We fit the recapture probability without trapping according to eq. (5.6) to recover the temperature. The best fit, shown as a solid blue line on figure E.1 (b), corresponds to a temperature $T = 25 \pm 7\,\mu\text{K}$ and is in good agreement with T_0. However, the significant uncertainty in the fitted value does not rule out the possibility of interaction-mediated mechanical effects such as those described at the end of section 5.1.2.

Such a flat (normalized to the thermal decay) recapture probability is observed at each individual trapping site, as shown in figure E.1 (c). This demonstrated our ability to generate BoB traps over a range of $75 \times 30\mu\text{m}$, with sufficient quality to retain atoms for 1 µs.

It is interesting to note that this signal differs qualitatively from the data presented in the main text. Indeed, in the latter, we observe an excess loss of population starting at

approximately 500 µs, which does not appear in the data that we presently discuss. We can think of two possible reasons to explain such a difference.

- A higher total laser power available to the BoB traps in the early data. The direct consequence would be an increased trap depth and therefore less losses.
- A drift in the aberrations introduced along the optical path. This could be caused by the slow deposit of dust on the optics. It would result in deformed and therefore less efficient BoB traps.

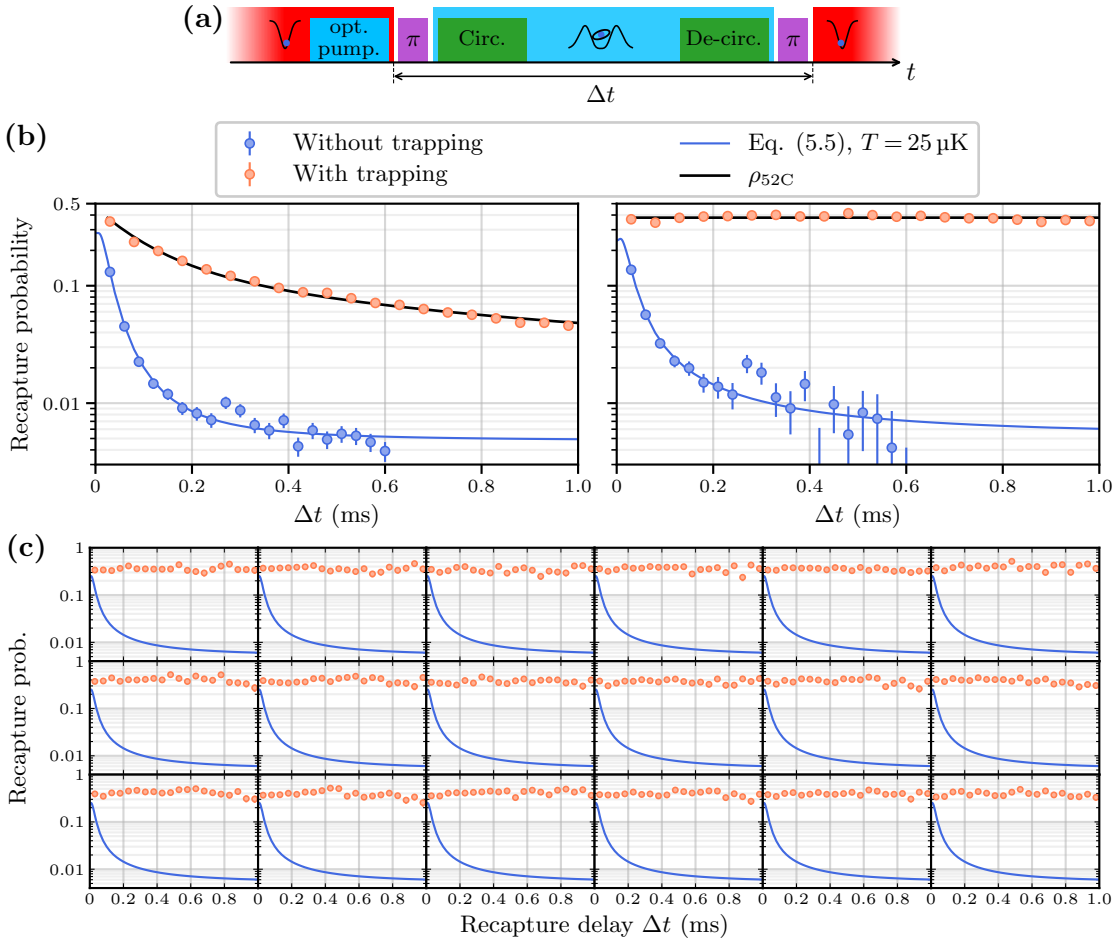

Figure E.1: Early signature of the ponderomotive trapping of 52C. (a) Scheme of the sequence. There is no adiabatic cooling prior to trapping (compare with figure 5.4 (a)). (b) Average recapture probability obtained without (blue discs) and with (orange discs) trapping. Left: raw data. The black solid line corresponds to the theoretical population decay ρ_{52C} properly scaled to the data. Right: data corrected by ρ_{52C} (now appearing as a straight line). The two panels also show (blue line) a simulation of the recapture probability in the case of free atoms according to eq. (5.6). (c) Recapture probability for individual trapping sites. The data in the absence of trapping is noisy and thus replaced by the simulation carried on the average data (blue line) for a better visualization and comparison.

E.1.2 Trap frequency

We schematize in figure E.2 (a) the sequence that was used to record the oscillation signal reported in figure E.2 (b). Its only difference with the one discussed in the main text is a slightly longer total duration (230 µs as compared to 210 µs in chapter 5). The use the same offset between the gaussian tweezers and the BoB traps to induce oscillations: 300 nm along the x-direction.

As mentioned earlier, this sequence was not recorded with enough repetitions to obtain individual site resolution. The oscillations are nevertheless clearly visible on the averaged signal. We can carry the same analyses as in section 5.2.2 to estimate the power per trap. Assuming harmonic motion with the frequency obtained from table 5.2, we get a power $P_0 = 23.1 \pm 0.5\,\mathrm{mW}$. Using the Monte-Carlo fitting procedure (see appendix D), we obtain $P_0 = 17.5 \pm 0.2\,\mathrm{mW}$. As expected, the two values disagree similarly to what we observed in section 5.2.2.

We nevertheless note that the estimated power per trap in our early measurement was about 15% higher than that pertaining to the data presented in chapter 5. This can explain in part the better trapping signal presented in the previous section.

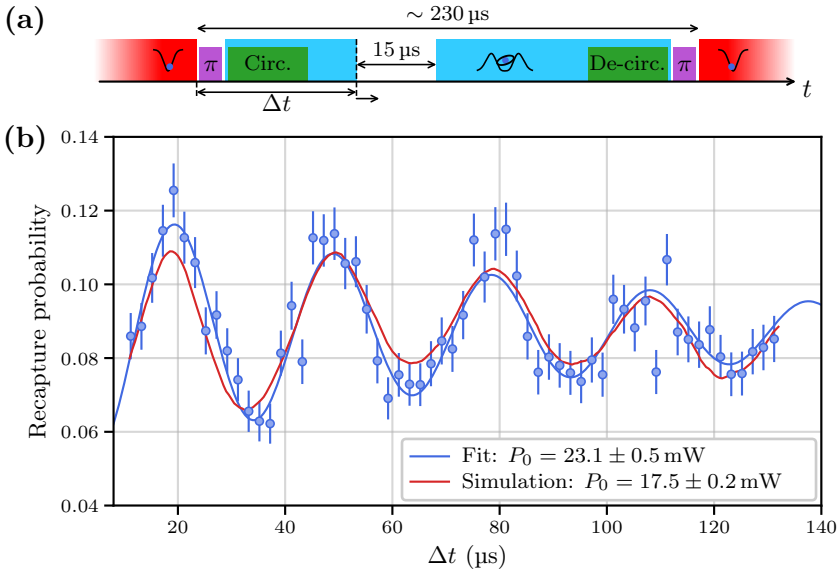

Figure E.2: Early measurement of the transverse trap frequency. (a) Scheme of the experimental sequence. (b) Oscillation signal from the averaged recapture probability, with corresponding damped-sinus fit (blue line) and Monte-Carlo simulation (red line).

E.2 Power-line-induced magnetic field noise measurement

We present in figure E.3 (a) the Ramsey fringes obtained from a single-atom measurement, with and without trapping. The right panels of this figure correspond to the data discussed in section 5.3.3 (see figure 5.12), recorded by triggering the sequence on the power line. The Left panels correspond to the same experiment, without synchronizing the sequence triggering and the power line. A clear beating appears, which is highlighted in the Fourier power spectra of figure E.3 (b). The single peak in the trigger-on-line condition gets split in two peaks, with a spacing of about 20 kHz.

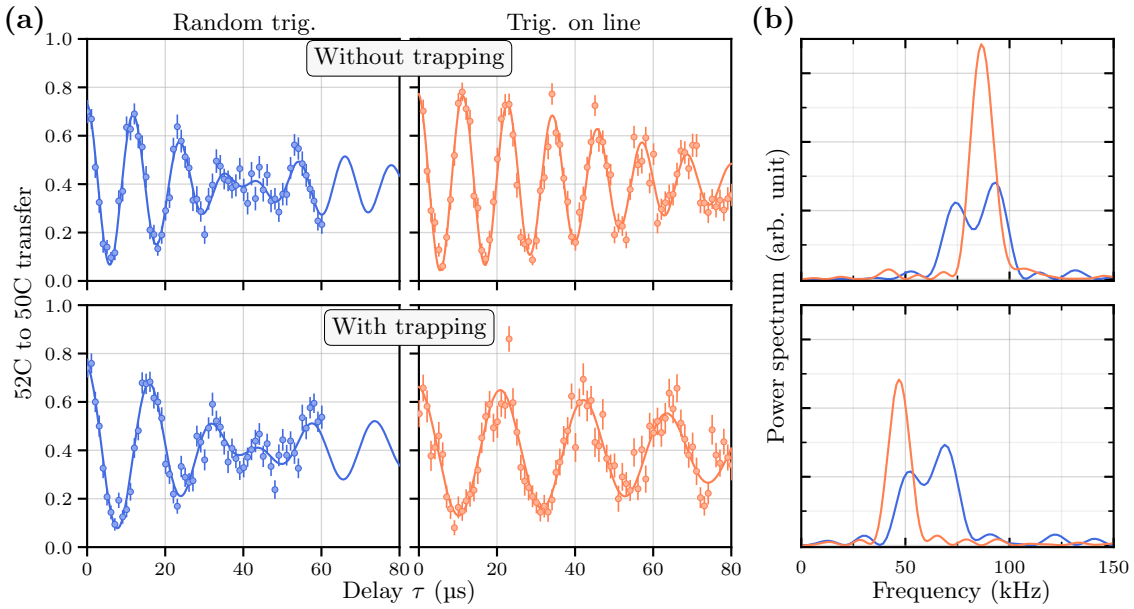

Figure E.3: Single-atom Ramsey oscillations. (a) Measurement in four different conditions: without (top) and with (bottom) BoB trapping; sequence triggered at random (left) or on the power line (right). (b) Corresponding Fourier power spectra.

This splitting thus originates from 50 Hz power line noise pick-up by the experiment. The scheme of figure E.4 describes the effect observed. When triggered randomly, the Rydberg experiment begins at a random point φ of the 50 Hz cycle, which causes the 52C to 50C transition to be shifted by $\delta\nu = \delta\nu_0 \sin(\varphi)$. The probability distribution of $\sin(\varphi)$ for φ uniformly distributed among $[0, 2\pi]$ is known as an arcsine distribution:

$$\rho(u) = \frac{1}{\pi\sqrt{1-u^2}}. \tag{E.1}$$

The observed signal can therefore be described as the raw signal of eq. 5.17 with the oscillation frequency Δ_0 convolved with an arcsine distribution:

$$p(\tau) = y_0 + Ae^{-\frac{\tau^2}{2T_2}} \int_{-1}^{1} \frac{\sin(2\pi(\Delta_0 + u\,\delta\nu_0)\tau + \phi_0)}{\pi\sqrt{1-u^2}} \mathrm{d}u. \tag{E.2}$$

The corresponding fits, shown as solid lines, give almost equal frequency shifts, with $\delta\nu_0 = 9.45 \pm 0.31$ kHz in the absence of trapping and 9.06 ± 0.36 kHz with BoB trapping. This is compatible with the splitting (twice this value) observed on the Fourier spectra. We also expect that triggering the sequence on line locks the Ramsey frequency in the range delimited by the two peaks of the random triggering case. This is indeed what we observe on the signals recorded without trapping, but not in the presence of the traps. The reason is that the trap power was uncontrolled when we ran the sequence with random triggering. The frequency difference in this case corresponds to a trap power of 250 mW.

We can use the above results to get some insight on the 50 Hz power line noise to which the experiment is subject. We saw that power line pick-up corresponds to approximately 20 kHz peak-to-peak frequency shift. At a field $F_0 \sim 2\,\mathrm{V\,cm^{-1}}$, recalling a transition subject to a differential quadratic Stark shift of $540\,\mathrm{kHz\,V^{-2}\,cm^2}$ we deduce peak-to-peak electric field fluctuations $\delta F_{\mathrm{pp}} \sim \frac{20}{540\times 2F_0} \approx 10\,\mathrm{mV\,cm^{-1}}$. This would result in a broadening of 1 MHz for the $|52\mathrm{C}\rangle \longrightarrow |53\mathrm{E}^+\rangle$ transition described in 4.3.1, which we did not observe (see figure 4.15).

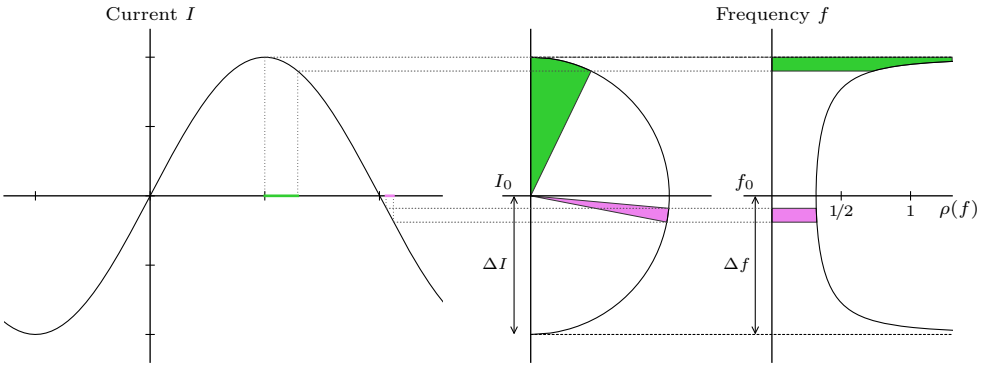

Figure E.4: Illustration of the uniform sampling of a sinus, giving rise to arcsine-distributed frequencies.

The other candidate to the broadening is the magnetic field, with power line noise getting in the coils producing the directing magnetic field. For a $\Delta m = 2$ transition, the 20 kHz shift corresponds to magnetic field fluctuations $\delta B_{\mathrm{pp}} \sim \frac{20}{2\mu_{\mathrm{B}}} \approx 7\,\mathrm{mG_{pp}}$. The response of our pair of coils being approximately $2\,\mathrm{G\,A^{-1}}$, this amounts to a peak to peak noise current of $\sim 3.5\,\mathrm{mA_{pp}}$, or relative fluctuations of about 0.1%. This situation is quite likely, with the noise coming either from the current source itself or the voltage noise from the controlling DACs converted to current.

Let us finally mention that, in order to assess a possible effect of the power-line pick-up by the electric field control circuitry, we recorded the circular to elliptical spectrum (see figure 4.15) both with and without triggering on-line. The peak had the same shape in both conditions. We therefore conclude that the electric field is, at our level of precision, not subject to power-line noise.

Résumé en français

Chapitre 1

Ce chapitre introduit les concepts théoriques sous-jacents aux résultats présentés dans ce manuscrit. Nous y introduisons ainsi les bases d'atomistique par la description de l'atome d'hydrogène : fonctions d'onde et énergies propres associées à l'équation de Schrödinger qui décrit la dynamique d'un électron dans un potentiel coulombien. Sont aussi introduites diverses corrections à l'énergie d'origine relativiste ou associées à la structure du noyau (masse finie, moment magnétique, ...). Ceci permet d'aborder le cas des atomes de Rydberg alcalins, notamment le rubidium que nous utilisons, qui ont en commun avec l'hydrogène de n'avoir qu'un seul électron de valence, qui occupe un état de nombre quantique principal élevé.

Dans le cadre de la théorie du défaut quantique, l'interaction de cet électron avec le cœur ionique est caractérisée par un paramètre unique, le défaut quantique, qui dépend toutefois de l'état atomique. Parmi les niveaux de Rydberg, nous nous intéressons en particulier aux états circulaires, qui possèdent un moment angulaire maximal. L'orbite électronique se rapproche de la limite classique d'une orbite circulaire très éloignée du cœur ionique. Dans ce contexte, le défaut quantique ainsi que les corrections au modèle de Schrödinger sont négligeables.

Nous décrivons ensuite la réponse de ces états à différents champs extérieurs : champ magnétique et électrique statiques. Dans le cas d'un champ magnétique, on distingue deux régimes : Zeeman (champ magnétique faible) et Paschen-Bach (champ fort). Le champ magnétique ne se couplant qu'au mouvement angulaire de l'électron (ainsi qu'à son spin), le traitement s'applique sans grand changement à la fois aux états de Rydberg et aux états faiblement excités, et les déplacements d'énergie sont similaires pour les deux. Le cas d'un champ électrique est différent, les états de Rydberg s'y trouvent être très sensibles, ce dont nous tirons profit dans nos expériences. Un cas particulier intéressant est celui où le champ électrique est produit par un atome de Rydberg. On observe alors, selon la paire d'états considérée, une interaction dipolaire évoluant en $1/R^3$ pour une distance interatomique R ou une interaction de type van der Waals en $1/R^6$.

La manipulation de ces états atomiques se fait en général par des transitions radiatives. Nous introduisons ainsi le couplage au champ életromagnétique ainsi que le hamiltonien d'interaction H_I associé. Celui-ci peut s'exprimer sous deux formes. En général il s'écrit $H_I = \frac{e}{m_e}\mathbf{A}(\mathbf{r},t)\cdot\mathbf{p} + \frac{e^2}{2m_e}\mathbf{A}^2(\mathbf{r},t)$, où e est la charge élémentaire, m_e la masse de l'électron et $\mathbf{A}$ représente le potentiel vecteur du champ. Cette expression peut être simplifiée à l'approximation dipolaire, et s'écrire sous la forme plus familière $H_I = -\mathbf{d}\cdot\mathbf{F}$ faisant apparaitre le champ électrique $\mathbf{F}$ et le moment dipolaire $\mathbf{d} = -e\mathbf{r}$.

Cette seconde forme est le point de départ pour les calculs se rapportant à la méthode que nous utilisons pour préparer des états circulaires : le passage adiabatique. Le principe consiste à coupler de proche en proche une série de niveaux menant à l'état circulaire par un champ radiofréquence proche de résonance. On réalise ensuite le passage adiabatique en traversant la

résonance par un balayage de l'écart d'énergie entre les niveaux non couplés. Nous calculons aussi le déplacement des niveaux d'énergie par un champ fortement hors résonance, qui est un effet perturbatif du second ordre. L'une des applications directes est le piégeage dipolaire d'atomes dans des potentiels lumineux tels que les pinces optiques. Les états de Rydbergs réagissent différemment aux champs lumineux : l'interaction est toujours répulsive et donne lieu à l'effet pondéromoteur. Celui-ci provient tout simplement du terme $\frac{e^2}{2m_e}\mathbf{A}^2(\mathbf{r},t)$ issu de la première formulation du couplage H_I au rayonnement.

Chapitre 2

Nos résultats de piégeage d'états circulaires ont été obtenus à l'aide d'un nouveau dispositif expérimental. Celui-ci constitue une étape intermédiaire avant la mise en place de la plateforme de simulation définitive, opérant en environnement cryogénique. À cette fin, il est assemblé sur une table optique réalisée sur mesure pour permettre le transfert d'une partie de l'assemblage vers notre cryostat.

Le dispositif s'articule autour d'une pièce de saphir située au centre d'une enceinte à vide. Celle-ci dispose de 8 accès optiques, et est reliée à quatre sous-assemblages remplissant chacun une fonction : un système de pompe ionique, un raccord équipé de traversées de connecteurs électriques, un dispositif de détection d'ions ainsi qu'un piège magnéto-optique bi-dimensionnel (2D-MOT) situé en dessous, qui constitue notre source d'atomes. Le champ magnétique est contrôlé par trois paires de bobines orthogonales. La pièce de saphir est creuse le long de l'axe vertical et percée de quatre trous la traversant entièrement. Ceux-ci sont alignés avec les accès optiques de l'enceinte à vide et permettent aux différents faisceaux lasers utilisés de se croiser en son centre, où sont situés les atomes. En outre, la pièce de saphir supporte diverses électrodes permettant le contrôle du champ électrique ainsi que la préparation d'états circulaires par l'émission d'un champ radiofréquence. Deux lentilles asphériques placées dans leur monture viennent aussi s'insérer dans le cube. Elles sont destinées à la préparation de pinces optiques afin de piéger les atomes dans l'état fondamental d'une part et dans l'état circulaire d'autre part.

La préparation de pinces optiques présente une certaine complexité ainsi que certaines contraintes. La méthode retenue consiste en l'utilisation d'un modulateur spatial de lumière appliquant un masque de phase adéquat au faisceau incident. Celui-ci est alors converti en une distribution d'intensité donnée au plan focal de nos lentilles. Avant de préparer le masque pour les pinces optiques, il nous faut corriger les aberrations introduites par les optiques le long du chemin du faisceau. Nous utilisons pour cela une version modifiée de l'algorithme de Gerchberg-Saxton, qui tient compte de l'information contenue hors du plan focal. Pour la détermination du masque de phase générant le pince optiques, toute la difficulté se trouve dans la recherche de ce masque de phase, et l'algorithme utilisé n'est pas détaillé ici.

Toutes nos séquences expérimentales partent d'une vapeur de ^{87}Rb refroidie transversalement par le 2D-MOT. Cette vapeur s'élève jusqu'au centre de la pièce de saphir, et sont ensuite capturés dans un MOT tri-dimensionnel en présence des pinces optiques. Les atomes qui se sont retrouvés capturés dans ces dernières sont ensuite refroidis par une mélasse optique. Une image en fluorescence est ensuite prise par une caméra EMCCD très sensible avant une seconde étape de mélasse et le démarrage de la séquence expérimentale à proprement parler.

Chapitre 3

La préparation de pinces optiques étant nouvelle pour notre équipe, nous décrivons ici de façon assez détaillée les caractérisations que nous avons effectuées sur les pièges gaussiens destinés aux atomes dans l'état fondamental. Nous travaillons pour cela avec un tableau de 9×9 pièges espacés de 10 µm.

Nous décrivons le signal de fluorescence qui, dans nos conditions expérimentales, nous permet de discriminer la présence d'atomes dans les pièges par la détection d'environ 300 photons de fluorescence et d'établir des seuils de détections à partir desquels nous obtenons une probabilité de chargement moyenne de 60%. L'enregistrement d'une image avant et après la séquence expérimentale nous permet de déterminer pour chaque site la probabilité de recapture ou de perte d'un atome, qui constitue la base de toutes nos analyses.

Nos pièges gaussiens sont caractérisés en mesurant d'une part le déplacement lumineux induit sur la transition $\left|5\mathrm{S}_{1/2}, F = 1\right\rangle \longrightarrow \left|5\mathrm{P}_{3/2}, F' = 2\right\rangle$ et d'autre part la fréquence du piège en y faisant osciller mécaniquement les atomes. De la première mesure nous déduisons une profondeur de $990 \pm 42\,\mu\mathrm{K}$, de la seconde une fréquence de $80.9 \pm 2.0\,\mathrm{kHz}$. Dans toutes ces mesures, les variations mentionnées (après le symbole "$\pm$") correspondent à l'écart type calculé à partir des valeurs obtenues pour chaque site. Ces valeurs permettent de remonter au rayon de gorge w_0 ainsi qu'à la puissance P_0 des pièges :

$$\langle w_0 \rangle = 1.21 \pm 0.01\,\mu\mathrm{m}, \quad \langle P_0 \rangle = 2.62 \pm 0.12\,\mathrm{mW}.$$

La dispersion est de l'ordre de 1% pour le rayon de gorge (qui est proche de la limite de diffraction de 1.14 µm pour notre dispositif) et de 5% pour la puissance.

Par ailleurs, nous obtenons un temps de maintien moyen dans les pinces optiques de $12.6 \pm 0.2\,\mathrm{s}$, les données mettant en évidence la possibilité d'un chargement des pièges inoccupés par les atomes environnants. Enfin, la température est déterminée par une séquence de "release-recapture" consistant à mesurer la probabilité de recapture après libération des atomes pendant un temps donné. Les données sont ajustées en simulant une courbe théorique pour une série de valeurs de température et en retenant celle qui minimise l'écart quadratique. Nous obtenons de cette façon une température moyenne $\langle T \rangle = 14.4 \pm 1.4\,\mu\mathrm{K}$. La carte des températures pour les sites individuels révèle une forte inhomogénéité, les atomes étant plus froids le long d'une bande verticale située au centre.

Chapitre 4

Le transfert dans l'état circulaire à partir des atomes piégés s'effectue en quatre étapes :

(1) l'état initial est pompé optiquement vers $\left|5\mathrm{S}_{1/2}, F = 2, m_F = 2\right\rangle$. Nous utilisons pour cela laser de polarisation σ^+ accordé sur la transition $\left|5\mathrm{S}_{1/2}, F = 2\right\rangle \longrightarrow \left|5\mathrm{P}_{3/2}, F' = 3\right\rangle$, l'axe de quantification étant défini par le champ magnétique. La spectroscopie Raman sur les sous-niveaux hyperfins de l'état $\left|5\mathrm{S}_{1/2}\right\rangle$ nous permet d'une part d'évaluer le champ magnétique $B = 7.01 \pm 0.02\,\mathrm{G}$, d'autre part d'estimer l'efficacité du pompage optique. Nous obtenons ainsi, après optimisation, une pureté $\eta_{\mathrm{OP}} = 0.97 \pm 0.01$.

(2) L'étape suivante est l'excitation vers l'état de Rydberg $\left|52\mathrm{D}_{5/2}, m_j = +5/2\right\rangle$. Nous adressons une transition à deux photons avec l'état $\left|6\mathrm{P}_{3/2}\right\rangle$ comme état intermédiaire. L'analyse des spectres et des oscillations de Rabi réalisées avec détection optique nous conduit à une efficacité d'excitation $\eta_{52\mathrm{D}} = 0.89 \pm 0.01$ effectuée avec un fréquence de Rabi moyenne $\langle \Omega \rangle = 2\pi \times 660 \pm 50\,\mathrm{kHz}$. Nous sommes principalement limités par la puissance laser disponible.

(3) La troisième étape consiste en un transfert micro-onde vers l'état $|52\mathrm{F}, m_l = +2\rangle$. Une analyse similaire à celle réalisée pour l'excitation laser conduit à estimer l'efficacité du transfert $\langle \eta_{\mathrm{DF}} \rangle = 0.88 \pm 0.05$.

(4) L'état précédent se branche, lorsque l'on applique un champ électrique sur le niveau qui constitue notre point de départ pour le transfert adiabatique vers l'état circulaire 52C. Le transfert est réalisé en réduisant le champ électrique de $2.25\,\mathrm{V\,cm^{-1}}$ à $2.05\,\mathrm{V\,cm^{-1}}$ en présence de radiofréquence polarisée σ^+ à 225 MHz.

Une fois préparés nous réalisons des spectres micro-onde vers les niveaux environnants. La transition à deux photons $52\mathrm{C} \longrightarrow 50\mathrm{C}$ permet d'estimer la pureté de nos états circulaires : $\eta_{\mathrm{circ}} = 0.90 \pm 0.02$. Le champ électrique est estimé à partir de la transition $52\mathrm{C} \longrightarrow 53\mathrm{E}^+$, insensible au champ magnétique. La mesure donne ainsi un champ $F_0 = 2.0887 \pm 0.0001\,\mathrm{V\,cm^{-1}}$.

Enfin, la détection optique des états circulaires impose le retour à l'état fondamental, que nous décrivons brièvement et qui s'effectue moins efficacement que l'aller. En combinant les efficacités de chaque étape, nous arrivons à une valeur finale $\eta_{\mathrm{tot}} = 0.31 \pm 0.04$.

Chapitre 5

Ce chapitre final présente les principaux résultats obtenus au cours de ma thèse.

Afin de décrire de façon complète les résultats présentés ensuite, nous abordons dans un premier temps le piégeage des états de Rydberg. L'approche retenue est purement empirique et ne considère pas en détail la dynamique au sein des pièges. Nous décrivons dans un premier temps le piégeage des états 52D préparés par excitation laser, qui nous permet de nous affranchir des détails techniques inhérents aux états circulaires. Les données obtenues s'accordent assez bien à un déclin exponentiel dont le temps caractéristique mesuré, $66 \pm 1\,\mu\mathrm{s}$, est proche de la valeur théorique attendue, 74 µs.

L'analyse des données de piégeage se rapportant aux circulaires est plus délicate, d'une part à cause de l'efficacité limitée de la séquence aller-retour, et d'autre part par la dynamique complexe des états circulaires. Ceux-ci subissent des transferts thermiques successifs qui les font diffuser vers l'ensemble des niveaux environnants, l'évolution des populations est décrite par une équation pilote dont le détail n'est pas donné ici. En normalisant les données par la population théorique attendue pour l'état 52C à température ambiante, nous observons une diminution en excès de la population à partir de 500 µs. L'origine exacte des pertes en excès n'est pas élucidée clairement, mais nous conjecturons toutefois un effet des fortes interactions dipolaires qui apparaissent lorsque l'un des atomes est transféré thermiquement vers un état voisin. Le piégeage des atomes ainsi mis en évidence est à la base des expériences qui suivent.

Nous décrivons ensuite le piège de façon théorique : la préparation d'un faisceau en bouteille idéalisé et sa convolution avec la distribution de charge de différents états circulaires. Nous obtenons des valeurs théoriques pour le déplacement des niveaux au fond du piège (et notamment un différentiel entre les niveaux 50C et 52C), ainsi que ses fréquences. Ces valeurs nous permettent de confronter la théorie aux expériences qui suivent.

Cela s'illustre dans un premier temps par la mesure de la fréquence transverse des pièges. Nous obtenons une fréquence moyenne de 15.8 ± 0.1 kHz qui s'accorde, en supposant un mouvement harmonique, avec une puissance par piège de 20 mW en accord avec nos estimations. Cependant, une simulation de la dynamique dans les pièges conclut à une puissance sensiblement plus faible, de l'ordre de 15 mW. Une telle baisse obtenue par simulation est en accord au moins qualitatif avec le caractère anharmonique du piège.

Nous vérifions ensuite que la présence des pièges n'affecte pas l'évolution des états en détectant par ionisation les populations à différents délais. Les courbes obtenues sont sensiblement les mêmes et ne permettent pas de discerner un effet des pièges à ce niveau.

Les oscillations de Rabi bénéficient grandement de la détection optique résolue spatialement. En effet, celles-ci permettent d'interpréter un signal d'ionisation qui présente plusieurs nœds. L'ajustement de la fréquence de Rabi pour chaque piège (qui donne une valeur de l'ordre de 850 kHz) met en évidence un gradient d'amplitude micro-onde, qui est à l'origine des battements observés sur le signal d'ionisation.

Nous concluons avec une expérience d'interférométrie de Ramsey. La mesure effectuée sur le tableau de taille 6×3 met en évidence deux choses.

- D'une part les fréquences de Ramsey diffèrent d'environ 5 kHz selon que l'on est en présence ou en absence de piégeage. Ceci s'explique en partie par le différentiel de déplacement des niveaux prédit par l'analyse théorique mentionnée plus haut. On s'attend à une valeur de $92\,\mathrm{kHz\,W^{-1}}$ et ainsi la puissance attendue des pièges, 20 mW, rend compte d'environ la moitié de la différence mesurée. Le reste peut être causé par plusieurs facteurs, sans qu'aucun ne soit quantitatif. Mentionnons les interactions entre états circulaires. Une analyse détaillée sort toutefois du cadre du présent manuscrit.
- Le temps caractéristique du déclin se situe entre 15 et 20 µs. Cette valeur, qui semble assez faible, peut toutefois s'expliquer par les interactions. Le transfert thermique d'un atome vers un état voisin donne lieu à l'apparition de couplage dipolaire du premier ordre. Celui-ci est de l'ordre du MHz et est susceptible de déplacer hors résonance la transition Ramsey que nous adressons, et ce sur une large étendue spatiale. La seconde impulsion micro-onde est alors inefficace, ce qui se traduit par l'atténuation du signal.

Cette dernière hypothèse semble validée lorsque l'on réduit la mesure à un atome unique. Le temps de cohérence passe à 61 ± 8 µs en présence des pièges, et dépasse même les valeurs en l'absence de piégeage, 45 ± 3 µs. Toutefois, la précision des mesures ne nous permet pas de conclure sur l'origine de cette différence. Enfin, il est à noter que toute la puissance disponible a été utilisée pour préparer un piège unique. Nous observons alors un décalage conséquent de la transition, qui atteint 40 kHz. Ceci nous permet de remonter à une puissance totale de 440 mW pour le piège, en bon accord avec notre estimation pour la puissance. Dans ce cas les autres processus potentiellement responsables du décalage de la transition sont probablement éclipsés par l'effet dû à l'intensité du piège.

References

[1] Niels Henrik David Bohr. "The Structure of the Atom". In: 1922.

[2] Kent A. Peacock. *The Quantum Revolution: A Historical Perspective*. 1st edition. Westport, Conn: Greenwood, Dec. 30, 2007. 240 pp. ISBN: 978-0-313-33448-1.

[3] D. R. Yennie. "Precision tests of QED". In: *AIP Conference Proceedings* 123.1 (Nov. 15, 1984). Publisher: American Institute of Physics, pp. 468–476. ISSN: 0094-243X. DOI: 10.1063/1.34892.

[4] Mario Bertolotti. *Masers and Lasers: An Historical Approach*. 2nd edition. Boca Raton, Florida: CRC Press, Mar. 13, 2015. 502 pp. ISBN: 978-1-4822-1777-3.

[5] John Bardeen. "Semiconductor Research Leading to the Point Contact Transistor". In: *NobelPrize.org*. Nobel Lecture. 1956.

[6] Peter Szekeres. *A course in modern mathematical physics: groups, Hilbert space, and differential geometry*. Cambridge, UK ; New York: Cambridge University Press, 2004. 600 pp. ISBN: 978-0-521-82960-1.

[7] Philip Ball. "Where does quantum weirdness end?" In: *New Scientist* 251.3349 (Aug. 2021), pp. 38–39. ISSN: 02624079. DOI: 10.1016/S0262-4079(21)01518-9.

[8] David Deutsch and Roger Penrose. "Quantum theory, the Church–Turing principle and the universal quantum computer". In: *Proceedings of the Royal Society of London. A. Mathematical and Physical Sciences* 400.1818 (July 8, 1985). Publisher: Royal Society, pp. 97–117. DOI: 10.1098/rspa.1985.0070.

[9] John Preskill. *Quantum computing and the entanglement frontier*. Nov. 10, 2012. arXiv: 1203.5813[cond-mat,physics:quant-ph].

[10] Frank Arute et al. "Quantum supremacy using a programmable superconducting processor". In: *Nature* 574.7779 (Oct. 2019). Number: 7779 Publisher: Nature Publishing Group, pp. 505–510. ISSN: 1476-4687. DOI: 10.1038/s41586-019-1666-5.

[11] Han-Sen Zhong et al. "Quantum computational advantage using photons". In: *Science* 370.6523 (Dec. 18, 2020). Publisher: American Association for the Advancement of Science, pp. 1460–1463. DOI: 10.1126/science.abe8770.

[12] Emanuele Pelucchi et al. "The potential and global outlook of integrated photonics for quantum technologies". In: *Nat Rev Phys* 4.3 (Mar. 2022). Number: 3 Publisher: Nature Publishing Group, pp. 194–208. ISSN: 2522-5820. DOI: 10.1038/s42254-021-00398-z.

[13] Stephen Jordan. *Quantum Algorithm Zoo*. Quantum Algorithm Zoo. URL: https://quantumalgorithmzoo.org/ (visited on 08/17/2022).

[14] Lieven M. K. Vandersypen et al. “Experimental realization of Shor’s quantum factoring algorithm using nuclear magnetic resonance”. In: *Nature* 414.6866 (Dec. 2001). Number: 6866 Publisher: Nature Publishing Group, pp. 883–887. ISSN: 1476-4687. DOI: 10.1038/414883a.

[15] Stephan Gulde et al. “Implementation of the Deutsch–Jozsa algorithm on an ion-trap quantum computer”. In: *Nature* 421.6918 (Jan. 2003). Number: 6918 Publisher: Nature Publishing Group, pp. 48–50. ISSN: 1476-4687. DOI: 10.1038/nature01336.

[16] Kun Zhang et al. “Implementation of efficient quantum search algorithms on NISQ computers”. In: *Quantum Inf Process* 20.7 (July 10, 2021), p. 233. ISSN: 1573-1332. DOI: 10.1007/s11128-021-03165-2.

[17] Michel Dyakonov. “When will we have a quantum computer?” In: *Future Trends in Microelectronics: Vingt Ans Après*. Sardaigna, Italy, June 2018.

[18] IUrii Ivanovich Manin. *Vychislimoe i nevychislimoe [Computable and Noncomputable]*. OCLC: 11674220. Moskow: Sovetskoye Radio Press, 1980.

[19] Richard P. Feynman. “Simulating physics with computers”. In: *Int J Theor Phys* 21.6 (June 1, 1982), pp. 467–488. ISSN: 1572-9575. DOI: 10.1007/BF02650179.

[20] Richard P. Feynman, Robert B. Leighton, and Matthew Sands. *The Feynman Lectures on Physics, Vol. II: The New Millennium Edition: Mainly Electromagnetism and Matter*. New York: Basic Books, Oct. 4, 2011. 592 pp. ISBN: 978-0-465-02494-0.

[21] I. M. Georgescu, S. Ashhab, and Franco Nori. “Quantum simulation”. In: *Rev. Mod. Phys.* 86.1 (Mar. 10, 2014). Publisher: American Physical Society, pp. 153–185. DOI: 10.1103/RevModPhys.86.153.

[22] K. De Raedt et al. “Massively parallel quantum computer simulator”. In: *Computer Physics Communications* 176.2 (Jan. 15, 2007), pp. 121–136. ISSN: 0010-4655. DOI: 10.1016/j.cpc.2006.08.007.

[23] Luca D’Alessio et al. “From quantum chaos and eigenstate thermalization to statistical mechanics and thermodynamics”. In: *Advances in Physics* 65.3 (May 3, 2016). Publisher: Taylor & Francis _eprint: https://doi.org/10.1080/00018732.2016.1198134, pp. 239–362. ISSN: 0001-8732. DOI: 10.1080/00018732.2016.1198134.

[24] Fabien Alet and Nicolas Laflorencie. “Many-body localization: An introduction and selected topics”. In: *Comptes Rendus Physique*. Quantum simulation / Simulation quantique 19.6 (Sept. 1, 2018), pp. 498–525. ISSN: 1631-0705. DOI: 10.1016/j.crhy.2018.03.003.

[25] László Erdős, Benjamin Schlein, and Horng-Tzer Yau. “Rigorous Derivation of the Gross-Pitaevskii Equation”. In: *Phys. Rev. Lett.* 98.4 (Jan. 26, 2007). Publisher: American Physical Society, p. 040404. DOI: 10.1103/PhysRevLett.98.040404.

[26] J. Bardeen, L. N. Cooper, and J. R. Schrieffer. “Theory of Superconductivity”. In: *Phys. Rev.* 108.5 (Dec. 1, 1957). Publisher: American Physical Society, pp. 1175–1204. DOI: 10.1103/PhysRev.108.1175.

[27] Steven R. White. “Density matrix formulation for quantum renormalization groups”. In: *Phys. Rev. Lett.* 69.19 (Nov. 9, 1992). Publisher: American Physical Society, pp. 2863–2866. DOI: 10.1103/PhysRevLett.69.2863.

[28] C. J. Turner et al. “Weak ergodicity breaking from quantum many-body scars”. In: *Nature Phys* 14.7 (July 2018). Number: 7 Publisher: Nature Publishing Group, pp. 745–749. ISSN: 1745-2481. DOI: 10.1038/s41567-018-0137-5.

[29] Ehud Altman et al. "Quantum Simulators: Architectures and Opportunities". In: *PRX Quantum* 2.1 (Feb. 24, 2021). Publisher: American Physical Society, p. 017003. DOI: 10.1103/PRXQuantum.2.017003.

[30] M. H. Devoret, A. Wallraff, and J. M. Martinis. *Superconducting Qubits: A Short Review*. Nov. 6, 2004. DOI: 10.48550/arXiv.cond-mat/0411174. arXiv: cond-mat/0411174.

[31] Morten Kjaergaard et al. "Superconducting Qubits: Current State of Play". In: *Annual Review of Condensed Matter Physics* 11.1 (2020), pp. 369–395. DOI: 10.1146/annurev-conmatphys-031119-050605.

[32] Ruichao Ma et al. "A dissipatively stabilized Mott insulator of photons". In: *Nature* 566.7742 (Feb. 2019). Number: 7742 Publisher: Nature Publishing Group, pp. 51–57. ISSN: 1476-4687. DOI: 10.1038/s41586-019-0897-9.

[33] N. K. Langford et al. "Experimentally simulating the dynamics of quantum light and matter at deep-strong coupling". In: *Nat Commun* 8.1 (Nov. 23, 2017). Number: 1 Publisher: Nature Publishing Group, p. 1715. ISSN: 2041-1723. DOI: 10.1038/s41467-017-01061-x.

[34] C. Monroe et al. "Programmable quantum simulations of spin systems with trapped ions". In: *Rev. Mod. Phys.* 93.2 (Apr. 7, 2021). Publisher: American Physical Society, p. 025001. DOI: 10.1103/RevModPhys.93.025001.

[35] P. Jurcevic et al. "Quasiparticle engineering and entanglement propagation in a quantum many-body system". In: *Nature* 511.7508 (July 2014). Number: 7508 Publisher: Nature Publishing Group, pp. 202–205. ISSN: 1476-4687. DOI: 10.1038/nature13461.

[36] Justin G. Bohnet et al. "Quantum spin dynamics and entanglement generation with hundreds of trapped ions". In: *Science* 352.6291 (June 10, 2016). Publisher: American Association for the Advancement of Science, pp. 1297–1301. DOI: 10.1126/science.aad9958.

[37] Florian Schäfer et al. "Tools for quantum simulation with ultracold atoms in optical lattices". In: *Nat Rev Phys* 2.8 (Aug. 2020). Number: 8 Publisher: Nature Publishing Group, pp. 411–425. ISSN: 2522-5820. DOI: 10.1038/s42254-020-0195-3.

[38] Markus Greiner et al. "Quantum phase transition from a superfluid to a Mott insulator in a gas of ultracold atoms". In: *Nature* 415.6867 (Jan. 2002). Number: 6867 Publisher: Nature Publishing Group, pp. 39–44. ISSN: 1476-4687. DOI: 10.1038/415039a.

[39] Jacob F. Sherson et al. "Single-atom-resolved fluorescence imaging of an atomic Mott insulator". In: *Nature* 467.7311 (Sept. 2010). Number: 7311 Publisher: Nature Publishing Group, pp. 68–72. ISSN: 1476-4687. DOI: 10.1038/nature09378.

[40] Immanuel Bloch, Jean Dalibard, and Sylvain Nascimbène. "Quantum simulations with ultracold quantum gases". In: *Nature Phys* 8.4 (Apr. 2012). Number: 4 Publisher: Nature Publishing Group, pp. 267–276. ISSN: 1745-2481. DOI: 10.1038/nphys2259.

[41] Christian Gross and Immanuel Bloch. "Quantum simulations with ultracold atoms in optical lattices". In: *Science* 357.6355 (Sept. 8, 2017). Publisher: American Association for the Advancement of Science, pp. 995–1001. DOI: 10.1126/science.aal3837.

[42] M. Pasienski et al. "A disordered insulator in an optical lattice". In: *Nature Phys* 6.9 (Sept. 2010). Number: 9 Publisher: Nature Publishing Group, pp. 677–680. ISSN: 1745-2481. DOI: 10.1038/nphys1726.

[43] D. Frese et al. "Single Atoms in an Optical Dipole Trap: Towards a Deterministic Source of Cold Atoms". In: *Phys. Rev. Lett.* 85.18 (Oct. 30, 2000). Publisher: American Physical Society, pp. 3777–3780. DOI: 10.1103/PhysRevLett.85.3777.

[44] N. Schlosser et al. "Sub-poissonian loading of single atoms in a microscopic dipole trap". In: *Nature* 411.6841 (June 28, 2001), pp. 1024–1027. ISSN: 0028-0836. DOI: 10.1038/35082512.

[45] Manuel Endres et al. "Atom-by-atom assembly of defect-free one-dimensional cold atom arrays". In: *Science* 354.6315 (Nov. 25, 2016). Publisher: American Association for the Advancement of Science, pp. 1024–1027. DOI: 10.1126/science.aah3752.

[46] Daniel Barredo et al. "An atom-by-atom assembler of defect-free arbitrary two dimensional atomic arrays". In: *Science* 354.6315 (Nov. 25, 2016). Publisher: American Association for the Advancement of Science, pp. 1021–1023. DOI: 10.1126/science.aah3778.

[47] Pascal Scholl et al. "Quantum simulation of 2D antiferromagnets with hundreds of Rydberg atoms". In: *Nature* 595.7866 (July 2021). Number: 7866 Publisher: Nature Publishing Group, pp. 233–238. ISSN: 1476-4687. DOI: 10.1038/s41586-021-03585-1.

[48] Sepehr Ebadi et al. "Quantum phases of matter on a 256-atom programmable quantum simulator". In: *Nature* 595.7866 (July 2021). Number: 7866 Publisher: Nature Publishing Group, pp. 227–232. ISSN: 1476-4687. DOI: 10.1038/s41586-021-03582-4.

[49] Daniel Barredo et al. "Synthetic three-dimensional atomic structures assembled atom by atom". In: *Nature* 561.7721 (Sept. 2018). Number: 7721 Publisher: Nature Publishing Group, pp. 79–82. ISSN: 1476-4687. DOI: 10.1038/s41586-018-0450-2.

[50] Woojun Lee, Hyosub Kim, and Jaewook Ahn. "Three-dimensional rearrangement of single atoms using actively controlled optical microtraps". In: *Opt. Express, OE* 24.9 (May 2, 2016). Publisher: Optica Publishing Group, pp. 9816–9825. ISSN: 1094-4087. DOI: 10.1364/OE.24.009816.

[51] Nikolaus Lorenz et al. "Raman sideband cooling in optical tweezer arrays for Rydberg dressing". In: *SciPost Physics* 10.3 (Mar. 1, 2021), p. 052. ISSN: 2542-4653. DOI: 10.21468/SciPostPhys.10.3.052.

[52] M. A. Norcia, A. W. Young, and A. M. Kaufman. "Microscopic Control and Detection of Ultracold Strontium in Optical-Tweezer Arrays". In: *Phys. Rev. X* 8.4 (Dec. 28, 2018). Publisher: American Physical Society, p. 041054. DOI: 10.1103/PhysRevX.8.041054.

[53] Ivaylo S. Madjarov et al. "High-fidelity entanglement and detection of alkaline-earth Rydberg atoms". In: *Nat. Phys.* 16.8 (Aug. 2020). Number: 8 Publisher: Nature Publishing Group, pp. 857–861. ISSN: 1745-2481. DOI: 10.1038/s41567-020-0903-z.

[54] J. T. Wilson et al. "Trapping Alkaline Earth Rydberg Atoms Optical Tweezer Arrays". In: *Phys. Rev. Lett.* 128.3 (Jan. 20, 2022). Publisher: American Physical Society, p. 033201. DOI: 10.1103/PhysRevLett.128.033201.

[55] Hannes Bernien et al. "Probing many-body dynamics on a 51-atom quantum simulator". In: *Nature* 551.7682 (Nov. 2017). Number: 7682 Publisher: Nature Publishing Group, pp. 579–584. ISSN: 1476-4687. DOI: 10.1038/nature24622.

[56] Sylvain de Léséleuc et al. "Observation of a symmetry-protected topological phase of interacting bosons with Rydberg atoms". In: *Science* (Aug. 23, 2019). Publisher: American Association for the Advancement of Science. DOI: 10.1126/science.aav9105.

[57] Vincent Lienhard et al. "Observing the Space- and Time-Dependent Growth of Correlations in Dynamically Tuned Synthetic Ising Models with Antiferromagnetic Interactions". In: *Phys. Rev. X* 8.2 (June 18, 2018). Publisher: American Physical Society, p. 021070. DOI: 10.1103/PhysRevX.8.021070.

[58] G. Semeghini et al. "Probing topological spin liquids on a programmable quantum simulator". In: *Science* 374.6572 (Dec. 3, 2021). Publisher: American Association for the Advancement of Science, pp. 1242–1247. DOI: 10.1126/science.abi8794.

[59] Yunheung Song et al. "Quantum simulation of Cayley-tree Ising Hamiltonians with three-dimensional Rydberg atoms". In: *Phys. Rev. Research* 3.1 (Mar. 29, 2021). Publisher: American Physical Society, p. 013286. DOI: 10.1103/PhysRevResearch.3.013286.

[60] Sebastian Weber et al. "Tutorial: Calculation of Rydberg interaction potentials". In: *J. Phys. B: At. Mol. Opt. Phys.* 50.13 (July 14, 2017), p. 133001. ISSN: 0953-4075, 1361-6455. DOI: 10.1088/1361-6455/aa743a. arXiv: 1612.08053[physics,physics:quant-ph].

[61] A. W. Glaetzle et al. "Quantum Spin-Ice and Dimer Models with Rydberg Atoms". In: *Phys. Rev. X* 4.4 (Nov. 25, 2014). Publisher: American Physical Society, p. 041037. DOI: 10.1103/PhysRevX.4.041037.

[62] Antoine Browaeys and Thierry Lahaye. "Many-body physics with individually controlled Rydberg atoms". In: *Nat. Phys.* 16.2 (Feb. 2020). Number: 2 Publisher: Nature Publishing Group, pp. 132–142. ISSN: 1745-2481. DOI: 10.1038/s41567-019-0733-z.

[63] J. M. Kosterlitz. "The critical properties of the two-dimensional xy model". In: *J. Phys. C: Solid State Phys.* 7.6 (Mar. 1974). Publisher: IOP Publishing, pp. 1046–1060. ISSN: 0022-3719. DOI: 10.1088/0022-3719/7/6/005.

[64] B. Berge et al. "Phase transitions in two-dimensional uniformly frustrated XY spin systems". In: *Phys. Rev. B* 34.5 (Sept. 1, 1986). Publisher: American Physical Society, pp. 3177–3184. DOI: 10.1103/PhysRevB.34.3177.

[65] M. D. Lukin et al. "Dipole Blockade and Quantum Information Processing in Mesoscopic Atomic Ensembles". In: *Phys. Rev. Lett.* 87.3 (June 26, 2001). Publisher: American Physical Society, p. 037901. DOI: 10.1103/PhysRevLett.87.037901.

[66] D. Jaksch et al. "Fast Quantum Gates for Neutral Atoms". In: *Phys. Rev. Lett.* 85.10 (Sept. 4, 2000). Publisher: American Physical Society, pp. 2208–2211. DOI: 10.1103/PhysRevLett.85.2208.

[67] M. Saffman, T. G. Walker, and K. Mølmer. "Quantum information with Rydberg atoms". In: *Rev. Mod. Phys.* 82.3 (Aug. 18, 2010). Publisher: American Physical Society, pp. 2313–2363. DOI: 10.1103/RevModPhys.82.2313.

[68] Harry Levine et al. "High-Fidelity Control and Entanglement of Rydberg-Atom Qubits". In: *Phys. Rev. Lett.* 121.12 (Sept. 20, 2018). Publisher: American Physical Society, p. 123603. DOI: 10.1103/PhysRevLett.121.123603.

[69] T. M. Graham et al. "Rydberg-Mediated Entanglement in a Two-Dimensional Neutral Atom Qubit Array". In: *Phys. Rev. Lett.* 123.23 (Dec. 4, 2019). Publisher: American Physical Society, p. 230501. DOI: 10.1103/PhysRevLett.123.230501.

[70] Giuliano Giudici, Mikhail D. Lukin, and Hannes Pichler. "Dynamical Preparation of Quantum Spin Liquids in Rydberg Atom Arrays". In: *Phys. Rev. Lett.* 129.9 (Aug. 22, 2022). Publisher: American Physical Society, p. 090401. DOI: 10.1103/PhysRevLett.129.090401.

[71] R. Celistrino Teixeira et al. "Microwaves Probe Dipole Blockade and van der Waals Forces in a Cold Rydberg Gas". In: *Phys. Rev. Lett.* 115.1 (June 30, 2015). Publisher: American Physical Society, p. 013001. DOI: 10.1103/PhysRevLett.115.013001.

[72] Isabelle Bouchoule and Klaus Mølmer. "Spin squeezing of atoms by the dipole interaction in virtually excited Rydberg states". In: *Phys. Rev. A* 65.4 (Apr. 10, 2002). Publisher: American Physical Society, p. 041803. DOI: 10.1103/PhysRevA.65.041803.

[73] G. Pupillo et al. "Strongly Correlated Gases of Rydberg-Dressed Atoms: Quantum and Classical Dynamics". In: *Phys. Rev. Lett.* 104.22 (June 1, 2010). Publisher: American Physical Society, p. 223002. DOI: 10.1103/PhysRevLett.104.223002.

[74] J. E. Johnson and S. L. Rolston. "Interactions between Rydberg-dressed atoms". In: *Phys. Rev. A* 82.3 (Sept. 14, 2010). Publisher: American Physical Society, p. 033412. DOI: 10.1103/PhysRevA.82.033412.

[75] Johannes Zeiher et al. "Coherent Many-Body Spin Dynamics in a Long-Range Interacting Ising Chain". In: *Phys. Rev. X* 7.4 (Dec. 14, 2017). Publisher: American Physical Society, p. 041063. DOI: 10.1103/PhysRevX.7.041063.

[76] Johannes Zeiher et al. "Many-body interferometry of a Rydberg-dressed spin lattice". In: *Nature Phys* 12.12 (Dec. 2016). Number: 12 Publisher: Nature Publishing Group, pp. 1095–1099. ISSN: 1745-2481. DOI: 10.1038/nphys3835.

[77] Lea-Marina Steinert et al. *Spatially programmable spin interactions in neutral atom arrays*. June 24, 2022. DOI: 10.48550/arXiv.2206.12385. arXiv: 2206.12385[cond-mat,physics:physics,physics:quant-ph].

[78] Alessio Celi et al. "Emerging Two-Dimensional Gauge Theories in Rydberg Configurable Arrays". In: *Phys. Rev. X* 10.2 (June 16, 2020). Publisher: American Physical Society, p. 021057. DOI: 10.1103/PhysRevX.10.021057.

[79] Hannes Pichler et al. *Quantum Optimization for Maximum Independent Set Using Rydberg Atom Arrays*. Aug. 31, 2018. DOI: 10.48550/arXiv.1808.10816. arXiv: 1808.10816[cond-mat,physics:physics,physics:quant-ph].

[80] S. Ebadi et al. "Quantum optimization of maximum independent set using Rydberg atom arrays". In: *Science* 376.6598 (June 10, 2022). Publisher: American Association for the Advancement of Science, pp. 1209–1215. DOI: 10.1126/science.abo6587.

[81] Thanh Long Nguyen. "Study of dipole-dipole interaction between Rydberg atoms : toward quantum simulation with Rydberg atoms". These de doctorat. Paris 6, Nov. 18, 2016.

[82] S. K. Dutta et al. "Ponderomotive Optical Lattice for Rydberg Atoms". In: *Phys. Rev. Lett.* 85.26 (Dec. 25, 2000). Publisher: American Physical Society, pp. 5551–5554. DOI: 10.1103/PhysRevLett.85.5551.

[83] S. E. Anderson, K. C. Younge, and G. Raithel. "Trapping Rydberg Atoms in an Optical Lattice". In: *Phys. Rev. Lett.* 107.26 (Dec. 20, 2011). Publisher: American Physical Society, p. 263001. DOI: 10.1103/PhysRevLett.107.263001.

[84] D. Barredo et al. "Three-Dimensional Trapping of Individual Rydberg Atoms in Ponderomotive Bottle Beam Traps". In: *Phys. Rev. Lett.* 124.2 (Jan. 16, 2020). Publisher: American Physical Society, p. 023201. DOI: 10.1103/PhysRevLett.124.023201.

[85] R. G. Cortiñas et al. "Laser Trapping of Circular Rydberg Atoms". In: *Phys. Rev. Lett.* 124.12 (Mar. 23, 2020). Publisher: American Physical Society, p. 123201. DOI: 10.1103/PhysRevLett.124.123201.

[86] R. M. Potvliege and C. S. Adams. "Photo-ionization in far-off-resonance optical lattices". In: *New J. Phys.* 8.8 (Aug. 2006). Publisher: IOP Publishing, pp. 163–163. ISSN: 1367-2630. DOI: 10.1088/1367-2630/8/8/163.

[87] R. Cardman et al. "Photoionization of Rydberg atoms in optical lattices". In: *New J. Phys.* 23.6 (June 2021). Publisher: IOP Publishing, p. 063074. ISSN: 1367-2630. DOI: 10.1088/1367-2630/ac07ca.

[88] P. Avan et al. "Effect of high frequency irradiation on the dynamical properties of weakly bound electrons". In: *J. Phys. France* 37.9 (Sept. 1, 1976). Publisher: Société Française de Physique, pp. 993–1009. ISSN: 0302-0738, 2777-3396. DOI: 10.1051/jphys:01976003709099300.

[89] Sam R. Cohen and Jeff D. Thompson. "Quantum Computing with Circular Rydberg Atoms". In: *PRX Quantum* 2.3 (Aug. 6, 2021). Publisher: American Physical Society, p. 030322. DOI: 10.1103/PRXQuantum.2.030322.

[90] T. L. Nguyen et al. "Towards Quantum Simulation with Circular Rydberg Atoms". In: *Phys. Rev. X* 8.1 (Feb. 26, 2018). Publisher: American Physical Society, p. 011032. DOI: 10.1103/PhysRevX.8.011032.

[91] P. Scholl et al. "Microwave Engineering of Programmable XXZ Hamiltonians in Arrays of Rydberg Atoms". In: *PRX Quantum* 3.2 (Apr. 5, 2022). Publisher: American Physical Society, p. 020303. DOI: 10.1103/PRXQuantum.3.020303.

[92] Daniel Kleppner. "Inhibited Spontaneous Emission". In: *Phys. Rev. Lett.* 47.4 (July 27, 1981). Publisher: American Physical Society, pp. 233–236. DOI: 10.1103/PhysRevLett.47.233.

[93] Randall G. Hulet, Eric S. Hilfer, and Daniel Kleppner. "Inhibited Spontaneous Emission by a Rydberg Atom". In: *Phys. Rev. Lett.* 55.20 (Nov. 11, 1985). Publisher: American Physical Society, pp. 2137–2140. DOI: 10.1103/PhysRevLett.55.2137.

[94] T. Cantat-Moltrecht et al. "Long-lived circular Rydberg states of laser-cooled rubidium atoms in a cryostat". In: *Phys. Rev. Research* 2.2 (May 7, 2020). Publisher: American Physical Society, p. 022032. DOI: 10.1103/PhysRevResearch.2.022032.

[95] Haiteng Wu. "Millisecond-lived Circular Rydberg Atoms in a Room Temperature Experiment". PhD thesis. 2022.

[96] Rodrigo Gastón Cortiñas. "Laser trapped Circular Rydberg atoms for quantum simulation". PhD thesis. Université Paris sciences et lettres, May 5, 2020.

[97] Yohann Machu. PhD thesis. 2024.

[98] Tigrane Cantat-Moltrecht. "Atomes de Rydberg en interaction : des nuages denses d'atomes de Rydberg à la simulation quantique avec des atomes circulaires". PhD thesis. Ecole Normale Supérieure, Paris ; PSL Research University, Jan. 11, 2018.

[99] Harold J. Metcalf and Peter Van Der Straten. *Laser Cooling and Trapping*. New York: Springer-Verlag New York Inc., Nov. 1, 1999. 339 pp. ISBN: 978-0-387-98747-7.

[100] Ingolf V. Hertel and Claus-Peter Schulz. *Atoms, Molecules and Optical Physics 1: Atoms and Spectroscopy*. 2015th edition. Heidelberg Berlin: Springer, Nov. 13, 2014. 726 pp. ISBN: 978-3-642-54321-0.

[101] Thomas F. Gallagher. *Rydberg Atoms*. Cambridge Monographs on Atomic, Molecular and Chemical Physics. Cambridge: Cambridge University Press, 1994. ISBN: 978-0-521-02166-1. DOI: 10.1017/CBO9780511524530.

[102] E. Schrödinger. "An Undulatory Theory of the Mechanics of Atoms and Molecules". In: *Phys. Rev.* 28.6 (Dec. 1, 1926), pp. 1049–1070. ISSN: 0031-899X. DOI: 10.1103/PhysRev.28.1049.

[103] G. E. Uhlenbeck and S. Goudsmit. "Spinning Electrons and the Structure of Spectra". In: *Nature* 117.2938 (Feb. 1926), pp. 264–265. ISSN: 0028-0836, 1476-4687. DOI: 10.1038/117264a0.

[104] Albert Messiah. *Quantum Mechanics*. OCLC: 874097814. Dover Publications, 2014. ISBN: 978-0-486-78455-7.

[105] Willis E. Lamb and Robert C. Retherford. "Fine Structure of the Hydrogen Atom by a Microwave Method". In: *Phys. Rev.* 72.3 (Aug. 1, 1947). Publisher: American Physical Society, pp. 241–243. DOI: 10.1103/PhysRev.72.241.

[106] G. Breit and G. E. Brown. "Effect of Nuclear Motion on the Fine Structure of Hydrogen". In: *Phys. Rev.* 74.10 (Nov. 15, 1948). Publisher: American Physical Society, pp. 1278–1284. DOI: 10.1103/PhysRev.74.1278.

[107] Daniel A. Steck. "Rubidium 87 D Line Data". In: (Jan. 1, 2003).

[108] Steven Weinberg. *The Quantum Theory Of Fields: Foundations - Vol 1*. Cambridge: Cambridge University Press, June 2, 2005. 636 pp. ISBN: 978-0-521-67053-1.

[109] John M. Harriman. "Numerical Values for Hydrogen Fine Structure". In: *Phys. Rev.* 101.2 (Jan. 15, 1956). Publisher: American Physical Society, pp. 594–598. DOI: 10.1103/PhysRev.101.594.

[110] S. Klarsfeld and A. Maquet. "Bethe sums for Lamb shift calculations in higher excited states". In: *Physics Letters B* 43.3 (Feb. 5, 1973), pp. 201–203. ISSN: 0370-2693. DOI: 10.1016/0370-2693(73)90268-2.

[111] Hans A. Bethe and Edwin E. Salpeter. *Quantum Mechanics of One-And Two-Electron Atoms*. Softcover reprint of the original 1st ed. 1977 édition. New York: Kluwer Academic/Plenum Publishers, Apr. 30, 1977. 370 pp. ISBN: 978-0-306-20022-9.

[112] M. J. Seaton. "Quantum defect theory". In: *Rep. Prog. Phys.* 46.2 (Feb. 1983). Publisher: IOP Publishing, pp. 167–257. ISSN: 0034-4885. DOI: 10.1088/0034-4885/46/2/002.

[113] David Robert Bates, Agnete Damgaard, and Harrie Stewart Wilson Massey. "The calculation of the absolute strengths of spectral lines". In: *Philosophical Transactions of the Royal Society of London. Series A, Mathematical and Physical Sciences* 242.842 (Jan. 1949). Publisher: Royal Society, pp. 101–122. DOI: 10.1098/rsta.1949.0006.

[114] V. Alan Kostelecký and Michael Martin Nieto. "Analytical wave functions for atomic quantum-defect theory". In: *Phys. Rev. A* 32.6 (Dec. 1, 1985). Publisher: American Physical Society, pp. 3243–3246. DOI: 10.1103/PhysRevA.32.3243.

[115] M. J. Seaton. "Quantum defect theory I. General formulation". In: *Proc. Phys. Soc.* 88.4 (Aug. 1966). Publisher: IOP Publishing, pp. 801–814. ISSN: 0370-1328. DOI: 10.1088/0370-1328/88/4/302.

[116] Dieter Meschede. "Centimeter-wave spectroscopy of highly excited rubidium atoms". In: *J. Opt. Soc. Am. B, JOSAB* 4.3 (Mar. 1, 1987). Publisher: Optica Publishing Group, pp. 413–419. ISSN: 1520-8540. DOI: 10.1364/JOSAB.4.000413.

[117] Wenhui Li et al. "Millimeter-wave spectroscopy of cold Rb Rydberg atoms in a magneto-optical trap: Quantum defects of the ns, np, and nd series". In: *Phys. Rev. A* 67.5 (May 13, 2003). Publisher: American Physical Society, p. 052502. DOI: 10.1103/PhysRevA.67.052502.

[118] Jianing Han et al. "Rb nf quantum defects from millimeter-wave spectroscopy of cold $^{85}\mathrm{Rb}$ Rydberg atoms". In: *Phys. Rev. A* 74.5 (Nov. 16, 2006). Publisher: American Physical Society, p. 054502. DOI: 10.1103/PhysRevA.74.054502.

[119] Markus Mack et al. "Measurement of absolute transition frequencies of ^{87}Rb to nS and nD Rydberg states by means of electromagnetically induced transparency". In: *Phys. Rev. A* 83.5 (May 23, 2011). Publisher: American Physical Society, p. 052515. DOI: 10.1103/PhysRevA.83.052515.

[120] Silpa B. S et al. "Transition frequency measurement of highly excited Rydberg states of ^{87}Rb for a wide range of principal quantum numbers". In: *Opt. Continuum, OPTCON* 1.5 (May 15, 2022). Publisher: Optica Publishing Group, pp. 1176–1192. ISSN: 2770-0208. DOI: 10.1364/OPTCON.458153.

[121] Arno Bohm. *Quantum Mechanics: Foundations and Applications*. Softcover reprint of the original 3rd ed. 1993 edition. New York: Springer, July 27, 2001. 707 pp. ISBN: 978-0-387-95330-4.

[122] N. Šibalić et al. "ARC: An open-source library for calculating properties of alkali Rydberg atoms". In: *Computer Physics Communications* 220 (Nov. 1, 2017), pp. 319–331. ISSN: 0010-4655. DOI: 10.1016/j.cpc.2017.06.015.

[123] I. I. Ryabtsev et al. "Coherence of three-body Förster resonances in Rydberg atoms". In: *Phys. Rev. A* 98.5 (Nov. 13, 2018). Publisher: American Physical Society, p. 052703. DOI: 10.1103/PhysRevA.98.052703.

[124] Maria Göppert-Mayer. "Über Elementarakte mit zwei Quantensprüngen". In: *Annalen der Physik* 401.3 (1931), pp. 273–294. ISSN: 1521-3889. DOI: 10.1002/andp.19314010303.

[125] Makoto Morinaga. *Deriving the static interaction between electric dipoles via the quantum gauge transformation*. Feb. 14, 2013. DOI: 10.48550/arXiv.1302.0920. arXiv: 1302.0920[physics,physics:quant-ph].

[126] Claude Cohen-Tannoudji, Jacques Dupont-Roc, and Gilbert Grynberg. *Photons and Atoms: Introduction to Quantum Electrodynamics*. New e. édition. Weinheim: John Wiley & Sons, Feb. 24, 1997. 488 pp. ISBN: 978-0-471-18433-1.

[127] Randall G. Hulet and Daniel Kleppner. "Rydberg Atoms in "Circular" States". In: *Phys. Rev. Lett.* 51.16 (Oct. 17, 1983). Publisher: American Physical Society, pp. 1430–1433. DOI: 10.1103/PhysRevLett.51.1430.

[128] Claude Cohen-Tannoudji, Jacques Dunpont-Roc, and Gilbert Grynberg. *Atom-Photon Interactions: Basic Process and Applications*. Reprint édition. New York: Wiley-VCH, Mar. 30, 2010. 680 pp. ISBN: 978-0-471-29336-1.

[129] M. J. Englefield. *Group Theory and the Coulomb Problem*. New York: John Wiley & Sons, Jan. 1, 1972. 120 pp. ISBN: 978-0-471-24165-2.

[130] Jan R. Rubbmark et al. "Dynamical effects at avoided level crossings: A study of the Landau-Zener effect using Rydberg atoms". In: *Phys. Rev. A* 23.6 (June 1, 1981). Publisher: American Physical Society, pp. 3107–3117. DOI: 10.1103/PhysRevA.23.3107.

[131] Rudolf Grimm, Matthias Weidemüller, and Yurii B. Ovchinnikov. "Optical Dipole Traps for Neutral Atoms". In: *Advances In Atomic, Molecular, and Optical Physics*. Ed. by Benjamin Bederson and Herbert Walther. Vol. 42. Academic Press, Jan. 1, 2000, pp. 95–170. DOI: 10.1016/S1049-250X(08)60186-X.

[132] R. W. Gerchberg and W. O. Saxton. "A Practical Algorithm for the Determination of Phase from Image and Diffraction Plane Pictures". In: *Optik* 35.2 (1971), pp. 237–246.

[133] Dorian Grosso. "Des atomes froids pour sonder et manipuler des photons piégés". These de doctorat. Paris 6, Dec. 1, 2017.

[134] C. Tuchendler et al. "Energy distribution and cooling of a single atom in an optical tweezer". In: *Phys. Rev. A* 78.3 (Sept. 23, 2008). Publisher: American Physical Society, p. 033425. DOI: 10.1103/PhysRevA.78.033425.

[135] Paul Méhaignerie, Guillaume Roux, and Michel Brune. "Dynamics of two trapped circular Rydberg atoms under realistic experimental conditions". In: ().

[136] S. J. M. Kuppens et al. "Loading an optical dipole trap". In: *Phys. Rev. A* 62.1 (June 13, 2000). Publisher: American Physical Society, p. 013406. DOI: 10.1103/PhysRevA.62.013406.

[137] A. Fuhrmanek et al. "Light-assisted collisions between a few cold atoms in a microscopic dipole trap". In: *Phys. Rev. A* 85.6 (June 25, 2012). Publisher: American Physical Society, p. 062708. DOI: 10.1103/PhysRevA.85.062708.

[138] George A. F. Seber. *Nonlinear Regression*. New e. édition. Hoboken, N.J: Wiley-Interscience, Sept. 5, 2003. 800 pp. ISBN: 978-0-471-47135-6.

[139] M. Saffman and T. G. Walker. "Analysis of a quantum logic device based on dipole-dipole interactions of optically trapped Rydberg atoms". In: *Phys. Rev. A* 72.2 (Aug. 31, 2005). Publisher: American Physical Society, p. 022347. DOI: 10.1103/PhysRevA.72.022347.

[140] Roee Ozeri, Lev Khaykovich, and Nir Davidson. "Long spin relaxation times in a single-beam blue-detuned optical trap". In: *Phys. Rev. A* 59.3 (Mar. 1, 1999). Publisher: American Physical Society, R1750–R1753. DOI: 10.1103/PhysRevA.59.R1750.

[141] Ira Levine. *Quantum Chemistry*. 7th edition. Boston: Pearson, Feb. 6, 2013. 720 pp. ISBN: 978-0-321-80345-0.

[142] E. A. Donley et al. "Double-pass acousto-optic modulator system". In: *Review of Scientific Instruments* 76.6 (June 2005). Publisher: American Institute of Physics, p. 063112. ISSN: 0034-6748. DOI: 10.1063/1.1930095.

[143] R. W. P. Drever et al. "Laser phase and frequency stabilization using an optical resonator". In: *Appl. Phys. B* 31.2 (June 1, 1983), pp. 97–105. ISSN: 1432-0649. DOI: 10.1007/BF00702605.

[144] Y. Park et al. "Work function of indium tin oxide transparent conductor measured by photoelectron spectroscopy". In: *Appl. Phys. Lett.* 68.19 (May 6, 1996). Publisher: American Institute of Physics, pp. 2699–2701. ISSN: 0003-6951. DOI: 10.1063/1.116313.

[145] Antoine Kahn. "Fermi level, work function and vacuum level". In: *Materials Horizons* 3.1 (2016). Publisher: Royal Society of Chemistry, pp. 7–10. DOI: 10.1039/C5MH00160A.

[146] Paul Horowitz and Winfield Hill. *The Art of Electronics*. 3e édition. New York, NY: Cambridge University Press, Mar. 30, 2015. 1220 pp. ISBN: 978-0-521-80926-9.

[147] Paul Horowitz and Winfield Hill. *The Art of Electronics: The x Chapters*. Cambridge ; New York, NY: Cambridge University Press, Jan. 30, 2020. 522 pp. ISBN: 978-1-108-49994-1.

[148] *Rejection sampling*. In: *Wikipedia*. Page Version ID: 1116989498. Oct. 19, 2022.

[149] Lorenza Viola and Seth Lloyd. "Dynamical suppression of decoherence in two-state quantum systems". In: *Phys. Rev. A* 58.4 (Oct. 1, 1998). Publisher: American Physical Society, pp. 2733–2744. DOI: 10.1103/PhysRevA.58.2733.

[150] Lorenza Viola, Emanuel Knill, and Seth Lloyd. "Dynamical Decoupling of Open Quantum Systems". In: *Phys. Rev. Lett.* 82.12 (Mar. 22, 1999). Publisher: American Physical Society, pp. 2417–2421. DOI: 10.1103/PhysRevLett.82.2417.

RÉSUMÉ

La simulation quantique offre des perspectives intéressantes pour la compréhension de systèmes complexes dans des régimes qui se prêtent difficilement à une approche numérique du problème. Dans cette perspective, une nouvelle architecture de simulateur quantique a récemment été proposée. Celle-ci modélise un hamiltonien *XXZ* à spin 1/2 dont les paramètres peuvent être contrôlés sur une large gamme. Les états de spin sont encodés sur des états de Rydberg circulaires en interaction dipolaire. Ceux-ci présentent des temps de vie plus longs que les états correspondants de bas moment angulaire utilisés actuellement pour réaliser des simulations quantiques. En outre ils peuvent être piégés par laser en tirant profit de l'effet pondéromoteur, et voir leur temps de vie augmenté considérablement par l'inhibition de l'émission spontanée.

Nous présentons dans cette thèse la première étape vers la mise en place ce simulateur quantique. Nous préparons dans un premier temps un tableau d'atomes de rubidium 87 piégés individuellement dans des pinces optiques. Ceux-ci sont alors excités vers l'état de Rydberg circulaire $n = 52$ et transférés dans des pièges creux en forme de bouteille. Nous mettons ainsi en évidence le piégeage pondéromoteur de ces états sur des durées de plusieurs millisecondes. Nous tirons ensuite profit de la détection optique des états ainsi préparés au cours de diverses expériences. Le potentiel de piégeage est caractérisé en mesurant sa fréquence d'oscillation transverse de chaque piège. Enfin, nous concluons en réalisant la manipulation cohérente de ces états circulaires piégés au travers d'oscillations de Rabi ainsi que la mesure de franges de Ramsey pour déterminer leur cohérence.

MOTS CLÉS

atomes de Rydberg, atomes froids, simulation quantique, atomes de Rydberg circulaires, spectroscopie, pinces optiques, piégeage dipolaire, piégeage pondéromoteur

ABSTRACT

Quantum simulation offers interesting perspectives for the understanding of complex systems that are out of reach for numerical approaches. In this line, a new quantum simulation platform has recently been proposed. A spin-1/2 *XXZ* hamiltonian is thus realized in which the parameters can be controlled over a large range. The spin states are encoded by circular Rydberg states coupled through dipole-dipole interaction. These states benefit from longer lifetimes compared to the low angular momentum states used for current quantum simulations. In addition, they can be laser-trapped through the ponderomotive effect, and their lifetime can be further enhanced by spontaneous emission inhibition.

We present in this thesis the first step towards the implementation of the proposed quantum simulator. We first prepare an array of rubidium 87 atoms trapped individually in optical tweezers. These atoms are subsequently excited to the circular Rydberg state $n = 52$ and transferred to hollow bottle-beam traps. We thus demonstrate the ponderomotive trapping of these states over durations of several milliseconds. We take advantage of the optical detection of the states thus prepared with various experiments. We characterize the trapping potential by measuring its transverse frequency. We finally conclude with the coherent manipulation of these trapped circular states through Rabi oscillations and Ramsey interferometry to determine their coherence.

KEYWORDS

Rydberg atoms, cold atoms, quantum simulation, circular Rydberg atoms, spectroscopy, optical tweezers, dipole trap, ponderomotive trapping